TESIS DE LA UNIVERSIDAD DE ZARAGOZA

2017

79

Clara Rivas Alonso

Estudio termodinámico de sistemas ricos en CO_2 en condiciones de interés para la tecnología CCS

Departamento
Química Física

Director/es
Blanco Ariño, Sofía Teresa
Artal Lerín, Manuela

ISSN 2254-7606

Prensas de la Universidad
Universidad Zaragoza

ISSN 2254-7606

Universidad Zaragoza
1542

Tesis Doctoral

ESTUDIO TERMODINÁMICO DE SISTEMAS RICOS EN CO_2 EN CONDICIONES DE INTERÉS PARA LA TECNOLOGÍA CCS

Autor

Clara Rivas Alonso

Director/es

Blanco Ariño, Sofía Teresa
Artal Lerín, Manuela

UNIVERSIDAD DE ZARAGOZA

Química Física

2017

Universidad Zaragoza
1542

FACULTAD DE CIENCIAS
DEPARTAMENTO DE QUÍMICA FÍSICA

TESIS DOCTORAL

ESTUDIO TERMODINÁMICO DE SISTEMAS RICOS EN CO_2 EN CONDICIONES DE INTERÉS PARA LA TECNOLOGÍA CCS

CLARA RIVAS ALONSO
ZARAGOZA 2017

A mis padres, Ángeles y Miguel,
por su amor, su apoyo y su constante lección de vida,
no podría contar con dos mejores maestros.

A mi "hada madrina", Ángeles Vielba,
por su infinito amor incondicional y libre.

A la memoria de mi abuela, Esteli Llana,
una pequeña castellana
de sabiduría innata a la que tanto añoro.

Gracias,

Al Ministerio de Educación, Cultura y Deporte, a la DGA a la Universidad de Zaragoza y a la Caixa por aportar la financiación necesaria a través de diversos proyectos para poder abordar cada uno de los trabajos de investigación que conforman esta Tesis.

A todos y cada uno de los miembros que integraban el Grupo Especializado en Termodinámica Teórica y Aplicada de la Facultad de Ciencias de la Universidad de Zaragoza, por dejarme formar parte de su grupo y por todos los felices momentos que compartimos.

En especial, a las Dras. Manuela Artal Lerín y Sofía Teresa Blanco Ariño, por dirigirme en esta larga andadura, por su paciencia y sus sabias indicaciones.

A todos los compañeros del Departamento de Química Física.

A mis compañeros de SELECT BOTANICAL, a las que ya se fueron pero se han convertido en parte de mi vida, Sara y Natalia, y a los que cada día continúan trabajando codo a codo conmigo luchando en esta difícil y apasionante tarea que supone el mundo de los extractos vegetales: a Bea, Bego, Guille, Jorge, Nati, Paco, Ricardo, Rosana, y a todos los demás, gracias por estar ahí de una manera u otra. Gracias en especial a Antonio Rubiralta que confió en mí y me brindó la oportunidad de subir a este barco en el que navegamos.

A mi familia, mis tíos, Nin y Mª José, mi prima Judith y David y sus dos pequeñas princesas, Ingrid y Paula y a mi "familia de vida": Julia, Pedro, Paula y Miguel.

A mis amigas del "cole", Gaby y Alexandra, por vuestra preciosa amistad después de tantos años.

A todos los amigos que me han escuchado y apoyado y que siempre han confiado en que algún día estaría escribiendo estas líneas: Almu, Bea, Betty, Cris, Guillermo, Luisa, Mery, Patricia, Pilar, Sergio, "mi tía Toñi", Xavi,…

A Josean, que apareció al final de esta aventura, con quien siento cada día que "la química" es mucho más que ciencia.

Y por último, a Paula Marugán, "mi persona favorita", por su amistad, su amor y su apoyo incondicional. Mi historia no podría contarse sin ti a mi lado.

ESTA TESIS DOCTORAL HA SIDO ESCRITA EN LA MODALIDAD DE COMPENDIO DE TRABAJOS PREVIAMENTE PUBLICADOS Y SU ESTRUCTURA, RECOGIDA EN EL ÍNDICE, SE AJUSTA A LA NORMATIVA VIGENTE. LAS PUBLICACIONES PRESENTADAS SON LAS SIGUIENTES:

- Inmaculada Velasco, Clara Rivas, José F. Martínez-López, Sofía T. Blanco, Santos Otín and Manuela Artal. **Accurate Values of Some Thermodynamic Properties for Carbon Dioxide, Ethane, Propane and Some Binary Mixtures**. *Journal of Physical Chemistry B*. 2011, 115, 8216-8230.

- Sofía, T. Blanco, Clara Rivas, Javier Fernández, Manuela Artal and Inmaculada Velasco. **Influence of Methane in CO_2 Transport and Storage for CCS Technology**. *Environmental Science &Technology.* 2012, 46, 13016-13023.

- Clara Rivas, Sofía T. Blanco, Javier Fernández, Manuela Artal, Inmaculada Velasco. **Influence of methane and carbon monoxide in the volumetric behaviour of the anthropogenic CO_2: Experimental data and modelling in the critical region**. *International Journal of Greenhouse Gas Control*. 2013, 18, 264-276.

- Sofía T. Blanco, Clara Rivas, Ramón Bravo, Javier Fernández, Manuela Artal and Inmaculada Velasco. **Discussion of the Influence of CO and CH_4 in CO_2 Transport, Injection and Storage for CCS Technology**. *Environmental Science &Technology*. 2014, 48, 10984-10992.

- Clara Rivas, Beatriz Gimeno, Ramón Bravo, Manuela Artal, Javier Fernández, Sofía Teresa Blanco, María Inmaculada Velasco. **Thermodynamic properties of a CO_2-rich mixture (CO_2+CH_3OH) in conditions of interest for carbon dioxide capture and storage technology and other applications.** *Journal of Chemical Thermodynamics*. 2016, 98, 272-281.

INFORME DIRECTORES

AUTORIZACIÓN PRESENTACIÓN DE TESIS DOCTORAL EN MODALIDAD DE COMPENDIO DE PUBLICACIONES

Dª MANUELA ARTAL LERÍN, Profesora Titular del Departamento de Química Física de la Universidad de Zaragoza y Dª SOFÍA TERESA BLANCO ARIÑO, Profesora Titular del Departamento de Química Física de la Universidad de Zaragoza,

AUTORIZAN

La presentación en la modalidad de compendio de publicaciones de la siguiente memoria de Tesis Doctoral titulada:

"Estudio termodinámico de sistemas ricos en CO_2 en condiciones de interés para la tecnología CCS", presentada por Dª CLARA RIVAS ALONSO para optar al Grado de Doctor por la Universidad de Zaragoza, y

HACEN CONSTAR

Que ha sido realizada bajo su dirección en el Departamento de Química Física (Facultad de Ciencias) de la Universidad de Zaragoza.

Y para que conste a los efectos oportunos expiden la presente autorización

En Zaragoza, a 23 de Marzo de 2017

Fdo.: Manuela Artal Lerín

Fdo.: Sofía T. Blanco Ariño

INFORME MOTIVADO DE LA COMISIÓN ACADÉMICA DE DOCTORADO

Dª MARÍA INMACULADA VELASCO ALBILLOS, Presidente de la Comisión Académica de Doctorado del Programa de Doctorado de Química Física de la Universidad de Zaragoza,

CERTIFICA:

Que el trabajo correspondiente a la presente Memoria titulada:

"Estudio termodinámico de sistemas ricos en CO_2 en condiciones de interés para la tecnología CCS"

Ha sido realizada en dicho Departamento por Dª Clara Rivas Alonso bajo la dirección de las Dras. Dª Manuela Artal Lerín y Dª Sofía Teresa Blanco Ariño, para optar al grado de Doctor.

En Zaragoza, a 29 de Marzo de 2017

Fdo.: Mª Inmaculada Velasco Albillos

ÍNDICE

Índice

INTRODUCCIÓN

1. INTRODUCCIÓN

Uno de los mecanismos que posibilitan la vida en la Tierra es el efecto invernadero. Parte de la radiación emitida por el Sol que llega a nuestro planeta es reflejada por los gases atmosféricos y devuelta al espacio exterior, pero la mayoría penetra en la propia atmósfera. Una fracción es absorbida por los propios gases y la otra por la superficie terrestre. Asimismo, la Tierra emite radiación infrarroja que es a su vez reflejada, absorbida o transmitida por ciertos gases atmosféricos. La fracción de radiación absorbida por tales gases contribuye al denominado efecto invernadero, que posibilita mantener la temperatura media del planeta en márgenes muy uniformes y compatibles con las formas actuales de vida. El aumento en la concentración de esos compuestos participativos, denominados GEI –gases de efecto invernadero- ocasiona una mayor opacidad infrarroja de la atmósfera, con lo que se produce un efecto invernadero intensificado. Si los niveles de estos compuestos ascienden demasiado, un calentamiento excesivo puede trastornar las pautas naturales del clima. Las concentraciones de GEI tales como dióxido de carbono, metano y óxido nitroso han aumentado, sobre todo, por la utilización de combustibles fósiles, la deforestación y otras actividades humanas, promovidas por el crecimiento económico y demográfico y son en la actualidad muy superiores a los valores preindustriales.

El potencial de calentamiento ambiental, PCA, más conocido en su terminología inglesa como GWP (Global Warming Potential) es el calentamiento que produce la liberación de un kilogramo de un gas de efecto invernadero en relación con el causado por un kilogramo de CO_2 en un periodo de 100 años. Si bien el CO_2 es el GEI que menos potencial de calentamiento atmosférico tiene, 1 frente a 21 el metano, 310 el óxido nitroso y hasta 23900 el hexafluoruro de azufre,[65] la cantidad de CO_2 emitida a la atmósfera es mucho mayor que la de cualquier otro gas, lo que hace que el porcentaje del efecto invernadero debido al CO_2 sea, con diferencia el mayor de todos.

Este efecto tiene como consecuencia un aumento de la temperatura terrestre y del nivel de los océanos e incide directamente sobre el calentamiento global y el cambio climático. En las Figuras 1a) y 1b) se observa el cambio en la temperatura del globo terráqueo desde 1884 hasta 2015 .[40]

Así pues, la reducción de las emisiones de CO_2 producido por actividades humanas, CO_2 antropogénico, es un tema de vital importancia que atañe a todos los seres vivos del planeta.

a)

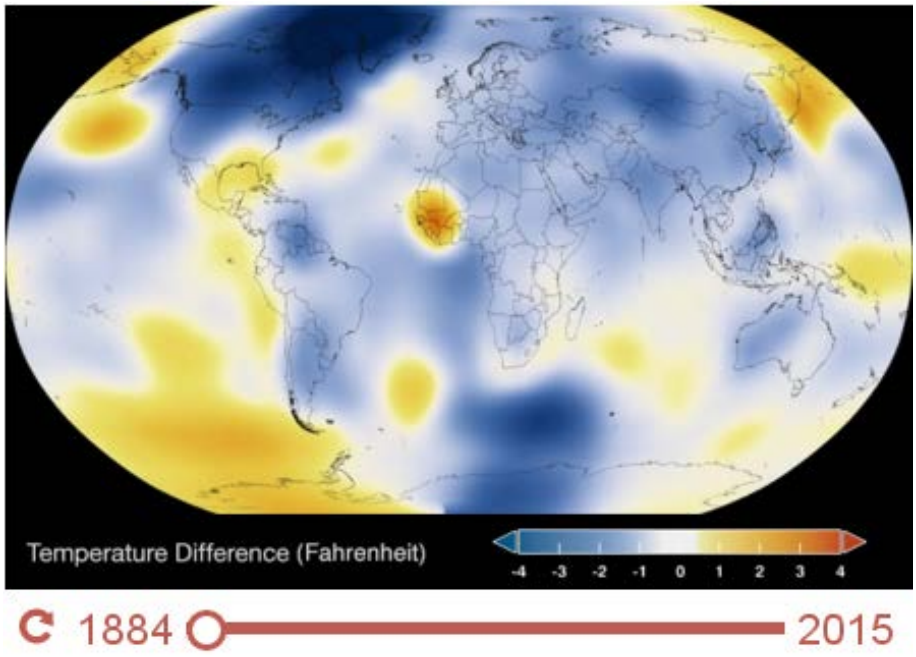

b)

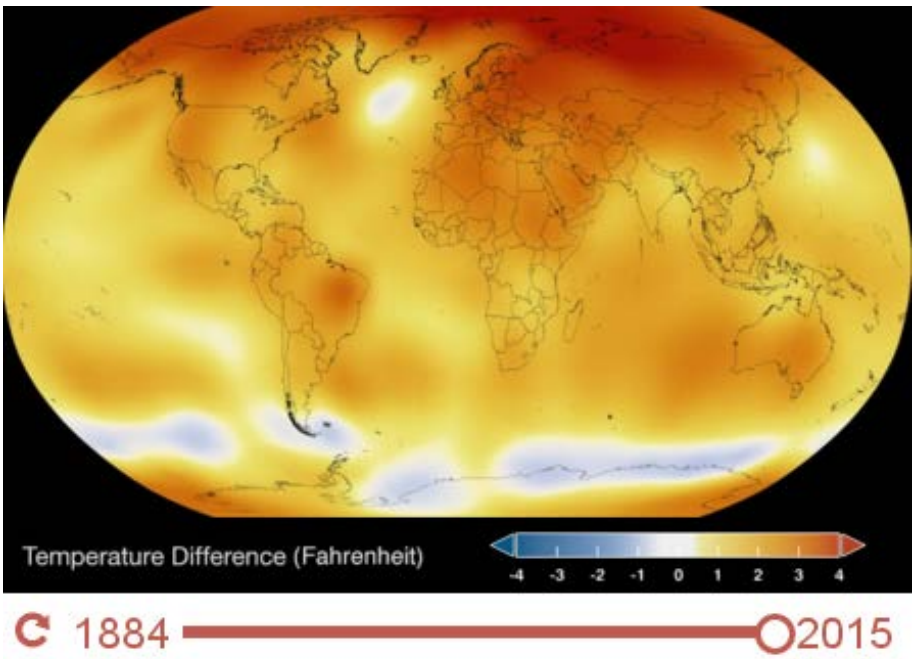

Figura 1. Imágenes de las emisiones de gases en la Tierra a) en 1884, b) en 2015.[40]

Una de las estrategias más efectivas para reducir las emisiones de CO_2 atmosférico es la tecnología CCS (Carbon Capture and Storage). Esta tecnología consiste en la captura, acondicionamiento, transporte, inyección y almacenamiento geológico del CO_2 producido por la actividad humana, más del 95% del cual procede del sector energético. Esta tecnología se menciona de forma explícita en las Estrategias Europeas 2020 y 2050 [29, 30] como uno de los métodos que debe contribuir a alcanzar el objetivo de reducir las emisiones europeas de GEI en un 80-95% para 2050. También se cita en la "Estrategia Española de Ciencia y Tecnología y de Innovación 2013-2020". [27]

En agosto de 2013 el Global CCS Institute tenía identificados 65 proyectos CCS a gran escala en diversas etapas de desarrollo, de los cuales se ha estimado que 19 estén operativos en la actualidad.[92] Estos 19 proyectos suman una capacidad de almacenamiento de 38,5 millones de toneladas por año (Mtpa), muy lejana de las 7.000 Mtpa que se pretenden alcanzar para el año 2050.

Bajo el "27th Framework Programme (FP7)" de la Comisión Europea, la tecnología CCS se convirtió en un tema prioritario en la investigación energética dentro de la Unión Europea, con aproximadamente 160 millones de euros destinados como inversión para proyectos de investigación. Parte de estos proyectos incluyen la reducción de costes en la captura del CO_2, evaluación de riesgos y peligros asociados al transporte del CO_2, ampliación de la tecnología CCS a lo largo de las redes de cada país, y aseguramiento de la seguridad y eficacia del almacenamiento geológico.

La captura del CO_2 se puede lograr por postcombustión, precombustión u oxicombustión. Su acondicionamiento tras la captura, puede llevarse a cabo mediante deshidratación, separación de gases no condensables y/o licuefacción, compresión y bombeo. El transporte se realiza generalmente por tubería, y el CO_2 antropogénico finalmente se inyecta y se almacena en yacimientos de petróleo o de gas en explotación o agotados, yacimientos mineros agotados o formaciones salinas profundas (Figura 2).

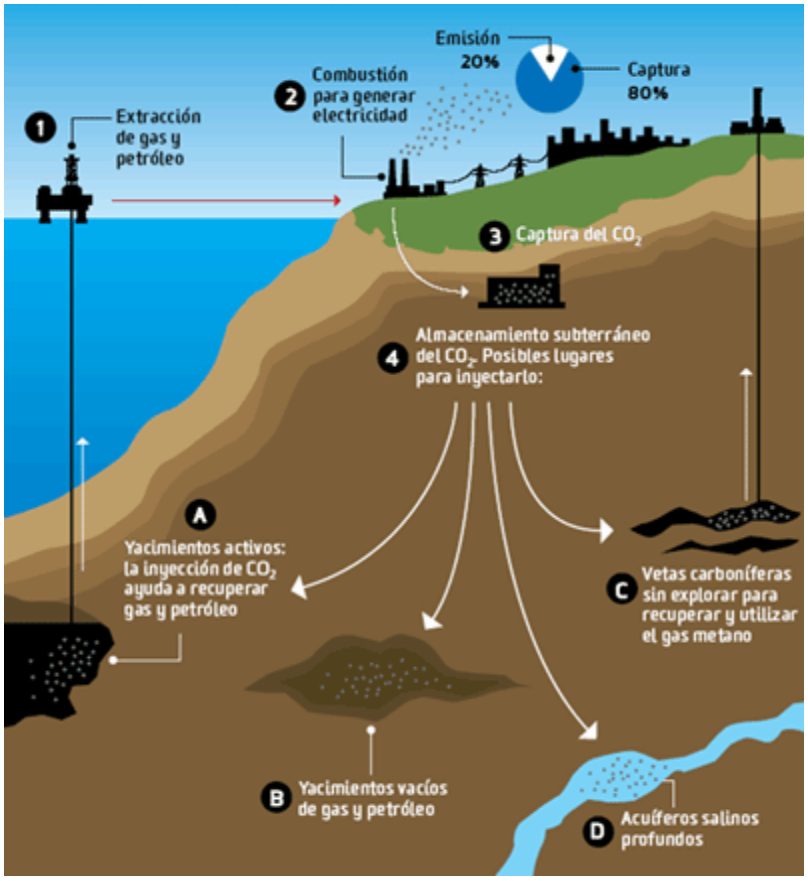

Figura 2. Representación de la emisión de CO_2 en una central eléctrica, su captura y su almacenamiento subterráneo en formaciones geológicas.

El diagrama de fases del CO_2 puro muestra como a temperaturas y presiones por encima de su punto crítico (P_C= 7.383 MPa, T_C= 304.21 K), las fases gas y líquido son indistinguibles y existe una única fase presente. Dicha fase, conocida como supercrítica, exhibe valores de viscosidad y densidad intermedios entre los de un líquido y un gas. La forma más económica y eficiente de transportar el CO_2 por tubería es hacerlo en condiciones de T y P en las que este compuesto se encuentra en fase densa (por encima de P_C y por debajo de T_C) o supercrítica. Esto es debido a que el volumen ocupado por el CO_2 bajo condiciones supercríticas es unas 350 veces menor que el que ocupa en fase gaseosa y además su viscosidad es menor que la de los líquidos.

Sin embargo, el CO_2 transportado no es puro, proviene de muchas posibles fuentes, tales como centrales eléctricas de carbón, refinerías, reformado de asfalto, plantas de gas o de acero y cementeras. Por ello, el flujo de CO_2 contiene diversas impurezas, tales como: N_2, O_2, Ar, CH_4, CO, SO_x, NO_x, H_2S, H_2, etc., en diferentes concentraciones. El aumento de la pureza del CO_2 evita posibles riesgos como por ejemplo la corrosión de las tuberías, y dependiendo de las impurezas que se eliminan, mejora el almacenamiento pero aumenta considerablemente el coste de la captura y del acondicionamiento.

La presencia y el tipo de impurezas afectan a las propiedades químico físicas del fluido, y como consecuencia al diseño y a la operación de los equipos necesarios en la tecnología CC.[63]. Además, en las diferentes etapas de la tecnología se cubren rangos de presión y temperatura muy amplios, ya que se transporta y se almacena en fase densa y/o supercrítica. En consecuencia, las propiedades químico físicas de la corriente de CO_2 antropogénico difieren de forma importante según su procedencia, y se modifican de forma más importante aún durante el proceso.

La presencia de impurezas en el CO_2 modifica la posición del punto crítico con respecto al CO_2 puro y la línea del equilibrio líquido-vapor (ELV) se transforma en una envolvente de fases que rodea a la región de coexistencia de las fases líquido y vapor (Figura 3), así la composición del fluido condiciona el valor de la presión mínima necesaria para asegurar el transporte en fase densa o supercrítica. Una de las características de los fluidos supercríticos en la región cercana al punto crítico es la gran variación en los valores de densidad, ρ, y de compresibilidad isotérmica, κ_T, cuando se producen pequeños cambios en la presión, temperatura y composición. Todas estas propiedades termodinámicas, influyen en varios parámetros que afectan a los procesos de transporte[98]: diámetro de tubería, caída de presión, velocidad de erosión, capacidad de las estaciones de recompresión, etc; y a los procesos de inyección y almacenamiento: parámetro de solubilidad, capacidad de almacenamiento, velocidad de ascensión de la pluma en acuíferos salinos y flujo de permeación.[23]

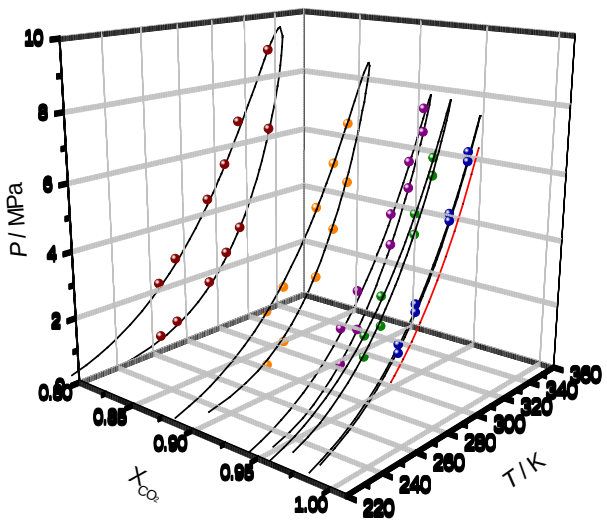

Figura 3. Presión de vapor del CO_2 puro (línea roja) y envolventes de fase de mezclas CO_2+SO_2 con diferentes valores de fracción molar de CO_2, x_{CO_2} (puntos: valores experimentales; líneas: calculados con PC-SAFT)[35]

Además del conocimiento de las propiedades volumétricas y del equilibrio líquido vapor del fluido a transportar y almacenar, la determinación de la velocidad del sonido, c, también es de gran interés puesto que permite durante la fase de transporte: i) conocer la distribución de tamaños de las burbujas en el líquido;[56] ii) detectar fugas;[66, 69, 90, 104] y

iii) estudiar la propagación de fracturas, puesto que depende de la relación entre la velocidad de la onda de presurización, v_P (directamente relacionada con c) y la velocidad de fractura, v_f: si $v_P > v_f$, la fractura se detendrá y si $v_P < v_f$, se propagará hasta encontrar algún impedimento mecánico.[5,26]. Asímismo, durante la fase de almacenamiento el conocimiento de c es necesario para: i) estudiar fugas en los almacenamientos[10,56] ii) realizar estudios sísmicos iii) optimizar procesos EOR; y iv) monitorizar el comportamiento de la pluma.[54,87]

En esta Tesis se estudian dos impurezas no condensables que puede contenter el CO_2 antropogénico: el metano y el monóxido de carbono. El primero proviene, entre otros, de procesos derivados de la eliminación de los gases ácidos (H_2S y/o CO_2) en el gas natural y el CO, es habitual de procesos como la producción de petróleo. Tanto este compuesto como el metano pueden ser subproductos de la captura de pre-combustión en centrales energéticas.

Existe un vacío legal en lo referente al rango de composiciones permitido en el CO_2 antropogénico. Como consecuencia, el estudio experimental de los sistemas CO_2 + impurezas y la modelización termodinámica de los mismos cobra importancia a la hora de entender como su composición afecta a su comportamiento con el objeto de rentabilizar la tecnología asegurando al mismo tiempo la seguridad de la misma.

También hay poca definición en lo que respecta al cálculo económico del proceso dado que ninguno de los modelos utilizados en la actualidad tienen en cuenta el impacto de las impurezas en los diferentes parámetros de diseño. Además, la escasez de datos experimentales, en especial de propiedades volumétricas bajo las condiciones relevantes para la tecnología CCS, tiene como consecuencia que no haya todavía un modelo termodinámico validado en los rangos de la tecnología para predecir el comportamiento del fluido transportado y almacenado. Los modelos más comunes, basados en ecuaciones de estado, EoS, de distinta naturaleza, deberían comprobarse con datos experimentales de las mezclas en las condiciones en las que se produce el transporte y almacenamiento del CO_2 antropogénico.

Los trabajos que conforman esta Tesis recogen la puesta a punto de dos instalaciones experimentales, una para la medida de la densidad y otra para la determinación de velocidades del sonido, tanto en fluidos puros como en mezclas. Asímismo, proporcionan datos experimentales presión-densidad-temperatura-composición, $P - \rho - T - x_{\mathrm{CO_2}}$ y del ELV de los sistemas CO_2+CH_4 y CO_2+CO en composiciones, presiones y temperaturas de interés para la tecnología CCS. Estos datos nos permiten comprobar la capacidad predictiva de las EoS PR,[75] PC-SAFT[36] y GERG-2008[50] en los rangos estudiados en este trabajo mediante la comparación de los valores de las propiedades volumétricas y del ELV con los calculados con estas ecuaciones. A través del concepto de función de Krichevskii y de la teoría de Kirdwood-Buff se muestra el estudio teórico realizado sobre las interacciones existentes entre CO_2/CH_4 ó CO cerca del punto

crítico. Por último, mediante los valores experimentales de densidad y ELV y los calculados de viscosidad, se determina la influencia del CO y del CH_4 sobre diversos parámetros que afectan al transporte, inyección y almacenamiento en la tecnología CCS. El análisis de estos parámetros es necesario para la construcción y operación seguras de los ceoductos, así como, para el almacenamiento fiable del CO_2 antropogénico a largo plazo en formaciones geológicas.

OBJETIVOS

2. OBJETIVOS

La adquisición y el mantenimiento de las instalaciones experimentales utilizadas en esta Tesis Doctoral, así como los trabajos realizados fueron financiados con los siguientes proyectos de investigación:

- CTQ2005-02213: "Equilibrio de fases a altas presiones de mezclas binarias y multicomponentes de fluidos petrolíferos y compuestos alternativos a las CFC".
- CTQ2008-02037: "Determinación de velocidades del sonido a altas presiones en fluidos petrolíferos y compuestos alternativos a los CFC; obtención de propiedades termodinámicas derivadas y modelización con EOS y RNA".
- UZ2008-CIE-02: "Obtención de propiedades derivadas de la velocidad del sonido en fluidos puros y gases".
- INF2008-CIE-05. "Mejora de una instalación de medida de velocidades del sonido a alta presión".
- CONVENIO CAIXA-DGA 2009: "Reducción de las emisiones de CO_2: Determinación y predicción de las condiciones químico-físicas idóneas en el transporte y almacenamiento de CO_2".
- CTQ2011-24875: Avances en la investigación para reducir las emisiones de gases de efecto invernadero: dióxido de carbono y refrigerante con alto potencial de calentamiento global".
- UZ2012-CIE-13: "Avances en la investigación para reducir las emisiones de gases de efecto invernadero: CO_2 y refrigerantes con alto potencial de calentamiento global (GWP)".

Los objetivos del presente trabajo han sido los siguientes.

1. Puesta a punto de una instalación de tubo vibrante para la determinación, en un amplio rango de presión y temperatura, de propiedades volumétricas para fluidos puros y mezclas.
2. Calibrado y puesta a punto de una instalación para la medida de velocidades del sonido en un amplio rango de presión y temperatura, en fluidos puros y mezclas.

3. Estudio experimental volumétrico y del equilibrio líquido-vapor de los sistemas CO_2+CH_4 y CO_2+CO. Cálculo de incertidumbres. Determinación de propiedades derivadas y de sus precisiones.

4. Modelización de los sistemas CO_2+CH_4 y CO_2+CO mediante Ecuaciones de Estado Cúbicas (PR)[75] y no cúbicas (PC-SAFT[36], GERG-2008[50]).

5. Estudio estructural de los sistemas CO_2+CH_4 y CO_2+CO en la región crítica a partir de la determinación de sus propiedades volumétricas a dilución infinita.

6. Estudio de la influencia de CH_4 y CO en el transporte, inyección y almacenamiento del CO_2 antropogénico en la tecnología CCS mediante el cálculo de parámetros característicos de dichos procesos a partir de las propiedades determinadas experimentalmente.

APORTACIONES DEL DOCTORANDO

3. APORTACIONES DEL DOCTORANDO

A continuación se describen las aportaciones realizadas por el doctorando para el desarrollo del presente trabajo y por tanto para la consecución de los objetivos concretos.

OBJETIVO 1

Puesta a punto de una instalación de tubo vibrante para la determinación, en un amplio rango de presión y temperatura, de propiedades volumétricas para fluidos puros y mezclas.

La instalación de tubo vibrante permite trabajar de forma dinámica asegurando que el sistema se encuentre en cada instante en cuasi-equilibrio termodinámico. Para ello, es necesario mantener un régimen cuasi-estático mediante la utilización del flujo óptimo del fluido de medida. El primer trabajo realizado fue determinar el valor óptimo de flujo necesario para realizar correctamente las medidas experimentales.

Se realizaron diferentes pruebas para optimizar el proceso de reducción de datos ya que el sistema de adquisición de datos de la instalación permite disponer de un gran número de ellos pero deben reducirse para facilitar cálculos posteriores.

Antes de elaborar el procedimiento operativo idóneo y de calcular la precisión de las variables determinadas, es necesario calibrar los diferentes equipos que las miden. Se realizó el calibrado de los dos medidores de presión. Una empresa externa calibró el sensor de temperatura.

La propiedad que determinan los equipos basados en el método del tubo vibrante es el periodo de vibración del tubo, τ, función de la densidad del fluido confinado en él. Por ello es necesario calibrar la célula de medida en todo el rango de temperaturas y de presiones usando un fluido de referencia; en nuestro caso, CO_2.

Se verificó el calibrado y procedimiento operacional determinando la densidad de etano y propano y comparando los valores obtenidos con los calculados a partir de sus correspondientes EoS de referencia.

Debido al elevado número de puntos experimentales $P - \rho - T$ que se obtienen en esta instalación, es posible calcular diferentes propiedades derivadas de la densidad tales como: compresibilidad isotérmica, κ_T, expansividad isóbara, α_P, presión interna, π_i, y

coeficiente de temperatura, $(\partial \pi_i / \partial T)$. Se obtuvieron los valores de estas propiedades para CO_2 y etano así como su precisión.

Se elaboró el procedimiento experimental para mezclas binarias realizando las modificaciones necesarias con respecto al procedimiento para compuestos puros.

La consecución del objetivo 1 se recoge en el Artículo: *J. of Physical Chemistry B, 2011, 115, 8216.*

OBJETIVO 2

Calibrado y puesta a punto de una instalación para la medida de velocidades del sonido, en un amplio rango de presión y temperatura, para fluidos puros y mezclas.

El método de medida de esta instalación está basado en la relación existente entre la longitud que recorren los ecos de un pulso ultrasónico y el desfase que se produce entre ellos. Para determinar dicha longitud es necesario realizar el calibrado a una presión y temperatura utilizando un fluido de referencia con una EoS precisa. En este caso, se utilizó agua MiliQ desgasificada a T = 298.12 K y P = 1.00 MPa. Dado que las calibraciones de los medidores de presión y temperatura estaban vigentes, no fue necesario recalibrarlos.

Se verificó la calibración y se determinó la precisión en la medida de velocidades del sonido de líquidos puros mediante la comparación de los valores experimentales obtenidos para el agua en un amplio rango de P y T con los proporcionados por la EoS.

Debido a que la instalación estaba diseñada únicamente para la medida de la velocidad del sonido en líquidos, hubo que modificarla para trabajar con gases comprimidos y comprobar su precisión en esas condiciones. Para ello, se determinó c en etano a ocho temperaturas y a presiones hasta 175 MPa y se compararon los datos con los proporcionados por la EoS de referencia de este compuesto.

A partir de los datos experimentales ($P - \rho - T$ y $P - c - T$) obtenidos para etano se calculó la compresibilidad isentrópica, κ_S, y la capacidad calorífica a presión constante, C_P. Su precisión se calculó, asímismo, por comparación con los valores proporcionados por su Eos de referencia.

Se puso a punto la instalación de medida de velocidades del sonido para mezclas que contienen gases comprimidos suficientemente densos. Se estableció el procedimiento experimental para la preparación y medida de estas mezclas y se determinó la incertidumbre en los valores experimentales de velocidad del sonido del sistema gas

comprimido+líquido, CO_2+CH_3OH. Las composiciones de las mezclas y las condiciones de trabajo se eligieron para que incluyeran las habituales de la tecnología CCS.

La consecución del objetivo 2 se recoge en los Artículos: *J. of Physical Chemistry B, 2011, 115, 8216, y J. of Chemical Thermodynamics, 2016, 98, 272-281.*

OBJETIVO 3

Estudio experimental de los sistemas CO_2+CH_4 y CO_2+CO. Cálculo de incertidumbres. Determinación de propiedades derivadas y de sus precisiones.

Se determinó la densidad de los sistemas: CO_2+CH_4 (6 composiciones; 9 temperaturas) y CO_2+CO (5 composiciones; 10 temperaturas) a presiones desde 0.1 a 20 MPa. Se calculó, mediante la Ley de Propagación de Errores, la incertidumbre expandida en la determinación de la densidad, $U(\rho)$.

A partir de los datos experimentales ($P-\rho-T-x_{CO_2}$) se calcularon las siguientes propiedades y sus respectivas incertidumbres: puntos de rocío y de burbuja, y densidades de las fases en equilibrio, ($P_r-\rho_V$; $P_b-\rho_L$); compresibilidad isotérmica, κ_T; expansividad isóbara, α_P; presión interna, π_i; volúmenes molares de exceso, V_m^E; y volúmenes parciales molares, $\bar{V}_2$.

Por último, se realizó una búsqueda bibliográfica de todas las propiedades, experimentales y calculadas, y se compararon con los datos obtenidos en este trabajo.

La consecución del objetivo 3 se recoge en los artículos*: Environmental Science & Technology. 2012, 46, 13016; International Journal of Greenhouse Gas Control. 2013, 264; y Environmental Science & Technology. 2014, 48, 10984.*

OBJETIVO 4

Modelización de los sistemas CO_2+CH_4 y CO_2+CO mediante Ecuaciones de Estado cúbicas (PR) y no cúbicas (PC-SAFT, GERG-2008).

Se modelizaron los sistemas CO_2+CH_4 y CO_2+CO con tres Ecuaciones de Estado: Peng-Robinson, de gran aplicabilidad en ingeniería por su simplicidad; GERG-2008, muy precisa pero compleja de implementar; y PC-SAFT, con características intermedias entre las anteriores. Se obtuvieron los parámetros de interacción binaria cuando fue necesario, y se calcularon las desviaciones medias relativas de todas las propiedades volumétricas y del equilibrio líquido vapor:

La consecución del artículo 4 se recoge en los artículos*: Environmental Science & Technology. 2012, 46, 13016; International Journal of Greenhouse Gas Control. 2013, 264; y Environmental Science & Technology. 2014, 48, 10984.*

OBJETIVO 5

Estudio estructural de los sistemas CO_2+CH_4 y CO_2+CO en la región crítica a partir de la determinación de sus propiedades volumétricas a dilución infinita.

Se determinó la naturaleza de las interacciones entre las moléculas de disolvente, CO_2, y las de soluto, CH_4 o CO, a 304.21 y 308.15 K utilizando el concepto de Función de Krichevskii y de la inversión de la Teoría de Kirkwood-Buff. Para ello, se calculó el volumen molar parcial del soluto a dilución infinita, $\bar{V}_2^{\infty}$, el número de coordinación de exceso, N_{exc}^{∞} y el tamaño del clúster, N_1^{exc}.

La consecución del objetivo 5 se recoge en el artículo: *International Journal of Greenhouse Gas Control. 2013, 264.*

OBJETIVO 6

Estudio de la influencia de CH_4 y CO en el transporte, inyección y almacenamiento del CO_2 antropogénico en la tecnología CCS mediante el cálculo de parámetros característicos de dichos procesos a partir de las propiedades determinadas experimentalmente.

Se identificaron, mediante el estudio de la bibliografía existente, los parámetros característicos de las etapas de transporte, inyección y almacenamiento, así como los procedimientos de cálculo idóneos para cada uno. A partir de los datos ($P-\rho-Tx_{CO_2}$; P_r-P_b) obtenidos en parte de las composiciones estudiadas y los de viscosidad calculados, se obtuvieron diferentes parámetros para las distintas etapas de la tecnología CCS.

- Transporte: Presión mínima de operación, P_{min}; Perfil de presión a lo largo de la tubería, $P(d)$; Distancia máxima de presurización, L; Capacidad de las estaciones de represurización, W; y Diámetro interno de la tubería, D.

- Inyección y almacenamiento: Parámetro de solubilidad, δ; Capacidad de almacenamiento normalizada, M/M_0; Velocidad de ascenso normalizada en acuíferos salinos, v/v_0; y Flujo de permeación normalizado, $\dot{M}/\dot{M}_0$.

La consecución del objetivo 6 se recoge en los artículos*: Environmental Science & Technology. 2012, 46, 13016; International Journal of Greenhouse Gas Control. 2013, 264; y Environmental Science & Technology. 2014, 48, 10984.*

METODOLOGÍA

4. METODOLOGÍA

4.1. INSTALACIONES Y PROCEDIMIENTOS

A) PROPIEDADES VOLUMÉTRICAS Y EQUILIBRIO LÍQUIDO VAPOR

A.1.) Instalación para la determinación de medidas experimentales.

i. Descripción de la instalación

En la Figura 4 se muestra un esquema de la instalación que se ha empleado para determinar los datos presión – densidad – temperatura, $P-\rho-T$, de fluidos puros y sus mezclas en las regiones subcrítica, crítica y supercrítica.

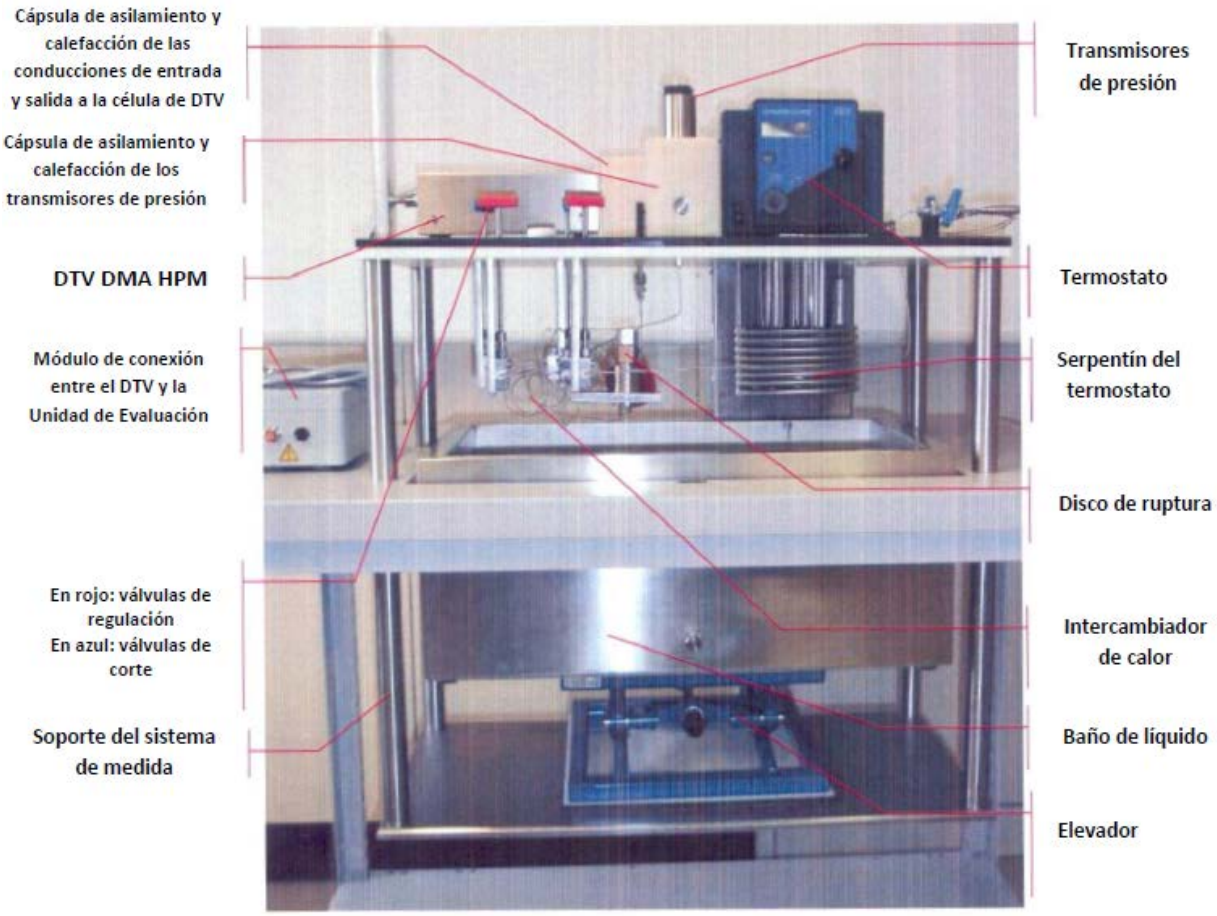

Figura 4. Instalación experimental para la determinación de datos $P-\rho-T$ de fluidos puros y sus mezclas.

La instalación, que fue diseñada por ARMINES y el Laboratoire de Thermodynamique des Equilibres entre Phases de l´Ecole Nationale Supérieure des Mines de Paris en Francia, permite obtener datos $P-\rho-T$ de fluidos puros y mezclas en un rango de temperaturas desde 253 a 423 K y desde presión atmosférica hasta 70 MPa.

Su componente principal es una célula de Densimetría de Tubo Vibrante (DTV) AntonPaar KG, modelo DMA HPM, conectada a una unidad de evaluación mPDS 2000V3 que recoge datos de forma continua. La instalación se completa con las conducciones de entrada y de salida a la célula, diferentes módulos de regulación y corte y el sistema de termostatización. Este último consiste en un doble recubrimiento del densímetro de tubo vibrante que permite la regulación térmica mediante un baño externo (Fischer Bioblock, Cryo-polystat 71 modelo C85408). La temperatura del resto del circuito está regulada por otro baño (misma marca y modelo) en un valor ligeramente diferente que permite evitar que la primera burbuja de gas (medidas en fase condensada) o primera gota de líquido (medidas en fase gaseosa) se originen fuera de la célula de medida.

La presión se mide mediante dos transductores de presión regulados térmicamente (GE Infrastructure modelo PTX 611); uno de ellos se utiliza para presiones hasta 6 MPa y el otro hasta 70 MPa.

ii. Procedimiento y calibración

El procedimiento experimental comienza con la limpieza de la instalación que consiste en hacer circular una corriente de nitrógeno a 0.2-0.3 MPa durante dos horas a lo largo de toda la instalación y después hacer vacío durante 4 horas. El fluido a estudiar se introduce mediante una célula de carga de volumen variable (Figuras 5(a) y 5(b)) fabricada en Hastelloy que se conecta a una bomba manual de alta presión que permite alcanzar presiones de hasta 100 MPa. El paso del fluido desde la célula a la bomba se lleva a cabo por compresión con He. Cuando el fluido es una mezcla, ésta se prepara en la célula de carga por diferencia de pesada introduciendo los fluidos en orden de menor a mayor presión de vapor. Para ello se emplea un comparador de masas (Sartorius, modelo CCE2004) que tiene una capacidad máxima de pesada de 2500 g, cuya legibilidad es de 0.0001 g y la repetibilidad es de 0.0002 g.

Figura 5. Células de volumen variable (a) Pequeña (0.05 l) y (b) Grande (0.51 l) .

Cuando se determinan densidades en condiciones críticas o supercríticas, donde no hay cambio de fase, la medida del periodo de vibración es descendente, partiendo de la presión máxima de medida y adquiriendo datos en todo el rango de presión para una temperatura dada hasta alcanzar la presión atmosférica. Dado que a la temperatura crítica de un fluido (o en su cercanía), pequeñas variaciones de presión suponen grandes cambios en la densidad, se realizaron pruebas en diferentes condiciones para optimizar la medida de estas isotermas.

Si a la temperatura de trabajo el fluido presenta cambio de fase, isotermas subcríticas, las medidas de densidad se realizan en dos tramos: uno ascendente en el que las medidas se toman desde presión de vacío hasta la presión de vapor (en el caso de los fluidos puros) o hasta la presión de rocío (en mezclas); y otro descendente, en el que se parte desde la presión máxima de medida para cada isoterma hasta la presión de vapor (en el caso de fluidos puros) o hasta la presión de burbuja (para el caso de las mezclas).

La adquisición de medidas $P - \tau - T$ a una temperatura dada puede llegar hasta los 5000 puntos. Este es un número demasiado elevado para su posterior tratamiento, por ello es necesario descartar parte de estos puntos de forma que las isotermas son reducidas a un número alrededor de 1500.

Los límites del ELV a una temperatura determinada (presión de vapor de compuestos puros y presiones de rocío y de burbuja en mezclas), se determinan gráficamente, mediante el método de las tangentes (Figura 6). En este método las medidas precedentes y posteriores a los puntos del límite del ELV se ajustan mediante dos ecuaciones lineales; el punto de cruce de ambas corresponde a los puntos de rocío o de burbuja, según la medida corresponda a la fase vapor o a la líquida respectivamente.

En todos los casos, para asegurar el equilibrio a través de transformaciones cuasi-estáticas, los flujos de fluido se ajustan convenientemente hasta una velocidad óptima de 0.005 $MPas^{-1}$.

Presión /MPa

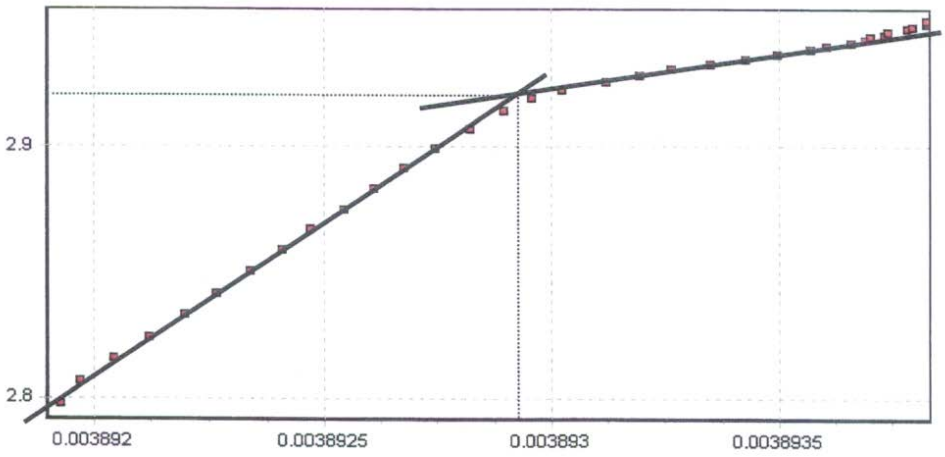

Periodo /s

Figura 6. Determinación del punto de rocío de un fluido por el método de las tangentes.

El principio de medida de los densímetros de tubo vibrante se basa en la dependencia del periodo de oscilación del tubo en U situado en su interior con la masa conjunta del propio tubo y del fluido que circula por él. El comportamiento del tubo vibrante puede ser modelado como un sistema de amortiguador masa-resorte.[48]

El periodo de oscilación o vibración, $\tau(s)$,viene dado por la siguiente expresión:

$$\tau(s) = 2\pi\sqrt{\frac{M_0 + V\rho}{D}} \qquad \text{(Ec. 1)}$$

Donde

M_0 masa del tubo en U vacío (kg)
V volumen del tubo vibrante (m^3)
ρ densidad del fluido que circula por el interior del tubo en U ($kg \cdot m^{-3}$)
D constante de muelle (N/m)

A partir de la ecuación anterior, sustituyendo la constante mecánica, se llega a la ecuación clásica para densímetros de tubo vibrante:

$$\rho = A\tau^2 - B \qquad \text{(Ec. 2)}$$

Los parámetros A y B pueden obtenerse mediante un calibrado utilizando fluidos de densidad conocida y midiendo el periodo de oscilación provocado por ellos. Sin embargo, en este trabajo hemos preferido utilizar como modelo de calibrado el desarrollado por Bouchot y Richon[12] Path Mechanical Calibration Model, FPMC; el objetivo del mismo es limitar la influencia del método de calibrado en la determinación de la densidad a partir de las medidas del periodo de vibración. El modelo busca relaciones para las dependencias de la presión y la temperatura que tengan consideraciones realistas, de forma que representen el comportamiento del material del tubo vibrante ante la deformación y la tensión.

Así, la ecuación que relaciona la densidad del fluido en unas condiciones dadas, $\rho(T,P)$, con el periodo de oscilación del tubo vibrante, τ , es:

$$\rho(T,P) = \frac{M_0}{L_{00}} \cdot \left[\frac{1}{\pi r_i^2} exp\left(\int \alpha(T) dT + \gamma_T P\right)\right] \left|\left(\frac{\Delta r^4}{\Delta r_0^4}\right) exp(-3\gamma_T P)\left(\frac{\tau^2}{\tau_0^2}\right) - 1\right| \qquad \text{(Ec. 3)}$$

Donde

T	Temperatura en el interior del tubo vibrante
P	Presión en el interior del tubo vibrante
M_0	Masa en el vacío del tubo vibrante
L_{00}	Longitud del tubo vibrante en el vacío a 273.15 K
$\alpha(T)$	Coeficiente de dilatación lineal
γ_T	Coeficiente de expansión del tubo vibrante a la temperatura T
r_i	Radio interno del tubo vibrante a la temperatura T y la presión P
Δr	Diferencia entre el radio interno y el externo del tubo vibrante a la temperatura T y la presión P
Δr_0	Diferencia entre el radio interno y el externo del tubo vibrante a la temperatura T y a vacío
τ	Periodo de vibración del tubo vibrante a la temperatura T y la presión P
τ_0	Periodo de vibración del tubo vibrante a la temperatura T en el vacío

En el modelo FPMC, se usa un único fluido de referencia para obtener los valores de las constantes M_0/L_{00} y γ_T.

Se eligió el CO_2 como fluido de calibración por poder adquirirse con elevada pureza (99.998% molar), por presentar valores de densidad similares a los fluidos estudiados en esta Tesis y disponer de una EoS precisa que permite calcular valores de densidad de referencia en todo el rango de medida. La EoS utilizada fue la de Span y Wagner[89] que tiene un rango de aplicabilidad de hasta 800 MPa y 1000 K y con una incertidumbre

estimada en el cálculo de la densidad de $u(\rho) = \pm 0.03\% - \pm 0.05\%$. La calibración se llevó a cabo a once temperaturas (253.15, 273.15, 293.15, T_c (CO_2)=304.21, 308.15, 313.15, 333.15, 353.15, 373.15, 393.15 y 423.15K) y desde presión atmosférica hasta 70 MPa, estudiando así tres estados del fluido: subcrítico, crítico y supercrítico.

Las desviaciones medias relativas (Anexo I Ecuación A.I) al comparar las densidades experimentales obtenidas en el calibrado y las calculadas con la EoS[89] fueron: $MRD(\rho)$ = 0.09% si se incluyen las medidas en la región crítica y $MRD(\rho)$ = 0.07% si se excluye esta región.

Los transductores fueron calibrados en los laboratorios de nuestro grupo de investigación utilizando un calibrador Wika CPH 6000 con una precisión de 0.025% en toda la escala. Las precisiones expresadas como incertidumbres para los medidores son $u(P) = \pm 0.015$ MPa para el medidor de hasta 6 MPa y $u(P) = \pm$ 0.0175 MPa para el medidor de 6 hasta 70 MPa.

Las sondas de temperatura fueron calibradas por el Centro Español de Metrología, CEM, siguiendo el procedimiento CEM-PT-4.2-40. La incertidumbre en su medida es $u(T) = \pm 0.006$K.

iii. Precisión

Compuestos puros

Con el objetivo de calcular la ***precisión*** de la instalación en la medida de densidades de compuestos puros se realizaron medidas de densidad de etano (99.995% molar) a nueve temperaturas, incluyendo la temperatura crítica del etano, en el rango desde 253.15 hasta 423.15 K y desde presión atmosférica hasta 70 MPa. Las ecuaciones de referencia utilizadas fueron la de Buecker y Wagner[13] para la región desde 0.1 a 30 MPa y la de Friend et al.[31]para presiones desde 30 hasta 70 MPa. En la Figura 7 se muestran las desviaciones obtenidas en la densidad para el etano con respecto a las EoS de referencia empleadas. El valor promedio de $MRD(\rho)$ para el etano en el rango de temperaturas estudiado es de 0.13%.

Para comprobar la calidad de las medidas en las regiones con mayor dificultad experimental (cercanías del punto crítico), se realizaron medidas $P - \rho - T$ para el propano (99.95 % molar) a las temperaturas: $T = T_C$ (C_3H_8) = 369.82, 373.15, 393.15 y 423.15K y desde presión atmosférica hasta 20 MPa. Se compararon los datos obtenidos con los que proporciona la EoS de referencia de este compuesto[58] obteniéndose un valor promedio: $MRD(\rho)$ = 0.20%.

Con el objetivo de determinar la ***repetibilidad*** en la medida de la densidad, se midió la densidad del dióxido de carbono a 273.15, 304.21 y 353.15 K desde presión atmosférica

hasta 70 MPa. Cada isoterma se midió tres veces y se calculó la desviación estándar relativa (Anexo I, Ecuación A.II): $\bar{S}_\rho^r$ = 0.05 % y $\bar{S}_P^r$ = 0.3 %. El último valor corresponde a la repetibilidad en la región crítica extendida que comprende: $0.6\ \rho_C < \rho < 1.4\ \rho_C$; $0.98\ T_C < T < 1.2 T_C$.

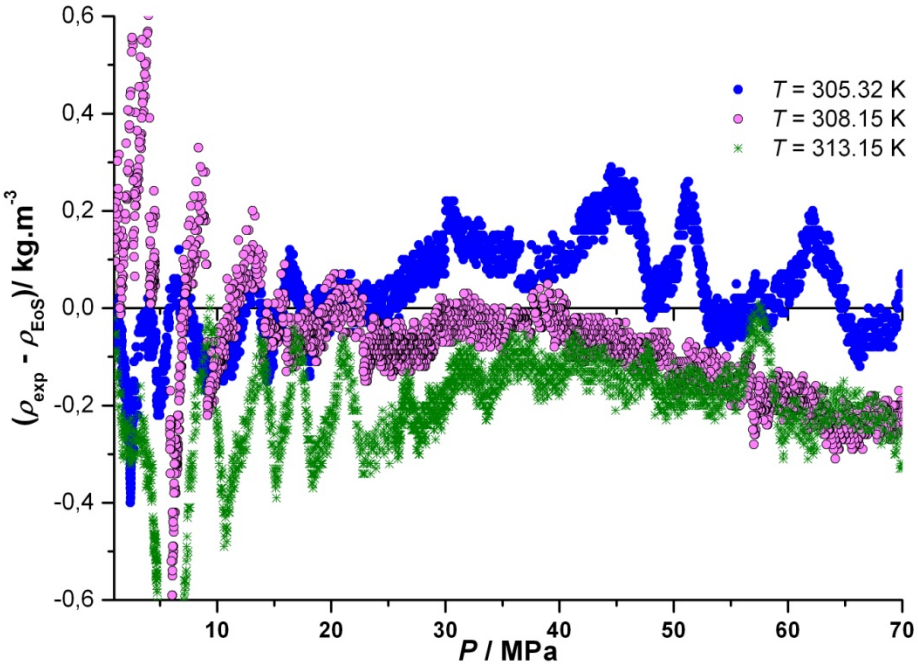

Figura 7. Desviaciones absolutas entre datos experimentales de densidad para etano a distintas temperaturas y las de referencia a partir de las EoS de Buecker y Wagner[13] y de Friend et al.[31]

Mezclas

Para desarrollar un método óptimo de determinación de densidades de mezclas binarias y evaluar la precisión de las mismas, se estudiaron a T = 308.15 K dos mezclas de CO_2 + C_2H_6 de diferente composición y en distinto rango de presión, comprobando así la influencia de dichas variables sobre la precisión. Cada una de las isotermas se midió dos veces para determinar la repetibilidad expresada como desviación estándar relativa (Anexo I Ecuación A.II). Las mezclas estudiadas fueron x_{CO_2}= 0.4999 hasta 20 MPa y x_{CO_2}= 0.9540 hasta 70 MPa y los valores encontrados fueron $\bar{S}_\rho^r$ = 0.13% y 0.06%, respectivamente.

A.2.) Cálculo de propiedades derivadas

A partir de los datos $P-\rho-T$ obtenidos experimentalmente para CO_2 y C_2H_6, se ha evaluado el efecto de la presión y la temperatura en su densidad a través de la compresibilidad isotérmica, κ_T, y la expansividad térmica isobárica, α_P. Además, se ha calculado la presión interna, π_i, propiedad relacionada con el orden molecular en el fluido. Las ecuaciones usadas han sido:

$$\kappa_T = \left(\frac{1}{\rho}\right)\left(\frac{\partial \rho}{\partial P}\right)_T \qquad \text{(Ec. 4)}$$

$$\alpha_P = -\left(\frac{1}{\rho}\right)\left(\frac{\partial \rho}{\partial T}\right)_P \qquad \text{(Ec. 5)}$$

$$\pi_i = \left(\frac{\partial U}{\partial V}\right)_T = T\left(\frac{\partial P}{\partial T}\right)_V - P = T\left(\frac{\alpha_P}{\kappa_T}\right) - P \qquad \text{(Ec. 6)}$$

Los valores calculados se han comparado con los proporcionados por las respectivas EoS[13,31,50] obteniendo las siguientes desviaciones medias relativas (Anexo I Ecuación A.I):

$MRD_{CO_2}(\kappa_T) < 1.2\ \%$; $MRD_{CO_2}(\alpha_P) < 5.0\ \%$; $MRD_{CO_2}(\pi_i) < 7.0\ \%$

$MRD_{C_2H_6}(\kappa_T) < 1.2\ \%$; $MRD_{C_2H_6}(\alpha_P) < 7.4\%$; $MRD_{C_2H_6}(\pi_i) < 8.0\%$

La dependencia de κ_T y α_P para el CO_2 y el etano respecto a la temperatura y la presión es bastante similar (Figuras 8 y 9). En el punto crítico, la altísima sensibilidad de la densidad con pequeñas variaciones de presión o temperatura hace que $\kappa_T, \alpha_P \rightarrow \infty$[94] y supone que los valores de ambas propiedades en esa región sean similares a los de la fase líquida. Por otro lado, se puede apreciar que la presión interna en el dióxido de carbono es mucho mayor que la del etano (Figura 10). Esto se puede explicar por la existencia de un momento cuadrupolar importante derivado de la deficiencia electrónica en la molécula de CO_2.

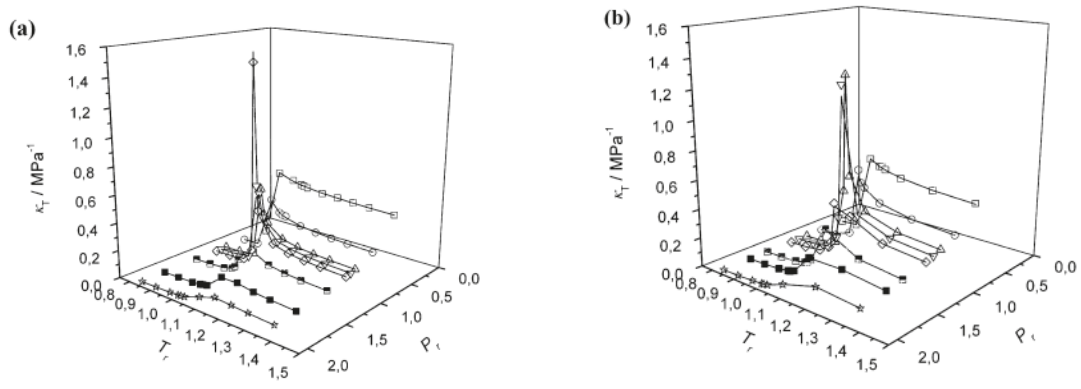

Figura 8. Representación de $P_r - \kappa_T - T_r$ para (a) dióxido de carbono (b) etano; (símbolos) valores experimentales y (líneas) EoS.

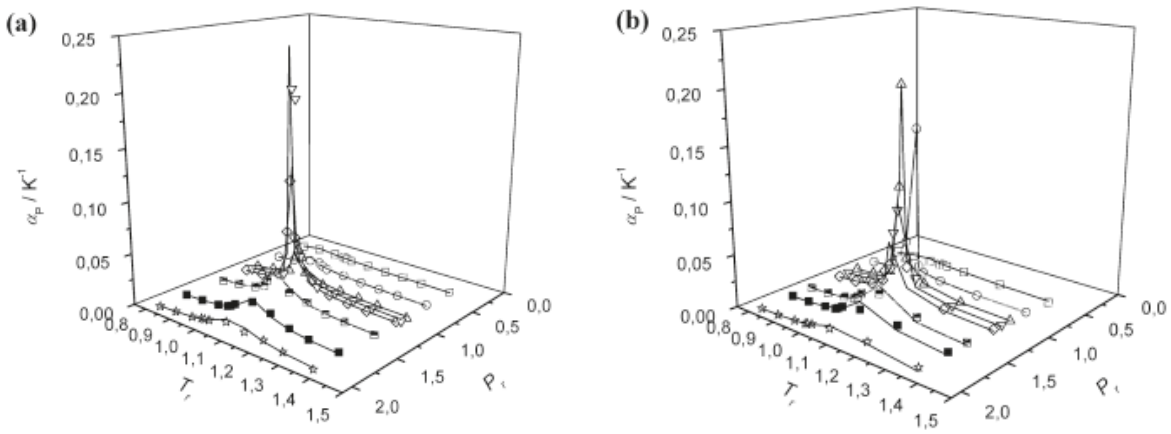

Figura 9. Representación de $P_r - \alpha_P - T_r$ para (a) dióxido de carbono y (b) etano; (símbolos) valores experimentales y EoS (líneas).

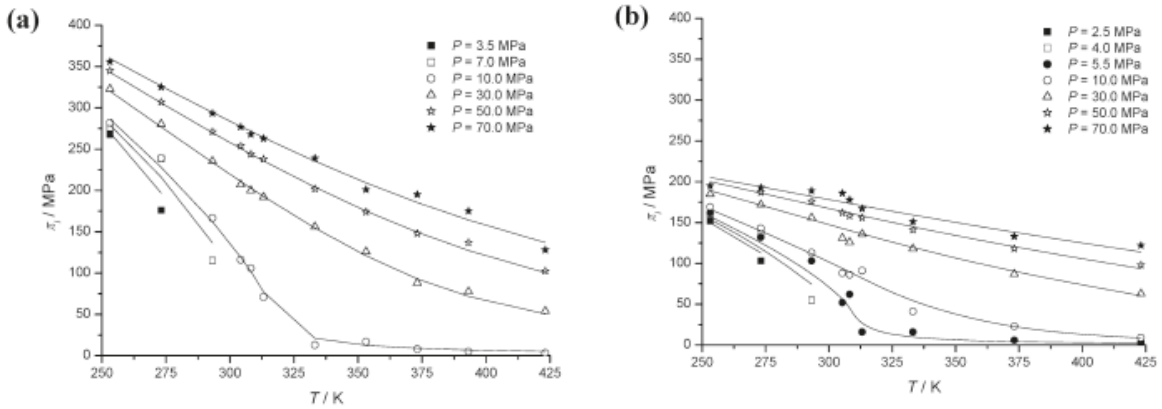

Figura 10. Representación de la presión interna, π_i, frente a la temperatura, T, para (a) dióxido de carbono (P_c =7.383 MPa y T_c =304.21 K) y (b) etano (P_c =4.882 MPa y T_c =305.32 K); valores experimentales (símbolos) y EoS (líneas).

B) VELOCIDAD DEL SONIDO

B.1.) Instalación para la determinación de medidas experimentales

i. Descripción de la instalación

La instalación experimental para la determinación de velocidades del sonido, c, se muestra en la Figura 11. Esta instalación, fabricada en el Imperial College de Londres, se basa en el método descrito en la bibliografía[8.19] que emplea un sistema de pulso ultrasónico de 5 MHz para obtener medidas de velocidades del sonido en líquidos. Sus componentes principales son: (1) bomba de presión manual, (2) entrada de fluido, (3) bomba de recirculación, (4) transductor de presión, (5) célula de presión, (6) baño de líquidos para la regulación de temperatura, (7) osciloscopio, (8) sonda de temperatura de platino, (9) línea de venteo, (10) unidad de evaluación y adquisición de datos y (11) línea de limpieza y vacío.

La instalación experimental permite la determinación de c en una amplio rango de temperaturas y presiones: T = 253.15 – 473.15 K y P = 0.1 – 200 MPa:

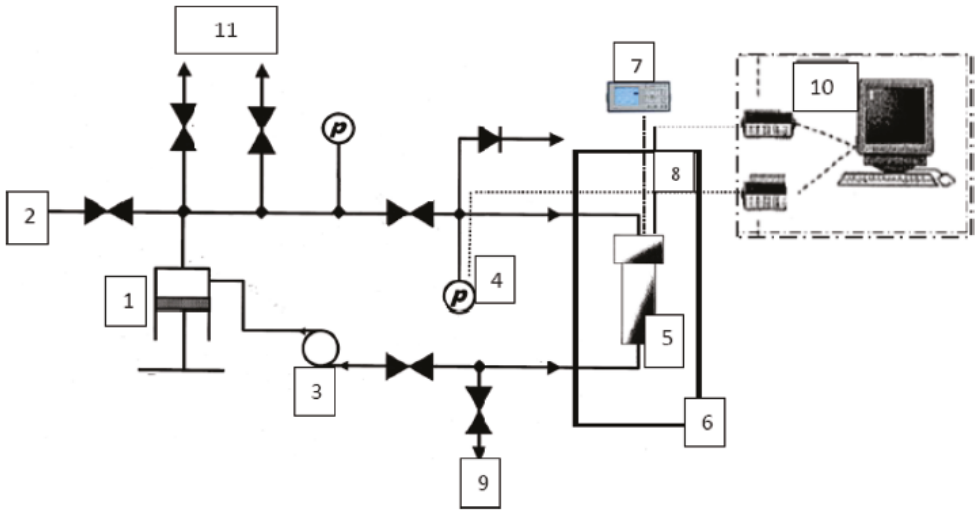

Figura 11. Esquema de la instalación experimental para la determinación de velocidades del sonido.

La célula de ultrasonidos se muestra en la Figura 12a). Sus principales elementos son: dos reflectores (2) y un transductor piezoeléctrico (5) fijado por medio de dos discos (4) usados como contactos eléctricos (6). La célula está introducida en una celda para altas presiones fabricada con una aleación de níquel y cromo, Nimonic80 A, que permite trabajar hasta 200 MPa (Figura 12b)). La celda tiene 50 cm^3 de volumen interno, una conexión de entrada para introducir el fluido de medida y el cable del transductor, y una

de salida. La resistencia de platino del termómetro se introduce por un orificio de la celda en la parte superior.

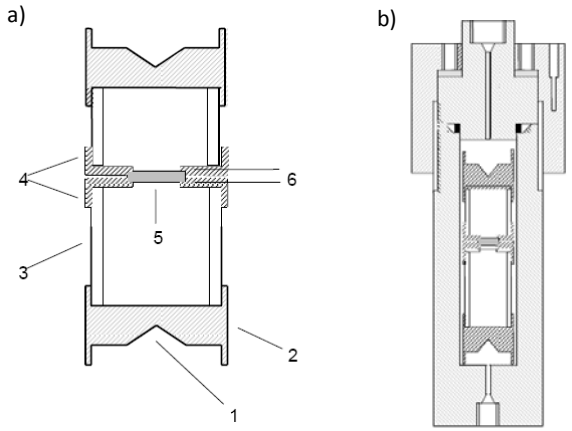

Figura 12. a)La célula de ultrasonidos, cavidad cónica (1), reflector (2), tubo de cuarzo (3), anillos de fijación de acero inoxidable (4), transductor piezoeléctrico (5), cables eléctricos (6). b) Celda para altas presiones.

Para presurizar el fluido de medida se utiliza una bomba manual de jeringa de 12 cm^3 de capacidad. La presión se mide con un transductor de presión de la marca Paroscientific con una incertidumbre $u(P) = 0.02$ MPa.

La instalación está diseñada para trabajar con líquidos aunque también pueden utilizarse gases comprimidos siempre y cuando su densidad sea lo suficientemente alta. En este caso, los gases son introducidos con una bomba ISCO que se conecta a la entrada de la instalación; el gas, se comprime en la bomba ISCO y una vez licuado se transvasa a la bomba manual de la instalación. De esta manera es posible introducir la masa de fluido necesaria para alcanzar 200 MPa.

La celda de alta presión, con la celda de ultrasonidos en su interior, está inmersa en un baño termostatizado de unos 6.5 l de capacidad (FLUKE modelo 6020). Para temperaturas de trabajo inferiores a 293.15 K se utiliza un baño adicional (GRANT modelo GR150) que se regula a una temperatura de 20 K por debajo del baño principal. El fluido del baño es un aceite de silicona que puede ser utilizado en el rango completo de temperatura. La temperatura se mide con un termómetro calibrado por comparación con una resistencia estándar de platino previamente calibrada por el UK National Physics Laboratory. La incertidumbre en la medida de la temperatura, $u(T)$, es 0.015 K.

ii. Procedimiento y calibración

El transductor piezoeléctrico de la célula de ultrasonidos es excitado con un tono de cinco ciclos generado a 5 MHz con una amplitud de 20 V entre picos. Esto provoca que el transductor emita pulsos acústicos simultáneamente en direcciones opuestas. La señal

que atraviesa el transductor se digitaliza mediante un osciloscopio digital. En la Figura 13a) se puede ver la señal de excitación del generador y otros dos tonos más pequeños que se corresponden con los primeros ecos provenientes de cada reflector.

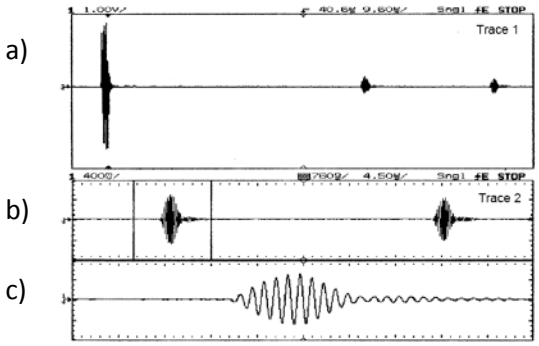

Figura 13. a) Pulso de excitación y ecos de respuesta emitidos; b) ampliación de los ecos; c) ampliación del primer eco.

En la Figura 13b) se muestran con más detalle los dos ecos donde se puede ver que su forma es prácticamente la misma. Si el tiempo en el que aparece un pico determinado de la señal del primer eco es t_1 (se puede elegir el primer pico o el más alto), el tiempo en el que aparece el mismo pico en el segundo eco es t_2 y la distancia entre los picos de los ecos es ΔL, la velocidad del sonido, c, se obtiene como:

$$c = 2\Delta L/\Delta t \qquad \text{(Ec.7)}$$

Donde $\Delta t = (t_2 - t_1)$. La ventaja de este método es que al utilizar la diferencia entre los tiempos correspondientes a los dos ecos, los errores debidos a la difracción o a retrasos en la señal electrónica se reducen e incluso se eliminan.

La distancia ΔL se determina mediante la calibración con un fluido dado a P_0 y T_0. La variación de ΔL con la temperatura , T, y la presión , P, se calcula mediante la siguiente ecuación:

$$\Delta L(T,P) = \Delta L(T_0,P_0)\{1 + \alpha(T - T_0) - \tfrac{1}{3}\kappa_T(P - P_0)\} \qquad \text{(Ec.8)}$$

Donde

α es la dilatación térmica del cuarzo, que se asume independiente de T y de P

κ_T es la compresibilidad isotérmica media del cuarzo a presiones entre P_0 y P, que se calcula con la siguiente ecuación:

$$\kappa_T/\mathrm{MPa}^{-1} = \{107820 + 36(T/\mathrm{K} - 273.15) - 17.1\ \mathrm{P/MPa}\} \qquad \text{(Ec.9)}$$

El término de la compresibilidad isotérmica supone el 0.18% del valor de ΔL, a 200 MPa y 423.15 K, mientras que el de la dilatación térmica no supera el 0.01% en el rango de temperatura estudiado.

La instalación experimental se calibró con agua desionizada (Milli Q) y desgasificada a 298.12 K y 1 MPa. Se determinó el desfase en el tiempo que tienen los dos ecos producidos en el fluido de calibración por un pulso ultrasónico a 5MHz, que fue de 13.245 µs. Bajo estas condiciones de presión y de temperatura, el valor de la velocidad del sonido según la EoS IAPWS-95[101]es 1498.13 m s^{-1}, de forma que el valor de la longitud de la celda calculado fue L_0=19.84 x 10^{-3} m.

iii. Precisión en fluidos puros.

Líquidos

Se midió la velocidad del sonido del agua desionizada en un rango de temperaturas desde 280.13 hasta 463.26 K a presiones comprendidas entre 1.0 y 190.0 MPa, obteniendo un valor de repetibilidad en la medida de c de ±0.02 ms^{-1}.

Los valores experimentales obtenidos para el agua se compararon con los de la EoS de referencia de Wagner y Pruss[101], que tiene una incertidumbre en la región líquida para c desde ±0.03 a ±0.2% y se calculó la $MRD(c)$ siendo inferior a 0.06% para este fluido. Los valores obtenidos en este trabajo son similares a los de la literatura[22,45,51,52,76,78,79,93,94,100] determinados con sistemas de pulso ultrasónico que operan en la mayor parte de los casos hasta presiones más bajas que las alcanzadas en este trabajo.

Fluidos comprimidos

Con el objetivo de verificar el adecuado funcionamiento de la instalación con gases comprimidos y obtener la precisión en la determinación de c para este tipo de sistemas, se midió c en etano puro (≥99.995 % molar) en un rango de temperatura entre 273.19 y 423.21 K a presiones desde 3.93 hasta 170.0 MPa. Este rango de presiones cubre un amplio intervalo (entre 36.8 y 170.0 MPa) para el cual no existen valores de velocidades del sonido en la bibliografía.[1,17,28,57,74,78,91,94]

Se compararon los valores de c experimentales con los calculados con la EoS de referencia de Buecker y Wagner[13]. Las desviaciones encontradas fueron mayores que para el agua: 0.05% a T = 333.15 K hasta 0.16% a T = 273.15 K. La mayor desviación de las medidas con respecto a la EoS puede deberse al amplio rango de velocidades del sonido medido para este fluido (de 538.15 a 1774.91 ms^{-1}) en comparación con el rango de medida para el agua (de 1432.81 a 1845.40 ms^{-1}) y/o a la imprecisión de la EoS debido a la escasez de datos experimentales en la bibliografía. En las Figuras 14a) y b) se representan valores experimentales $P-c-T$ para el agua y para el etano respectivamente, así como los valores calculados con las EoS de referencia[13,101].

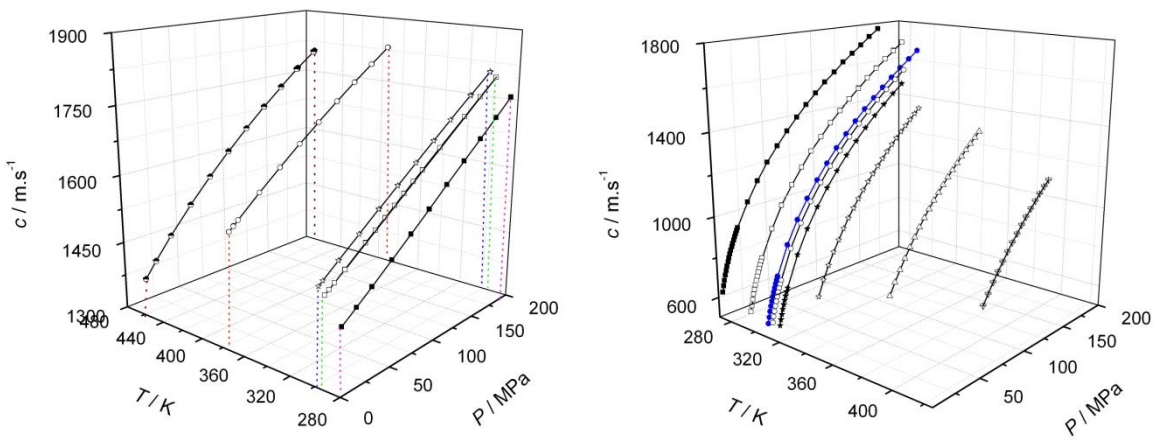

Figura 14. Representación $P-c-T$ para (a) agua y (b) etano a varias presiones y temperaturas; valores experimentales (símbolos) y EoS (líneas). La isoterma crítica para el etano está representada por puntos azules.

iv. Puesta a punto de la instalación para mezclas. Velocidad del sonido en el sistema CO_2+ CH_3OH.

La puesta a punto de la instalación para la medida de velocidades del sonido se llevó a cabo para mezclas gas comprimido + líquido. Se eligió el sistema CO_2+ CH_3OH porque el metanol puede estar presente en el CO_2 antropogénico transportado y almacenado debido a su utilización para prevenir hidratos o como producto residual del proceso de secado del ceoducto. Se utilizaron CO_2 y metanol de pureza del 99.998 y 99.93 % molar, respectivamente. Se estudiaron las mezclas de composición x_{CO_2} = 0.7534, 0.8502, 0.9250, 0.9700 y 0.9803 a T = 263.15, 298.15 y 323.15 K y presiones hasta 195 MPa. De la mezcla con x_{CO_2} = 0.9700 se determinaron además las isotermas a 273.15, 283.15, 293.15, 304.21 y 313.15 K**.**

Las mezclas CO_2+metanol se prepararon en una célula de volumen variable proporcionada por Top Industrie S.A.S., con un volumen máximo de 0.51 L y una presión máxima de 30 MPa (Figura 5.b). Después de introducir el metanol en la célula previamente evacuada, se inyectó el CO_2 mediante una bomba de jeringa ISCO modelo 260D, que trabaja hasta 50 MPa. La mezcla se trasvasó a una bomba ISCO empujando el émbolo de la célula con un gas inerte y de ella a la bomba manual incluida en la instalación. La combinación de ambas bombas permitió cargar la masa suficiente para alcanzar la presión máxima de trabajo. La homogeneidad de la mezcla se aseguró mediante agitación tanto en la célula de volumen variable como en cada una de las bombas (ISCO, manual y de recirculación en el interior de la instalación).

Las masas de los distintos componentes se determinaron por pesadas sucesivas en un comparador de masas Sartorius modelo CCE 2004. La fracción molar del componente que se introduce en primer lugar, x_1, se determinó mediante la relación:

$$x_1 = \left[\frac{(m_2-m_1)}{M_1}\right] / \left[\frac{(m_3-m_2)}{M_2} + \frac{(m_2-m_1)}{M_1}\right] \qquad \text{(Ec.10)}$$

Donde m_1 es la masa del matraz o de la célula a vacío, m_2 es la masa tras la introducción del primer componente, m_3 tras la introducción del segundo componente, M_1 es la masa molar del componente que se introduce en primer lugar y M_2 la del que se introduce en segundo lugar. El cálculo de las incertidumbres se realizó a partir de la Ley de Propagación de errores.

Así, la incertidumbre estándar en la fracción molar, u_X, se calculó con la ecuación:

$$u_x^2 = [(\partial x/\partial m_1)u_m]^2 + [(\partial x/\partial m_2)u_m]^2 + [(\partial x/\partial m_3)u_m]^2 \qquad \text{(Ec.11)}$$

Donde u_m es la incertidumbre en la pesada, que fue tomada como ±2×10^{-4}g. El valor obtenido para u_x fue de ±2·10^{-6} .

La ecuación usada para el cálculo de la incertidumbre estándar de las medidas experimentales de c, u_c, es:

$$u_c^2 = [(\partial c/\partial T)_P u_T]^2 + [(\partial c/\partial P)_T u_P]^2 + [(\partial c/\partial x)u_x]^2 + (u_c^*)^2 \qquad \text{(Ec.12)}$$

Donde u_P=0.02 MPa y u_T=0.015 K.

u_c^* es la incertidumbre estándar de repetibilidad (Lin, 2014). Para determinar su valor, se prepararon dos mezclas de composición $x_{\mathrm{CO_2}} = 0.9250$. Para cada una, se midieron dos isotermas a las siguientes temperaturas: 263.15, 298.15 y 323.15 K. Las desviaciones entre los valores de c a cada T para cada una de las mezclas se representan en la Figura 15. El valor determinado para $u_c^*(c)$ fue 5.3·10^{-4}·c.

Para obtener las contribuciones a la incertidumbre estándar debidas a las incertidumbres en la medida de la presión y de la temperatura se correlacionaron los valores experimentales de c mediante las siguientes ecuaciones:

$$(p - p^{\neq})/\mathrm{MPa} = \sum_{i=1}^{3}\sum_{j=0}^{2} a_{ij}\,\{(c - c^{\neq})/(m \cdot s^{-1})\}^i\,(\mathrm{T/K})^{-j} \qquad \text{(Ec.13)}$$

Donde $c^{\neq}$ es la velocidad del sonido a $p = p^{\neq}$, la cual se correlaciona como función de la temperatura mediante la siguiente ecuación:

$$c^{\neq}/(m \cdot s^{-1}) = \sum_{j=0}^{2} b_j\,(\mathrm{T/K})^j \qquad \text{(Ec.14)}$$

Para determinar la contribución en u_c de la incertidumbre en la composición se utilizaron las medidas de c de todas las mezclas CO_2+CH_3OH obtenidas a 263.15, 298.15 y 323.15 K. Tanto esta contribución como las debidas a las incertidumbres en las medidas de P y T, respectivamente, resultan muy inferiores a u_c^*, por lo que la incertidumbre relativa estimada en la medida de c para el sistema CO_2+CH_3OH fue $u(c) = 5.9{\cdot}10^{-4}\cdot c$. Este valor se encuentra dentro del rango de incertidumbres

estándar obtenido por otros autores utilizando un aparato similar tanto para mezclas líquidas como mezclas binarias de gases comprimidos[8,19,64].

La Figura 16 muestra la evolución de c con la presión a las temperaturas de trabajo para la composición $x_{CO_2} = 0.9700$ siendo el comportamiento el mismo para todas las composiciones:

$$\downarrow T, \uparrow P \Rightarrow \boldsymbol{c} \uparrow$$

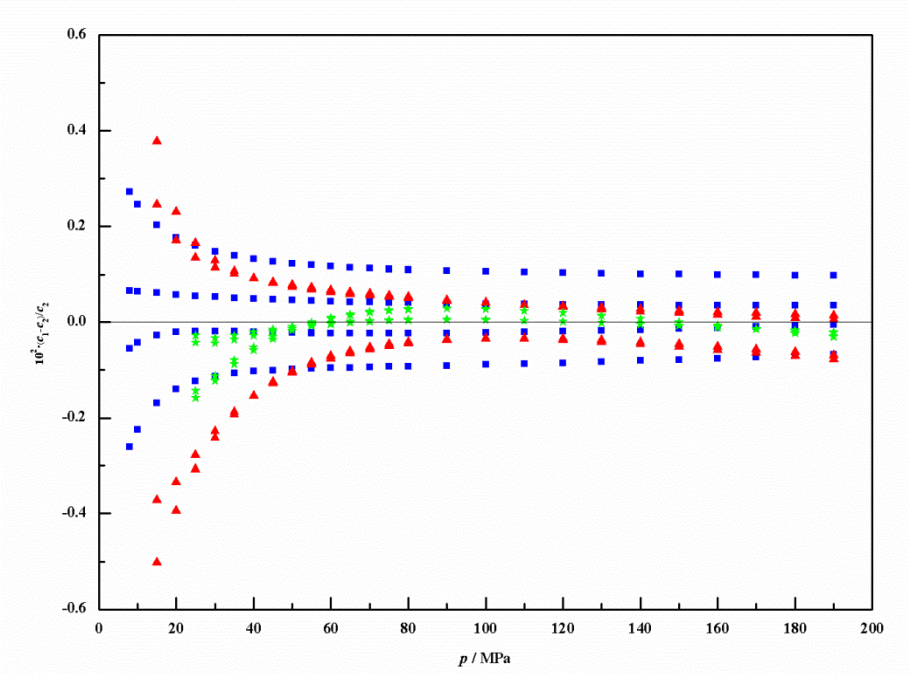

Figura 15. Desviaciones entre los valores de c para dos mezclas CO_2+CH_3OH con $x_{CO_2} = 0.9250$, a tres temperaturas, T, frente a presión, P. Cada mezcla se midió dos veces a cada temperatura. ■, T= 263.15 K; ▲, T= 298.15 K; ✱, T= 323.15 K.

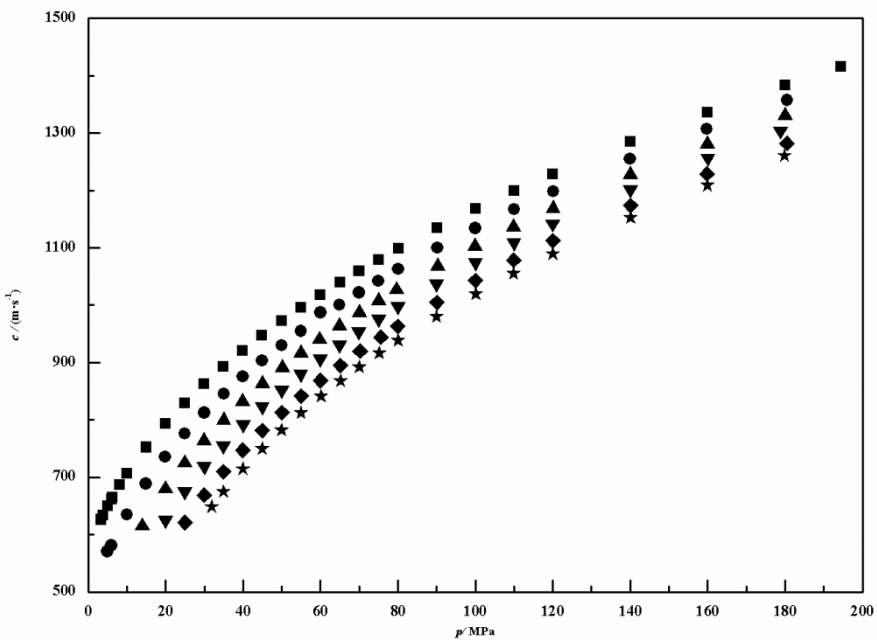

Figura 16. Velocidades del sonido experimentales, c, para la mezcla CO_2 + CH_3OH con $x_{CO_2} = 0.9700$ a varias temperaturas, *T*:. ■, *T* = 263.15 K;●, *T* = 273.15 K ▲, *T* = 283.15 K;▼, *T* = 293.15 K; ◆, *T* = 304.21 K ★, *T* = 313.15 K.

B.2.) Cálculo de propiedades derivadas

- Compresibilidad isentrópica, κ_S, y capacidad calorífica isobárica, C_P.

Con los valores de c y ρ determinados experimentalmente para el etano y los calculados κ_T y α_P se han obtenido κ_S y C_P a partir de las siguientes ecuaciones:

$$\kappa_S = \frac{1}{\rho c^2} \qquad \text{(Ec. 15)}$$

$$C_P = \frac{\alpha^2 T}{\rho(\kappa_T - \kappa_S)} \qquad \text{(Ec.16)}$$

Los valores de estas propiedades se han comparado con los obtenidos con la EoS de referencia de Buecker[13]. Las desviaciones obtenidas fueron $MRD(\kappa_S) = 0.19$ % y $MRD\ (C_P) = 3$ %.

En la Figura 17 se representan los valores calculados de C_P junto con los predichos por la EoS.[13]

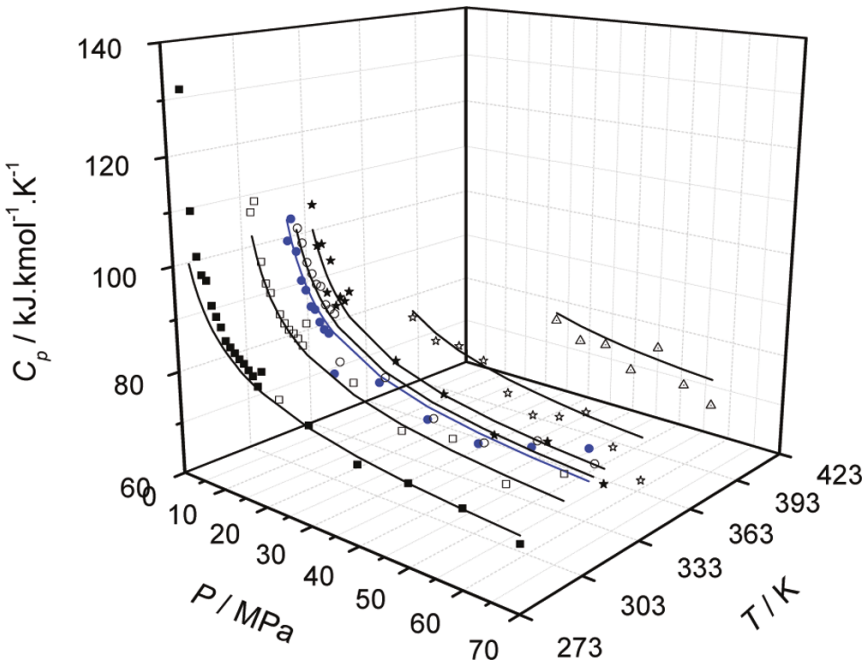

Figura 17. Representación $P - C_P - T$ para el etano a varias presiones y temperaturas; valores calculados a partir delos c experimentales (símbolos) y EoS (líneas). La isoterma crítica para el etano está representada por puntos azules.

4.2. ESTUDIO DEL COMPORTAMIENTO VOLUMÉTRICO Y DEL ELV DE LAS MEZCLAS CO_2+CH_4 Y CO_2+CO RICAS EN CO_2.

La determinación experimental de estas propiedades para los sistemas CO_2+CH_4 y CO_2+CO se ha realizado utilizando la instalación y el procedimiento experimental descritos en el apartado 4.1 de esta memoria.

Los valores experimentales del equilibrio de fase y de densidad, son necesarios para evaluar cuantitativamente la influencia de la presencia de CH_4 y CO en el CO_2 antropogénico y poder validar Ecuaciones de Estado que permitan predecir el comportamiento de estas mezclas en diferentes condiciones. Si bien en la literatura hemos encontrado datos experimentales $P-\rho-T-x_{CO_2}$ y ELV para la mezcla CO_2+CH_4[21,67,102], las condiciones y composiciones de trabajo no son las de interés para la tecnología CCS. Para la mezcla CO_2+CO los datos encontrados en la literatura son mucho más escasos, la mayor parte de los estudios se basan en modelos predictivos y no cubren los rangos de interés para la tecnología CCS.

Las impurezas que provienen de los gases de emisiones industriales condicionan la composición del fluido a almacenar, y por tanto deben tenerse en cuenta para el correcto diseño y operación de la tecnología CCS. El CH_4 es un compuesto habitualmente emitido en las industrias relacionadas con los sectores de agricultura, cerámica y gestión de residuos y el CO con los procesos de post-combustión. Ambos compuestos son altamente tóxicos con una influencia elevada en el efecto invernadero. Las composiciones estudiadas en este trabajo incluyen las recogidas en los registros oficiales de emisiones de España, Unión Europea y Estados Unidos[2,3,82,.] Los rangos de P y T elegidos tienen en cuenta las presiones y temperaturas estimadas en el interior de las tuberías de CO_2 [62] y en los lugares de almacenamiento geológico[6].

A) PROPIEDADES VOLUMÉTRICAS Y EQUILIBRIO LÍQUIDO VAPOR

En la Tabla 1 se resumen las mezclas estudiadas para los dos sistemas así como la concentración, presión y temperatura de trabajo.

Tabla 1 Composiciones, temperaturas y presiones objeto de estudio en este apartado. (En azul: estudiado para la mezcla CO_2+CH_4; en gris: estudiado para la mezcla CO_2+CO; en blanco: no estudiado)

$P = 0.1 - 20$ MPa												
x_{CO_2}		$T = 253.15$ K	$T = 263.15$ K	$T = 273.15$ K	$T = 283.15$ K	$T = 293.15$ K	$T = 298.15$ K	$T = 304.21$K	$T = 308.15$K	$T = 323.15$K	$T = 333.15$K	$T = 343.15$K
0.8525	CO_2+CH_4											
-	CO_2+CO											
0.9719	CO_2+CH_4											
0.9700	CO_2+CO											
0.9809	CO_2+CH_4											
0.9810	CO_2+CO											
0.9902	CO_2+CH_4											
0.9902	CO_2+CO											
0.9932	CO_2+CH_4											
0.9930	CO_2+CO											
0.9961	CO_2+CH_4											
0.9960	CO_2+CO											

Se han determinado un total de 104 isotermas $P-\rho-T-x_{CO_2}$ con una incertidumbre expandida (k = 2) en la densidad (Anexo I, Ecuación A.V): $U(\rho)$ =0.35-0.80 kg·m^{-3}.

A modo de ejemplo, en las Figuras 18a) y b) se muestran las densidades experimentales para $x_{CO_2} \cong 0.97$ para ambos sistemas a las temperaturas y presiones de trabajo. Como es de esperar, la densidad de las mezclas en las isotermas supercríticas es una línea continua cuya pendiente es máxima a la temperatura crítica y disminuye a medida que ésta aumenta.

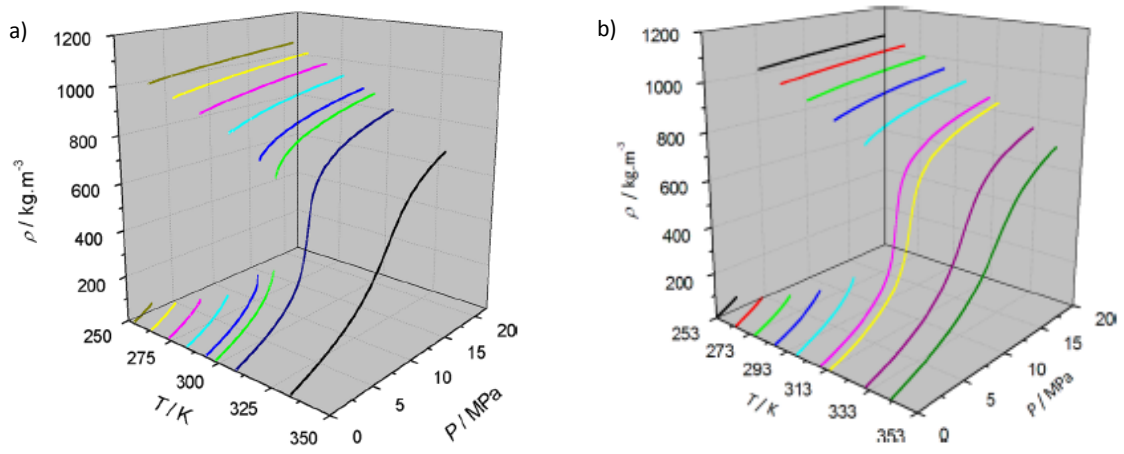

Figura 18. Densidades experimentales, ρ, para las mezclas a) CO_2+CH_4 con $x_{CO_2} = 0.9719$ y b) CO_2+CO con $x_{CO_2} = 0.9700$.

La región del equilibrio líquido vapor aparece delimitada por las discontinuidades de las isotermas subcríticas y sus puntos se pueden calcular como se ha descrito en la sección 4.1.A.1. La Figura 19 muestra las presiones de rocío y de burbuja experimentales y las densidades de las fases en equilibrio para tres mezclas CO_2+CH_4. Las envolventes de fase para las cinco mezclas CO_2+CO así como la línea de saturación del CO_2 puro se encuentran recogidas en la Figura 20. Todos los resultados fueron consistentes con los encontrados en la bibliografía[21,67,102]

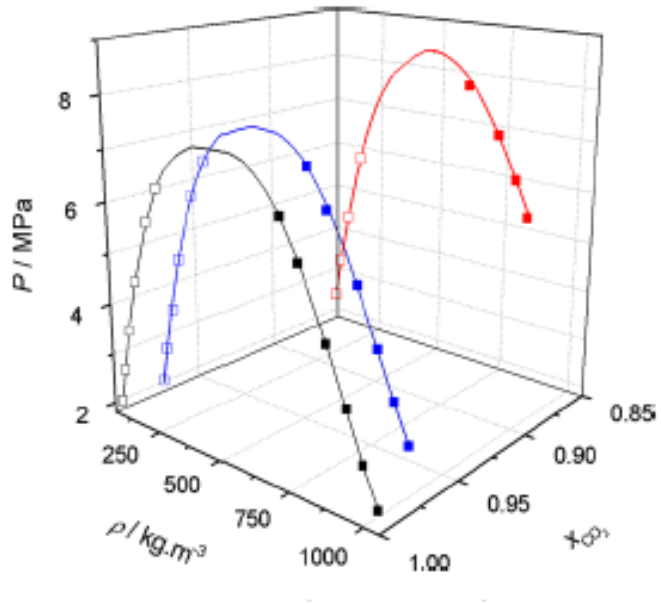

Figura 19. Presiones experimentales de rocío, P_r , (símbolos en blanco) de burbuja, P_b , (símbolos sólidos) y ρ_V, ρ_L del equilibrio de fases para las mezclas CO_2+CH_4 con x_{CO_2} =0.8525 (rojo), x_{CO_2} = 0.9719 (azul) y x_{CO_2} = 0.9961 (negro).

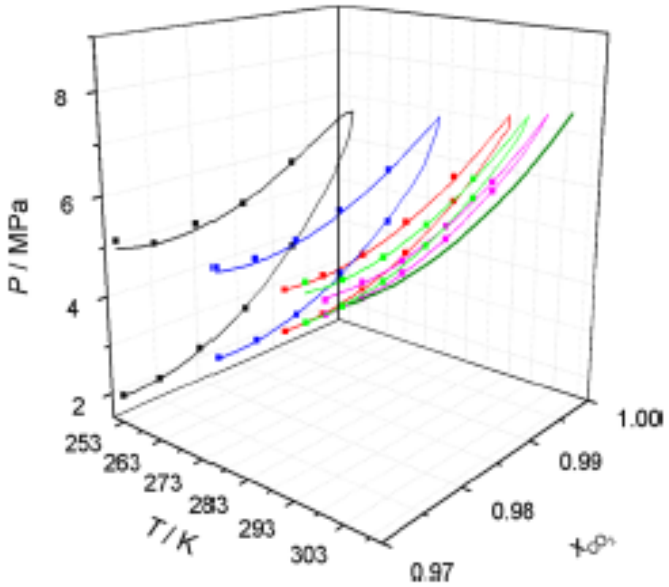

Figura 20. Presión de vapor de CO_2 [59] (verde oliva) y envolventes de fase experimentales para las mezclas CO_2+CO con x_{CO_2}=0.9700 (negro), x_{CO_2}=0.9810 (azul), x_{CO_2}=0.9902 (rojo), x_{CO_2}=0.9930 (verde) y x_{CO_2}=0.9960 (rosa).

De especial interés es el comportamiento volumétrico que presentan los sistemas en la región crítica. Por ello, también se han calculado los volúmenes molares de exceso, V_m^E, y los volúmenes parciales molares, $\bar{V}_i$ de ambos sistemas a $T = T_c(CO_2)$ = 304.21 y 308.15 K:

$$V_m^E = V_{mezcla} - V_1 - V_2 = \frac{x_1 M_1 + x_2 M_2}{\rho_{mezcla}} - \frac{x_1 M_1}{\rho_1} - \frac{x_2 M_2}{\rho_2} \quad \text{(Ec.17)}$$

$$\bar{V}_2 = V_m + (1 - x_2)\left(\frac{\partial V_m}{\partial x_2}\right)_{P,T} \quad \text{(Ec. 18)}$$

Donde los subíndices 1 y 2, hacen referencia al disolvente (CO_2) y al soluto (CH_4 o CO); M es la masa molar; V_m y ρ son el volumen molar y la densidad, respectivamente, a la temperatura, T, y presión, P.

Las incertidumbres expandidas en el cálculo de ambas propiedades (Anexo 1, Ecuación A.V) fueron: $U(V_m^E) = 0.1$ - 1 $cm^3 \cdot mol^{-1}$ y $U(\bar{V}_2)$ = 3 - 85 $cm^3 mol^{-1}$.

En la Figura 21 se recoge el V_m^E para ambos sistemas a las dos temperaturas y a las composiciones $x_{CO_2} \cong 0.971$ y $x_{CO_2} \cong 0.993$; dichas mezclas son supercríticas en esas condiciones. V_m^E depende fuertemente de la presión y de la composición, lo que indica un comportamiento alejado de la idealidad. Se observa un máximo para el volumen molar de exceso en función de la presión, y la disminución de su valor a medida que aumenta la temperatura y la fracción molar de CO_2. El V_m^E es mayor para el sistema CO_2+ CO que para CO_2+CH_4, lo que supone que la sustitución de una molécula de CO_2 por otra de CO produce una mayor perturbación en el sistema que en el caso de CH_4. Esto puede deberse al mayor valor del momento dipolar de la molécula de CO (μ_{CO} = 0.122 D) frente a $\mu_{CO_2} = \mu_{CH_4} = 0$, al tamaño de los componentes o a ambos factores.

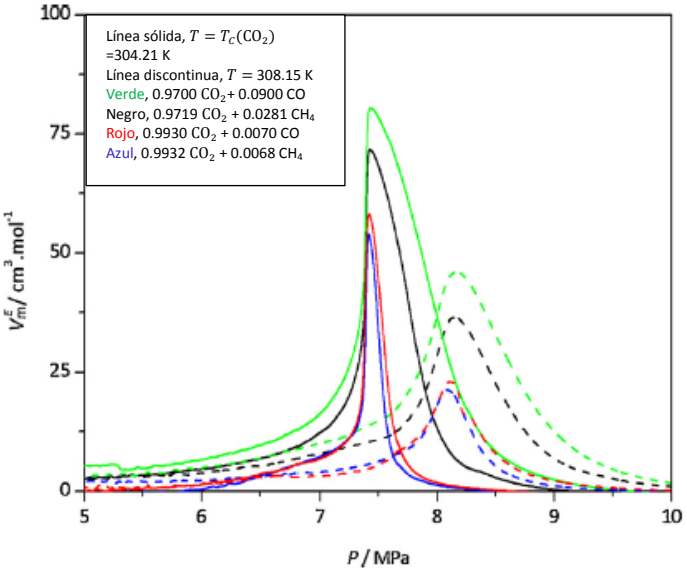

Figura 21. Representación $V_m^E - P$ para los sistemas estudiados a $T = T_c(CO_2)$ =304.21 K y T = 308.15 K, para las composiciones $x_{CO_2} \cong 0.971$ y $x_{CO_2} \cong 0.993$.

La Figura 22 muestra los volúmenes molares parciales del soluto, $\bar{V}_2$, para las cinco composiciones estudiadas de ambos sistemas, a las dos temperaturas y a las

presiones $P = P_c(\mathrm{CO_2})$ = 7.383 y 8.000 MPa. Para ambos sistemas se observa un comportamiento similar. A 7.383 MPa, $\bar{V}_2$ disminuye al aumentar la concentración de soluto a ambas temperaturas de trabajo, con una pendiente mucho más pronunciada a 308.15 K. Sin embargo, a la presión supercrítica, 8.000 MPa, $\bar{V}_2$ aumenta al aumentar la concentración del soluto a 304.21 K y disminuye a 308.15K.

De nuevo, los valores de $(\partial \bar{V}_2 / \partial x_2)$ indican que el sistema CO_2+CO muestra una mayor desviación de la idealidad que el CO_2+CH_4.

Los valores de $\bar{V}_2$ calculados en este trabajo para la mezcla {0.9961 CO_2+0.0039 CH_4} a 308.15 K se han comparado con los publicados por Zhang y colaboradores[103], observándose buena concordancia, especialmente en la región densa. La desviación media relativa en el punto correspondiente al máximo valor de $\bar{V}_2$ es $MRD_{\bar{V}_2} < 6\%$.

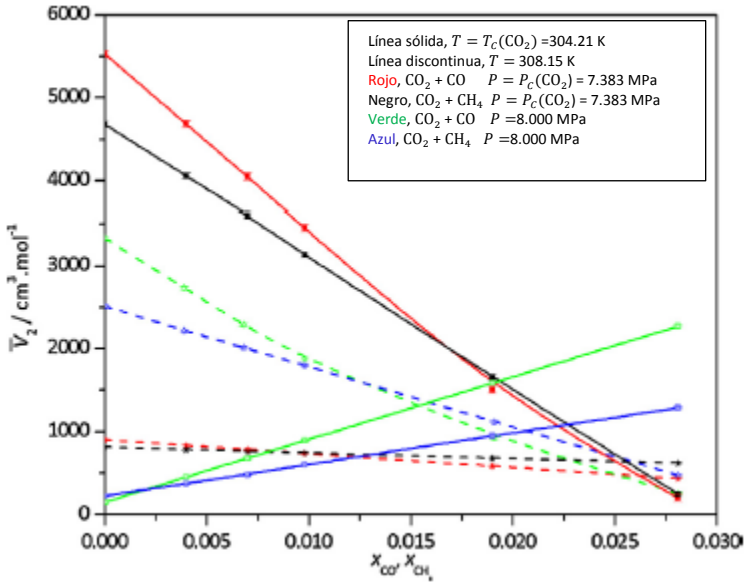

Figura 22. Representación de volumen parcial molar del soluto, $\bar{V}_2$ frente a la fracción molar $x_{\mathrm{CO}}, x_{\mathrm{CH_4}}$ para los sistemas estudiados a P = 7.383 y 8.000 MPa a T =304.21 y 308.15 K.

B) PROPIEDADES DERIVADAS DE LA DENSIDAD

A partir de los datos experimentales $P - \rho - T - x_{\mathrm{CO_2}}$ se han calculado los valores de compresibilidad isotérmica, κ_T, expansividad térmica isobárica, α_P, y presión interna, π_i, (Ecuaciones 4, 5 y 6) en todas las condiciones estudiadas.

En la Tabla 2 se recogen algunos de los datos calculados a 304.21 K para las mezclas CO_2+CO y CO_2+CH_4 con $x_{\mathrm{CO_2}}$ = 0.993. Se observa que la dependencia de la compresibilidad isotérmica con la presión es similar para ambos sistemas, y la tendencia para α_P es similar a la de la compresibilidad isotérmica.

Los valores de presión interna son mayores para la mezcla CO_2+CO que para la mezcla CO+CH_4 aumentando en ambos casos al aumentar la presión del sistema.

Tabla 2. Valores de κ_T, α_P, y π_i para CO_2+CO y CO_2+CH_4 a 304.21 K para x_{CO_2}=0.993.

P /MPa	κ_T/MPa^{-1}		α_P/K^{-1}		π_i/MPa	
	CH_4	CO	CH_4	CO	CH_4	CO
8	$2.72\cdot10^{-1}$	-	$2.0\cdot10^{-2}$	-	14	-
9	$3.02\cdot10^{-1}$	$6.12\cdot10^{-2}$	$3.3\cdot10^{-2}$	$1.9\cdot10^{-2}$	25	85
10	$2.47\cdot10^{-1}$	$3.74\cdot10^{-2}$	$3.7\cdot10^{-2}$	$1.4\cdot10^{-2}$	36	104
11	$1.50\cdot10^{-1}$	$2.76\cdot10^{-2}$	$2.9\cdot10^{-2}$	$1.4\cdot10^{-2}$	48	143
12	$8.70\cdot10^{-2}$	$2.26\cdot10^{-2}$	$2.2\cdot10^{-2}$	$1.1\cdot10^{-2}$	63	136
13	$5.99\cdot10^{-2}$	$1.82\cdot10^{-2}$	$1.7\cdot10^{-2}$	$8.9\cdot10^{-3}$	72	136
14	$4.36\cdot10^{-2}$	$1.53\cdot10^{-2}$	$1.4\cdot10^{-2}$	$8.5\cdot10^{-3}$	82	155
15	$3.37\cdot10^{-2}$	$1.38\cdot10^{-2}$	$1.2\cdot10^{-2}$	$7.7\cdot10^{-3}$	91	155
16	$2.77\cdot10^{-2}$	$1.24\cdot10^{-2}$	$1.0\cdot10^{-2}$	$7.3\cdot10^{-3}$	98	163
17	$2.30\cdot10^{-2}$	$1.12\cdot10^{-2}$	$9.3\cdot10^{-3}$	$6.6\cdot10^{-3}$	106	162
18	$2.04\cdot10^{-2}$	$1.02\cdot10^{-2}$	$8.4\cdot10^{-3}$	$6.5\cdot10^{-3}$	107	176
19	$1.76\cdot10^{-2}$	$9.12\cdot10^{-3}$	$7.7\cdot10^{-3}$	$5.9\cdot10^{-3}$	115	178
20	$1.54\cdot10^{-2}$	$7.81\cdot10^{-3}$	$7.2\cdot10^{-3}$	$5.6\cdot10^{-3}$	122	198

C) MODELIZACIÓN

a. Ecuación de Estado Peng-Robinson[75]

Las ecuaciones cúbicas son las ecuaciones de estado más sencillas que predicen la existencia del punto crítico y proporcionan una representación cuantitativa del ELV. Generalmente, predicen de forma razonable el comportamiento de fases de los sistemas binarios mientras que la modelización de la densidad requiere la introducción de un factor de corrección; sin embargo, su simplicidad las hace preferibles en muchas aplicaciones de ingeniería.

Para compuestos puros, solo se requiere para su aplicación las coordenadas del punto crítico (P_c, T_c, V_c) y el valor del factor acéntrico, ω. En el caso de mezclas, se introduce un parámetro de interacción binaria, k_{ij}. En este trabajo, hemos usado la formulación original que incluye las reglas de mezclas clásicas de van der Waals. Las ecuaciones son:

$$P = \frac{RT}{V-b} - \frac{a\alpha(T_r,\omega)}{V(V+b)+b(V-b)} \quad \text{(Ec. 19)}$$

$$a = 0.45724\,\frac{RT_C^{2.5}}{P_C} \quad \text{(Ec. 20)}$$

$$b = 0.07780\,\frac{RT_C}{P_C} \quad \text{(Ec. 21)}$$

$$\alpha(T_r,\omega) = [1 + m(1 - T_r^{0.5})]^2; \quad \text{(Ec. 22)}$$

$$m = 0.37464 - 1.54226\omega - 0.26992\omega^2 \quad \text{(Ec. 23)}$$

$$a = \sum_i \sum_j x_i x_j a_{ij}; \quad b = \sum_i \sum_j x_i x_j b_{ij} \quad \text{(Ec. 24)}$$

$$a_{ij} = \sqrt{a_i a_j}(1 - k_{ij}); b_{ij} = \frac{1}{2}(b_i + b_j) \quad \text{(Ec. 25)}$$

b. Ecuación de Estado GERG-2008[50]

Se trata de una ecuación de estado basada en una aproximación multifluido donde la energía de Helmholtz adimensional se divide en dos contribuciones: mezcla ideal, $\tilde{a}_i^{id}$ y parte residual, $\tilde{a}_i^{res}$.

$$\tilde{a} = \tilde{a}^{id} + \tilde{a}^{res} = \sum_{i=1}^{N} x_i\left[\tilde{a}_i^{id} + lnx_i\right] + \sum_{i=1}^{N} x_i \tilde{a}_i^{res} + \Delta\tilde{a}^{res} \quad \text{(Ec. 26)}$$

Donde i hace referencia a la sustancia pura y $\Delta\tilde{a}^{res}$ es la función de partición.

Fue desarrollada inicialmente como EoS de referencia para las mezclas de Gas Natural y, por lo general, ofrece mejores resultados que otras EoS. Sin embargo, es limitada en cuanto a su aplicación, costosa en cuanto al tiempo computacional que necesita[41] y no está validada en las condiciones de presión, temperatura y composición características en la Tecnología CCS.

c. Ecuación de Estado PC-SAFT[36,37]

En este modelo, basado en teorías de perturbación, el fluido de referencia se denomina fluido de cadena rígida. Las fuerzas de interacción atractivas entre moléculas se expresan a través de diferentes contribuciones, por lo que la energía de Helmholtz, $\tilde{a}$, se escribe como suma de las contribuciones siguientes: una para el gas ideal, $\tilde{a}^{id}$, un término de cadena rígida, $\tilde{a}^{hc}$, una contribución debida a la atracción dispersiva, $\tilde{a}^{dis}$, y varios términos relacionados con la asociación de las moléculas, $\tilde{a}^{asoc}$, e interacciones dipolo-dipolo, $\tilde{a}^{DD}$, cuadropolo-cuadrupolo, $\tilde{a}^{QQ}$ y dipolo-cuadrupolo, $\tilde{a}^{QD}$:

$$\tilde{a} = \tilde{a}^{id} + \tilde{a}^{hc} + \tilde{a}^{dis} + \tilde{a}^{asoc} + \tilde{a}^{DD} + \tilde{a}^{QQ} + \tilde{a}^{QD} \quad \text{(Ec. 27)}$$

En este trabajo, no hemos tenido en cuenta las contribuciones polares y de asociación por lo que:

$$\tilde{a} = \tilde{a}^{id} + \tilde{a}^{hc} + \tilde{a}^{dis} \qquad \text{(Ec. 28)}$$

Los compuestos puros están caracterizados por tres parámetros geométricos: el número de segmento, m, el diámetro de segmento, σ y el parámetro de energía de segmento, ε. Si se obtienen a partir de presiones de vapor y de densidades líquidas, estos parámetros proporcionan una representación precisa tanto de las propiedades volumétricas como del ELV de las mezclas, sin embargo, sobreestiman los valores de las propiedades críticas. Con el objetivo de describir la región crítica, distintos autores[11,16,33,34] los reajustan incluyendo en la función objetivo sus puntos críticos. En esta Tesis se ha aplicado el modelo de dos maneras: utilizando parámetros de compuestos puros originales y reajustados. Además en ambos casos, hemos introducido traslación volúmica para representar mejor la densidad en un intervalo amplio de presión.

Para las mezclas, se han aplicado las reglas de Lorentz-Berthelot donde el parámetro de interacción binaria, k_{ij}, corrige el término de dispersión de las moléculas:

$$\varepsilon_{ij} = \sqrt{\varepsilon_i \varepsilon_j}(1 - k_{ij}); \sigma_{ij} = \frac{1}{2}(\sigma_i + \sigma_j) \qquad \text{(Ec. 29)}$$

En la Tabla 3 se muestran los parámetros utilizados para la modelización. En la Tabla 4 se resume el estudio comparativo entre nuestros datos y los obtenidos con las diferentes EoS, en términos de MRD_x (Anexo I Ecuación A.I). En la región crítica de ambos sistemas, dada su complejidad, se hizo la modelización con PC-SAFT con parámetros originales y reajustados. En la Figura 23 se presentan las desviaciones obtenidas para la densidad en todo el rango de presiones.

Tabla 3. Parámetros usados para la modelización de los sistemas CO_2+CH_4 y CO_2+CO con PR y PC-SAFT EoS

Parámetro	CO_2	CH_4	CO
T_C /K	304.21[32]	190.56[53]	132.86[53]
P_C/MPa	7.383[32]	4.599[53]	3.494[53]
ω	0.224[53]	0.011[53]	0.066[53]
m	2.0730[36]/2.1276[11]	1.0000[36]/1.0039**	1.3097[36]/1.3063**
σ/Å	2.7852[36]/2.8251[11]	3.7039[36]/3.7126**	3.2507[36]/3.2565**
ε/K	169.21[36]/163.76[11]	150.03[36]/149.11**	92.15[36]/91.48**
$\Delta v_C(PR\ EoS)/(10^{-3}\mathrm{m^3kg^{-1}})$	0	0	0
$\Delta v_C(PC-SAFT\ EoS)/(10^{-3}\mathrm{m^3kg^{-1}})$	0.02*	0*	-0.10*
k_{ij}(PR EoS)	CO_2+CH_4 = 0.12[53]		CO_2+CO = 0.205
k_{ij}(PC − SAFT EoS)	CO_2+CH_4 = 0.07*/0.05**		CO_2+CO =0.12*/0**

*PC-SAFT modelo original (Este trabajo)

**PC-SAFT modelo reajustado (Este trabajo)

Tabla 4. Desviaciones relativas promedio con respecto a las tres EoS de referencia para, P_r, P_b, ρ_V, ρ_L y densidades, ρ, para regiones distintas a la crítica, para las mezclas CO_2+CH_4 y CO_2+CO.

	CO_2 + CH_4			CO_2 + CO		
	PR EoS	PC-SAFT EoS	GERG-2008 EoS	PR EoS	PC-SAFT EoS	GERG-2008 EoS
$MRD_{P_b}/\%$	0.69	1.7	0.18	1.9	1.6	1.3
$MRD_{P_r}/\%$	0.48	1.7	0.13	0.47	1.4	0.38
$MRD_{\rho_L}/\%$	4.5	1.8	0.24	3.8	0.39	0.45
$MRD_{\rho_V}/\%$	1.5	5.8	0.66	1.8	4.3	1.4
$MRD_{\rho}^{a}/\%$	2.3	1.1	0.28	2.9	1.2	0.73
$MRD_{\rho}^{b}/\%$	3.6	1.7*/2.8**	0.40	3.2	1.5*/2.7**	1.1

[a] T ≠304.21 y 308.15 K

[b] T =304.21 y 308.15 K

*PC-SAFT modelo original (Este trabajo)

** PC-SAFT modelo reajustado (Este trabajo)

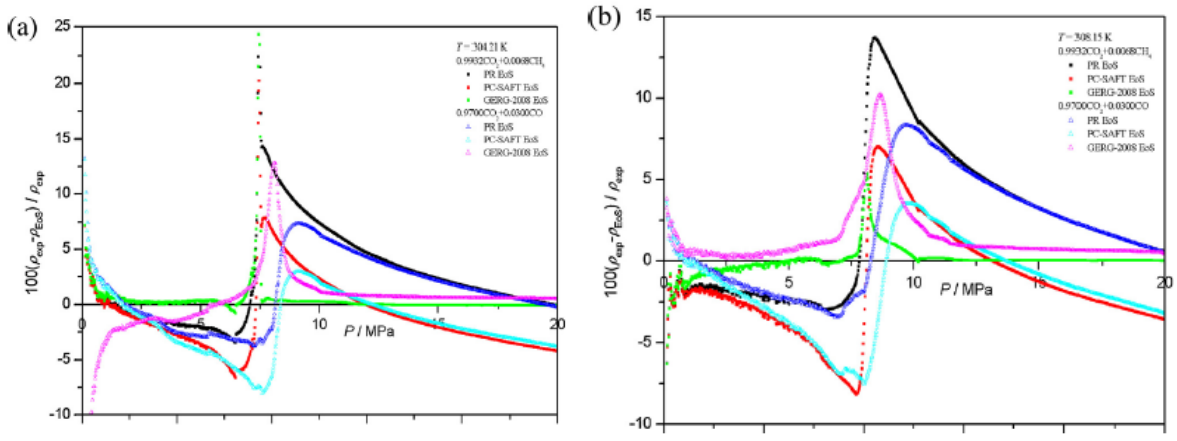

Figura 23. Desviación estándar relativa entre las densidades determinadas experimentalmente y los valores calculados utilizando diferentes EoS para distintas mezclas estudiadas en este trabajo. (a) T = 304.21 K y (b) T = 308.15 K.

A pesar de su simplicidad, la concordancia de la EoS PR con los datos experimentales es buena a presiones por debajo de la presión crítica para ambos sistemas y aceptable a presiones mayores.

La modelización con PC-SAFT utilizando los parámetros originales para los compuestos puros predice un estado subcrítico erróneo para nuestras mezclas ya que experimentalmente observamos un estado supercrítico. Sin embargo, las predicciones fuera de la región crítica son buenas. Por otro lado, si se utilizan los parámetros reajustados utilizando los puntos críticos para los compuestos puros, el modelo predice las regiones crítica y supercrítica de manera más precisa aunque las desviaciones fuera de estas regiones son mayores.

La comparación entre nuestros datos experimentales y los calculados con la EoS GERG-2008 es muy buena para ambos sistemas siendo las desviaciones menores para el sistema CO_2+CH_4. Esto podría deberse a que la ecuación está implementada con un gran número de datos experimentales para estas mezclas.

La EoS GERG-2008 es la ecuación que mejor representa nuestros resultados aunque presenta problemas al extenderla a mezclas de compuestos que no se encuentran en su base de datos. PC-SAFT presenta desviaciones ligeramente mayores que GERG-2008 pero su uso puede extenderse fácilmente a mezclas multicomponentes. Por último, PR puede también ser adecuada dependiendo de las presiones de trabajo y de la precisión requerida.

D) ESTUDIO ESTRUCTURAL

La eficiencia y la selectividad de los procesos de almacenamiento están influenciados por el tipo de interacciones entre el CO_2 y las moléculas presentes en el reservorio, y por tanto, por su afinidad. En esta sección se determina la naturaleza de las interacciones entre las moléculas de disolvente, CO_2 y las de soluto, CH_4 o CO a través del estudio volumétrico de disoluciones infinitamente diluidas, IDS, para los sistemas CO_2+CH_4 y CO_2+CO en condiciones cercanas a la temperatura crítica del CO_2. Se usarán el concepto de Función de Krichevskii y la Teoría de Kirkwood-Buff.[43,46]

El comportamiento termodinámico de una disolución puede ser descrito a través del efecto que produce sustituir, de forma isoterma e isocora, una molécula de disolvente por una de soluto a dilución infinita[42,60] . Cuando las condiciones de estudio coinciden con las críticas del disolvente se define el *parámetro de Krichevskii*, $A_{K_r} = (\partial P/\partial x_2)^{\infty}_{T_c,V_c}$ y si no coinciden, la *función de Krichevskii*, $J = (\partial P/\partial x_2)^{\infty}_{T,V}$.

Por lo tanto, J estará relacionada con magnitudes termodinámicas de la mezcla. Se puede deducir[11]:

$$\bar{V}_2^{\infty} = \rho_1^{0^{-1}}[1 + \kappa_T^0 J] \qquad \text{(Ec. 30)}$$

Donde los superíndices 0 y ∞ denotan componente puro y dilución infinita, respectivamente; ρ_1^0 es la densidad del disolvente puro y $\kappa_{T,1}^0$ su compresibilidad isotérmica.

Por otro lado, se puede establecer una relación entre la función de Krichevskii, J, con las propiedades estructurales del fluido a través de la llamada Inversión de la Teoría de Kirkwood-Buff, desarrollada por Ben-Naim en 1978.[9] En ella, las propiedades termodinámicas determinadas experimentalmente son utilizadas para calcular las integrales de Kirkwood-Buff (KBI), $G_{ij} = \int_0^\infty [g_{ij}(r) - 1]\, 4\pi r^2 dr$, lo que permite conocer el entorno local de cada especie en el sistema multicomponente. $g_{ij}(r)$ es la función de correlación de pares para las especies i y j, también llamada función de distribución radial, que representa la probabilidad de encontrar la partícula i a una distancia r de la partícula j.

Alternativamente, se puede trabajar en términos de la Función Integral de Correlación Directa (DCFI), $C_{ij} = \int c_{ij} dr$, donde c_{ij} (función de correlación directa) representa la correlación debida únicamente a las fuerzas de interacción existentes entre dos partículas i y j en un sistema de N-2 partículas.

Para una mezcla binaria en condiciones de dilución infinita, $x_2 \to 0$, las ecuaciones de Kirkwood-Buff se simplifican[18, 55]:

$\rho_1^0 RT\kappa_T^0 = 1 + \rho_1^0 G_{11}^0$ (Ec. 31) $\quad (\kappa_T^0)^{-1} = \rho_1^0 RT(1 - C_{11}^0)$ (Ec. 32)

$\rho_1^0 \bar{V}_2^\infty = 1 + \rho_1^0 (G_{11}^0 - G_{12}^\infty)$ (Ec. 33) $\quad \rho_1^0 \bar{V}_2^\infty = \rho_1^0 RT\kappa_T^0 (1 - C_{12}^\infty)$ (Ec. 34)

$J\,\kappa_T^0 = \rho_1^0 (G_{11}^0 - G_{12}^\infty)$ (Ec. 35) $\quad J = \rho_1^0 RT(C_{11}^0 - C_{12}^\infty)$ (Ec. 36)

Como se puede apreciar en la Ecuación 35, el reordenamiento del disolvente alrededor del soluto en la IDS, en relación a la estructura del disolvente puro, no viene dado por la fortaleza de la interacción entre las moléculas de disolvente y las del soluto sino por la asimetría intermolecular y la diferencia existente entre las interacciones disolvente-disolvente (1-1) y las disolvente-soluto (1-2). Todo ello permite valorar la idealidad de la mezcla.

El estudio se completa con el cálculo del número de coordinación de exceso, N_{exc}^∞, y el tamaño de clúster, N_1^{exc}. El primero se define como la diferencia entre el número de moléculas de disolvente que rodean a una molécula de soluto en condiciones de dilución infinita y el número de moléculas de disolvente alrededor de otra igual. El segundo, N_1^{exc}, indica la afinidad que presentan las moléculas de disolvente por una molécula de soluto en las cercanías del punto crítico del solvente.

$$N_{exc}^{\infty} = 4\pi\rho \int_0^r [g_{12}(r) - g_{11}(r)] r^2 dr = -\kappa_T^0 \left(\frac{\partial P}{\partial_{x_2}}\right)_{T,V}^{\infty} \quad \text{(Ec. 37)}$$

$$N_1^{exc} = 4\pi\rho \int_0^r [g_{12}(r) - 1] r^2 dr = \rho_1^0 RT\kappa_T^0 (1 - A_{\kappa_r}^*) \quad \text{(Ec. 38)}$$

Donde $A_{\kappa_r}^* = \frac{A_{\kappa_r}}{\rho_1^{'0} RT'}$

Cuando se dispone de datos volumétricos a dilución infinita, los valores de la función de Krichevskii (incluidos el parámetro de Krichevskii, A_{κ_r}) se calculan a partir de las pendientes de las isotermas-isocoras $P - x_2$ cuando $x_2 \to 0$ (Figura 24).

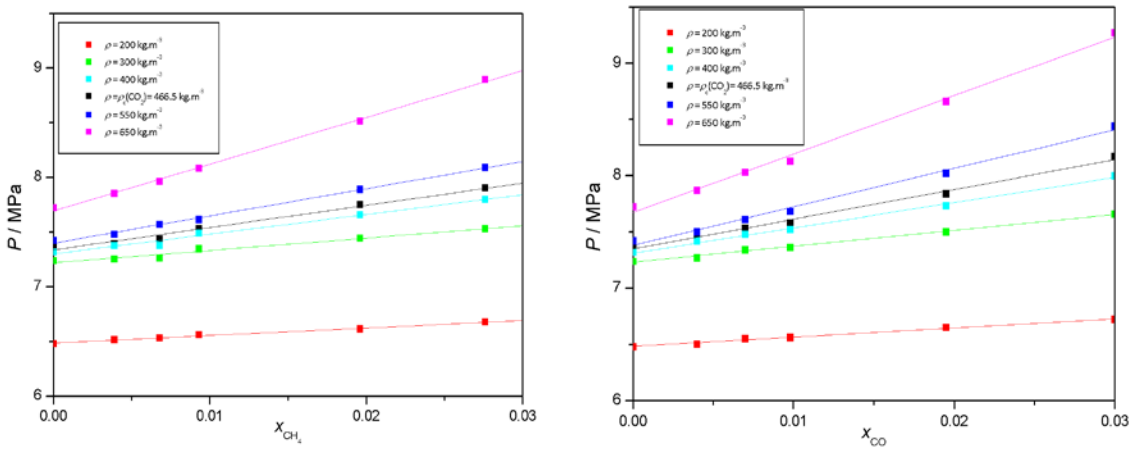

Figura 24. Datos $P - x_{CH_4}/x_{CO}$ de mezclas diluidas (a) CO_2 + CH_4 y (b) CO_2 + CO, para varias isocoras a T =304.21 K.

La Figura 25 muestra la diferencia de comportamiento de ambos sistemas en condiciones de dilución infinita, a la temperatura de 304.21 K, a través de la comparación de sus valores de J. Así, sustituir una molécula de CO_2 por una de CO o de CH_4 en el dióxido de carbono puro supone en ambos casos un aumento de presión del sistema, siendo más acusado en el caso del CO que del CH_4.

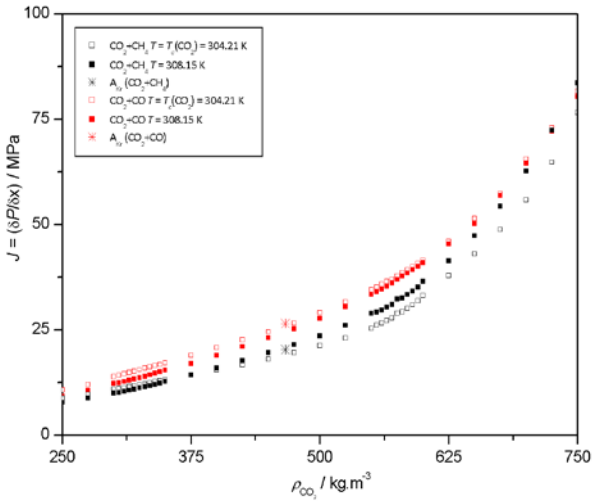

Figura 25. Función de Krichevskii, J, frente a densidad del disolvente puro, ρ_{CO_2} para los sistemas CO_2 + CO y CO_2 + CH_4 a T =304.21 K y T =308.15 K.

En las proximidades del punto crítico del disolvente puro, $x_2 \to 0$, la función de Krichevskii converge al parámetro de Krichevskii, $J \xrightarrow{a\ T=T_c} A_{\kappa_r}$ y la compresibilidad isotérmica del disolvente puro diverge, $\kappa_T^0 \to +\infty$. Por ello, en estas condiciones, las funciones termodinámicas y parámetros estructurales que dependen de κ_T^0 también serán divergentes con un signo de divergencia que dependerá del signo del parámetro de Krichevskii, A_{κ_r}; para los sistemas estudiados en este trabajo, $\to +\infty$.

En la Tabla 5 se recogen los datos de los parámetros para los dos sistemas estudiados. Se puede observar que

- Los valores obtenidos de C_{ij} son superiores en la mezcla CO_2+CH_4, pero la gran asimetría del sistema CO_2+CO produce un cambio mayor en la estructura del disolvente, tal y como queda patente en sus valores mayores de $(C_{11} - C_{12})$.
- En ambos sistemas $N_{exc}^{\infty} < 0$. Es decir, la sustitución, en condiciones de dilución infinita a temperatura y volumen constantes, de una molécula de disolvente por una de soluto provoca una disminución en la densidad local (el número de coordinación) respecto a la existente en la mezcla ideal. La disminución es más acusada para el sistema CO_2+CO.
- La afinidad de las moléculas de CO_2 por el soluto es mayor cuando éste es metano.

Tabla 5. Comparación entre los valores obtenidos para los sistemas CO_2 + CO y CO_2 + CH_4 para varios parámetros estructurales y propiedades.

Parametro / Propiedad	T / K	Sistema	
		CO_2 + CH_4	CO_2 + CO
A_{Kr} / MPa	304.21	20.383 ± 0.004	26.418 ± 0.005
A_{Kr}^*	304.21	0.76	0.98
$(\bar{V}_2^{\infty})_{max}$ / cm^3.mol^{-1}	308.15	3300	3950
$(N_{exc}^{\infty})_{min}$	308.15	-33	-38
$(N_1^{exc})_{max}$	308.15	11	3
$10^{-3}(C_{12})_{\rho_c}$ / cm^3.mol^{-1}	308.15	0.020	0.006
$10^{-3}(C_{11} - C_{12})_{\rho_c}$ / cm^3.mol^{-1}	308.15	0.072	0.085

Debenedetti y Mohamed[20] establecieron que dependiendo del signo de las divergencias de $\bar{V}_2^{\infty}, N_{exc}^{\infty}$ y N_1^{exc} las disoluciones infinitamente diluidas en las cercanías del punto crítico del disolvente puro presentan uno de estos tres tipos de comportamiento: atractivo, débilmente atractivo o repulsivo.

Para nuestros sistemas a $T = T_c$ (CO_2) y $\rho = \rho_c$ (CO_2):

$$A_{\kappa_r} > 0; \qquad \bar{V}_2^{\infty} \to +\infty; \qquad N_{exc}^{\infty} \to -\infty; \qquad 1 > A_{\kappa_r}^{*} > 0; \qquad N_1^{exc} \to +\infty$$

Es decir, al añadir de forma isoterma e isóbara una molécula de soluto a la IDS, se produce un aumento de volumen y un enriquecimiento de disolvente alrededor del soluto para ambos sistemas, esto es, tienen un *comportamiento débilmente atractivo*.

E) APLICACIÓN A LA TECNOLOGÍA CCS PARA LA REDUCCIÓN DE LAS EMISIONES DE CO_2

La presencia y el tipo de impurezas que acompañan al CO_2 antropogénico influyen en sus propiedades termofísicas y en el comportamiento de éste y, como consecuencia, en el diseño y operación de las instalaciones de la tecnología CCS. Debido a los escasos datos experimentales relativos tanto a las impurezas objeto de esta Tesis como a otras, la mayor parte de los estudios de la bibliografía desarrollan simulaciones para predecir tanto el comportamiento termodinámico como los valores de los parámetros asociados con la tecnología CCS.

A partir de los valores experimentales de densidad y equilibrio líquido-vapor y de las propiedades derivadas obtenidas, así como de valores calculados de viscosidad, hemos cuantificado y comparado el efecto de la presencia de CO y CH_4 en parámetros seleccionados asociados con el transporte, la inyección y el almacenamiento del CO_2 antropogénico. La evaluación de estos parámetros es imprescindible para el diseño, construcción y operación de redes de tuberías de transporte y de equipos de inyección fiables y seguros, así como para el almacenamiento seguro a largo plazo.

E.1.) Influencia del CH_4 y del CO en el transporte del CO_2 antropogénico por ceoducto

La presencia de impurezas en el CO_2 antropogénico incluso en pequeñas concentraciones, afecta en gran medida a la hidráulica de la tubería y a otros muchos aspectos de la operación y el diseño.[86] A partir de los datos experimentales presentados en este trabajo y de viscosidades calculas con REFPROP[59] se obtienen valores de los siguientes parámetros: Flujo másico, m; diámetro interno de la tubería, D; velocidad de erosión, v_E; número de Reynolds, R_e; capacidad de las estaciones de represurización, W; factor de fricción de Darcy-Weisbach, f y caída de presión por metro, $\Delta P/L$.

En la Tabla 6 se encuentran las ecuaciones utilizadas para el cálculo de estos parámetros y de otros necesarios en cálculos intermedios. Para ello se han utilizado valores

experimentales de densidad de este Trabajo y valores de viscosidad calculados con REFPROP 9.0.[59]

Los resultados obtenidos para los dos sistemas, CO_2+CO y CO_2+CH_4 se compararán entre sí y con los correspondientes al CO_2 puro.

Tabla 6. Resumen de ecuaciones para el cálculo de varios parámetros para el diseño de la tubería y su operación.[25]

Parámetros	Fórmula	Símbolos
Flujo másico	$m = \rho v A$	m: flujo másico (kg·s^{-1}) ρ: densidad del fluido (kg·m^{-3}) v: velocidad del fluido (m·s^{-1}) A: sección interna de la tubería (m^2)
Diámetro interno de la tubería	$D = \left(\frac{4m}{v\pi\rho}\right)^{1/2}$	D: diámetro interno de la tubería (m) m: flujo másico (kg·s^{-1}) v: velocidad del fluido (m·s^{-1}) ρ: densidad del fluido (kg·m^{-3})
Velocidad de erosión	$v_E = \frac{C}{\sqrt{\rho}}$	v_E: velocidad de erosión (m·s^{-1}) C: constante empírica ρ: densidad del fluido (kg·m^{-3})
Número de Reynolds	$R_e = \frac{\rho v D}{\mu}$	R_e:número de Reynolds ρ: densidad del fluido (kg·m^{-3}) v: velocidad del fluido (m·s^{-1}) D: diámetro interno de la tubería (m) μ: viscosidad del fluido (Pa·s)
Capacidad de las estaciones de re-presurización	$W = \frac{m}{\rho} \cdot \frac{(P_{out} - P_{in})}{\eta_{booster}}$	W: Capacidad de la estación de bombeo (MW) m: flujo másico (kg·s^{-1}) P_{out}: presión a la salida del compresor (MPa) P_{in} : presión a la entrada del compresor (MPa) ρ: densidad del fluido (kg·m^{-3}) $\eta_{booster}$: rendimiento del compresor
Factor de fricción de Darcy-Weisbach	$f = \frac{1.325}{\left[ln\left[(e/3.7D) - \left(5.74/{R_e}^{0.9}\right)\right]\right]^2}$	f : Factor de fricción de Darcy-Weisbach e : altura aproximada (m) D: diámetro interno de la tubería (m) R_e:número de Reynolds
Caída de presión por metro	$\frac{\Delta p}{L} = \frac{8 f m^2}{\rho \pi^2 D^5}$	$(\Delta p/L)$: caída de presión por metro (Pa·m^{-1}) m: flujo másico (kg·s^{-1}) ρ: densidad del fluido (kg·m^{-3}) f : Factor de fricción de Darcy-Weisbach D: diámetro interno de la tubería (m)

E.1.1. Presión mínima de operación, P_{min}

La manera más rentable de transportar el CO_2 antropogénico es en estado supercrítico ($P > P_c$ y $T > T_c$) o estado denso ($P > P_c$ y $T < T_c$). Esto es debido a que, en esas condiciones, su viscosidad es menor que la del líquido y el volumen que ocupa es muy inferior al que ocuparía si estuviera en fase gas. A pesar de ello, algunos proyectos consideran el transporte en fase gas como alternativa cuando la longitud de la tubería y/o el flujo de masa son pequeños.

En cualquier caso, es importante evitar flujos bifásicos durante el transporte de fluidos por tuberías ya que originan[47]: (i) cavitación: producida por la implosión de la burbuja en la región bifásica, que genera ondas de choque que pueden causar roturas en la tubería; (ii) turbulencias causadas por las burbujas que obstaculizan el correcto funcionamiento de los compresores y las bombas; y (iii) pérdida en la capacidad de transporte.

En la bibliografía se han encontrado dos formas de operar distintas para transportar CO_2 antropogénico en fase densa:

i) Mantener la presión de transporte por encima de un valor mínimo, P_{min}^{800},, que asegure una densidad del fluido transportado superior a 800 kg·m^{-3}. En la Tabla 7 se recoge la presión mínima de operación para asegurar una densidad de 800 kg·m^{-3}, P_{min}^{800},,, en el caso del CO_2 puro y de las mezclas CO_2+CO a x_{CO_2} = 0.9902 y x_{CO_2} = 0.9700.

No considerar las impurezas supondría un error de 62% en el valor de P_{min}^{800} en el caso de una mezcla CO_2+CO con un 3% por mol de CO mientras que la misma cantidad de CH_4 daría lugar a un error de 27%.

ii) Mantener la presión de transporte por encima de un valor mínimo, P_{min}, que corresponde a la presión de burbuja del fluido transportado. Las impurezas que acompañan al CO_2 antropogénico afectan significativamente a las características y localización de la región bifásica. Por ejemplo, si se transporta CO_2 puro a 283.15 K, la fase vapor aparecerá a la presión de saturación, P_{sat} =4.50 MPa. Sin embargo, si el fluido contiene un 3% de CH_4 por mol, la zona bifásica se encuentra comprendida entre P_b = 6.57 y P_r =4.72 MPa. (Tabla 8 y Figura 26)
Para el CO_2 antropogénico transportado en fase densa o supercrítica, la literatura proporciona valores de P_{min} de 7.5-11 MPa y de 9-30 MPa de presión máxima de operación, P_{max}.

Tabla 7. Valores de presión mínima requeridos para obtener una densidad de 800 kg·m^{-3} para varias temperaturas de transporte, al transportar CO_2 puro o mezclas CO_2+CO.

T_{tr}/K	P_{min}^{800} /MPa		
	CO_2 puro	x_{CO_2} =0.9902	x_{CO_2} =0.9700
253.15	1.970	2.979	5.208
263.15	2.649	3.578	5.400
273.15	3.485	4.277	5.991
283.15	4.502	5.216	6.574
293.15	6.626	7.601	9.448
304.21	11.987	12.851	15.060
308.15	13.904	14.804	16.851
323.15	21.371	>20 MPa	>20 MPa
333.15	26.398	>20 MPa	>20 MPa
343.15	31.445	>20 MPa	>20 MPa

Tabla 8. Valores de presión de rocío y burbuja y densidades de la fase líquida y vapor para la mezcla CO_2+CH_4 a varias temperaturas y composiciones.

T /K	P_r /MPa	P_b /MPa	ρ_L /kg·m^{-3}	ρ_V /kg·m^{-3}	P_r /MPa	P_b /MPa	ρ_L /kg·m^{-3}	ρ_V /kg·m^{-3}
$x_{CO_2} = 0.9700$					$x_{CO_2} = 0.9810$			
253.15	2.070	5.208	1014.58	53.25	2.038	4.033	1021.71	53.66
263.15	2.770	5.400	966.00	74.40	2.741	4.477	970.42	73.19
273.15	3.680	5.991	909.35	102.10	3.577	5.087	916.50	101.98
283.15	4.720	6.574	840.50	141.71	4.695	5.905	850.08	137.92
293.15	6.080	7.465	752.15	207.60	5.912	6.871	758.54	202.01
$x_{CO_2} = 0.9902$					$x_{CO_2} = 0.9930$			
253.15	1.989	2.979	1026.86	52.45	1.988	2.978	1026.89	52.54
263.15	2.681	3.578	975.73	71.36	2.67	3.293	978.09	70.56
273.15	3.527	4.277	921.85	97.61	3.520	4.060	924.11	99.04
283.15	4.579	5.216	852.66	136.39	4.556	4.999	859.42	135.89
293.15	5.847	6.345	766.26	189.91	5.762	6.162	777.60	187.60
$x_{CO_2} = 0.9960$					$x_{CO_2} = 1$ (CO_2 puro)			
253.15	1.977	2.327	1031.12	52.46	1.9696*		1031.7	51.700
263.15	2.657	3.054	979.86	70.72	2.6487*		982.93	71.185
273.15	3.527	3.804	924.55	98.24	3.4851*		927.43	97.647
283.15	4.530	4.811	857.70	135.26	4.5022*		861.12	135.16
293.15	5.778	5.962	764.73	193.76	5.7291*		773.39	194.20

(*) valores de P_{sat}

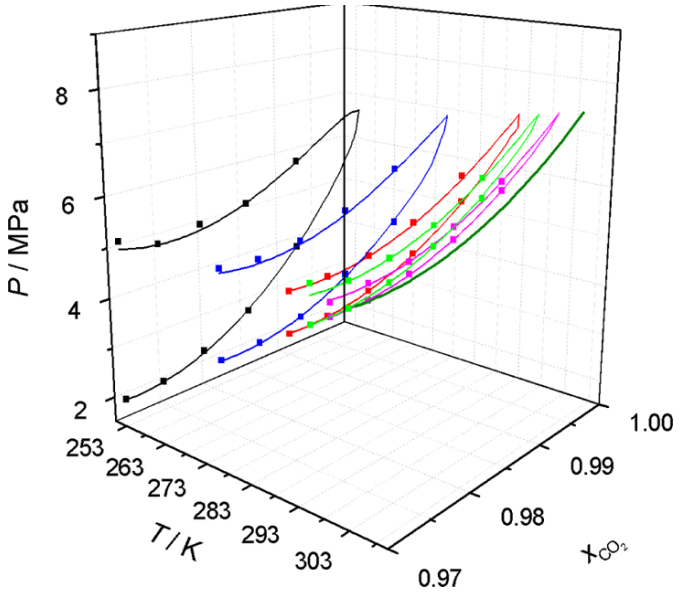

Figura 26. Presión de vapor para CO_2 [59](verde oliva) y envolventes de fase experimentales para las mezclas CO_2+CO con $x_{CO_2} = 0.9700$ (negro), $x_{CO_2} = 0.9810$ (azul), $x_{CO_2} = 0.9902$ (rojo), $x_{CO_2} = 0.9930$ (verde) y $x_{CO_2} = 0.9960$ (rosa).

E.1.2. Caída de presión a lo largo de la tubería, $P(d)$.

La caída de presión está originada por la orografía del terreno y por el conjunto de fuerzas de fricción. Estas las ejercen tanto las paredes de la tubería sobre la capa de fluido que está en contacto con ellas como cada capa de fluido sobre las adyacentes. Como consecuencia, se produce una pérdida de energía en el sistema que se transforma en una disminución de la presión conforme el fluido va avanzando. Este factor es de gran importancia cuando se trata de transporte a grandes distancias.

La disminución en la densidad y en la viscosidad de la mezcla hace que la caída de presión aumente al aumentar la temperatura (Figura 27) y la concentración de impurezas no condensables, influyendo de forma muy similar el CH_4 y el CO.

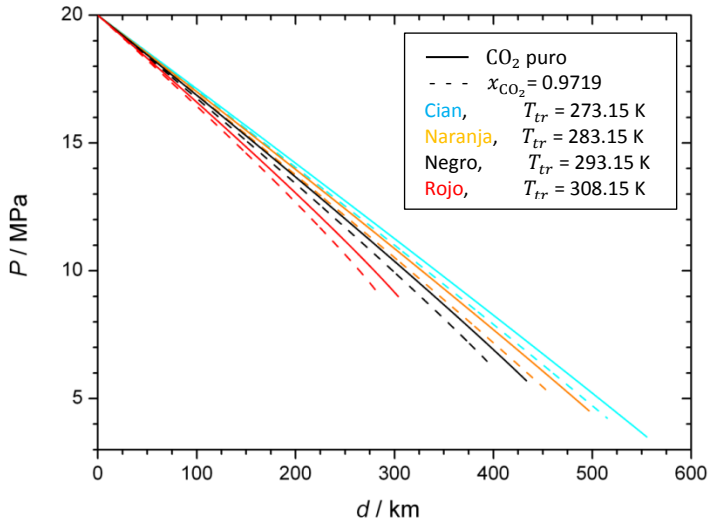

Figura 27. Comparación entre la caída de presión a lo largo de la tubería para CO_2 puro (líneas sólidas) y las mezclas (a) CO_2+CO y (b) CO_2+CH_4 (líneas discontinuas) a varias temperaturas de transporte, T_{tr}. Se ha utilizado para el cálculo: fujo másico m = 317 kg·s^{-1}, diámetro interno de la tubería D = 0.508 m y coeficiente de rugosidad e = 4.6·10^{-5} m, para una tubería con una presión inicial de 20.0 MPa.

Para una presión inicial P_{ini}= 20 MPa, una distancia d = 250 km, y una temperatura, T = 273.15 K:

CO_2 puro ⇒ P_{fin}= **12.7** MPa

CO_2 + CH_4 / CO (x_{CO_2} ≅0.97) ⇒ P_{fin}= **12.5** MPa

Para una presión inicial P_{ini}= 20 MPa, una presión final, P_{fin}= 10 MPa, y una temperatura, T = 308.15 K:

CO_2 puro ⇒ d= **280** km

CO_2 + CH_4 / CO (x_{CO_2} ≅0.97) ⇒ d= **262** km

La caída de presión junto con el diámetro de la tubería, la presión en su interior y las propiedades de transporte del fluido, determinan el lugar y el número de estaciones de bombeo o presurización necesarias para el transporte en fase densa. Así, para el diseño eficiente de la red de transporte se debe conseguir un compromiso entre el diámetro, la presión en el interior de la tubería y el número y la potencia de las estaciones de bombeo.

E.1.3. Distancia máxima de represurización, L.

La caída de presión anteriormente citada junto a la necesidad de garantizar una presión mínima de trabajo (E.1.1.) obliga a realizar operaciones de represurización cada cierta distancia. En la Figura 28 se muestra la distancia máxima de represurización, L, frente a la temperatura de transporte, T_{tr}, para el fluido transportado en tubería y unas

condiciones habituales de flujo másico, m, diámetro interno, D y coeficiente de rugosidad, e.

SET A se refiere a las condiciones que garantizan que la densidad del fluido transportado sea superior a 800 kg·m^{-3} y SET B a las que garantizan que la presión en el interior de la tubería esté por encima de 9 MPa (valor promedio entre los límites inferior y superior del rango encontrado en la bibliografía para las P_{min} de transporte: 7.5-11 MPa).

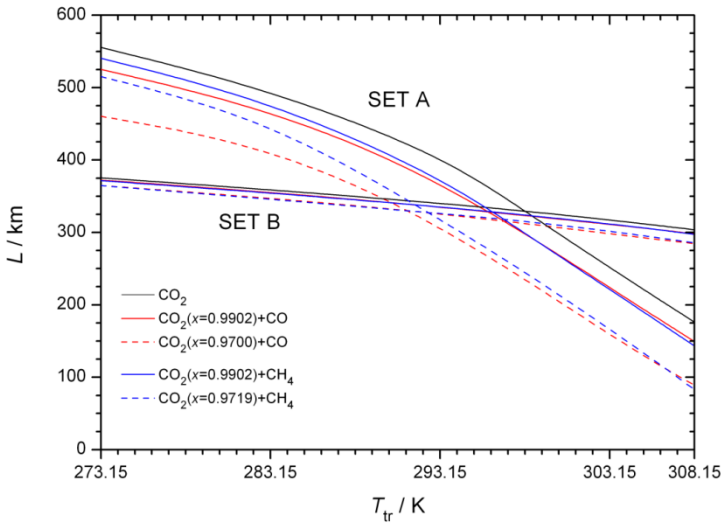

Figura 28. Distancias máximas de represurización, L, frente a temperaturas de transporte, T_{tr} , para CO_2 puro y las mezclas CO_2+CO y CO_2+CH_4. Set A: L requerido para mantener la densidad del fluido por encima de 800 kg·m^{-3}. Set B: L requerido para mantener la presión por encima de 9.0 MPa. Flujo másico elegido $m = 317\ \mathrm{kg \cdot s^{-1}}$, diámetro interno de la tubería $D = 0.508\ \mathrm{m}$ y coeficiente de rugosidad $e = 4.6x\ 10^{-5}\ \mathrm{m}$ para una tubería con una presión inicial de 20.0 MPa.

Se puede observar que cuando se trabaja con el objetivo de mantener la presión que garantice una densidad mínima, P_{min}^{800}, la distancia máxima de represurización, L, es más sensible al tipo y concentración de impurezas a bajas T y disminuye mucho al aumentar la temperatura de trabajo. Por otro lado, L apenas varía cuando se opera a P_{min} = 9.0 MPa mostrando un comportamiento más estable.

Para las impurezas estudiadas dependiendo de la composición del fluido a T = 283.15 K:

SET A (P_{min}^{800}) ⇒ L= **420-497** km

SET B (P_{min} = 9.0 MPa) ⇒ L= **346-359** km

E.1.4. Potencia de las estaciones de recompresión, W.

Las presiones de entrada y de salida y el tipo de fluido a represurizar determinan la potencia requerida para las estaciones de recompresión, W. En la Figura 29 se observa la influencia que ejercen las impurezas (tipo y concentración) en W a una temperatura típica en la fase de transporte, T = 283.15 K, y cuando la presión de salida es $P_{máx}$= 20

MPa. El cálculo se muestra para las dos formas de operar que estamos considerando, la mejor opción dependerá del tipo de red de tuberías que se esté operando.

Para las impurezas estudiadas (x_{CO_2} = 0.9700 - 0.9960) a T = 283.15 K y dependiendo de la composición del fluido :

Represurización para densidad de 800 kg·m^{-3} ⇒ W = **7-7.9** MW

Represurización hasta 9.0 MPa ⇒ W = **5.3-5.5** MW

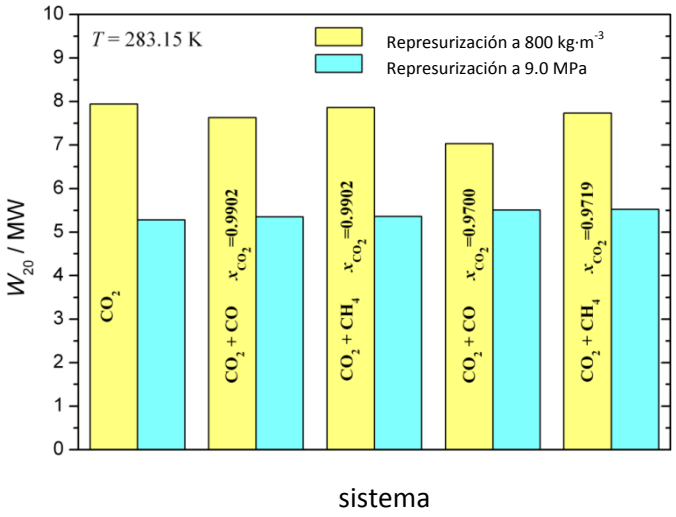

Figura 29. Máxima distancia de represurización, L, para para CO_2 puro y las mezclas CO_2+CO y CO_2+CH_4 a T_{tr} = 283.15 K. Amarillo: L para mantener la densidad del fluido por encima de 800 kg·m^{-3}. Azul: L para mantener la presión por encima de 9.0 MPa. Flujo másico elegido m =317.kg·s^{-1}, diámetro interno de la tubería D =0.508 m y coeficiente de rugosidad e = 4.6·10^{-5} m para una tubería con una presión inicial de 20.0 MPa.

E.1.5. Diámetro interno de la tubería, D.

El cálculo de este factor ha sido realizado para unas condiciones estándar de caída de presión y rugosidad y abarcando un rango de capacidad de aproximadamente 10 Mt/año. La Figura 30 muestra como para un diámetro determinado, el flujo másico transportado decrece a medida que la presión disminuye y la temperatura o la concentración de las impurezas aumentan.

En el caso más desfavorable (alta temperatura, alta concentración de impurezas y baja presión), la mayor diferencia entre el diámetro de la tubería calculado para el CO_2 puro y las mezclas estudiadas, es de 27 mm (se corresponde con la mezcla CO_2+CO con x_{CO_2}=0.9700 a T = 308.15K y P = 9.0 MPa), lo que se traduce en un aumento de masa de tubería de 11 toneladas de acero por kilómetro de tubería.

D (Mezcla CO_2 + CO x_{CO_2} = 0.9700) = D (CO_2 puro) + **27** mm ⇒ Aumento masa tubería standard= + **11** Tn/km.

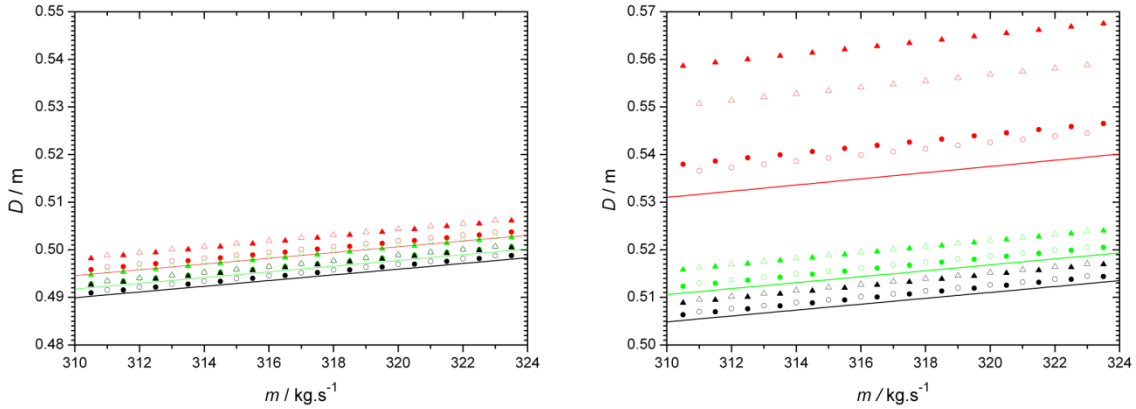

Figura 30. Diámetro interno de la tubería, D, frente a flujo másico (capacidad), m, para CO_2 puro y las mezclas CO_2+CO y CO_2+CH_4 a (a) 273.15 K y (b) 308.15 K a varias presiones, P. El coeficiente de rugosidad se ha fijado como $e = 4.6 \cdot 10^{-5}$ m y se ha utilizado un valor promedio de caída de presión de 33 Pa·m^{-1}. Rojo, P = 9.0 MPa, Verde, P = 15.0 MPa, Negro , P = 20.0 MPa; Líneas sólidas, CO_2; Simbolos sólidos, CO_2+CO; Símbolos en blanco, CO_2 + CH_4; Círculos, $x_{CO_2} \cong$ 0.99; Triángulos, $x_{CO_2} \cong$ 0.97..

E.2.) Influencia del CH_4 Y CO_2 en la inyección y el del almacenamiento del CO_2 antropogénico.

El efecto de las impurezas en el CO_2 almacenado depende del tipo de reservorio y de las interacciones entre el CO_2 inyectado y las sustancias presentes previamente en el almacenamiento. En el caso del metano puede ser una impureza del CO_2 antropogénico y estar también presente en el almacenamiento antes de la inyección.

Los parámetros seleccionados para evaluar la influencia de la presencia del CO y del CH_4 en la inyección y almacenamiento, recogidos en la Tabla 9, son: parámetro de solubilidad, δ , capacidad de almacenamiento, M, velocidad ascensional de la pluma en acuíferos salinos, v, y flujo de permeación, $\dot{M}$. En el caso de los tres últimos se han obtenido valores normalizados con respecto a los correspondientes al CO_2 puro.

Tabla 9. Resumen de las ecuaciones de los parámetros empleados para evaluar la influencia de las impurezas en la inyección y el almacenamiento de CO_2 antropogénico.

Parámetros	Fórmula	Símbolos
Parámetro de solubilidad, δ	$\delta = \left(\frac{-E(T)}{V(T,P)}\right)^{1/2}$ $\delta = \pi^{1/2}$ $\pi = \left(\frac{\partial U}{\partial V}\right)_T = T\left(\frac{\partial P}{\partial T}\right)_V - P = T\frac{\alpha_P}{\kappa_T} - P$	$(-E/V)$: densidad de energía de cohesiva π_i: presión interna α_P: expansividad isobárica κ_T: compresibilidad isotérmica
Capacidad de almacenamiento normalizada, M/M_0	$\frac{M}{M_0} = \frac{\rho}{\rho_0\left[1+\sum_i\left(\frac{m_i}{m_0}\right)\right]}$	m_i/m_0: relación de la masa de impureza *i* con respecto a la masa de CO_2 en la mezcla $\rho\ y\ \rho_0$: densidad de la mezcla y del fluido puro respectivamente
Velocidad ascensional de la pluma normalizada, v/v_0	$\frac{v}{v_0} = \frac{F/(\rho\eta)}{F_0/(\rho_0\eta_0)} = \frac{(\rho_{salmuera}-\rho)(\rho_0\eta_0)}{(\rho_{salmuera}-\rho_0)(\rho\eta)}$	m_i/m_0: relación de la masa de impureza *i* con respecto a la masa de CO_2 en la mezcla $\rho\ y\ \rho_0$: densidad de la mezcla y del fluido puro respectivamente $\eta\ y\ \eta_0$: viscosidad de la mezcla y del fluido puro respectivamente $F\ y\ F_0$: fuerza de flotación de la mezcla y del fluido puro respectivamente $\rho_{salmuera}$: densidad de la salmuera
Flujo de permeación normalizado, $\dot{M}/\dot{M}_0$	$\frac{\dot{M}}{\dot{M}_0} = \frac{\rho\left(\frac{\eta_0}{\eta}\right)}{\rho_0\left[1+\sum_i\left(\frac{m_i}{m_0}\right)\right]}$	m_i/m_0: relación de la masa de impureza *i* con respecto a la masa de CO_2 en la mezcla $\rho\ y\ \rho_0$: densidad de la mezcla y del fluido puro respectivamente $\eta\ y\ \eta_0$: viscosidad de la mezcla y del fluido puro respectivamente

E.2.1. Parámetro de solubilidad, δ

Debido a los valores de temperatura y presión en el interior de los reservorios, los fluidos confinados se encuentran en estado supercrítico y por tanto una de sus principales características es su gran capacidad de disolución. δ ha sido ampliamente utilizado para predecir de manera semicuantitativa el comportamiento de mezclas líquidas [7, 38, 39, 99] y de fluidos supercríticos ligeramente polares.[4]

En este trabajo, hemos empleado el parámetro de solubilidad para estudiar las interacciones entre el fluido inyectado (considerado como el disolvente) y otras sustancias presentes en el reservorio. Los parámetros de solubilidad para CO_2 puro y para las mezclas de composición x_{CO_2} =0.9902 y x_{CO_2} =0.9700 correspondientes al sistema CO_2 + CO a tres temperaturas, se muestran en la Figura 31.

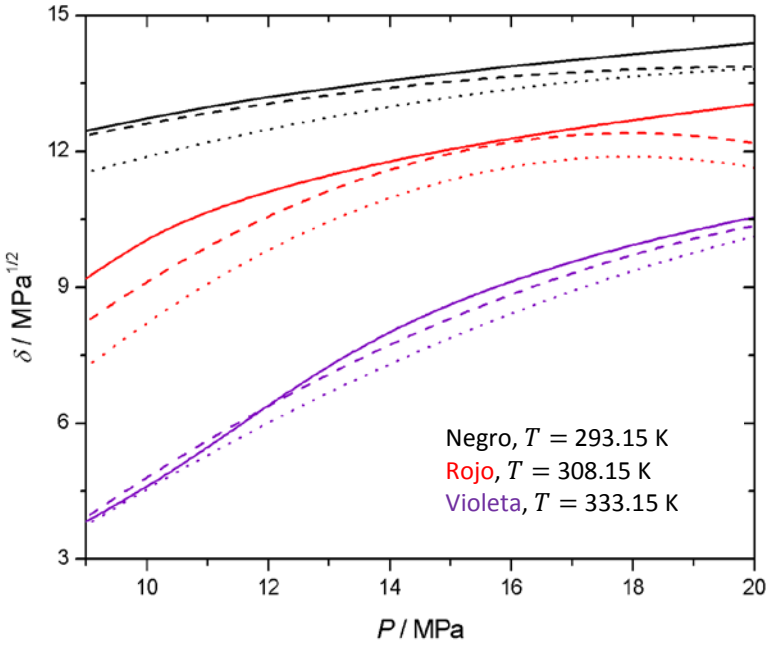

Figura 31. Parámetros de solubilidad, δ, frente a presión para el CO_2 puro y la mezcla CO_2+CO a varias temperaturas. Líneas sólidas, CO_2 puro; líneas discontinuas, x_{CO_2} = 0.9902; líneas punteadas, x_{CO_2} = 0.9700.

Como se puede observar, la presencia de CO en el CO_2 antropogénico provoca una disminución de δ en comparación con el CO_2 puro, reduciendo el poder de disolución del fluido y por lo tanto dificultando su captura. El mismo efecto se observa para el sistema CO_2+CH_4. Para las condiciones estudiadas en esta Tesis, el parámetro de solubilidad disminuye al aumentar la temperatura y disminuir la presión. Los valores obtenidos para el parámetro de solubilidad son consistentes con los encontrados en la literatura para la mezcla CO_2+CO a 333.15K[15] aunque no son directamente comparables debido a las diferentes composiciones estudiadas.

Allada y colaboradores[4] sugieren que el parámetro de solubilidad es la clave determinante de la solubilidad en los disolventes supercríticos, y han sido capaces de unificar diversos comportamientos de los disolventes independientemente de la temperatura, la presión y de su naturaleza. Además, diferentes autores[15] apuntan a que la densidad es la propiedad que más influencia tiene en la capacidad de disolución de los fluidos densos.

La Figura 32 muestra δ frente a ρ para CO_2 puro, seis mezclas de este trabajo y otras recogidas en la literatura.[15] El gráfico muestra una buena correlación $\delta - \rho$ dentro del rango de densidad representado. Esto significa que sistemas con diferente T o P pero con la misma densidad, tendrán el mismo parámetro de solubilidad y que por lo tanto, la capacidad de solubilización del CO_2 inyectado puede ser conocida a partir de su densidad en las condiciones de almacenamiento.

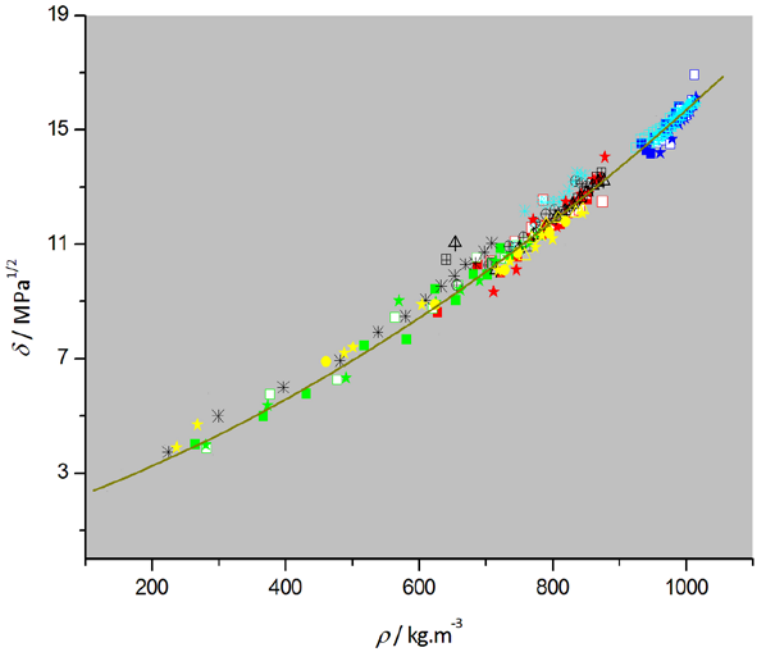

Figura 32. Parámetro de solubilidad, δ, frente a densidad, ρ, para CO_2 puro (línea); mezclas CO_2+CO con x_{CO_2}= 0.9700 (■), x_{CO_2}= 0.9902 (□) and x_{CO_2}= 0.9930 (★) a 273.15 K (azul), 304.21 K (rojo) and 323.15 K (verde); mezclas CO_2+CH_4 con x_{CO_2}= 0.8525 (✳), x_{CO_2}= 0.9719 (⊕) y x_{CO_2}=0.9932 (⊞) a 273.15 K (cian) y 304.21 K (negro); CO_2+CO (▲), CO_2+H_2 (●) y mezclas CO_2+CO+H_2 (★)(amarillo).[15]

E.2.2. Capacidad de almacenamiento normalizada, M/M_0

Este parámetro depende de la composición, temperatura y presión de manera que la presencia de impurezas no condensables reduce esta capacidad sobre todo si nos encontramos en unas condiciones cercanas a las críticas de la mezcla (Figura 33). Por ejemplo, una cantidad del 15% de CH_4 reduce M/M_0 hasta aproximadamente 0.35 a 308.15 K y 8.5 MPa, lo que implica que un reservorio relativamente poco profundo no sería adecuado para almacenar corrientes con un alto nivel de este tipo de impurezas.

En la Figura 33 donde se representa M/M_0 versus P a varias temperaturas para CO_2+CO y CO_2+CH_4 con x_{CO_2} =0.9700, se observa que la disminución máxima se obtiene cerca del punto crítico del CO_2 antropogénico (M/M_0 ≅0.44 para CO_2+CO a 304.21 K y 7.5

MPa). Un aumento en la temperatura disminuye la magnitud del mínimo y lo desplaza a presiones mayores.

CO_2 + CO (x_{CO_2} ≅0.97); T = 304.21 K; P ≅7.5 MPa $\Rightarrow \left(\frac{M}{M_0}\right)_{min} \cong$ **0.44**

CO_2 + CO (x_{CO_2} ≅0.97); T = 343.15 K; P ≅ 14.1 MPa $\Rightarrow \left(\frac{M}{M_0}\right)_{min} \cong$ **0.89**

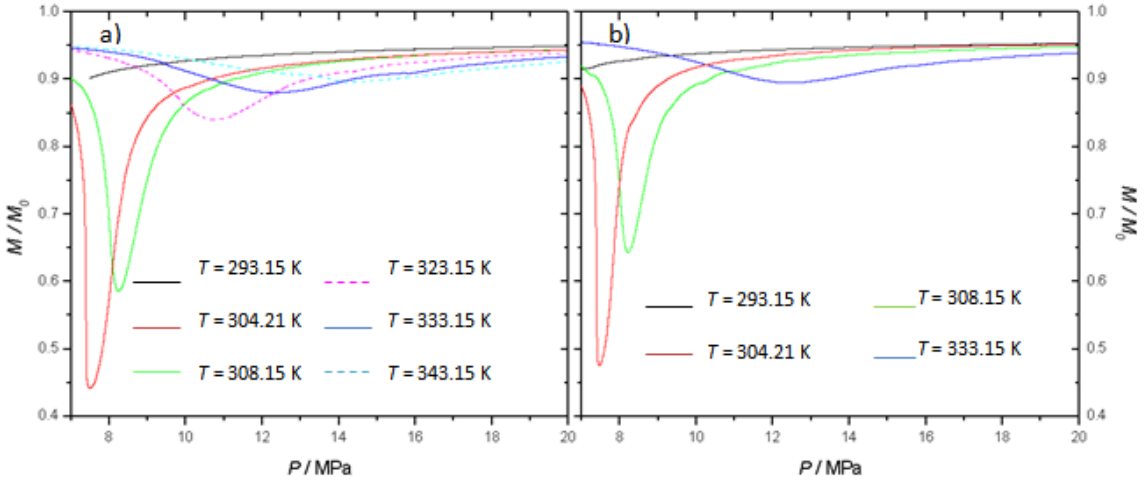

Figura 33. Capacidad normalizada de almacenamiento, M/M_0, frente a la presión a varias temperaturas para las mezclas (a) CO_2+CO ($x_{CO_2} = 0.9700$) y (b) CO_2+CH_4 ($x_{CO_2} = 0.9719$).

A medida que la profundidad de inyección aumenta, la influencia del tipo de impureza en la capacidad de almacenamiento disminuye.

El CO afecta de manera más negativa que el CH_4 a la masa de CO_2 antropogénico que puede almacenarse, de forma que para la misma masa de fluido sería necesaria más presión para confinar el sistema CO_2+CO que el CO_2+CH_4. La eficiencia en el almacenamiento puede mejorarse si la presión de inyección se encuentra bastante por encima de los valores mínimos que se representan. Para el caso de reservorios cerrados, este valor de presión debe encontrarse dentro de los rangos de sobrepresiones permitidos. Para formaciones abiertas, una posible opción sería incrementar la profundidad de inyección en el almacenamiento.

E.2.3. Velocidad ascensional de la pluma normalizada en acuíferos salinos, v/v_0

Si el reservorio es un acuífero salino, el fluido almacenado experimenta una fuerza de flotación ascendente que depende de la diferencia de densidades entre el fluido y la salmuera.[88] La velocidad con que se desplazará el fluido es directamente proporcional a la fuerza de flotación e inversamente proporcional a su viscosidad. A $T \geq$ 304.21 K (Figura 34) v/v_0 presenta un máximo de mayor magnitud para la impureza CO.

CO_2 + CO (x_{CO_2} ≅0.97); T =304.21 K; P ≅ 7.5 MPa; $\rho_{salmuera}$ =1025 kg·m^{-3} ⇒ $\left(\frac{v}{v_0}\right)_{máx}$ ≅**9.2**

CO_2 + CH_4 (x_{CO_2} ≅0.97); T =304.21 K; P ≅ 7.5 MPa; $\rho_{salmuera}$ =1025 kg·m^{-3} ⇒ $\left(\frac{v}{v_0}\right)_{máx}$ ≅**7.7**

Los máximos para cada temperatura se encuentran a presiones dentro del rango de profundidades de los acuíferos salinos.[71] La presencia de CO o CH_4 conduce a un incremento en la velocidad ascendente de la pluma, lo que se hace significativo cerca del punto crítico del fluido, resultando por tanto en una disminución del contacto del CO_2 con la salina y por tanto en un descenso del poder de disolución. La propagación lateral de la pluma también disminuye y como consecuencia lo hace la cantidad de fluido atrapado en los poros de la roca. Estos efectos reducen la seguridad en el almacenamiento del CO_2 y cobran más importancia cerca de la roca de sellado, a profundidades menores aumentando el riesgo de posibles fugas. Un incremento en la densidad de la salmuera reduce tanto F/F_0 como v/v_0.(Figura 34).

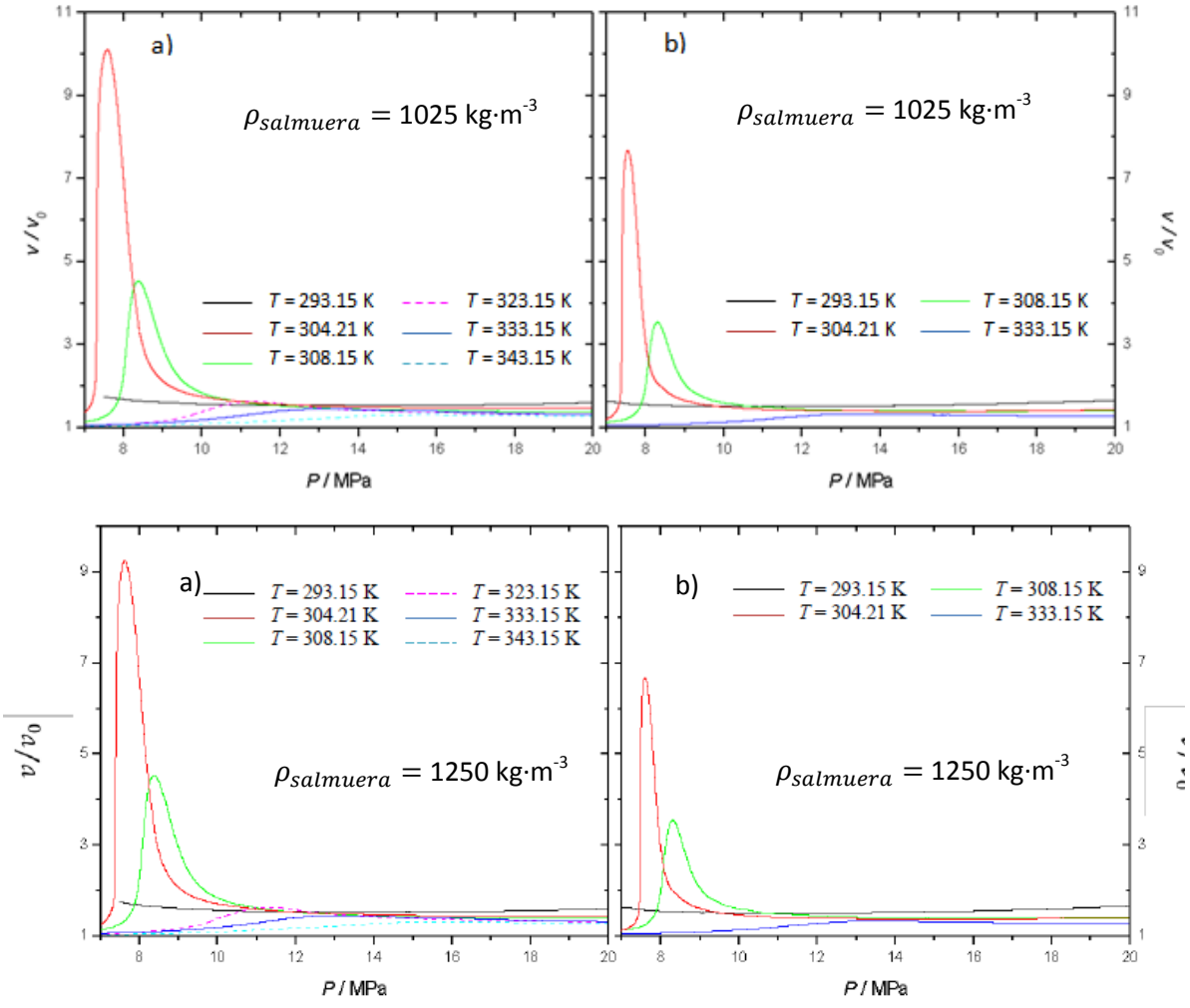

Figura 34. Velocidad ascensorial de la pluma normalizada , v/v_0, frente a la presión a varias temperaturas para las mezclas (a) CO_2+CO (x_{CO_2} =0.9700) y (b) CO_2+CH_4 (x_{CO_2} =0.9719)

E.2.4. Flujo de permeación normalizado, $\dot{M}/\dot{M}_0$

La inyectividad relativa de la corriente impura de CO_2 depende del efecto de las impurezas, de la temperatura, de la presión, de la densidad y la viscosidad. $\dot{M}$ se ve reducida como resultado de una disminución de la densidad de estas mezclas en relación con el CO_2 puro; sin embargo, debido a la compensación por el aumento de la viscosidad, la reducción es menor que en la capacidad de almacenamiento discutida anteriormente. En los sistemas incluidos en este trabajo, $\rho < \rho_0$ y $\eta < \eta_0$ pero debido a los valores relativos de ρ/ρ_0 y η_0/η, los valores obtenidos para $\dot{M}/\dot{M}_0$ pueden ser mayores o menores que la unidad. Las mayores diferencias se encuentran en las proximidades del punto crítico y se observa que la influencia del CO es mayor que la del CH_4 para este parámetro (Figura 35).

CO_2 + CO (x_{CO_2} ≅0.97); T =304.21 K; P ≅ 8.0 MPa $\Rightarrow \left(\frac{\dot{M}}{\dot{M}_0}\right)_{máx}$ ≅**1.25**

CO_2 + CH_4 (x_{CO_2} ≅0.97); T =304.21 K; P ≅ 8.0 MPa $\Rightarrow \left(\frac{\dot{M}}{\dot{M}_0}\right)_{máx}$ ≅**1.17**

Al aumentar la presión el efecto de la temperatura disminuye tendiendo $\dot{M}/\dot{M}_0$ a la unidad en el rango de temperatura estudiado.

Por otro lado, la presencia de impurezas no condensables en la etapa de inyección tiene como consecuencia la necesidad de incrementar la presión de cabeza debido a la disminución de la presión hidrostática en el pozo de inyección.[85]

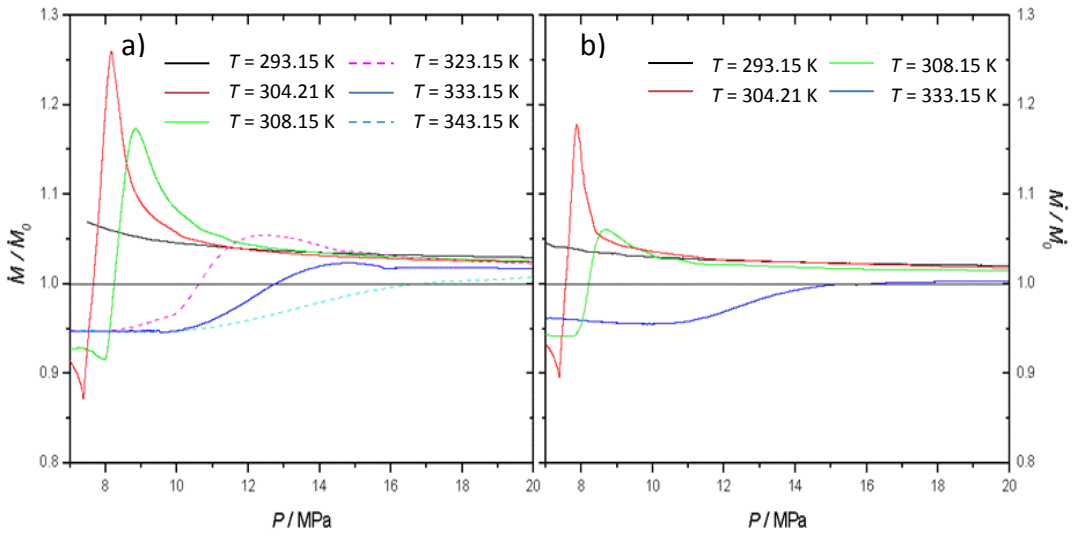

Figura 35. Flujo de permeación normalizado, $\dot{M}/\dot{M}_0$,frente a la presión a varias temperaturas para las mezclas (a) CO_2+CO (x_{CO_2} = 0.9700) y (b) CO_2+CH_4 (x_{CO_2} = 0.9719).

CONCLUSIONES FINALES

5. CONCLUSIONES FINALES

1.

Se ha elaborado el procedimiento para la determinación experimental de la densidad de fluidos puros y mezclas a diferentes presiones y temperaturas. Para ello, se ha utilizado CO_2, etano y propano, y el sistema CO_2+etano. La comparación de los valores obtenidos con los calculados usando las EoS de referencia así como con la bibliografía, confirma la calidad de los medidas experimentales. La precisión calculada en la medida de la densidad de compuestos puros, expresada como desviación relativa promedio, es MRD_ρ = 0.13%. Para las mezclas binarias, las desviaciones obtenidas fueron MRD_ρ = 0.70% para P=0.1-20 MPa y MRD_ρ = 0.20% en el rango hasta 70 MPa. La incertidumbre expandida ($k = 2$) en la medida de la densidad y su repetibilidad para las mezclas estudiadas fueron: $U(\rho)$ = 0.35-0.80 kg·m^{-3} y $\bar{S}_\rho^r = 0.13\%$, respectivamente.

Se calcularon para CO_2 y etano las propiedades derivadas de la densidad: κ_T, α_P, y π_i. La dependencia de las dos primeras con la temperatura y la presión es la esperada: los valores varían mucho en las cercanías del punto crítico, donde son divergentes, pero apenas cuando nos alejamos de él. Los valores de la presión interna para el CO_2 son más altos que los del etano, consecuencia del importante momento cuadrupolar que presenta el CO_2.

2.

Se ha elaborado el procedimiento para la determinación experimental de la velocidad del sonido de fluidos puros (líquidos y gases comprimidos) a diferentes presiones y temperaturas. Se ha utilizado agua y etano y se ha calculado la precisión de las medidas comparando con las EoS de referencia para ambos fluidos. Las desviaciones obtenidas fueron: MRD_c (H_2O) = 0.06% y $MRD_c(C_2H_6)$ = 0.1 %.

A partir de los valores experimentales de velocidades del sonido y densidad se ha obtenido la compresibilidad isentrópica y la capacidad calorífica del etano. La desviación media relativa entre C_P calculada y la proporcionada por la Eos referencia fue: $MRD_{C_P}(C_2H_6)$ = 3%.

Se ha puesto a punto la instalación para la medida de velocidades del sonido en mezclas mediante el estudio del sistema CO_2+CH_3OH con composiciones,

temperaturas y presiones elegidas para que incluyeran las condiciones de la tecnología CCS.
La incertidumbre estándar obtenida para este sistema es u_c=5.9·10^{-4}·c.

3.

Se han medido 54 isotermas $P-\rho-T-x_{\mathrm{CO_2}}$ para seis mezclas $\mathrm{CO_2}+\mathrm{CH_4}$ en los rangos de presión y temperatura que incluyen los estimados en el interior de las tuberías así como en los almacenamientos geológicos: $x_{\mathrm{CO_2}} \geq 0.85$; P = 0.1 – 20 MPa; T = 253.15 – 333.15 K. Para el sistema $\mathrm{CO_2}+\mathrm{CO}$, se han determinado 50 isotermas $P-\rho-T-x_{\mathrm{CO_2}}$ correspondientes a cinco composiciones en los rangos: $x_{\mathrm{CO_2}} \geq 0.97$; P = 0.1 – 20 MPa; T = 253.15 – 343.15 K.

A partir de estos datos experimentales se han calculado: las presiones de rocío y de burbuja y las densidades de las fases en el ELV para cada mezcla a las temperaturas subcríticas, $P_r - P_b - \rho_V - \rho_L$; propiedades derivadas, α_P, κ_T y π_i, para todas las isotermas; y los volúmenes molares de exceso, V_m^E, y volúmenes molares parciales, $\bar{V}_i$, en la región crítica.

Los valores obtenidos se han comparado con los escasos datos existentes en la bibliografía para estos sistemas en las condiciones estudiadas, encontrándose buenas concordancias en aquellos casos comparables.

4.

Se ha realizado la modelización de ambos sistemas con tres Ecuaciones de Estado de diferente tipo: (i) PR, ecuación cúbica; (ii) GERG-2008, ecuación basada en la aproximación multifluido; y (iii) PC-SAFT, ecuación basada en las teorías de la perturbación.

Las EoS se usaron en sus formulaciones originales pero en el caso de PC-SAFT, además se reajustaron los parámetros con el objetivo de mejorar la predicción en la zona crítica. De los resultados concluimos que las tres EoS predicen adecuadamente el comportamiento volumétrico y de fase de los sistemas CO_2 + CO y CO_2 + CH_4 en las condiciones estudiadas. Las desviaciones promedio obtenidas fueron:

PR EoS:	MRD_ρ < 3 %;	MRD_{P_r,P_b} < 1 %.
GERG-2008 EoS:	MRD_ρ < 1 %;	MRD_{P_r,P_b} < 2 %.
PC-SAFT EoS:	MRD_ρ < 2 %;	MRD_{P_r,P_b} < 1 %.

5.

Se ha realizado un estudio teórico de las interacciones entre las moléculas de CO_2 y las moléculas de CH_4 o CO utilizando el concepto de función de Krichevskii y la teoría de Kirkwood-Buff. Se calcularon diferentes parámetros que indican cómo se encuentran las moléculas dentro del sistema tales como: parámetro de Krichevskii, A_{Kr}; volumen parcial molar a dilución infinita, $\bar{V}_2^{\infty}$; tamaño de clúster, N_1^{exc} y número de coordinación de exceso, N_{exc}^{∞} . El signo de estos parámetros permite concluir la afinidad de las moléculas soluto-solvente; así, en nuestros sistemas se observa un comportamiento débilmente atractivo.

6.

Se ha evaluado la influencia de las impurezas CH_4 y CO en el transporte de CO_2 por ceoducto a través de la cuantificación de la modificación de los límites del ELV y del cálculo de varios parámetros tales como: presión mínima operacional, P_{min}, caída de presión a lo largo de la tubería, $P\ (d)$, distancia máxima de represurización, L, potencia de las estaciones de recompresión, W y diámetro interno de la tubería, D.

La presencia de las impurezas, ambas gases no-condensables, aumenta la presión de burbuja y, por lo tanto, la presión de trabajo mínima requerida para un óptimo transporte del fluido. Por otro lado, el efecto en los parámetros se hace más pronunciado al aumentar la temperatura y disminuir la presión.

Se ha evaluado la influencia de las impurezas CH_4 y CO en las etapas de almacenamiento e inyección. Se ha calculado el parámetro de solubilidad, δ, para CO_2 + CO y CO_2 + CH_4 y comparado con el de otras mezclas observando que sistemas con diferente composición, temperatura o presión pero con la misma densidad, tienen el mismo parámetro de solubilidad y por lo tanto, la misma capacidad de solubilización del fluido inyectado. El valor obtenido para las mezclas es menor que el del CO_2 puro por lo que su presencia dificultará la retención del mismo en el reservorio.

Además, se han calculado los parámetros normalizados (relativos a una corriente de CO_2 puro) siguientes: capacidad de almacenamiento, M; velocidad de ascenso de la pluma, v; y flujo de permeación, $\dot{M}$. De los resultados se puede concluir que la presencia de estas impurezas es perjudicial ya que disminuye la capacidad de almacenamiento y aumenta el riesgo de fuga en los acuíferos salinos.

En todos los casos, se ha observado que el efecto producido por la presencia de CO en el CO_2 antropogénico es mayor que el originado por el CH_4.


TRABAJO
ADICIONAL

6. TRABAJO ADICIONAL Y PERSPECTIVAS DE FUTURO

Como continuación lógica del trabajo presentado se plantea la determinación experimental de la velocidad del sonido en mezclas de interés en la Tecnología CCS. Estos valores, junto a las propiedades descritas anteriormente, permitirán el cálculo de otras propiedades termodinámicas tales como la capacidad calorífica y el coeficiente de Joule-Thomson.

La determinación experimental de la velocidad del sonido del CO_2 en estado denso presenta serias dificultades, debido a que tiene un valor de tiempo de relajación vibracional, τ, extraordinariamente alto, asociado a un elevado coeficiente de absorción del sonido, α. La adición de pequeñas cantidades de un compuesto adecuado, agente dopante, con tiempo de relajación pequeño reduce considerablemente el τ del sistema permitiendo la determinación de c en condiciones adecuadas. En nuestra investigación hemos optado por el metanol como dopante ya que es químicamente compatible con los componentes de la instalación, son conocidas sus propiedades como modificador en procesos de extracción supercrítica y se trata de un compuesto que puede aparecer como impureza en el CO_2 antropogénico (Proceso Rectisol) o ser añadido para favorecer la operatividad del proceso (agente desecante e inhibidor de la formación de hidratos).

i) Velocidad del sonido en el CO_2 puro

A partir de las medidas experimentales (Sección 4.1.B) de c de las mezclas ricas en CO_2 ($x_{CO_2} > 0.95$) y extrapolando a $x_{CO_2} = 1$, hemos estimado los valores de c para el CO_2 puro. Para disponer de valores de la velocidad del sonido a las mismas temperaturas y presiones en cada fracción molar, los valores de c experimentales de cada isopleta e isoterma se han ajustado al siguiente polinomio:

$$(P - P^{\#}) = \sum_{i=1}^{3} a_i (c - c^{\#})^i \qquad \text{(Ec. 39)}$$

Donde $P^{\#}$ = 70 MPa y $c^{\#}$ es la velocidad del sonido a $P = P^{\#}$.

Posteriormente, estos datos interpolados se han ajustado a una función cuadrática de la fracción molar:

$$c(x_{CO_2}) = c_0 + c_1(1 - x_{CO_2}) + c_2(1 - x_{CO_2})^2 \qquad \text{(Ec. 40)}$$

Donde $c\left(x_{CO_2}=1\right)=c_0$ es la velocidad del sonido en el CO_2 puro. La incertidumbre standard relativa en el cálculo de c_0 teniendo en cuenta el error experimental y el proveniente del análisis de regresión es $u_r(c_0)=0.14\%$, muy inferior a la desviación que presenta la EoS de referencia en esta región[89]: $MRD(c)$= 2 %.

Los valores obtenidos (Figura 36) han sido comparados con los únicos datos experimentales que existen en el rango de presiones y temperaturas que cubren este trabajo,[77] con los obtenidos por Lin y Trusler[64] mediante extrapolación usando propano como dopante, y con los valores proporcionados por la EoS de referencia para el CO_2 puro (Figura 37). Como puede observarse existe una gran concordancia, obteniendo unas desviaciones medias relativas: $MRD(c)=0.61$, 0.28 y 0.42 %, respectivamente.

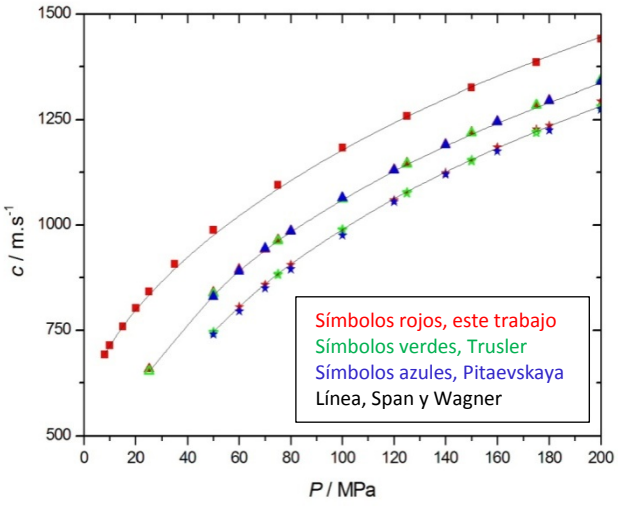

Figura 36. Velocidad del sonido, c, de CO_2 puro frente a la presión, P, a varias temperaturas, T. ■, T = 263.15 K; ▲, T = 298.15 K; ★, T = 323.15 K.

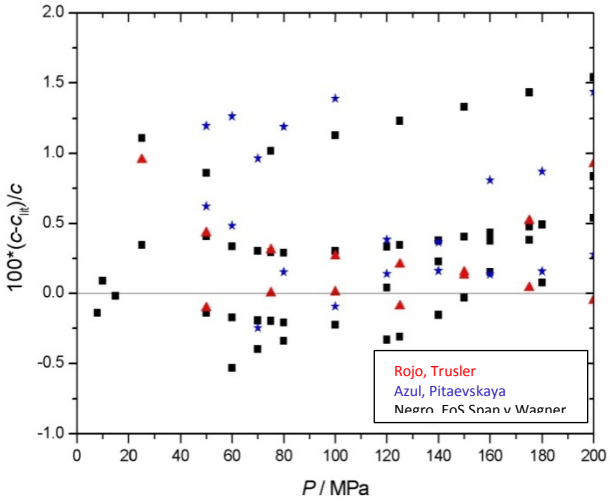

Figura 37. Comparación entre las velocidades del sonido para el CO_2 puro obtenidas en este trabajo, c, y de la literatura, c_{lit} ,▲, Trusler[64]; ★, Pitaevskaya[77]; ■, Span Wagner EoS[89].

ii) Efecto del metanol como agente dopante.

Como hemos comentado en el apartado 4.1.B.1. de esta Memoria, las medidas acústicas son necesarias para un correcto estudio de riesgos durante la monitorización de los procesos de transporte y almacenamiento del CO_2 antropogénico. Sin embargo, las especiales características del CO_2 puro hacen que, en ciertas condiciones, sea imposible su determinación con fiabilidad. Añadir pequeñas cantidades de un compuesto adecuado puede posibilitar la determinación experimental de c al disminuir mucho el tiempo de relajación del fluido. Así, añadiendo únicamente un 1 % en mol, la señal experimental es nítida a la frecuencia de 5 MHz en un rango de presiones y temperatura considerable. Por otro lado, la pequeña variación observada de c con la concentración nos permitirá dopar el CO_2 con más cantidad de metanol permitiéndonos un mayor rango de medida de c sin afectar apenas a su valor. En la Figura 38 se puede apreciar el error cometido al considerar las mezclas CO_2+CH_3OH como si fueran CO_2 puro. Dopar hasta con un 5% en mol de metanol supone, en los rangos de P y T estudiados, una desviación media relativa del 0.40%, con una desviación máxima del 1.1%, de nuevo inferior a la incertidumbre de la propia EoS de referencia para el CO_2.

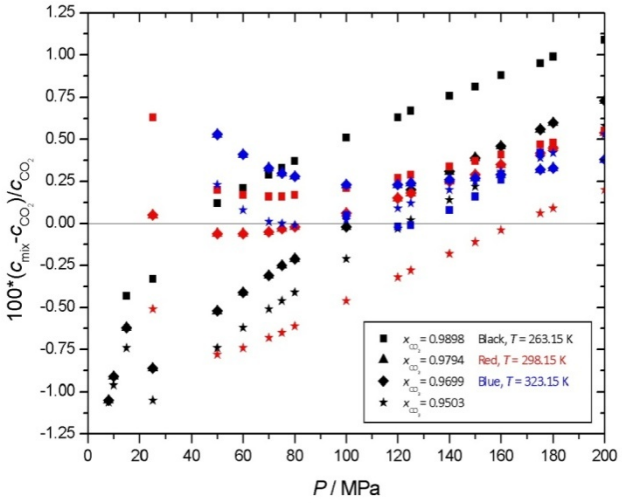

Figura 38. Comparación entre las mezclas de CO_2 estudiadas en este trabajo, c_{mix}, y las velocidades del sonido para el CO_2 puro a partir de la EoS de referencia, c_{CO_2}.

El trabajo adicional descrito ha permitido al grupo de investigación disponer en la actualidad de datos fiables de velocidades del sonido para los sistemas CO_2 + impurezas de interés para la tecnología CCS, mediante su dopaje con metanol. De otra forma, habría sido imposible abordar la investigación de una propiedad tan importante como es la velocidad del sonido dada la elevada concentración de CO_2 en los sistemas que han de ser estudiados.


ANEXO

7. ANEXO

Desviación Media Relativa en la propiedad x

$$MRD\ (x) = \frac{100}{N}\sum_{i=1}^{N}\left|\frac{x_i^{exp} - x_i^{cal}}{x_i^{exp}}\right| \qquad \text{(Ec. A.I)}$$

Donde

x_i^{exp} Son los datos experimentales

x_i^{*} Son los valores bibliográficos o los calculados

N Es el número de puntos

Desviación Estándar Media Relativa de la propiedad x

La desviación estándar media para la propiedad x, $\bar{S}_x^r$, se ha calculado utilizando las siguientes ecuaciones:

$$\bar{S}_x^r = \frac{100}{N}\sum_{j=1}^{N}({}_jS_x^r) \qquad \text{(Ec. A.II)}$$

Donde N es el número de puntos y ${}_jS_x^r$ es la desviación estándar relativa en cada punto:

$${}_jS_x^r = \frac{{}_jS_x}{(1/n)\sum_{i=1}^{n} x_i^{exp}} \qquad \text{(Ec. A.III)}$$

Y ${}_jS_x$ es la desviación estándar en cada punto:

$${}_jS_x = \sqrt{\frac{n\sum_{i=1}^{n}(x_i^{exp})^2 - \sum_{i=1}^{n}(x_i^{exp})^2}{n(n-1)}} \qquad \text{(Ec. A.IV)}$$

Siendo n el número de análisis para una T y P dadas.

Incertidumbre

La incertidumbre expandida se ha calculado mediante las reglas de la ley de propagación de errores:

$$U(y) = ku_c(y) = k\left[\sum_{i=1}^{N}\left(\frac{\partial f}{\partial x_i}\right)^2 u^2(x_i)\right]^{1/2} \qquad \text{(Ec. A.V)}$$

Donde

k Factor de cobertura ($k = 2$ en este trabajo)

$u_c(y)$	Incertidumbre estándar combinada del valor estimado y
N	Número de puntos
x_i	Cada una de las variables de las que depende y
$(\partial f / \partial x_i)$	Coeficiente de sensibilidad de la variable de entrada x_i
$u^2(x_i)$	Cuadrado de la incertidumbre asociada a la variable de entrada x_i

BIBLIOGRAFÍA

8. BIBLIOGRAFÍA

1. Abbaci, A. Thermodynamic properties of ethane in the critical region. *J.Mol.Liq.,* 118 (2005) 31-36.

2. Agencia Europea (2012). Annual European Union Greenhouse Gas Inventory 1990-2010 and Inventory Report 2012. Technical Report No.3/2012. http://www.eea.europa.eu/publications/european-union-greenhouse-gas-inventory-2012.

3. Agencia Europea (2012). Inventory of U.S. Greenhouse Gas Emissions and Sinks: 1990-2010. EPA 430-R-12-001.US. http://www.epa.gov/climatechange/ghgemissions/usinventoryreport.html.

4. Allada, S. Solubility parameters of supercritical fluids. *Ind. Eng. Chem. Proc.,* 23 (2) (1984) 344-348.

5. Aursand, P., Hammer, M. y Munkejord, S. T. Pipeline transport of CO_2 mixtures: Models for transient simulation. *Int.J. Greenhouse Gas Control*, 15 (2013) 174-185.

6. Bachu, S. Sreening and ranking of sedimentary basins for sequestration of CO_2 in geological media in response to climate change. *Environ. Geol.,* 44 (3) (2003) 277-289.

7. Bagley, E.B., Nelson, T.P. y Scigliano, J.M. 3- Dimensional solubility parameters and their relationship to internal pressure measurements in polar and hydrogen bonding solvents. *J. Paint Technol*., 43 (555) (1971) 35-42.

8. Ball, S.J. y Trusler, J.P.M. Speed of sound of n-hexane and n-hexadecane at temperatures between 298 and 373 K and pressures up to 100 MPa. *Int. J. Thermophysics*, 22 (2001) 427-443.

9. Ben-Naim, A. Inversion of the Kirkwood-Buff theory of solutions: application to the water-ethanol system. *J. Chem. Physics*, 67 (1977) 4884-4890.

10. Berges, B. J., Leighton, T. G. y White, P. R.. Passive acoustic quantification of gas fluxes during controlled gas released experiments. *Int.J. Greenhouse Gas Control,* 38 (2015) 64-79.

11. Blanco, S., Gil, L., García-Giménez, P., Artal, M., Otín, S. y Velasco, I. Critical Properties and High-Pressure Volumetric Behaviour of the Carbon Dioxide plus Propane System at T=308.15 K. Krichevskii Function and Related Thermodynamic Properties. *J. Phys.Chem. B*, 113 (2009) 7243-7256.

12. Bouchot, C. y Richon, D. An enhanced method to calibrate vibrating tube densimeters. *Fluid Phase Equilib.,* 191 (2001) 189-208.

13. Buecker, D. y Wagner, W. Reference Equations of State for the Thermodynamic Properties of Fluid Phase n-butane and Isobutane. *J. Phys. Chem. Ref. Data,* 35 (2006) 205.

14. Lin, C.W. y Trusler, J.P.M. Speed of sound in (carbon dioxide + propane) and derived sound speed of pure carbon dioxide at temperatures between (248 and 373) K and at pressures up to 200 MPa. *J.Chem. Eng. Data,* 59 (2014) 4099-4109.

15. Cipollina, A., Anselmo, R., Scialdone, O., Filardo, G. y Galia, A. Experimental P-T-rho measurements of carbon dioxide, carbon monoxide, and hydrogen and semiquantitative estimation of their solvent power using the solubility parameter conceot. *J. Chem. Eng. Data,* 52 (2007) 2291-2297.

16. Cismondi, M., Brignole, E.A. y Mollerup, J. Rescalling of three parameter equations of state: PC-SAFT and SPHCT. *Fluid Phase Equilib*., 234 (2005) 108-121.

17. Colgate, S., Sivaraman, A. y Dejsupa, C. Acoustic cavity method for sonic speed measurements in liquids and stock tank oils. *Fluid Phase Equilib.,*76 (1992) 175.

18. Chialvo, A., y Cummings, P.T. Near-Critical phase behavior of dilute mixtures-comment. *Mol. Phys.,* 84 (1995) 41-48.

19. Dávila, M., y Trusler, J.P.M. Thermodynamic properties of mixtures of N-methyl-2-pyrrolidinone and methanol at temperatures between 298.15 K and 343.15 K and pressures up to 60 MPa. *J. Chem. Thermodyn.,* 41 (2009) 35.

20. Debenedetti, P.G. y Mohamed, R.S. Attractive, weakly attractive, and repulsive near-critical systems. *J. Chem.Phys*., 90 (1989) 4528-4536.

21. Donnelly, H.G. y Katz, D.L. Phase Equilibria in the carbon dioxide methane system. *Ind. Eng. Chem.,* 46 (1954) 511-517.

22. Dzida, M. y Cempa, M. Thermodynamic and acoustic properties of (heptane plus dodecane) mixtures under elevated pressures. *J. Chem. Thermodyn*., 40 (2008) 1531.

23. *Effects of impurities on geological storage of CO_2; IEAGHG, (June 2011) Report: 2011/04.*

24. Egorov, S.A. Local density augmentation in attractive supercritical solutions: Inhomogeneous fluid approach. *J. Chem. Phys.,* 112 (2000) 7138.

25. *Element Energy, 2010. CO_2 pipeline infrastructure: an analysis of global challenges and opportunities. In: Final Report for IEA Greenhouse Gas Programme, 1-134. EON UK, 2011, Kingsnorth Carbon Capture & Storage Project. Post-FEED Project Cost.*

26. Elshahomi, A., Lu, C., Michal, G. y otros. Decompression wave speed in CO_2 mixtures: CFD modelling with the GERG-2008 equation of state. *App. Energy,* 140 (2015) 20-32.

27. Estrategia Española de Ciencia y Tecnología y de Innovación 2013-2020 *http://www.idi.mineco.gob.es/stfls/MICINN/Investigacion/FICHEROS/Estrategia_espanola_ciencia_tecnologia_Innovacion.pdf*.

28. Estrada-Alexanders, A.F. y Trusler, J.P.M. The speed of sound and derived thermodynamic properties of ethane at temperatures between 220 K and 450 K and pressures up to 10.5 MPa. *J.Chem. Thermodyn.,* 29 (1997) 991-1015.

29. European Comission (2017). 2020 Climate & Energy Package. Climate Action. https://ec.europa.eu/clima/policies/strategies/2020_en. https://ec.europa.eu/clima/policies/strategies/2020_en

30. European Comission (2017). 2050 Climate & Energy Package. Climate Action. https://ec.europa.eu/clima/policies/strategies/2020_en. *https://ec.europa.eu/clima/policies/strategies/2050_en*. Obtenido de 2050 low-carbon economy. Climate Action. European Comission.

31. Friend, D.G., Ingham, H. y Ely, F. Thermophysical properties of ethane. *J. Phys. Chem. Ref. Data,* 20 (1991) 275-347.

32. Gil, L.; Santos, O.; Muñóz-Embid, J.M y otros. Experimental setup to measure critical properties of pure and binary mixtures and their densities at different pressures and temperatures: determination of the precision and uncertainty in the results. *J. Supercritical Fluids.,* 44 (2008) 123-138.

33. Gil, L., Blanco, S., Rivas, C., Laga, E., Fernández, J., Artal, M., y otros. Experimental determination of the critical loci for {n-C6H14 or CO_2+ alkan-1-ol} mixtures. Evaluation of their critical and subcritial behavior using PC-SAFT EoS. *J. Supercritical Fluids*, 71 (2012) 26-44.

34. Gil, L., Martínez-López, J., Artal, M., Blanco, S., Muñoz Embid, J., Fernández, J., y otros. Volumetric Behavior of the { CO_2 (1) +C_2H_6 (2)} System in the Subcritical (T= 293.15 K), Critical, and Supercritical (T=308.15 K) Regions. *J. Phys. Chem. B,* 114 (2010) 5447-5469.

35. Gimeno, B., Fernández, J., Artal M., Blanco, S.T. y Velasco, I. CO_2+SO_2 co-capture assesment. Part 1. International Forum on Recent Developments of CCS Implementation. Athens, 26-27 March 2015)

36. Gross, J. y Sadowski, G. Perturbed-chain SAFT: An equation of state based on a perturbation theroy fo chain molecules. *Ind. Eng. Chem. Res.,* 4 (2001) 1244-1260.

37. Gross, J. y Sadowski, G. Application of the perturbed-chain SAFT equation of state to associating systems. *Ind.Eng. Chem. Res.,* 41 (22) (2002) 5510-5515.

38. Hansen, C. Universality of solubility parameter. *Ind. Eng. Chem. Prod.,* 8 (1) (1969) 2-11.

39. Hansen, C. *Hansen Solubility Parameters- A User´s Handbook.* CRC Press: Boca Raton, FL. (2000).

40. http://climate.nasa.gov/vital-signs/global-temperature/

41. Ibrahim, M. y Ertesvag, I.S. PVTx modeling of CO_2 pipeline at depressurization conditions using SPUNG Equation of State (EoS) with a comparison to SRK. *Energy Procedia*, (63) (2014) 2467-2474.

42. Japas, M. Á.P. Determination of the Krichevski function in near-critical dilute solutions of I_2(s) and CHI_3 (s). *J. Chem. Thermodyn.,* 30 (1998) 1603-1615.

43. Japas, M., Alvarez, J., Gutkowski, K. y Fernandez-Prini, R. Determination of the Krichevskii function in near-critical dilute solutions of I_2 (s) and CHI_3 (s). *J. Chem. Thermodyn.,* 30 (1998) 1603-1615.

44. Kaminishi, G.y Toriumi, T. Vapor-liquid equilibria in the systems: CO_2+CO, CO_2+CO+H_2 and CO_2-CH_4. *Rev. Phys. Chem. Jpn*. ,38 (1) (1968)79-84.

45. Khelladi, H. y Plantier, F. A phase comparison technique for sound velocity measurement in strongly dissipative liquids under pressure. *J. Accous.Soc.Am.,* 128 (2010) 672-678.

46. Kirkwood, J. y Buff, F. The statistical mechanical theory of solutions. 1. *I. J. Chem. Phys.* ,19 (1951) 774-777.

47. Knoope, M., Ramírez, A. y Faaij, A. A state-of-the-art review of techno-economic models predicting the costs of CO_2 pipeline transport. *Int. J. Greenhouse Gas Control*, 16 (2013) 241-270.

48. Kratky, O. y Leopold, H. Determination of density of liquids and gases to an accuracy of 10^{-6} g/cm^3 with a sample volume of only 0.6 cm^3. *Angew. Phys.,* 27 (1969) 273.

49. Kunz, O. K. (2006). *GERG Technical Monograph. Fortschr.-Ber.: VDI, VDI-Verlag: Düseldorf*.

50. Kunz, O. y Wagner, W. The GERG-2008 Wide-Range Equation of State for natural gases and other mixtures: An expansion of GERG-2004. *J. Chem.Eng. Data*, 57 (2012) 3032-3091.

51. Labes, P., Daridon, J., Lagourette, B. y otros. Measurement and prediction of ultrasonic speed under high-pressure in natural gases. *Int. J. Thermophys.,* 15 (1994) 803-819.

52. Lagourette, B. y Daridon, J. Speed of sound, density, and compressibility of petroleum fractions from ultrasonic measurements under pressure. *J. Chem. Thermodyn.,* 31 (1999) 987-1000.

53. Laursen, T. (2012). VLXE Aps. Scion-DTU, Diplomvej, Denmark.

54. Lebedev, M., Bilenko, O., Mikhaltsevitch, V. y otros. Laboratory measurements of ultrasonic velocities in CO_2 saturated brines. *12th International Conference on Greenhouse Gas Control Technologies (GHGT) Energy Procedia,* 63 (2014) 4273-428.

55. Lee, L., y Cochran, H. En *Supercritical Fluids: Fundamentals for Application, NATO, ASI Ser.273. Kluwer Academic Publisers* (1994) 365-383. The Netherlands.

56. Leighton, T. G., Baik, K., y Jiang, J. The use of acoustic inversion to estimate the bubble size distribution in pipelines. *PROCEEDINGS OF THE ROYAL SOCIETY A MATHEMATICAL PHYSICAL AND ENGINEERING SCIENCES 46* (2012) 2145 , 2461-2484.

57. Lemming, W. (1989). *Fortschr.-Ber.:VDI, Reihe 19, Nr. 32, VDI-Verlag Dusseldorf*.

58. Lemmon, E.; McLinden, M y Wagner W. Thermodynamic properties of propane. III. A reference Equation of State for temperatures from the melting line to 650 K and pressures up to 1000 MPa. *J.Chem. Eng. Data,* 54 (12) (2009) 3141-3180.

59. Lemmon, E., Huber, M., y Mc Linden, M. NIST Standard Reference Database 23: Reference Fluid Thermodynamic and Transport Properties-REFPROP, Version 9.0; . *National Institute of Standards and Technology, Standard Reference Data Program: Gaithersburg* (2010).

60. Levelt Sengers, J. En *Supercritical Fluids: Fundamentals for Application.* The Netherlands: Kluwer Academic Publishers. 3-38 (1994)

61. Levelt Sengers, J. Critical behaviour of fluids: concepts and applications. *Supercritical Fluids: Fundamentals for Application. NATO, ASI Ser. 273. Kluwer Academic Publishers, The Nederlands, pp. 3-38* (1994).

62. Li, H., Jakobsen, J., Wilhelmsen, O. y Yan, J. PVTx properties of CO_2 mixtures relevant for CO_2 capture, transport and storage: Review of available experimental data and theoretical models. *Appl. Energy* ,88 (11) (2011) 3567-3579.

63. Li, H., Yan, J., Yan, J. y Anheden, M. Impurity impacts on the purification process in oxy-fuel combustion based CO_2 capture and storage system. *Appl. Energy,* 86 (2) (2009) 202-213.

64. Lin, C. T. Speed of Sound in (carbon dioxide + propane) and derived sound speed of pure carbon dioxide at temperatures between 248 and 373 K at pressures up to 200 MPa. *J. Chem. Eng. Data,* 59 (2014) 4099-4109.

65. Luis Miguel Romeo, L. I. *Captura y almacenamiento de CO_2.* Prensas Universitarias de Zaragoza. (2010)

66. Lund, H., Flatten, T., y Munkejord, S. T. Depressurization of carbon dioxide in pipelines-models and methods. *10th International Conference on Greenhouse Gas Control Technologies* (*pp*. 2984-2991). Amsterdam, NETHERLANDS : Energy Procedia. (2010).

67. Magee, J.W. y Ely, J.F. Isochoric (PVT) measurements on CO_2 and (0.98 CO_2+0.02 CH_4) from 225 K to 400 K and pressures to 35 MPa. *Int. J.Thermophys.,* 9 (4) (1988) 547-557.

68. Malakondaiah, K., Kham, V. y Subrahmanyam, S. Internal pressure studies on binary mixtures of bezene with para-xylene, dioxane, toluene and chlorobenzene and of

isooctane with cyclohexane, benzene and carbon tetrachloride on basis of ultrasonic measurements. *Ind. J. Chem*., 16 (9) (1978) 733-735.

69. Medwin, H. Counting Bubbles Accoustically-Review. *Ultrasonics,* 15 (1) (1977) 7-13.

70. Merz, R., y Linder, F. Elastic and vibrationally inelastic scattering of low energy electrons from propane. *J. Phys. B: At. Mol. Opt. Phys.,* 36 (13) (2003) 2921-2941.

71. Michael, K., Golab, A., Shulakova, V., Ennis-King, J., Allison, G., Sharma, S., y otros. Geological storage in saline aquifers - A review of the experience from existing storage operations. *Int. J. Greenhouse Gas Control*, 4 (4) (2010) 659-667.

72. Nelson, J., R.D., Lide, J. D. y Maryott, A. Selected values of electric dipole moments for molecules in the gas phase. En *National Reference Data Series* (pp NBS 10). (1967)

73. Nishikawa, K., y Morita, T. Inhomogeneity of molecular distribution in supercritical fluids. *Chem. Phys. Lett.,* 316 (3-4) (2000) 238-242.

74. Noury, J. Vitesse des ultrasons de 960 KC dans l´ethane au voisinage de l´etat critique. *Comptes Rendus,* 234 (3) (1952) 303-305.

75. Peng, D y Robinson, D.B. A new two-constant Equation of State. *Ind. Eng.Chem.Fund.,* 15 (1) (1976) 59-64.

76. Piñeiro, M., Plantier, F., Bessières, D., Legido, J. y Daridon, J. High pressure speed of sound measurements in methyl nonafluorobutyl ether and ethyl nonafluorobutyl ether. *Fluid Phase Equil.*,222-223 (2004) 297-302.

77. Pitaevskaya, L.L. y Bilevich, A.V. Speed of ultrasound in carbonic-acid gas at pressures to 4,5 kilobars. *Russ. J. Phys. Chem.,* 47 (1) (1973) 126-127.

78. Plantier, F., Bessières, D., Daridon, J. y Montel, F. Structure and thermodynamic consistency of heavy oils: A study on the basis of acoustic measurements. *Fuel,* 87 (2) (2008) 196-201.

79. Plantier, F., Danesh, A., Sohrabi, M., Daridon, J., Gozalpour, F. y Todd, A. Measurements of the speed of sound for mixtures of methane plus butane with a particular focus on the critical state. *J. Chem. Eng. Data,* 50 (2) (2005) 673-676.

80. Poole, G. y Aziz, R. Law of corresponding states as applied to sound velocity in liquids consisting of elliptical molecules. *Can. J. Phys.,* 50 (7) (1972) 721-.

81. Ramos Moura, J. Molecular shape and orientational order- Effects in the energy of cavity formation in liquids, *J.Sol. Chem.,* 18 (10) (1989) 957-975.

82. Registro Estatal de Emisiones y Fuentes Contaminantes. www.prtr-es.es.

83. Reynolds, L., Gardecki, J., Frankland, S., Horng, M. y Maroncelli, M. Dipole solvation in nondipolar solvents: Experimental studies of reorganization energies and solvation dynamics. *J.Phys. Chem. A,* 100 (24) (1996) 10337-10354.

84. Ball S.J. Speed of sound of n-hexane and n-hexadecane at temperatures between 298 and 373 K and pressures up to 100 MPa. *Int.J. Thermophys.,* 22 (2001) 427-443.

85. Sass, B., Farzan, H., Prabhakar, R., Gerst, J., Sminchak, J., Bhargava, M., y otros. *Energy Procedia,* 1 (1) (2009) 535-542.

86. Seevam, P., Race, J., Downie, J. y Hopkins, P. *Proceedings of IPC2008 7th International Pipeline Conference (Canada)* (2008) 39-51.

87. Siggins, A. F., Lwin, M. y Wisman, P. Laboratory Calibration of the seismo-acoustic response of CO_2 saturated sandstones. *Int. J. Greenhouse Gas Control,* 4 (6) (2010) 920-927.

88. Some Fundamentals of Mineralogy and Geochemistry. Deep-basins brines I: Density, TDS, And chloride; *http://www.gly.uga.edu/railsback/Fundamentals/815BrinesDiagrams071P.pdf*.

89. Span, R. y Wagner, W. A new Equation of State for carbon dioxide covering the fluid region from the triple point temperature to 1100 K at pressures up to 800 MPa. *J.Phys. Chem. Ref. Data,* 25 (6) (1996) 1509-1596.

90. Stoianov, I., Nachman, L., Madden, S., y otros. PIPENET: A wireless sensor network for pipeline monitoring. *6th International Symposium on Information Processing Sensor Networks Ubicación: Cambridge, MA* (2007) 264-273.

91. Terres, E., Jahn, W. y Reissmann, H. *Brennstoff-Chem,* 38 (1957) 129.

92. *The Global Status of CCS: 2013; Global CCS Institute: Melbourne, Australia,* 2013. http://www.globalccinstitute.com/publications/global-status-ccs-2013.

93. Trusler, J.P.M. The speed of sound in (0.8 CH_4+0.2 C_2H_6) at temperatures between 200 K and 375 K and amount of substance densities up to 5 mol·dm^{-3}. *J. Chem. Thermodyn.,* 26 (7) (1994) 751-763.

94. Tsumura, R. y Straty, G. Speed of sound in saturated and compressed fluid ethane. *Cryogenics,* 17 (4) (1977) 195-200.

95. Goodyear, G. y Tucker, S.C. What causes the vibrational lifetime plateau in supercritical fluilds? J. *Chem. Phys.,* 110 (8) (1999) 3643-3646.

96. Valderrama, J.O. The state of the cubic equation of state. *Ind. Eng.Chem.Res.,* 42 (8) (2003) 1603-1618.

97. Van Itterbeek, A. y Van Dael. W. Velocity of sound in liquid oxygen and liquid nitrogen as a function of temperature and pressure. *Physica,* 28 (9) (1962) 861-870.

98. Vandeginste, V. y Piessens, K. Pipeline design for a least-cost router application for CO_2 transport in the CO_2 sequestration cycle. *Int. J. Greenhouse Gas Control,* 2 (4) (2007) 571-580.

99. Verdier, S., Duong, D. y Andersen, S. Experimental determination of solubility parameteres of oils as a function of pressure. *Energy Fuels*, 19 (4) (2005) 1225-1229.

100. Voronov, F., Pitaevskaya, L., y Bilevich, A. Rate of propagation of ultrasound in nitrogen at pressures up to 4 Kbar and temperatures in range 25-175 degrees C. *Russ.J.Phys.Chem.,* 43 (3) (1969) 321.

101. Wagner, W. y Pruss, A.The IAPWS formulation 1995 for the thernodynamic properties of ordinary water substance for general and scientific use. *J. Phys. Chem. Ref. Data,* 31 (2) (2002) 387-535.

102. Xu, N., Dong, J., Wang, Y. y Shi, J. High pressure vapor liquid equilibria at 293 K for systems containing nitrogen, methane and carbon dioxide. *Fluid Phase Equilib.,* 81 (1-2) (1992) 175-186.

103. Zhang, J., Zhang, X., Han, B., He, H., Liu, Z. y otros. Study on intermolecular interactions in supercritical fluids by partial molar volume and isothermal compressibility. *J. Supercritical Fluids*, 22 (1) (2002) 15-19.

104. Zhang, W. Designing a cost effective and reliable pipeline leak detection system. In: Pipeline Reliabiity Conference. Houston, USA. (1996).19th-22th December.

APÉNDICE

9. APÉNDICE

La normativa que regula la elaboración y defensa de Tesis Doctoral en la Universidad de Zaragoza indica que: "*Podrán optar por la presentación de tesis en la modalidad de compendio de publicaciones aquellos doctorandos que, previamente a la presentación de sus tesis y con la autorización expresa de su director o directores, tengan publicados o aceptados para su publicación, con fecha posterior a la del inicio de sus estudios de doctorado, un número mínimo de cuatro artículos con unidad temática, de los cuales tres habrán de estarlo en revistas científicas cuyo índice de impacto se encuentre incluido en la relación de revistas del Journal of Citation Reports".*

Los artículos que recogen el trabajo realizado en esta tesis doctoral son cinco, todos ellos, se han publicado en revistas de conocido prestigio cuya temática, índice de impacto y posición (JCR) se indican a continuación.

Se presenta una copia de las 5 publicaciones y la renuncia de los co-autores no doctores a que estos trabajos puedan ser incluidos en otra tesis doctoral presentada en esta modalidad.

9.1. RELEVANCIA DE LAS PUBLICACIONES

The Journal of Physical Chemistry B

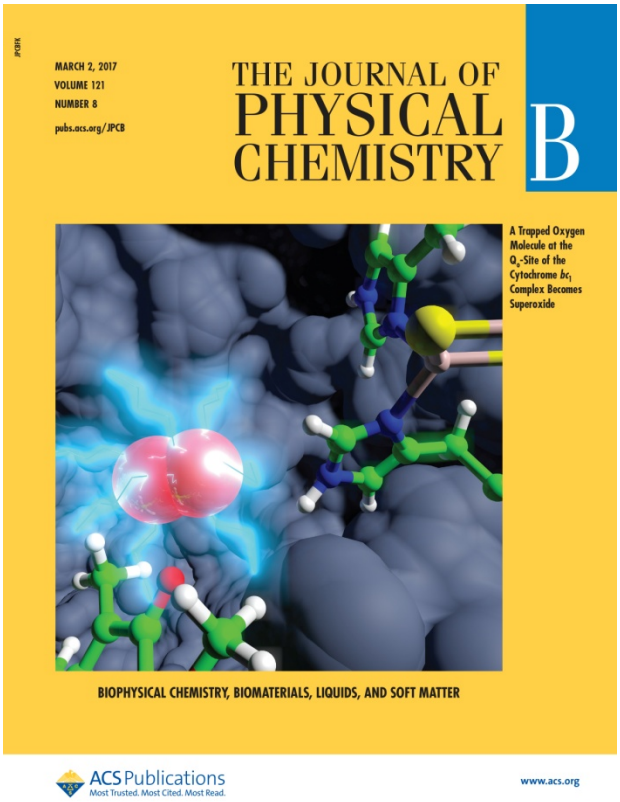

Publicación Internacional que recoge estudios relacionados con macromoléculas, surfactantes, membranas, mecánica estadística y termodinámica. Los artículos experimentales que se admiten en esta publicación deben ir acompañados de modelización o simulación y de una profunda discusión.

El artículo publicado en esta revista es:

Accurate Values of Some Thermodynamic Properties for Carbon Dioxide, Ethane, Propane, and Some Binary Mixtures. *J. Phys. Chem. B*, **2011**, 115, 8216-8230.

Año de publicación: 2011

Categoría de JCR: Chemistry Physical: 32 de 130

Índice de Impacto: 3.696

Environmental Science & Technology

Esta publicación recoge todo tipo de estudios relacionados con el medioambiente tales como modelización medioambiental, energía y medioambiente, procesos medioambientales, ecotoxicología y salud medioambiental humana.

Los artículos publicados en esta revista son:

Influence of Methane in CO_2 Transport and Storage for CCS Technology. *Environ. Sci. Technol.* **2012**, 46, 13016-13023.

Año de publicación: 2012

Categoría de JCR: Engineering, environmental: 2 de 42

Environmental, Science: 7 de 210

Índice de Impacto:.5.257

Discussion of the Influence of CO and CH_4 in CO_2 Transport, Injection and Storage for CCS Technology. *Environ. Sci. Technol.* **2014**, 48, 10984-10992.

Año de publicación: 2014

Categoría de JCR: Engineering, environmental: 3 de 47

Environmental, Science: 10 de 223

Índice de Impacto:.5.330

International Journal of Greenhouse Gas Control

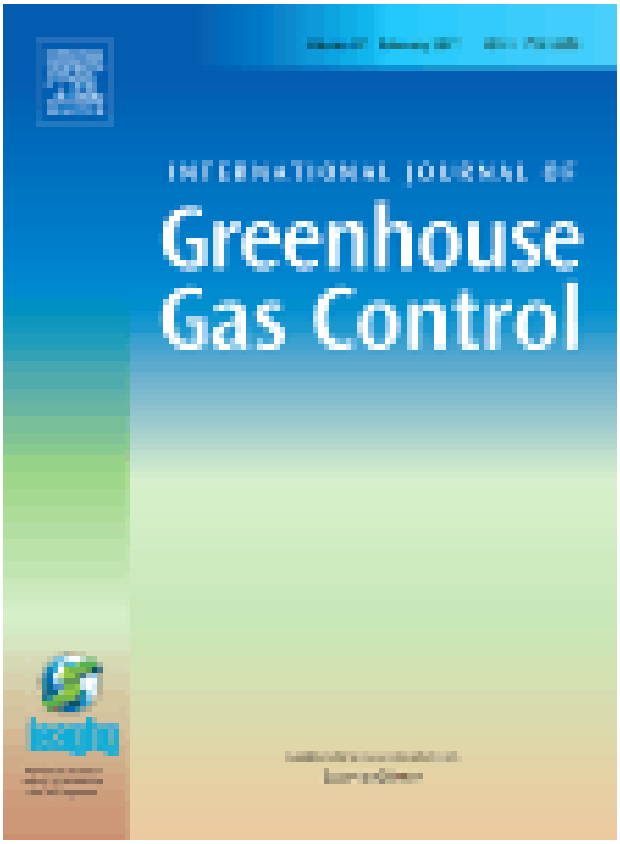

Esta publicación se centra en desarrollos científicos y de ingeniería enfocados al control de gases de efecto invernadero a través de su captura y almacenamiento en el sector energético y otras fuentes industriales. Entre los temas más comunes se encuentran la captura, transporte y almacenamiento geológico del CO_2 así como otras alternativas de almacenamiento.

El artículo publicado en esta revista es:

Influence of methane and carbon monoxide in the volumetric behaviour of the anthropogenic CO_2: Experimental data and modelling in the critical region. *International Journal of Greenhouse Gas Control*,**2013**, 18, 264-276.

Año de publicación: 2013

Categoría de JCR: Energy & Fuels: 16 de 83

Engineering, environmental: 8 de 46

Índice de Impacto:.3.821

Journal of Chemical Thermodynamics

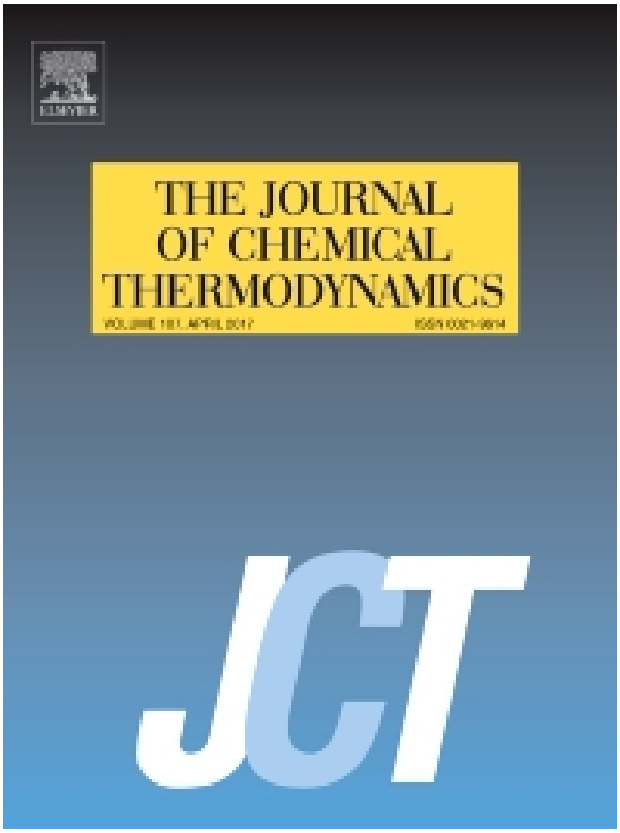

Revista especializada en los equilibrios termodinámicos y propiedades de transporte de los sistemas químicos y publica trabajos relacionados con gases, líquidos, sólidos, polímeros, mezclas, disoluciones e interfaces. Los métodos experimentales deben describirse con suficiente detalle como para permitir una evaluación crítica de la exactitud de los resultados.

El artículo publicado en esta revista es:

Thermodynamic properties of a CO_2-rich mixture (CO_2+CH_3OH) in conditions of interest for carbon dioxide capture and storage technology and other applications. *J. Chem. Thermodynamics*, **2016**, 98, 272-281.

Año de publicación: 2015

Categoría de JCR: Thermodynamics: 13 de 58

Índice de Impacto:.2.196

9.2. COPIA DE LOS TRABAJOS PUBLICADOS

A continuación se adjuntan los cinco trabajos publicados, por orden de publicación.

THE JOURNAL OF PHYSICAL CHEMISTRY B

ARTICLE

pubs.acs.org/JPCB

Accurate Values of Some Thermodynamic Properties for Carbon Dioxide, Ethane, Propane, and Some Binary Mixtures

Inmaculada Velasco, Clara Rivas, José F. Martínez-López, Sofía T. Blanco, Santos Otín, and Manuela Artal*

Departamento de Química Física, Facultad de Ciencias, Universidad de Zaragoza, 50009-Zaragoza, Spain

Supporting Information

ABSTRACT:

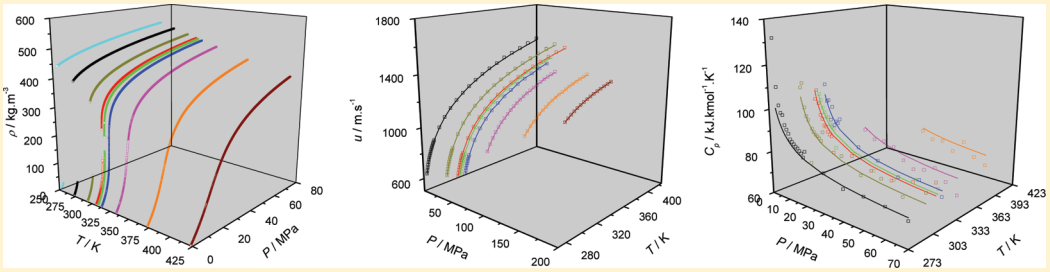

Quasicontinuous $P\rho T$ data of CO_2, ethane, propane, and the [CO_2 + ethane] mixture have been determined along subcritical, critical, and supercritical regions. These data have been used to develop the optimal experimental method and to determine the precision of the results obtained when using an Anton Paar DMA HPM vibrating-tube densimeter. A comparison with data from reference EoS and other authors confirm the quality of our experimental setup, its calibration, and testing. For pure compounds, the value of the mean relative deviation is MRD(ρ) = 0.05% for the liquid phase and for the extended critical and supercritical region. For binary mixtures the mean relative deviation is MRD(ρ) = 0.70% in the range up to 20 MPa and MRD(ρ) = 0.20% in the range up to 70 MPa. The number of experimental points measured and their just quality have enable us to determine some derivated properties with satisfactory precision; isothermal compressibilities, κ_T, have been calculated for CO_2 and ethane (MRD(κ_T) = 1.5%), isobaric expasion coefficients, α_P, and internal pressures, π_i, for CO_2 (MRD(α_P) = 5% and MRD(π_i) = 7%) and ethane (MRD(α_P) = 7.5% and MRD(π_i) = 8%). An in-depth discussion is presented on the behavior of the properties obtained along subcritical, critical, and supercritical regions. In addition, PuT values have been determined for water and compressed ethane from 273.19 to 463.26 K up to pressures of 190.0 MPa, using a device based on a 5 MHz pulsed ultrasonic system (MRD(u) = 0.1%). With these data we have calibrated the apparatus and have verified the adequacy of the operation with normal liquids as well as with some compressed gases. From density and speed of sound data of ethane, isentropic compressibilities, κ_s, have been obtained, and from these and our values for κ_T and α_P, isobaric heat capacities, C_p, have been calculated with MRD(C_p) = 3%, wich is within that of the EoS.

INTRODUCTION

The aim of this paper will be to obtain the accurate values of some thermodynamic properties, such as density, speed of sound, and other derivative properties such as isothermal and isentropic compressibility, isobaric coefficient thermal expansion, and isobaric heat capacity. The systems studied here are mainly carbon dioxide and ethane. Experimental measurements of density and speed of sound of the systems under study have been used for calibration purposes, for the development of the experimental procedure and for the determination of precisions of the two different devices used to measure these two properties.

Good quality data in a very broad range of pressures and temperatures (subcritical, critical, and supercritical region), of pure compounds and mixtures is as important to a number of industries, as it is for the development of new and improved equations of state, and they are fundamental in the investigation of intermolecular interactions and dynamic properties of phases. The experimental data presented here will help to improve the reference EoS for the fluids studied in the region of high pressure, where great deviations are obtained in their predicted properties.

From the experimental densities obtained in this work, the most characteristic properties of supercritical fluids were studied. Their variable densities, which can be changed continuously over all values between that of the liquid and that of the gas, could be considered a bridge between the condensed phase and the gas phase.

Furthermore, as we have worked at several temperatures, among them, at temperatures moderately greater than the critical temperature, a broad range of densities were obtained with just small changes in pressure and temperature.

Received: March 11, 2011
Revised: April 27, 2011
Published: June 03, 2011

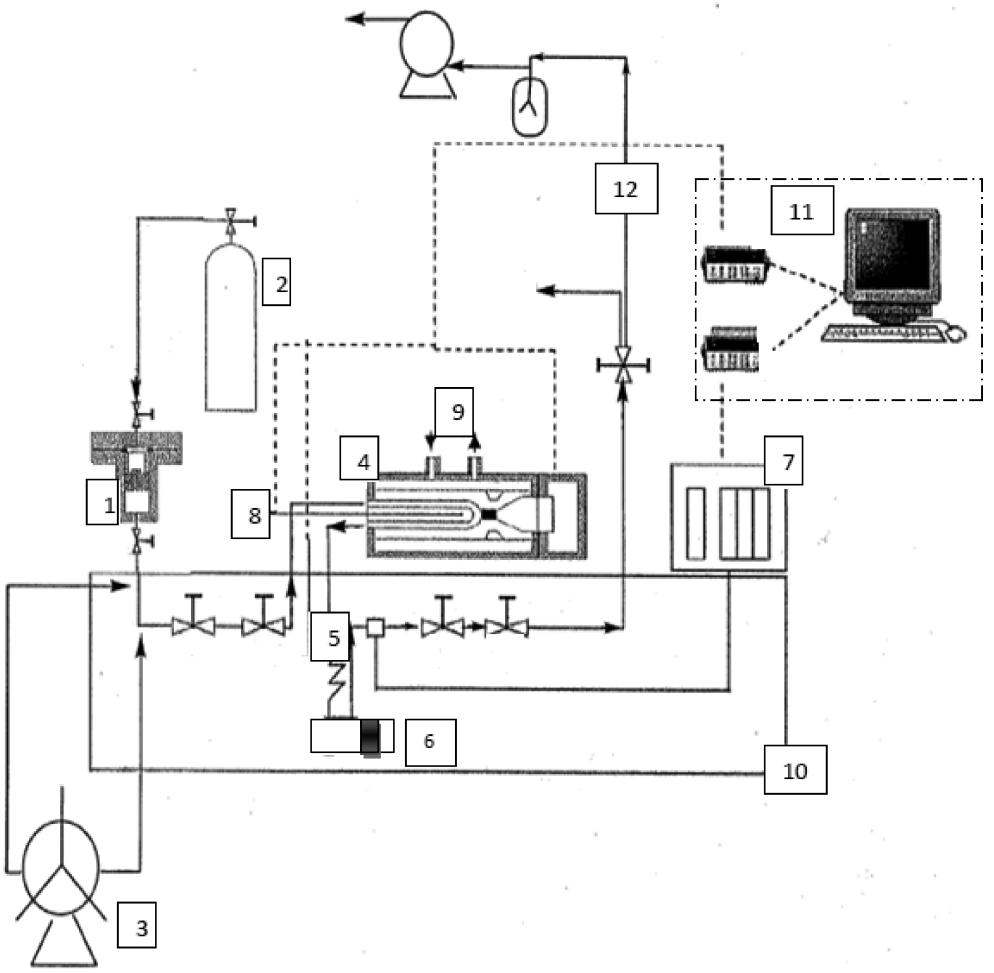

Figure 1. Experimental setup to measure volumetric properties of pure and binary mixtures: (1) loading cell, (2) nitrogen, (3) manual pump, (4) densimeter, (5) vibrating tube output, (6) rupture disk, (7) thermoregulated pressure transducers, (8) platinum temperature probe, (9) externally connected liquid thermoregulated bath, (10) liquid bath, (11) evaluation unit and data acquisition, and (12) evacuation and vacuum line.

EXPERIMENTAL SECTION

Measurement of $P\rho T$ Properties. *Apparatus Description.* Figure 1 illustrates a schematic of the apparatus that we have used for the determination of $P\rho T$ data of fluids in the subcritical, critical, and supercritical regions. The apparatus has been designed and built by ARMINES and the Laboratoire de Thermodynamique des Equilibres entre Phases de l'École Nationale Supérieure des Mines de Paris (France). It was designed for fast, reliable, and accurate generation of $P\rho T$ data over the whole state surface of a fluid encompassing the liquid and vapor compressed phases, and the saturation curve in the (253 to 423) K temperature range, up 70 MPa, for pure compounds and mixtures of defined compositions. The main component of the apparatus is an Anton Paar DMA HPM vibrating-tube densimeter. The measurement circuit contains the vibrating tube and its upstream and downstream tubing that are respectively the input and output ports of the fluid to be studied, and the regulating and shut-off valves. Increases or decreases in pressure are obtained through mass transfers with respect to the measurement circuit. To ensure equilibrium through quasi-static transformations, the corresponding flow rates have been kept sufficiently low (They are usually below 0.005 MPa s^{-1}). Considering the vibration period as pseudo state variable, the $P\tau T$ variables can describe the $P\rho T$ state surface as long as calibration provides a direct relation between τ and ρ.

The installation also includes an ensemble of devices and materials, like those for temperature regulation, particularly around the vibrating tube, and for measurements of pressures and temperatures.

The measurement circuit is composed of the DMA HPM external measuring cell, where the input tubing is connected to shut-off and regulating valves for compression of the vapor, and the output tubing is also connected to shut-off and regulating valves for decompression of liquid. Input and output tubing are thermo regulated by means of heating cartridges, and the remaining circuit sits in a thermo regulated liquid bath. At the circuit exit, a three-way shut-off valve allows the evacuation of the circuit by means of a vacuum pump before measurements and venting for liquid decompression after measurements. The circuit is connected to two pressure transducers for measuring pressures up to 6 and 70 MPa respectively.

The DMA HPM consists of the measuring cell and of an interface module. The interface module generates the period of oscillation, and measures the resulting period of oscillation and the cell temperature. The density measuring cell is connected to an evaluation unit mPDS 2000 V3 where the current oscillation period, measuring temperature and sample density are displayed.

Given that the apparatus is designed for quasi continuous data acquisition, the mPDS 2000 V3 Evaluation Unit is connected to an external computer with software written in LabVIEW to control the data acquisition.

The double envelop of the vibrating tube densimeter enables thermoregulation by an external liquid bath (Fischer Bioblock, Cryo-polystat 71 model C85408). The circuit is thermoregulated by a Fischer Bioblock Scientific Cryothermostat Variostat model C85775 and a liquid bath. In the case of measurements of condensed phases, the temperature of the vibrating tube is tuned to a value slightly lower than that of the measuring circuit. This ensures the initiation of the condensation to happen strictly within the tube. In the case of gas phase measurements, all of the external tubing is warmer than the vibrating tube to avoid local condensations alongside the measurement circuit.

The temperature is measured by means of two 100 ohms platinum probes connected to Data Acquisition Unit Model 34970A from Agilent. One probe is located inside the wall of the vibrating tube and the other inside the liquid bath. The probes and the Data Acquisition Unit were calibrated by the Centro Español de Metrología, CEM, following the CEM-PT-4.2−40 procedure. The precision in the measurement of the temperature is ±0.006 K.

The pressure is measured by means of two pressure transducers (GE Infrastructure model PTX 611) 6 and 70 MPa that are thermo regulated and connected to the measurement circuit and to a Data Acquisition Unit Model 34970A from Agilent. The pressure transducers were calibrated in our laboratories using a Wika CPH 6000 calibrator with an accuracy of 0.025% through the whole scale. The precisions observed in the measurement of pressure were 0.008 MPa for measurements up to 6 MPa and 0.001 MPa for measurements from 6 to 70 MPa.

A variable-volume cell is used for loading pure compounds and mixtures into the measurement circuit. The volume is modified thanks to a piston which separates the loaded fluids from pressurized nitrogen. The cell can be weighted on a mass comparator from Sartorius model CCE 2004, for maximum masses of 2500 g and repeatability better than 0.0002 g. Successive introductions of compounds allow the preparation of mixtures of accurately determined composition thanks to successive weighing of the cell (the components are introduced in order of increasing volatility). Mixtures are homogenized through efficient stirring and kept at pressures higher than their bubble pressures. The fluid is transmitted from the loading cell to the measurement circuit through a manual pump, made by Top Industrie, which makes it possible to achieve pressures up to 70 MPa inside the measurement circuit.

An isotherm consists of about 12000 density-pressure points, considered the raw data, which are evenly reduced to about 2000 points for easier handling in subsequent calculations. This large number of points makes quasi-continuous isotherms available along subcritical, critical and supercritical regions, and allows the accurate determination of the limits of vapor−liquid equilibrium.

Calibration. The measurement of density with a vibrating tube is not absolute; thus, the response of the instrument must be calibrated against fluids of known density. The reference fluid was carbon dioxide with a stated purity of 99.998% and the reference densities were calculated using the reference EoS.[1] The model of calibration used in this work is the Forced Path Mechanical Calibration model, FPMC, developed by Bouchot.[2] This includes realistic mechanical considerations and forces representing the stress and strain behavior of the tube material.

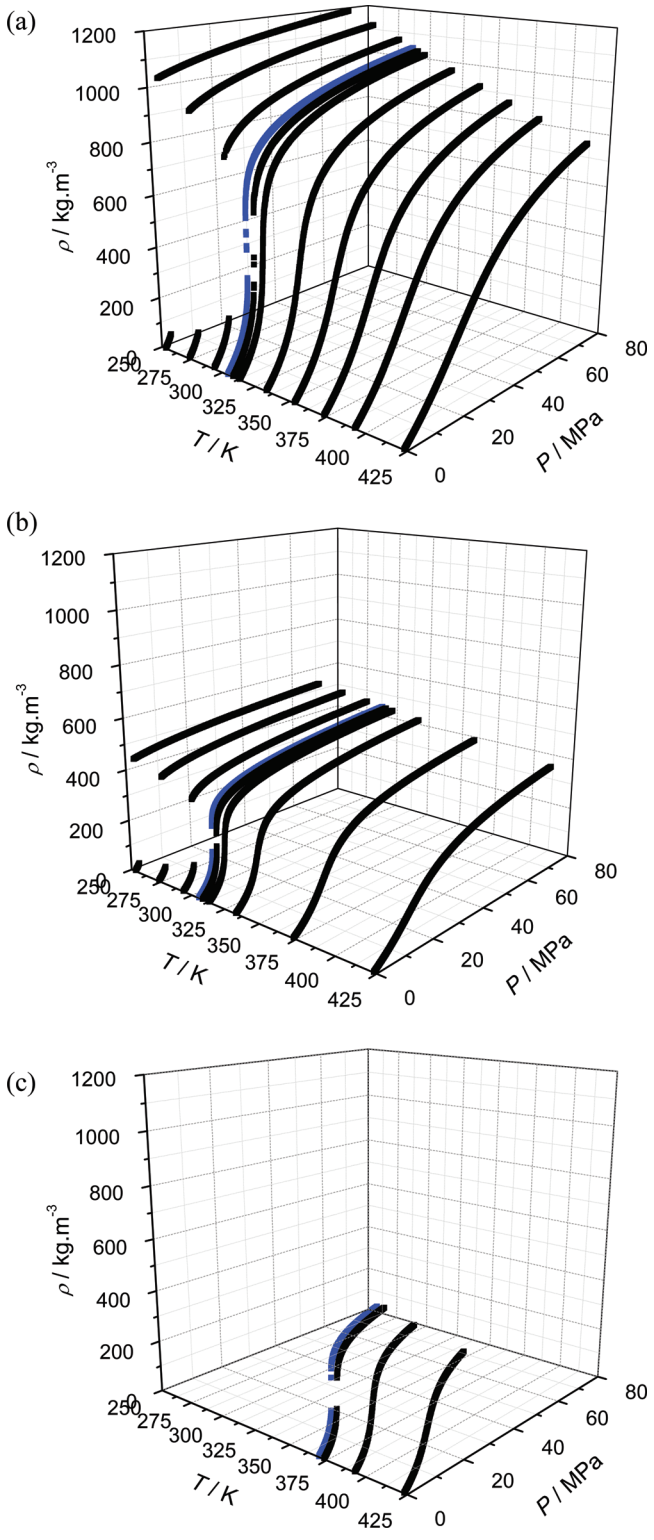

Figure 2. Experimental densities for (a) carbon dioxide, (b) ethane, and (c) propane at several pressures and temperatures. Critical isotherm for each compound is represented by blue dots.

The parameters determined from the calibrating operation were (M_0/L_{00}) and γ_T; both were found to be temperature dependent but pressure independent. Carbon dioxide was measured at 253.15, 273.15, 293.15, $T_c(CO_2)$ = 304.21, 308.15, 313.15,

Table 1. Deviations of Experimental Results for CO_2, C_2H_6, and C_3H_8 at Different Temperatures

	CO_2			C_2H_6			C_3H_8		
T/K	no. points	MRD(%) ρ	MRD(%) P	no. points	MRD(%) ρ	MRD(%) P	no. points	MRD(%) ρ	MRD(%) P
253.15	1700	0.02		2090	0.10				
273.15	2450	0.02		2230	0.05				
293.15	2420	0.02		2310	0.09				
304.21[a]	2980	0.06	0.07						
305.32[a]				2530	0.13	0.14			
308.15	2320	0.07	0.61	2570	0.14	0.12			
313.15	2120	0.05	0.46	2570	0.13	0.20			
333.15	1810	0.12	0.17	2360	0.11	0.20			
353.15	1880	0.05	0.07						
369.82[a]							1684	0.24	0.57
373.15	2290	0.04		2180	0.14		1841	0.30	0.16
393.15	2270	0.11					2110	0.18	0.15
423.15	2150	0.15		2100	0.25		1819	0.09	

[a] Critical temperature of different compounds. Extended critical region $\Rightarrow 0.6\rho_c < \rho < 1.4\rho_c$; $0.98T_c < T < 1.2T_c$.

333.15, 353.15, 373.15, 393.15, and 423.15 K up to 70 MPa. The densities obtained from experimental measurements and FPMC model (Figure 2a) were compared with those from the reference EoS,[1] and the Mean Relative Deviation (MRD(ρ), eq. A.1) obtained is 0.09%, if the critical region is included, and 0.07%, if the critical region is excluded.

The values of MRD(ρ) obtained in this work for the calibration are comparable with those from the literature[3−6] as determined with an Anton Paar DMA HPM vibrating-tube densimeter, but unlike us, following discontinuous procedures of measurement and without considering the critical and vapor regions. As a consequence, the goal of our work is to get quasicontinuous $P\rho T$ data along subcritical, critical, and supercritical regions of pure fluids and mixtures with adequate precisions and additionally, to be able to determine the limits of vapor−liquid equilibrium.

Experimental Results and Precision for Pure Compounds. With the aim to verify the calibration procedure detailed above, the densities of ethane (purity of 99.995%) and propane (purity of 99.95%) were obtained. Ethane was measured at 253.15, 273.15, 293.15, $T_c(C_2H_6)$ = 305.32, 308.15, 313.15, 333.15, 373.15, and 423.15 K over the whole range of pressure, and propane was measured at $T_c(C_3H_8)$ = 369.82, 373.15, 393.15, and 423.15 K, at pressures up to 20 MPa. These densities are shown in Figure 2, panels b and c, respectively. The measurements with propane were made along shorter ranges of temperature and pressure since our objective was to check only the regions with the most experimental difficulty: the critical isotherm and the supercritical region not far from the critical point. These fluids were chosen due to the fact that reference EoS exist for both in the literature, a fact that will allow us to establish comparisons with the experimental data obtained in the present study. In the case of ethane, the reference EoS used were: Buecker and Wagner,[7] for the region of 0.1 to 30 MPa, and Friend et al.,[8] for pressures from 30 to 70 MPa. Lemmon's[9] EoS was used for propane.

The densities obtained from experimental measurements and FPMC model for ethane and propane were compared with those from the reference EoS, and the precisions (MRD) calculated are presented in Table 1 together with those for carbon dioxide. In this table, values for MRD in density of subcritical isotherms are presented. For critical and supercritical isotherms, the values of MRD are given in density for points outside the extended critical region, and in pressure within the extended critical region as the EoS criterion. The ranges of density and temperature of the extended critical region for each compound are given also in Table 1. The MRD(ρ) values obtained for the liquid phase of the systems studied by us, MRD(ρ) = 0.05%, are similar to those from literature.[3−6] However, if we calculate the deviation for all the phases, we found higher values of MRD(ρ). As an example, the absolute deviations ($\rho_{exp} - \rho_{EoS}$) for ethane at three near critical temperatures are presented in Figure 3.

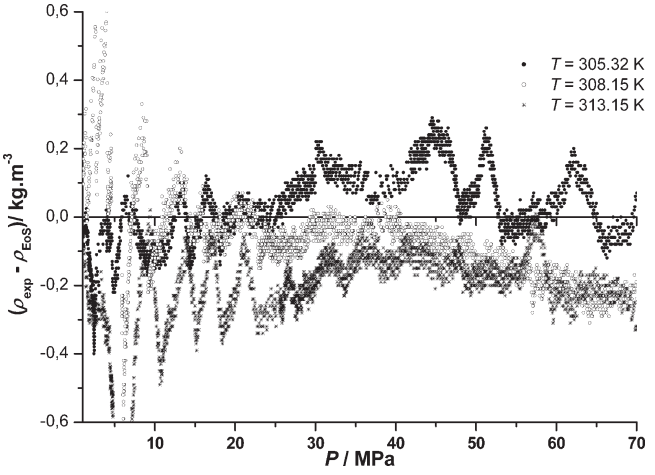

Figure 3. Absolute deviations between experimental density data of ethane at several temperatures and those from the reference EOS of Buecker and Wagner[7] and Friend et al.[8]

In order to determine the accuracy in the densities of pure compounds measured using our setup, the density of carbon dioxide was determined at 273.15, 304.21, and 353.15 K up to 70 MPa. Each isotherm was measured three times. The relative mean standard deviation, $\overline{S}^r_\rho$, (eq A.2) obtained was 0.05% in density and 0.3% in pressure. The later value is obtained within the extended critical region, which comprises densities from 200 to 680 kg/m^3 and temperatures from 298 to 365 K.

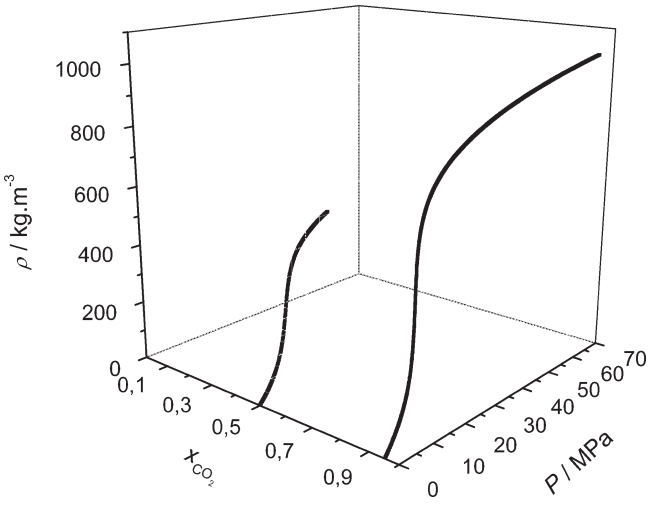

Figure 4. Experimental densities of $\{CO_2$ (1) + C_2H_6 (2)$\}$ binary mixtures at T = 308.15 K and several pressures..

Experimental Results and Precision for Binary Mixtures. To develop the optimal method for the determination of the densities of binary mixtures, and to evaluate the precision and accuracy in density results, the carbon dioxide + ethane system was studied at T = 308.15 K, with x_{CO_2} = 0.4999 up to 20 MPa and with x_{CO_2} = 0.9540 up to 70 MPa, and the results were compared with those from the reference EoS.[1] The MRDs(ρ) obtained were 0.7% for the mixture with x_{CO_2} = 0.4999 and 0.2% for x_{CO_2} = 0.9540. We have performed the precision study in two different ranges of pressure with the aim to observe the influence of high pressures on the precision obtained for density. These values of MRD(ρ) are comparable with those from experimental values used for EoS development. The mixtures are generated as explained above and each isotherm is measured twice times in order to determine the accuracy, expressed as the relative mean standard deviation, $\overline{S}^{r}_{\rho}$. The results are 0.13% for x_{CO_2} = 0.4999 and 0.06% for x_{CO_2} = 0.9540. The experimental values of the density for both mixtures are shown in Figure 4.

Measurement of Speed of Sound. The apparatus, shown in Figure 5, is a complete system for making speed-of-sound measurements in homogeneous liquids with viscosities up to 100 mPa s and may also be suitable for compressed gases, provided that the density of the gas is sufficiently high. It works over a range of temperatures and pressures from 273.15 K up to 473.15 K and from atmospheric pressure to 200 MPa. The apparatus is based on the method and detailed design published previously[10,11] and employs a 5 MHz pulsed ultrasonic system that allows accurate measurements of the speed of sound in compressed fluids.

The device was tested with deionized (Milli Q) and degassed water. The temperature was controlled at 298.12 K for the purpose of instrument calibration. The measured delay time between the two echos at T = 298.12 K and P = 1.00 MPa was 13.245 μs. Under those conditions of temperature and pressure, the value of the speed of sound from the IAPWS-95 EoS[12] is 1498.13 m s^{-1}; therefore, and the path length was calculated to be $L_0 = 19.84 \times 10^{-3}$ m. These calibration data were incorporated into the control program and then, the sound-speed of deionized and degassed water was measured at temperatures from 280.13 to 463.26 K at pressures from 1.0 to 190.0 MPa. The results obtained are represented in Figure 6a.

The repeatability (accuracy) of the u, T, p, quantities was $\pm$0.02 ms^{-1}, $\pm$0.005 K, and $\pm$0.005 MPa, respectively. The experimental values of speed of sound obtained for water were compared with those from the reference EoS,[12] and the precision (MRD(u)) obtained was better than 0.06%. The values of MRD(u) obtained in this work are comparable with those from the literature[13−23] determined with pulsed ultrasonic systems operating in most of the cases up to pressures lower than those reached in this work. Using the same technique, Gedanitz et al.[24] measured sound velocity in fluids up to 30 MPa in the temperature range between 250 and 350 K, and the deviations observed in their measurements are better than those given above.

In order to verify the adequate operation of the installation for some compressed gases, speeds of sound of pure ethane (purity of 99.995%) have been determined from 273.19 to 423.21 K at pressures up to 170.0 MPa. These data cover a wide range of pressures (from 36.8 to 170.0 MPa) for which we have not found ethane's speed of sound of in the literature.[17,25−31] Experimental data and values for MRD obtained from comparison between our experimental speeds of sound for ethane and those calculated with the reference EoS[7] are presented in Table 2 and represented in Figure 6b. The MRD(u) values are higher than those calculated for water; this can be due to the wide range of speeds of sound measured for ethane (from 538.15 to 1774.91 ms^{-1}) in comparison with a relatively narrow range for water (from 1435.81 to 1845.40 ms^{-1} only).

DERIVATED PROPERTIES AND DISCUSSION

Isothermal Compressibility. From the P-ρ-T experimental values of CO_2 and C_2H_6, we have evaluated the effect of pressure on the density by means of the isothermal compressibility κ_T, defined as

$$\kappa_T = \left(\frac{1}{\rho}\right)\left(\frac{\partial \rho}{\partial P}\right)_T \quad (1)$$

We have compared our values with those obtained from their respective EoS.[1,7,8] The mean relative deviation, MRD(κ_T), is better than 1.5% over the entire pressure and temperature ranges. Some of our results are shown in Tables 3 and 4. In general, the value of the isothermal compressibility, as well as its dependence on temperature and pressure for both compounds is quite similar, as can be appreciated in Figure 7, panels a and b. The behavior of the isothermal compressibility over the pressure and temperature ranges studied is the following:

- The isothermal compressibility increases when the temperature increases, at pressures below the critical pressure in the liquid phase, but decreases slowly with the increase of temperature in the gas phase.
- If the pressure is slightly greater than the critical pressure, κ_T in the liquid phase will increase when temperature is increased until it reaches a maximum, near the critical temperature. After this maximum the value of the isothermal compressibility (of this supercritical phase), decreases slowly, showing higher values than those of the liquid phase.
- If the pressure is much greater than the critical pressure, the isothermal compressibility increases slowly with temperature along the isobar, showing values similar to those of the liquid phase.

In our current study, the behavior of the isothermal compressibility on the subcritical, critical and supercritical isotherms has

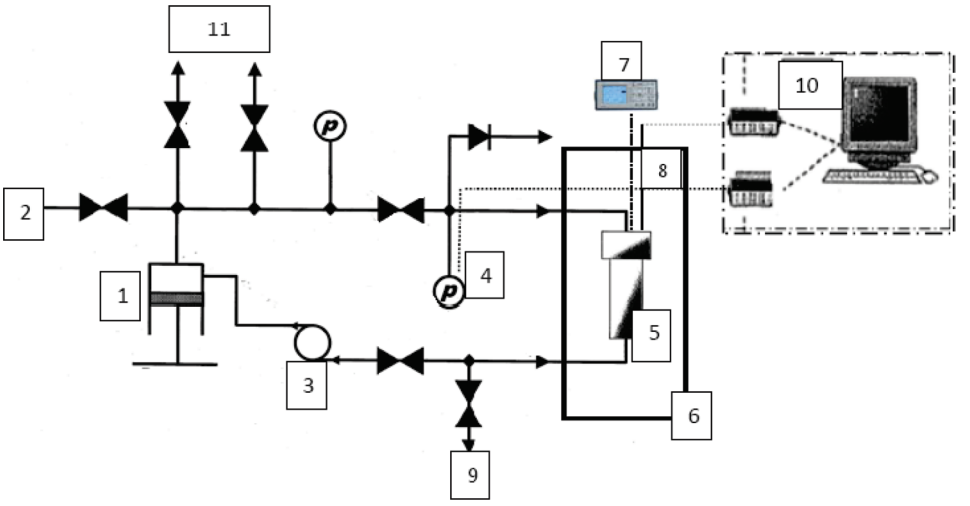

Figure 5. Experimental setup to measure speed of sound at high pressure of pure and binary mixtures: (1) pressure generator, (2) fluid inlet, (3) circulation pump, (4) pressure transducer, (5) pressure vessel, (6) liquid thermoregulated bath, (7) oscilloscope, (8) platinum temperature probe, (9) drain line, (10) evaluation unit and data acquisition, and (11) clean and vacuum line.

been verified. We have observed a discontinuity in the value of this property as the system approaches the liquid−vapor equilibrium. The liquid phase values for κ_T are 10^{-2} or 10^{-3} times those of the gas phase. At the critical isotherms (of CO_2 and C_2H_6), we have verified the very high value of the compressibility of these fluids in the regions around their respective critical points. At the critical point, the very high susceptibility of the density to small variations of pressure generates strong density fluctuations at the microscopic level.[32−34] The presence of such microscopic density inhomogeneities has significant consequences for the structure of compressible supercritical solutions, when they're used as SCF solvents. At the critical point, $\kappa_T \rightarrow \infty$, but when the pressure is increased to about 10 MPa, the isothermal compressibility values are similar of those of the liquid phase.

At 308.15 K, a supercritical temperature for both fluids, but still near their critical temperatures, the isothermal compressibility behavior is similar to the critical isotherms with the exception of the maximum value of the compressibility; in this case κ_T exhibits a finite value.

About 340 K, the maximum on κ_T disappears, and at even greater temperatures κ_T will always decrease as the pressure increases, reaching values similar to those of the liquid phase. In the condensed phases, we observed that when the temperature is increased, the compressibility of the compound increases, because the cohesion forces between molecules diminish, favoring the randomness of the molecular distribution and increasing the intermolecular distances. On the contrary, an increase in pressure has the opposite effect.

Isobaric Thermal Expansivity. From the *P*-ρ-*T* experimental values of CO_2 and C_2H_6, we have evaluated the effect of temperature on the density by means of the isobaric thermal expansivity, α_p, defined as

$$\alpha_p = -\left(\frac{1}{\rho}\right)\left(\frac{\partial \rho}{\partial T}\right)_p \qquad (2)$$

We have compared our values with those obtained from their respective EoS[1,7,8] and the mean relative deviation, MRD(α_P), is better than 5% for CO_2 and better than 7.5% for C_2H_6, over the entire pressure and temperature ranges, as shown in Tables 3 and 4.

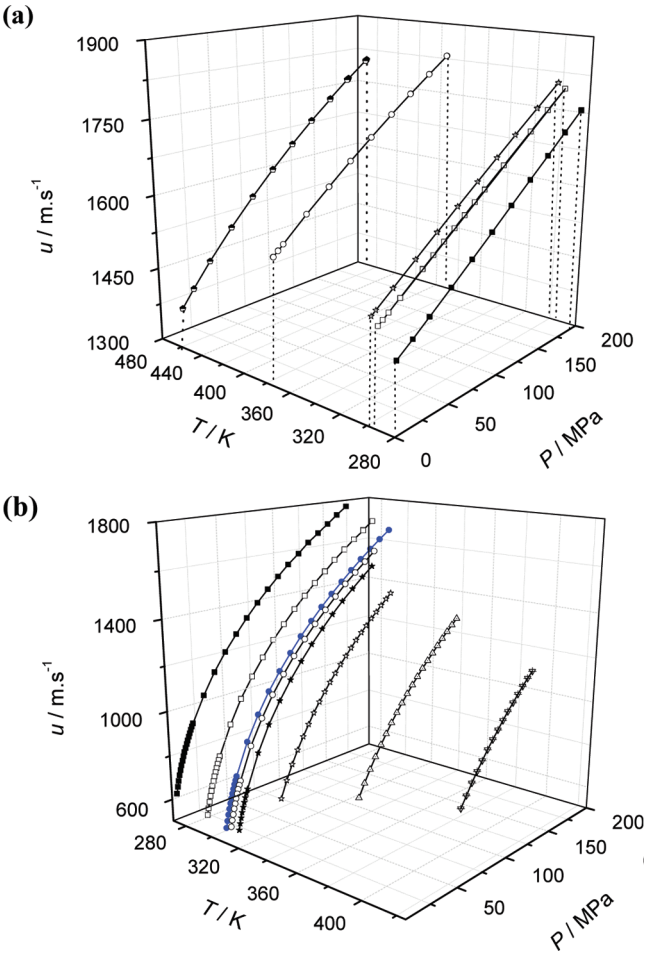

Figure 6. *u*−*T*−*P* representation for (a) water and (b) ethane at several pressures and temperatures; (symbols) experimental values and (lines) EoS. The critical isotherm for ethane is represented by blue dots.

The MRD(α_P) for ethane is higher due to the small number of experimental isotherms in the same range of studied temperature.

dx.doi.org/10.1021/jp202317n |J. Phys. Chem. B 2011, 115, 8216–8230

Table 2. Speed of Sound Experimental Data, u, for C_2H_6 at Several Pressures and Temperatures

T = 273.15 K		T = 293.15 K		$T = T_c(C_2H_6)$ = 305.32 K		T = 308.15 K	
P/MPa	u/m s^{-1}	P/MPa	u/m s^{-1}	P/MPa	u/m s^{-1}	P/MPa	u/m s^{-1}
3.93	632.6	7.94	572.2	9.94	538.1	10.94	547.5
4.93	661.2	8.89	599.9	10.94	567.0	11.93	574.7
5.93	687.1	9.93	627.4	11.94	593.3	12.93	599.4
6.92	710.8	10.94	651.5	12.93	617.2	13.94	622.9
7.93	732.8	11.93	673.9	13.94	639.8	14.93	644.2
8.94	753.7	12.93	694.5	14.94	660.7	15.94	660.0
9.93	772.5	13.93	714.2	15.93	680.2	16.93	683.7
10.92	790.7	14.94	732.8	16.93	698.9	17.93	701.8
11.92	808.1	15.94	750.6	17.94	717.0	18.93	719.1
12.93	824.6	16.93	767.2	18.93	733.8	19.93	735.6
13.94	840.6	17.93	783.5	19.93	749.9	29.93	872.6
14.94	855.9	18.94	798.7	29.94	885.0	39.93	978.3
15.94	870.5	19.93	813.6	39.93	989.3	49.94	1066.5
16.94	884.7	29.94	939.4	49.93	1076.8	59.94	1142.9
17.93	898.6	39.94	1038.9	59.94	1152.7	69.93	1210.8
18.93	911.7	49.93	1123.0	69.93	1220.4	79.94	1272.5
19.94	924.5	59.93	1196.0	79.93	1281.8	89.94	1329.6
29.94	1035.8	69.93	1262.3	89.93	1338.4	99.94	1381.8
39.95	1127.0	79.94	1321.4	99.93	1390.7	109.94	1431.2
49.93	1205.0	89.94	1377.7	109.93	1439.8	119.94	1477.8
59.93	1274.1	99.93	1428.1	119.93	1486.1	129.91	1521.4
69.93	1336.2	109.93	1476.7	129.94	1529.7	139.95	1563.2
79.94	1393.5	119.97	1520.2	139.93	1571.3	149.93	1603.0
89.94	1446.4	129.93	1565.4	149.92	1610.7		
99.95	1495.2	139.94	1605.6	159.94	1648.5		
109.93	1541.2	140.02	1604.8	169.92	1684.5		
120.18	1584.1	149.94	1645.1				
130.14	1628.4	159.89	1679.8				
140.10	1665.9	169.92	1718.1				
149.96	1701.9						
159.86	1739.4						
169.94	1774.9						
MRD(u) = 0.16%		MRD(u) = 0.12%		MRD(u) = 0.12%		MRD(u) = 0.10%	

T = 313.15 K		T = 333.15 K		T = 373.15 K		T = 423.15 K	
P/MPa	u/m s^{-1}	P/MPa	u/m s^{-1}	P/MPa	u/m s^{-1}	P/MPa	u/m s^{-1}
11.94	543.0	24.94	703.0	39.94	767.4	54.84	807.8
12.93	569.9	29.93	772.5	44.92	819.2	59.87	849.7
13.93	593.5	34.92	833.1	49.94	867.2	65.01	889.8
14.93	616.2	39.92	887.0	54.93	911.2	69.96	926.6
15.93	637.4	44.94	936.2	59.94	952.3	74.83	960.4
16.93	657.3	49.94	981.1	64.93	990.9	79.91	994.9
17.93	676.2	54.93	1022.9	69.93	1027.6	84.91	1027.1
18.94	694.2	59.93	1061.9	74.94	1062.2	89.94	1057.7
19.96	711.3	64.93	1098.4	79.94	1095.0	94.93	1087.4
29.94	851.3	69.93	1133.2	84.93	1126.5	99.94	1115.5
39.94	959.3	74.93	1166.2	89.94	1156.5	104.94	1143.3
49.99	1048.9	79.93	1197.5	94.93	1185.4	109.94	1169.6
59.93	1126.0	84.93	1227.8	99.93	1213.3	114.93	1195.4
69.93	1194.8	89.94	1256.7	104.93	1240.1	119.93	1220.4
79.94	1257.0	94.93	1284.4	109.93	1266.1	124.93	1243.0

dx.doi.org/10.1021/jp202317n |J. Phys. Chem. B 2011, 115, 8216–8230

Table 2. Continued

T = 313.15 K		T = 333.15 K		T = 373.15 K		T = 423.15 K	
P/MPa	u/m s^{-1}	P/MPa	u/m s^{-1}	P/MPa	u/m s^{-1}	P/MPa	u/m s^{-1}
89.93	1314.3	99.93	1311.3	114.93	1291.1		
99.93	1367.4	104.93	1337.2	119.94	1315.5		
109.93	1416.2	109.94	1362.1	124.91	1339.1		
119.93	1461.7	114.93	1386.4	129.94	1361.9		
129.99	1505.9	119.94	1409.9	134.85	1384.2		
139.92	1546.7	124.94	1433.1				
		129.93	1455.2				
MRD(u) = 0.06%		MRD(u) = 0.05%		MRD(u) = 0.06%		MRD(u) = 0.13%	

Table 3. Isothermal Compressibility, κ_T, Isobaric Thermal Expansivity, α_P, and Internal Pressure, π_i, for CO_2 at Several Pressures and Temperatures

P/MPa	κ_T/MPa^{-1}	α_P/K^{-1}	π_i/MPa	κ_T/MPa^{-1}	α_P/K^{-1}	π_i/MPa
	T = 253.15 K			T = 304.21 K		
0.2	5.10	4.1×10^{-3}		4.90	3.4×10^{-3}	
2.5	4.48×10^{-3}	4.4×10^{-3}	248	4.65×10^{-1}	5.6×10^{-3}	
5	3.90×10^{-3}	4.4×10^{-3}	281	3.10×10^{-1}	1.2×10^{-2}	
7	3.66×10^{-3}	4.1×10^{-3}	281	5.45×10^{-1}	3.5×10^{-2}	
7.5	3.61×10^{-3}	3.9×10^{-3}	267	5.80×10^{-1}	2.0×10^{-1}	41
10	3.26×10^{-3}	3.7×10^{-3}	282	3.32×10^{-2}	1.4×10^{-2}	116
20	2.48×10^{-3}	3.2×10^{-3}	310	8.35×10^{-3}	5.4×10^{-3}	177
30	2.03×10^{-3}	2.8×10^{-3}	323	5.07×10^{-3}	4.0×10^{-3}	207
40	1.73×10^{-3}	2.5×10^{-3}	334	3.58×10^{-3}	3.4×10^{-3}	247
50	1.51×10^{-3}	2.3×10^{-3}	345	2.80×10^{-3}	2.8×10^{-3}	254
60	1.34×10^{-3}	2.2×10^{-3}	353	2.34×10^{-3}	2.5×10^{-3}	265
70	1.22×10^{-3}	2.0×10^{-3}	356	1.99×10^{-3}	2.3×10^{-3}	277
	T = 308.15 K			T = 423.15 K		
0.2	5.00	3.4×10^{-3}		5.30	2.3×10^{-3}	
2.5	4.60×10^{-1}	5.0×10^{-3}		4.15×10^{-1}	3.0×10^{-3}	
5	2.98×10^{-1}	9.3×10^{-3}		2.15×10^{-1}	3.7×10^{-3}	
7	3.60×10^{-1}	2.8×10^{-2}		1.58×10^{-1}	1.9×10^{-3}	
7.5	5.27×10^{-1}	1.9×10^{-1}	20	1.48×10^{-1}	1.8×10^{-3}	4
10	5.27×10^{-2}	2.0×10^{-2}	106	1.15×10^{-1}	3.6×10^{-3}	4
20	9.49×10^{-3}	5.6×10^{-3}	163	5.65×10^{-2}	4.2×10^{-3}	3
30	5.45×10^{-3}	4.1×10^{-3}	200	2.84×10^{-2}	5.6×10^{-3}	12
40	3.82×10^{-3}	3.3×10^{-3}	227	1.55×10^{-2}	4.5×10^{-3}	54
50	2.98×10^{-3}	2.8×10^{-3}	244	9.90×10^{-3}	3.6×10^{-3}	82
60	2.44×10^{-3}	2.5×10^{-3}	259	7.02×10^{-3}	3.4×10^{-3}	103
70	2.09×10^{-3}	2.3×10^{-3}	268	5.33×10^{-3}	2.4×10^{-3}	121
MRD(κ_T) = 1.2%; MRD(α_P) = 5%; MRD(π_i) = 7%						

Table 4. Isothermal Compressibility, κ_T, Isobaric Thermal Expansivity, α_P, and Internal Pressure, π_i, for C_2H_6 at Several Pressures and Temperatures

P/MPa	κ_T/MPa^{-1}	α_P/K^{-1}	π_i/MPa	κ_T/MPa^{-1}	α_P/K^{-1}	π_i/MPa
	T = 253.15 K			T = 305.32 K		
0.2	5.50	4.5×10^{-3}		5.27	4.2×10^{-3}	
2.5	7.08×10^{-3}	4.3×10^{-3}	152	5.22×10^{-1}	8.2×10^{-3}	
4	6.37×10^{-3}	4.1×10^{-3}	160	5.50×10^{-1}	1.4×10^{-2}	
5	5.97×10^{-3}	3.9×10^{-3}	161	4.36×10^{-1}	9.2×10^{-2}	59
5.5	5.79×10^{-3}	3.8×10^{-3}	162	1.17×10^{-1}	2.2×10^{-2}	52
10	4.58×10^{-3}	3.2×10^{-3}	169	1.92×10^{-2}	6.4×10^{-3}	92
20	3.24×10^{-3}	2.5×10^{-3}	178	7.40×10^{-3}	3.3×10^{-3}	118
30	2.53×10^{-3}	2.1×10^{-3}	185	4.73×10^{-3}	2.7×10^{-3}	142
40	2.07×10^{-3}	1.9×10^{-3}	192	3.49×10^{-3}	2.2×10^{-3}	152
50	1.77×10^{-3}	1.7×10^{-3}	195	2.80×10^{-3}	1.9×10^{-3}	162
60	1.56×10^{-3}	1.6×10^{-3}	193	2.32×10^{-3}	1.8×10^{-3}	174
70	1.38×10^{-3}	1.4×10^{-3}	195	2.00×10^{-3}	1.7×10^{-3}	186
	T = 308.15 K			T = 423.15 K		
0.2	5.10	4.1×10^{-3}		5.40	2.5×10^{-3}	
2.5	5.22×10^{-1}	6.8×10^{-3}		4.26×10^{-1}	3.5×10^{-3}	
4	4.60×10^{-1}	1.3×10^{-2}		2.76×10^{-1}	3.5×10^{-3}	
5	1.24	1.8×10^{-1}	40	2.27×10^{-1}	4.0×10^{-3}	2
5.5	2.66×10^{-1}	5.8×10^{-2}	62	2.09×10^{-1}	4.3×10^{-3}	3
10	2.18×10^{-2}	6.8×10^{-3}	86	1.21×10^{-1}	5.5×10^{-3}	9
20	7.74×10^{-3}	3.4×10^{-3}	116	4.05×10^{-2}	5.7×10^{-3}	39
30	4.89×10^{-3}	2.7×10^{-3}	126	1.68×10^{-2}	3.7×10^{-3}	63
40	3.57×10^{-3}	2.2×10^{-3}	149	9.47×10^{-3}	2.8×10^{-3}	85
50	2.83×10^{-3}	1.9×10^{-3}	158	6.55×10^{-3}	2.3×10^{-3}	98
60	2.35×10^{-3}	1.8×10^{-3}	171	4.86×10^{-3}	2.0×10^{-3}	113
70	2.04×10^{-3}	1.6×10^{-3}	178	3.89×10^{-3}	1.8×10^{-3}	122
MRD(κ_T) = 1.2%; MRD(α_P) = 7.4%; MRD(π_i) = 8%						

Again, the values of the isobaric thermal expansivity for both compounds, as well as its dependence on the temperature and pressure, are quite similar. They are shown in Figure 8, panels a and b. For both carbon dioxide and ethane, the values of α_p are of the same order for the two phases, liquid and gas. The dependence on the temperature along the isobars for α_p is the same as k_T, throughout the range of pressures studied.

When the isobaric thermal expansivity, α_p, was analyzed along the subcritical isotherms, it was found that it increases with pressure in the gas phase but decreases in the liquid phase, showing a small discontinuity upon reaching the VLE.

Also $\alpha_p \rightarrow \infty$ at the critical point, and for both critical isotherms, the higher calculated value for α_p were found near their respective critical pressures. Later, α_p decreases slowly when pressure increases.

The behavior of the isobaric thermal expansivity, for the supercritical isotherms of both components, is quite similar to their respective critical isotherms, and with the exception of the maximum value of the expansivity α_p is a finite value which decreases when the temperature is increased.

Internal Pressure, π_i. Internal pressure, π_i, was defined[35] as a macroscopic property used for estimating the dispersion element of cohesion of liquids and reflecting molecular ordering. Its role

dx.doi.org/10.1021/jp202317n |J. Phys. Chem. B 2011, 115, 8216–8230

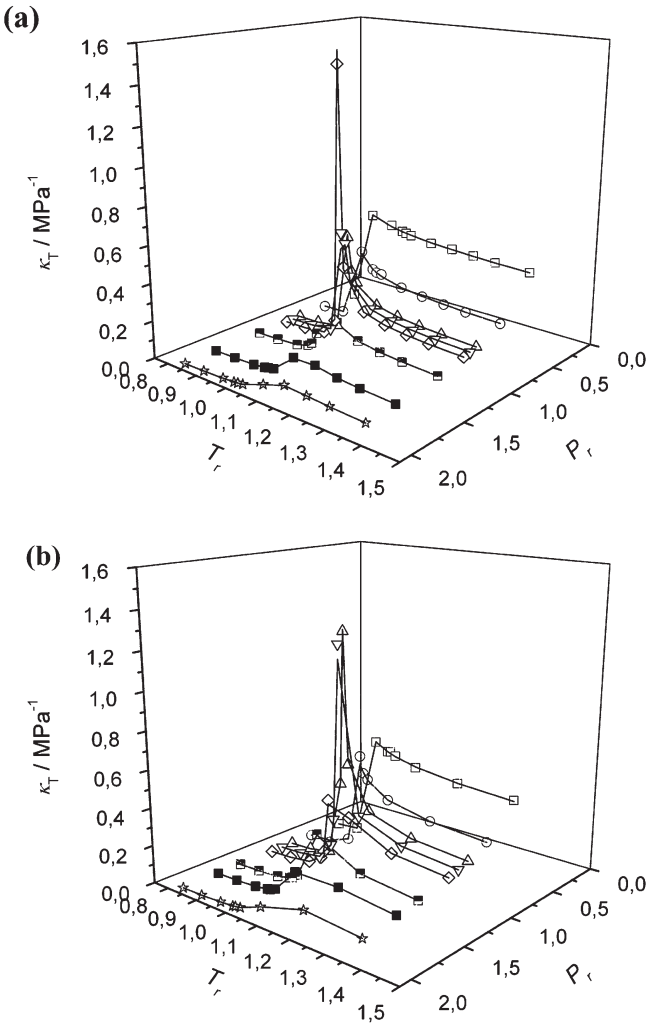

Figure 7. $\kappa_T - T_r - P_r$ representation for (a) carbon dioxide and (b) ethane; (symbols) experimental values and (lines) EoS.

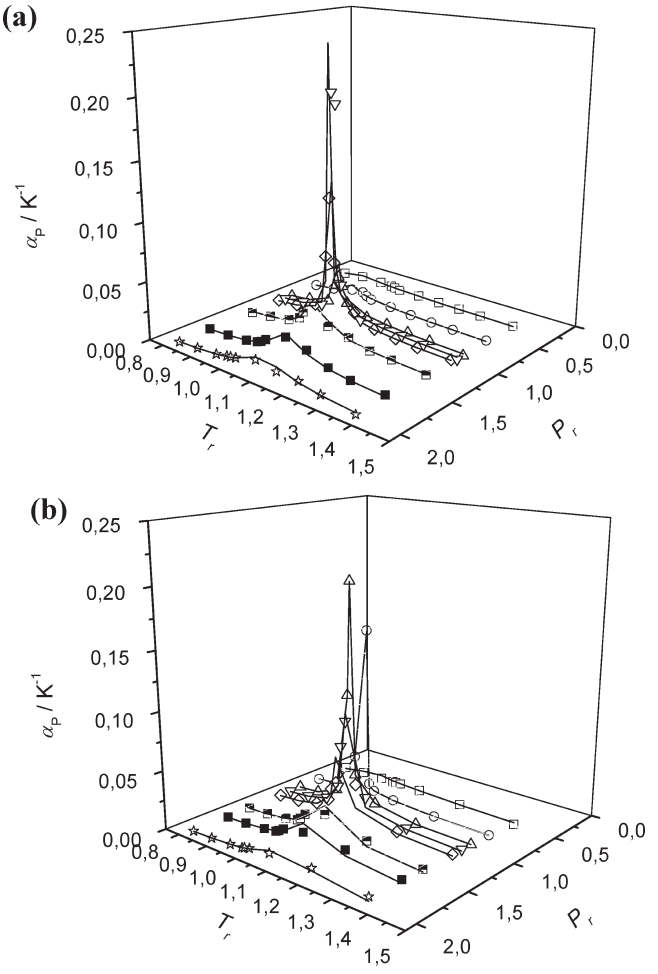

Figure 8. $\alpha_P - T_r - P_r$ representation for (a) carbon dioxide and (b) ethane; (symbols) experimental values and (lines) EoS.

in thermodynamics of liquid solutions was defined by Hildebrand. Internal pressure is understood to be a fundamental property used in the calculation of the energy of cavity formation.

The Internal pressure is closely related to different properties of liquids, such as ultrasonic velocity, free volume, viscosity, surface tension, and density.[36]

The precise meaning of the internal pressure is ilustrated in the following thermodynamic relation:

$$\pi_i = \left(\frac{\partial U}{\partial V}\right)_T = T\left(\frac{\partial P}{\partial T}\right)_V - P \qquad (3)$$

and combining eqs 1 and 2

$$\pi_i = T\left(\frac{\alpha_p}{\kappa_T}\right) - P \qquad (4)$$

Some of the values obtained for the internal pressure at different pressures and temperatures, and their comparison with those calculated with the corresponding reference EoS[1,7,8] are presented in Tables 3 and 4; The mean relative deviation, MRD(π_i), obtained is 7% for CO_2 and 8% for C_2H_6, respectively. Supercritical fluids may be considered as high-density condensed matter, and one of their greatest advantage has been the possibility to be described far above their critical temperatures (around 100 K); in view of this we have enlarged the internal pressure study to the supercritical region.

The internal pressure for the CO_2 and C_2H_6 decreases when temperature rises along isobars, Figure 9, panels a and b; this could mean that cohesive forces decrease when temperature increases. At the critical temperature, and above it, the internal pressure vanishes at the critical pressure or near it. On the other hand, the internal pressure increases when the pressure rises along isotherms, Figure 10, panels a and b.

The behavior of κ_T and α_p for carbon dioxide and ethane is similar, but values of the internal pressure for these two compounds are quite different. Thus, in the liquid region, and through the whole range of temperatures and pressures studied, the π_i values for CO_2 are much higher than those for ethane, but theses differences diminish at high temperatures in the supercritical region.

The internal pressure value for carbon dioxide is abnormally high if we compare it with that for ethane or propane. Although CO_2 has a zero dipole moment, the carbon atom in a CO_2 molecule is electron deficient, whereas the oxygen has two lone pairs of electrons; it is a charge-separated molecule with significant nonzero bond dipole moments. This charge separation results in a significant quadrupole moment; CO_2 is thus described as a quadrupolar solvent.[37,38]

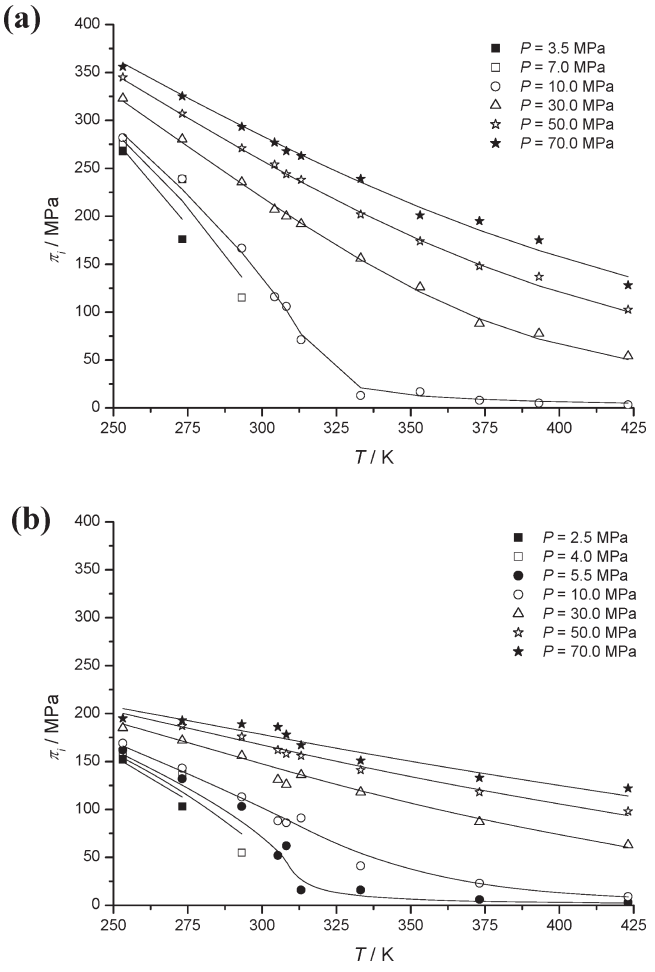

Figure 9. Representation of internal pressure, π_i, versus temperature, T, for (a) carbon dioxide (P_c = 7.383 MPa, T_c = 304.21 K) and (b) ethane (P_c = 4.882 MPa, T_c = 305.32 K); (symbols) experimental values and (lines) EoS.

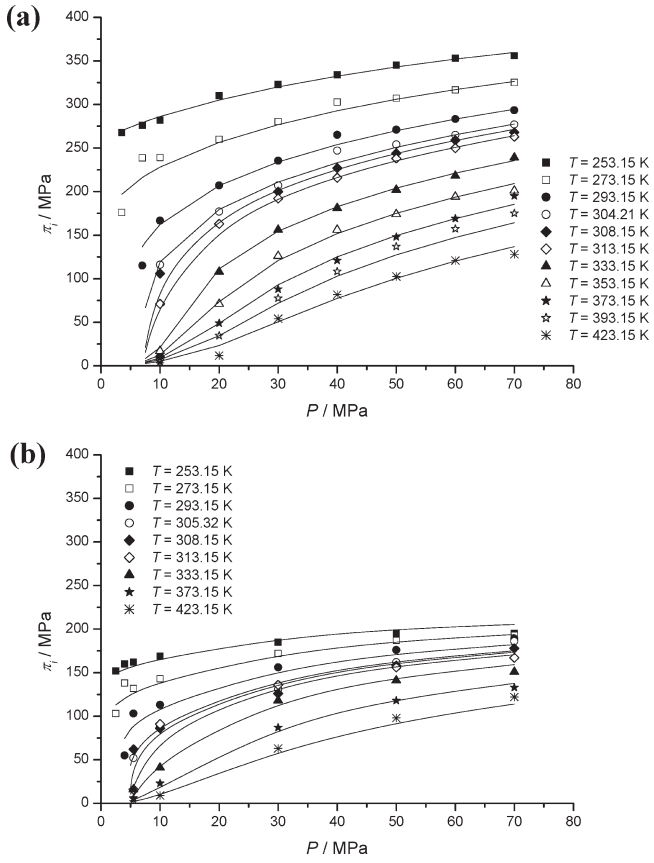

Figure 10. Representation of internal pressure, π_i, versus pressure, P, for (a) carbon dioxide (P_c = 7.383 MPa, T_c = 304.21 K) and (b) ethane (P_c = 4.882 MPa, T_c = 305.32 K); (symbols) experimental values and (lines) EoS.

Different authors have studied the microscopic structure of liquid and supercritical CO_2.[39−50] The aim of most of these papers was to determine the pair correlation function, and in some, an attempt was made to provide a qualitative description of local orientations. Different arrangements (parallel, cross-shaped, T-shaped, and chain-like arrangements) were identified, and different regions of the $T-P$ plane were mapped with varied orientational correlations: some of the authors matched the T-shaped arrangements with high density regions, others found parallel-arrangements in these areas. Generally, results from different authors are not in complete accordance. In our current study we have not been able to establish a direct correlation between the different arrangements and internal pressure.

Kartsev[51] indicates that the derivative $(\partial\pi_i/\partial T)_P$ is related to the structural organization of the fluids. Thus, according to the sign of the slope of the π_i versus T curve, liquids can be classified into two structural groups: Those fluids being $(\partial\pi_i/\partial T)_P < 0$, namely, non- or weakly associate fluids, and those being $(\partial\pi_i/\partial T)_P > 0$, the associated fluids, which have molecules linked by hydrogen bonds. For the last group, as the degree and the stability of the association increases, the slope also increases. In our study, $(\partial\pi_i/\partial T)_P$ are negative for both CO_2 and C_2H_6, and

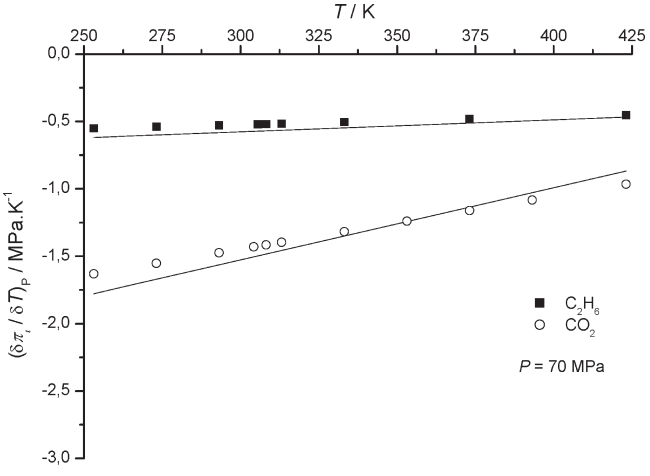

Figure 11. Thermal coefficient, $(\partial\pi_i/\partial T)_P$, versus temperature, T, for CO_2 and C_2H_6 compounds; (symbols) experimental values and (lines) EoS.

according to this classification, both fluids are weakly associated, with the CO_2 showing a steeper slope than that of C_2H_6. This fact is due to the differences between the values of the dipole and cuadrupole moments of these compounds.[37,52,53] Figure 11

dx.doi.org/10.1021/jp202317n |J. Phys. Chem. B 2011, 115, 8216–8230

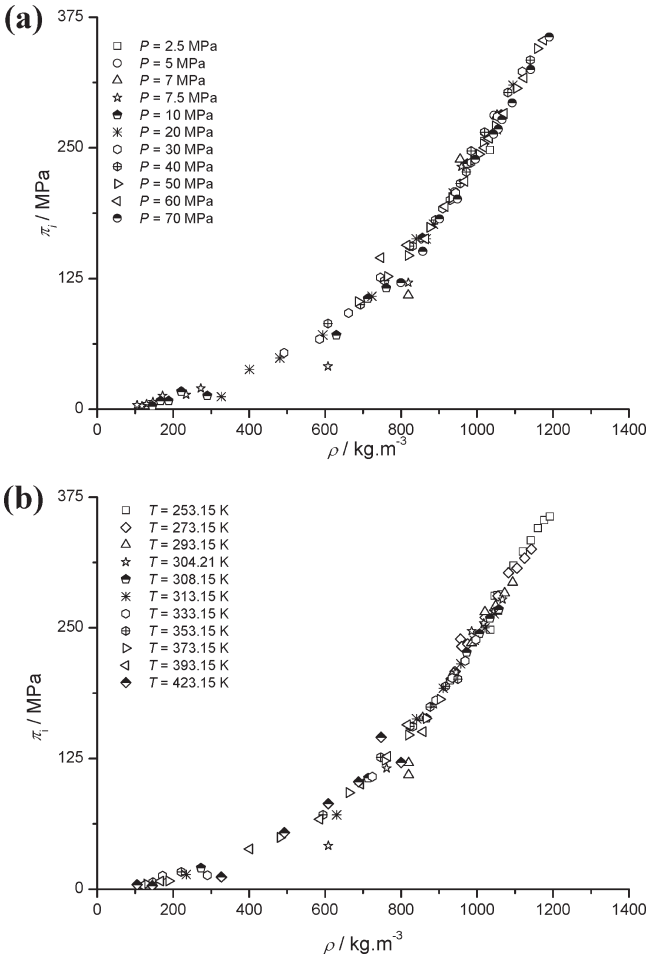

Figure 12. Representation of internal pressure, π_i, versus density, ρ, for CO_2; (a) isobar and (b) isotherm.

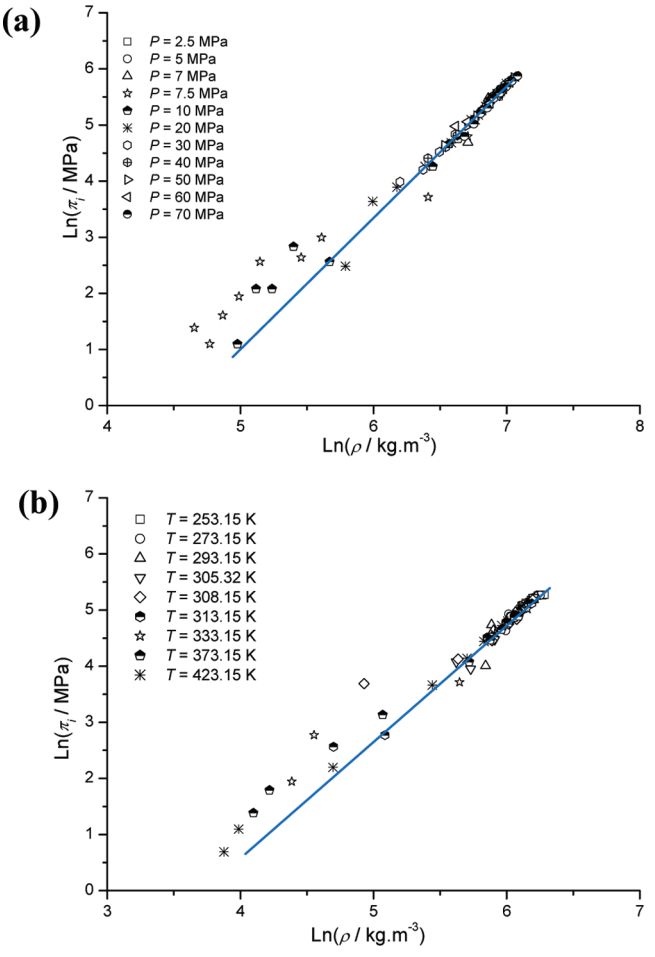

Figure 13. Representation of $\ln(\pi_i)-\ln(\rho)$ for (a) carbon dioxide (P_c = 7.383 MPa, T_c = 304.21 K) and (b) ethane (P_c = 4.882 MPa, T_c = 305.32 K); (symbols) experimental values.

shows the variation of the internal pressure coefficient for CO_2 and C_2H_6, along the 70 MPa isobars.

Finally, the dependence of the internal pressure on the density was analyzed for both fluids. It has been found that as the density increases along an isobar, the internal pressures increases, and does so with the same slope that increases of the density with respect to internal pressure in an isotherm. This can be seen in Figure 12, panels a and b, where we have chosen to show the isobar and isotherm plots for CO_2. However the more surprising result is that different dense states with the same internal pressure values have very similar densities. Different dense states mean states with different pressure or/and temperature and a density equal or greater than the critical density. In Figure 13, panels a and b, we have represented $\ln(\pi_i)$ versus $\ln(\rho)$ for CO_2 and C_2H_6, respectively. The observed deviations from linearity correspond with supercritical states ($T > T_c$ and $P > P_c$) of density smaller than the critical density.

We may thus conclude that the system's internal pressure is directly related to the density of the compound. The values of the internal pressure of the compound (at liquid or supercritical state) will be significant if it has a liquid-like density. On the other hand, if the compound is at its supercritical state, but its density is gas-like, the internal pressure will not be significant.

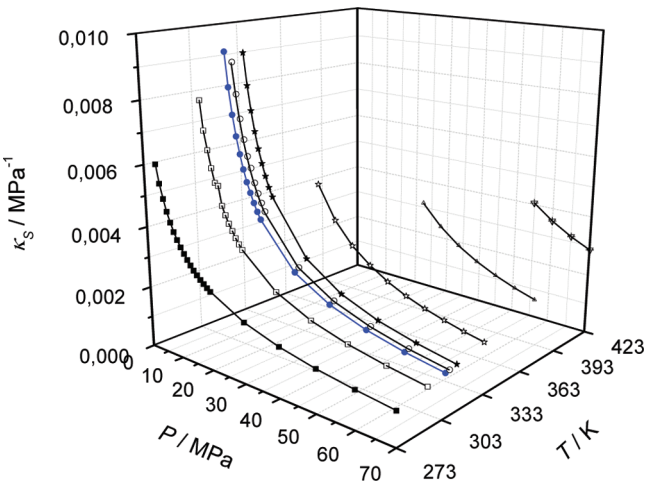

Figure 14. κ_s-P-T representation for ethane at several pressures and temperatures; (symbols) experimental values and (lines) EoS. The critical isotherm for ethane is represented by blue dots.

Isentropic Compressibility, κ_s, and Isobaric Heat Capacity, C_p. The isentropic compressibility, κ_s, for ethane has been

Table 5. Isentropic Compressibility, κ_s, and Isobaric Heat Capacity, C_p, for C_2H_6 at Several Pressures and Temperatures

T = 273.15 K			T = 293.15 K		
P/MPa	κ_s/MPa^{-1}	C_p/kJ kmol^{-1} K^{-1}	P/MPa	κ_s/MPa^{-1}	C_p/kJ kmol^{-1} K^{-1}
3.93	6.10×10^{-3}	132	7.94	7.94×10^{-3}	109
4.93	5.52×10^{-3}	111	8.89	7.02×10^{-3}	112
5.93	5.06×10^{-3}	103	9.93	6.42×10^{-3}	101
6.92	4.68×10^{-3}	100	10.94	5.88×10^{-3}	97
7.93	4.36×10^{-3}	99	11.93	5.44×10^{-3}	95
8.94	4.09×10^{-3}	95	12.93	5.37×10^{-3}	75
9.93	3.87×10^{-3}	93	13.93	4.75×10^{-3}	92
10.92	3.67×10^{-3}	91	14.94	4.47×10^{-3}	90
11.92	3.49×10^{-3}	89	15.94	4.23×10^{-3}	89
12.93	3.33×10^{-3}	88	16.93	4.02×10^{-3}	89
13.94	3.18×10^{-3}	87	17.93	3.83×10^{-3}	88
14.94	3.06×10^{-3}	86	18.94	3.66×10^{-3}	87
15.94	2.94×10^{-3}	86	19.93	3.51×10^{-3}	91
16.94	2.83×10^{-3}	85	29.94	2.50×10^{-3}	83
17.93	2.73×10^{-3}	84	39.94	1.98×10^{-3}	77
18.93	2.64×10^{-3}	82	49.93	1.64×10^{-3}	79
19.94	2.56×10^{-3}	85	59.93	1.42×10^{-3}	74
29.94	1.96×10^{-3}	79	69.93	1.25×10^{-3}	79
39.95	1.61×10^{-3}	75			
49.93	1.38×10^{-3}	75			
59.93	1.21×10^{-3}	74			
69.93	1.08×10^{-3}	72			

T = 305.32 K			T = 308.15 K		
P/MPa	κ_s/MPa^{-1}	C_p/kJ kmol^{-1} K^{-1}	P/MPa	κ_s/MPa^{-1}	C_p/kJ kmol^{-1} K^{-1}
9.94	9.37×10^{-3}	103	10.94	9.04×10^{-3}	106
10.94	8.29×10^{-3}	108	11.93	8.07×10^{-3}	103
11.94	7.45×10^{-3}	102	12.93	7.31×10^{-3}	99
12.93	6.80×10^{-3}	96	13.94	6.68×10^{-3}	98
13.94	6.25×10^{-3}	95	14.93	6.17×10^{-3}	96
14.94	5.79×10^{-3}	92	15.94	5.81×10^{-3}	96
15.93	5.41×10^{-3}	92	16.93	5.37×10^{-3}	92
16.93	5.08×10^{-3}	89	17.93	5.05×10^{-3}	92
17.94	4.78×10^{-3}	88	18.93	4.76×10^{-3}	91
18.93	4.53×10^{-3}	88	19.93	4.52×10^{-3}	82
19.93	4.30×10^{-3}	80	29.93	3.02×10^{-3}	82
29.94	2.92×10^{-3}	81	39.93	2.30×10^{-3}	77
39.93	2.24×10^{-3}	77	49.94	1.88×10^{-3}	76
49.93	1.83×10^{-3}	76	59.94	1.59×10^{-3}	79
59.94	1.56×10^{-3}	79	69.93	1.39×10^{-3}	79
69.93	1.36×10^{-3}	82			

T = 313.15 K			T = 333.15 K			T = 373.15 K		
P/MPa	κ_s/MPa^{-1}	C_p/kJ kmol^{-1} K^{-1}	P/MPa	κ_s/MPa^{-1}	C_p/kJ kmol^{-1} K^{-1}	P/MPa	κ_s/MPa^{-1}	C_p/kJ kmol^{-1} K^{-1}
11.94	9.31×10^{-3}	110	24.94	5.18×10^{-3}	89	39.94	4.38×10^{-3}	86
12.93	8.31×10^{-3}	102	29.93	4.13×10^{-3}	85	44.92	3.73×10^{-3}	84
13.93	7.54×10^{-3}	103	34.92	3.45×10^{-3}	86	49.94	3.24×10^{-3}	84
14.93	6.90×10^{-3}	94	39.92	2.97×10^{-3}	84	54.93	2.87×10^{-3}	81
15.93	6.37×10^{-3}	100	44.94	2.61×10^{-3}	79	59.94	2.58×10^{-3}	86
16.93	5.93×10^{-3}	92	49.94	2.33×10^{-3}	77	64.93	2.34×10^{-3}	80
17.93	5.54×10^{-3}	93	54.93	2.11×10^{-3}	78	69.93	2.14×10^{-3}	78

$\mathrm{MRD}(\kappa_s) = 0.19\%$; $\mathrm{MRD}(C_p) = 3\%$

dx.doi.org/10.1021/jp202317n |*J. Phys. Chem. B* 2011, 115, 8216–8230

Table 5. Continued

T = 313.15 K			T = 333.15 K			T = 373.15 K		
P/MPa	κ_s/MPa^{-1}	C_P/kJ kmol^{-1} K^{-1}	P/MPa	κ_s/MPa^{-1}	C_P/kJ kmol^{-1} K^{-1}	P/MPa	κ_s/MPa^{-1}	C_P/kJ kmol^{-1} K^{-1}
18.94	5.21×10^{-3}	93	59.93	1.93×10^{-3}	80			
19.96	4.92×10^{-3}	95	64.93	1.78×10^{-3}	75			
29.94	3.22×10^{-3}	84	69.93	1.65×10^{-3}	71			
39.94	2.42×10^{-3}	81						
49.99	1.96×10^{-3}	76						
59.93	1.66×10^{-3}	78						
69.93	1.44×10^{-3}	74						

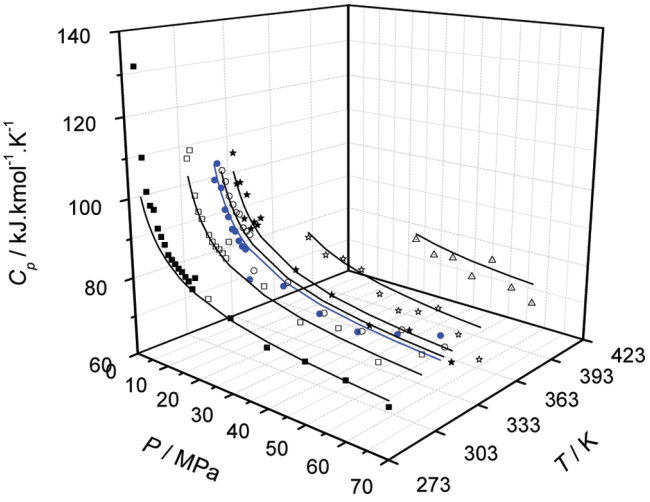

Figure 15. C_P−P−T representation for ethane at several pressures and temperatures; (symbols) experimental values and (lines) EoS. The critical isotherm for ethane is represented by blue dots.

obtained from our experimental density and speed of sound values using the following relationship:

$$\kappa_s = \frac{1}{\rho u^2} \tag{5}$$

The values for this property along with those from the EoS[7] are represented in Figure 14. In Table 5 are presented our κ_s data and the value for MRD(κ_s) obtained from comparison between our data with those obtained with the reference EoS.[7]

Finally, from our experimental density values, ρ, and those calculated for κ_T, α_p, and κ_s (eqs 1, 2, and 5), isobaric heat capacities, C_p, have been obtained for ethane, using the equation

$$C_P = \frac{\alpha^2 T}{\rho(\kappa_T - \kappa_s)} \tag{6}$$

These values along with those from EoS[7] are represented in Figure 15. Buecker and Wagner[7] highlight the scarcity and poor quality of experimental C_p data in the literature[54−62] and point out that it would be desirable to possess isobaric heat capacity data in the gas and also in the supercritical range up to high pressures. However, these requirements are probably unrealistic. In those regions, it may be more important to get good quality $P\rho T$ and speed-of-sound data to fill the gaps mentioned above. The mean relative deviation, MRD(C_p), between our values for C_p and those from EoS[7] is 3% (Table 5); this value is within that of the EoS: the uncertainties in heat capacities range from 2% in the vapor and liquid regions below 450 K and 30 MPa, to 5% at high pressures.

CONCLUSIONS

Quasi-continuous $P\rho T$ data of CO_2, ethane, propane, and the [CO_2 + ethane] mixture have been measured thoughout very broad temperature and pressure ranges. These data have been used to develop an optimal method and to determine the precision for the results obtained. A comparison with data from references EoS and other authors confirm the quality of our experimental setup, as well as its calibration and testing. The value of the mean relative deviation for pure compounds is MRD(ρ) = 0.13% and MRD(P) = 0.17% (in the extended critical region). For binary mixtures the value of the mean relative deviation is MRD(ρ) = 0.70% in the range up 20 MPa and MRD(ρ) = 0.20% in the range up to 70 MPa. As a consequence, the great number of experimental points obtained and their quality has enabled us to determine some derivated properties for CO_2 and ethane with the following precision: MRD(κ_T) =1.5%; MRD-(α_P) = 5% for CO_2 and MRD(α_P) = 7.5% for C_2H_6; MRD(π_i) = 7% for CO_2 and MRD(π_i) = 8% for C_2H_6.

The behavior of the isothermal compressibility on the subcritical, critical and supercritical isotherms has been studied, observing the dissapearance of the κ_T maximum around 340 K. In the condensed phases it is observed that temperature and pressure have opposite effects.

The dependence of α_P on temperature is the same as for κ_T in all range of pressures studied.

Since supercritical fluids may be regarded as high-density condensed matter, we have enlarged the internal pressure study to the supercritical region. In this paper, we have shown that although the values and behavior of κ_T and α_P for CO_2 and ethane are similar the internal pressures for these fluids are very different even though these differences minimize at high temperatures in the supercritical region. In fact, the values of internal pressure for CO_2 are abnormally high in comparison with those for ethane, and their behavior with temperature, given by the temperature coefficient, shows a much steeper slope than that for ethane. This can be explained if we take into account the charge separation in the molecule of CO_2, which shows as a consequence a significant cuadrupolar moment. Furthermore, the dependence of the internal pressure with density was analyzed. We have found that different dense states with the same internal pressure values possess very similar densities. Finally, we conclude that the system's internal pressure will be significant only if the supercritical fluid has density-like liquid.

Additionally, *PuT* values have been determined for water and ethane within a broad range of pressure and temperature, using a device based on a 5 MHz pulsed ultrasonic system. The precision of the experimental data obtained with this apparatus has been determined by comparison between our measured values of speed of sound and those from the reference EoS for water[12] and compressed ethane.[7] The values obtained, given as MRDs, are 0.06% for water and 0.1% for compressed ethane.

From speed of sound and density values, isentropic compressibilities, κ_s, have been obtained for ethane, and with these an our values of ρ, κ_T, and α_P, isobaric heat capacities, C_p, have been calculated and compared with those from EoS;[7] the MRD(C_p) obtained is 3%, which is acceptable since it is within that of the EoS.

APPENDIX A

The mean relative deviation, MRD(x), is calculated as follows:

$$\mathrm{MRD}(x) = \frac{100}{N}\sum_{i=1}^{N}\left|\frac{x_i^{\exp} - x_i^{\mathrm{cal}}}{x_i^{\exp}}\right| \qquad (A.1)$$

where

- $x_i^{\exp}$ experimental value of a point
- x_i^{cal} calculated value for a point
- N number of points

The relative mean standard deviation, $\overline{S}_x^r$ is calculated

$$\overline{S}_x^r = \frac{100}{N_p}\sum_{j=1}^{N_p}({}_jS_x^r) \qquad (A.2)$$

where the relative standard deviation by point is

$${}_jS_x^r = \frac{{}_jS_x}{\frac{1}{n}\sum_{i=1}^{n} x_i^{\exp}} \qquad (A.3)$$

and the standard deviation by point is

$${}_jS_x = \sqrt{\frac{n\sum_{i=1}^{n}(x_i^{\exp})^2 - (\sum_{i=1}^{n} x_i^{\exp})^2}{n(n-1)}} \qquad (A.4)$$

ASSOCIATED CONTENT

Supporting Information. Experimental values of $P-\rho-T$ for pure CO_2, ethane, propane, and binary mixtures [CO_2 + ethane]. This material is available free of charge via the Internet at http://pubs.acs.org.

AUTHOR INFORMATION

Corresponding Author
*E-mail: martal@unizar.es.

ACKNOWLEDGMENT

The authors gratefully acknowledge financial support received from the Ministerio de Educación y Ciencia of Spain (CTQ2005-02213), Ministerio de Ciencia e Innovación (CTQ2008-02037), and Convenio La Caixa - Gobierno de Aragón.

LIST OF SYMBOLS

P	pressure
T	temperature
ρ	density
u	sound-speed
κ_T	isothermal compressibility
α_P	isobaric thermal expansivity
π_i	internal pressure
κ_s	isentropic compressibility
C_p	isobaric heat capacity
EoS	equation of state
MRD	mean relative deviation

REFERENCES

(1) Kunz, O.; Klimeck, R.; Wagner, W.; Jaeschke, M. *GERG Technical Monograph. Fortschr.-Ber.*: VDI, VDI-Verlag: Düsseldorf, 2006.
(2) Bouchot, C.; Richon, D. *Fluid Phase Equilib.* **2001**, *191*, 189.
(3) Outcalt, S. L.; McLinden, M. O *Ind. Eng. Chem. Res.* **2007**, *46*, 8264.
(4) Comuñas, M. J. P.; Bazile, J.-P.; Baylaucq, A.; Boned, C. *J. Chem. Eng. Data* **2008**, *53*, 986.
(5) Segovia, J. J.; Fandiño, O.; López, E. R.; Lugo, L.; Martín, M. C.; Fernández, J. *J. Chem. Thermdyn.* **2009**, *41*, 632.
(6) Schedemann, A.; Ihmels, C.; Gmehling, J. *Fluid Phase Equilib.* **2010**, *295*, 201.
(7) Buecker, D.; Wagner, W. *J. Phys. Chem. Ref. Data* **2006**, *35*, 205.
(8) Friend, D. G.; Ingham, H.; Ely, J. *J. Phys. Chem. Ref. Data* **1991**, *20*, 275.
(9) Lemmon, E. W.; McLinden, M. O.; Wagner, W. *J. Chem. Eng. Data* **2009**, *54*, 3141.
(10) Ball, S. J.; Trusler, J. P. M. *Int. J. Thermophys.* **2001**, *22*, 427.
(11) Dávila, M. J.; Trusler, J. P. M. *J. Chem. Thermodyn.* **2009**, *41*, 35.
(12) Wagner, W.; Pruss, A *J. Phys.Chem. Ref. data* **2002**, *31*, 387.
(13) Van Itterbeek, A.; Van Dael, W. *Physica* **1962**, *28*, 861.
(14) Voronov, F. F.; Pitaevskaya, L. L.; Bilevich, A. V. *Russ. J. Phys. Chem.* **1969**, *43*, 321.
(15) Trusler, J. P. M. *J. Chem. Thermodyn.* **1994**, *26*, 105.
(16) Labes, P.; Daridon, J. L.; Lagourette, B.; H. *Int. J. Thermophys.* **1994**, *15*, 803.
(17) Tsumura, R.; Straty, G. C. *Cryogenics* **1997**, *26*, 195.
(18) Lagourette, B.; Daridon, J. L. *J. Chem. Thermodyn.* **1999**, *31*, 987.
(19) Piñeiro, M. M.; Plantier, F.; Bessières, D.; Legido, J. L.; Daridon, J. L. *Fluid Phase Equilib.* **2004**, *222*−*223*, 297.
(20) Plantier, F.; Danesh, A.; Sohrabi, M.; Daridon, J.-L.; Gozalpour, F.; Todd, A. C. *J. Chem. Eng. Data* **2005**, *50*, 673.
(21) Plantier, F.; Bessières, D.; Daridon, J. L.; Montel, F. *Fuel* **2008**, *87*, 196.
(22) Dzida, M.; Cempa, M. *J. Chem. Thermodyn.* **2008**, *40*, 1531.
(23) Khelladi, H.; Plantier, F. J. L. *J. Accous. Soc. Am.* **2010**, *128*, 672.
(24) Gedanitz, H.; Dávila, M. J.; Baumhögger, E.; Span, R. *J. Chem. Thermodyn.* **2010**, *42*, 478.
(25) Noury, J. *Comptes Rendus* **1952**, *234*, 303.
(26) Terres, E.; Jahn, W.; Reissmann, H. *Brennstoff-Chem.* **1957**, *38*, 129.
(27) Poole, G. R.; Aziz, R. A. *Can. J. Phys.* **1972**, *50*, 721.
(28) Lemming, W., *Fortschr.-Ber.*: VDI, Reihe 19, Nr. 32, VDI-Verlag Dusseldorf, 1989.
(29) Colgate, S. O.; Sivaraman, A.; Dejsupa, C. *Fluid Phase Equilib.* **1992**, *76*, 175.
(30) Estrada-Alexanders, A. F.; Trusler, J. P. M. *J. Chem. Thermodyn.* **1997**, *29*, 991.
(31) Abbaci, A. *J. Mol. Liq.* **2005**, *118*, 31.
(32) Tucker, S. C. *Chem. Rev.* **1999**, *99*, 391.
(33) Nishikawa, K.; Morita, T. *Chem. Phys. Lett.* **2000**, *316*, 238.
(34) Egorov, S. A. *Particle J. Chem. Phys.* **2000**, *112*, 7138.

(35) Ramos Moura, J. J. *J. Sol. Chem.* **1989**, *18*, 957.
(36) Malakondaiah, K.; Kham, V. H.; Subrahmanyam, S. V. *Ind. J. Chem.* **1978**, *16A*, 733.
(37) Reynolds, L.; Gardecki, J. A.; Frankland, S. J. V.; Horng, M. L.; Maroncelli, M. *J. Phys. Chem.* **1996**, *100*, 10337.
(38) Kauffman, J. F. *J. Phys. Chem. A* **2001**, *105*, 3433.
(39) Van Tricht, J. B.; Frederikze, H.; van der Laan, J. *Mol. Phys.* **1984**, *52*, 115.
(40) Adya, A. K.; Wormald, C. J. *Mol. Phys.* **1991**, *74*, 735.
(41) Bausenwein, T.; Bertagnolli, H.; Gutwerk, D.; Tödheide, K.; Chieux, P. *Mol. Phys.* **1992**, *76*, 127.
(42) Adya, A. K.; Wormald, C. J. *Mol. Phys.* **1992**, *77*, 1217.
(43) Nishikawa, K.; Takematsu, M. *Chem. Phys. Lett.* **1994**, *226*, 359.
(44) Ishii, R.; Okazaki, S.; Odawara, O.; Okada, I. *Fluid Phase Equilib.* **1995**, *104*, 291.
(45) Ishii, R.; Okazaki, S.; Okada, I.; Furusaka, M.; Watanabe, N.; Misawa, M.; Fukunaga, T. *Chem. Phys. Lett.* **1995**, *240*, 84.
(46) Chiappini, S.; Nardone, M.; Ricci, F. P.; Bellisent-Funel, M.-C. *Mol. Phys.* **1996**, *89*, 975.
(47) Ishii, R.; Okazaki, S.; Okada, I.; Furusaka, M.; Watanabe, N.; Misawa, M.; Fukunaga, T. *J. Chem. Phys.* **1996**, *105*, 7011.
(48) Morita, T.; Nishikawa, K.; Takematsu, M.; Iida, H.; Furutaka, S. *J. Phys. Chem. B* **1997**, *101*, 7158.
(49) Cipriani, P.; Nardone, M.; Ricci, M. A. *Mol. Phys.* **2001**, *99*, 301.
(50) Temleitner, L.; Pusztai, L. *J. Phys.: Condens. Matter* **2007**, *19*, 335203.
(51) Kartsev, V. N. *J. Struct. Chem.* **2004**, *45*, 832.
(52) Nelson, Jr., R. D.; Lide, Jr, D. R.; Maryott, A. A. *Ed. Selected values of electric dipole moments for molecules in the gas phase. National Reference Data Series — NBS 10*, 1967.
(53) Merz, R.; Linder, F. *J. Phys. B: At. Mol. Opt. Phys.* **2003**, *36*, 2921.
(54) Bender, R., Dissertation, Universität Karlsruhe, Germany, 1982.
(55) Bier, K.; Kunze, J.; Maurer, G. *J. Chem. Thermodynamics* **1976**, *8*, 857.
(56) Ernst, G.; Hochberg, U. E. *J. Chem. Thermodynamics* **1989**, *21*, 407.
(57) Kistiakowski, G. B.; Rice, W. W. *J. Chem. Phys.* **1939**, *7*, 281.
(58) Lammers, J. N. J. J.; van Kasteren, P. H. G.; Kroon, G. F.; Zeldenrust, H. *Enthalpy measurements of natural gas components and mixed refrigerants with a flow calorimeter. Proc. 57th Ann. Conf. Gas Proc. Assoc.* **1978**, 18.
(59) Furtado, A. Ph.D. Thesis, University of Michigan, MI, 1973.
(60) Miyazaki, T.; Hejmadi, A. V.; Powers, J. E. *J. Chem. Thermodynamics* **1980**, *12*, 105.
(61) Roder, H. M. *J. Res. NBS* **1976**, *80A*, 739.
(62) Van Kasteren, P. H. G.; Zeldenrust, H. *Ind. Eng. Chem. Fundam.* **1979**, *18*, 339.

Environmental Science & Technology

Article

pubs.acs.org/est

Influence of Methane in CO_2 Transport and Storage for CCS Technology

Sofía T. Blanco, Clara Rivas, Javier Fernández, Manuela Artal, and Inmaculada Velasco*

Departamento de Química Física, Facultad de Ciencias, Universidad de Zaragoza, 50009 Zaragoza, Spain

Supporting Information

ABSTRACT: CO_2 Capture and Storage (CCS) is a good strategy to mitigate levels of atmospheric greenhouse gases. The type and quantity of impurities influence the properties and behavior of the anthropogenic CO_2, and so must be considered in the design and operation of CCS technology facilities. Their study is necessary for CO_2 transport and storage, and to develop theoretical models for specific engineering applications to CCS technology. In this work we determined the influence of CH_4, an important impurity of anthropogenic CO_2, within different steps of CCS technology: transport, injection, and geological storage. For this, we obtained new pressure−density−temperature ($P\rho T$) and vapor−liquid equilibrium (VLE) experimental data for six CO_2 + CH_4 mixtures at compositions which represent emissions from the main sources in the European Union and United States. The P and T ranges studied are within those estimated for CO_2 pipelines and geological storage sites. From these data we evaluated the minimal pressures for transport, regarding the density and pipeline's capacity requirements, and values for the solubility parameter of the mixtures, a factor which governs the solubility of substances present in the reservoir before injection. We concluded that the presence of CH_4 reduces the storage capacity and increases the buoyancy of the CO_2 plume, which diminishes the efficiency of solubility and residual trapping of CO_2, and reduces the injectivity into geological formations.

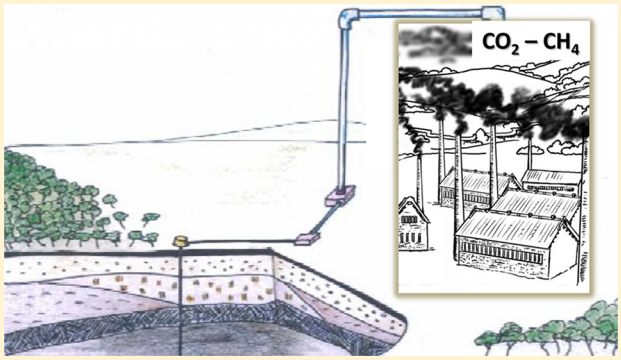

1. INTRODUCTION

Carbon Dioxide Capture and Storage (CCS) is one of several effective strategies (along with energy efficiency, fuel switching, and use of renewable energy sources) to reduce greenhouse gas (GHG) levels in the atmosphere in the medium term.[1−3]

CCS is usually considered as a process consisting of four main separate steps: CO_2 capture, CO_2 conditioning, CO_2 transport, and CO_2 injection and storage.

CO_2 capture can be performed by different techniques (postcombustion, precombustion decarbonization, and oxyfuel combustion) and conditioned via dehydration, noncondensable gas separation and/or liquefaction, and compression/pumping.[4−8] Even though this work is not devoted to CO_2 conditioning and capture, the technologies used will determine the composition of the gas to be handled. It is also important to take into account that it seems that CO_2 purification after capture will be very expensive. Thus, for many of the separation technologies the expense of purification greatly increases for a higher degree of purity of gaseous mixture,[6] therefore, it is essential the study of CO_2 behavior with different impurities.[9] On the other hand, quality specifications for transport are not currently stated. The elaboration of the corresponding regulations will require studying the influence of impurities on the thermodynamic properties of the transported and stored fluid as well. This is precisely the aim of our current study.

For over 30 years now, and within the context of EOR (enhanced oil recovery) and EGR (enhanced gas recovery), long-distance CO_2 transport and injection technologies have been developed. Nevertheless, there are some important differences between these technologies and CCS since CO_2 captured from power stations and industrial sources may contain different proportions and/or types of impurities from those found in the sources of CO_2 usually used in EOR and EGR. The design and operation of a CO_2 + impurities managing system is complicated, due to the highly nonlinear thermodynamic properties of the fluid and because it is normally transported as a dense-fluid, for operational and economic reasons.[10] Since the Kyoto Summit, an international network with specific research programmes devoted to CCS technology has been established. One such scheme is the FP7 Cooperation Work Programme, which includes a topic entitled "Impact of the Quality of CO_2 on Transport and Storage" within the Energy Theme.[11]

Literature shows that the presence and type of impurities clearly influence the fluid's properties and behavior, and as a consequence the design and operation of CCS facilities.[12]

Received: September 18, 2012
Revised: November 12, 2012
Accepted: November 14, 2012
Published: November 14, 2012

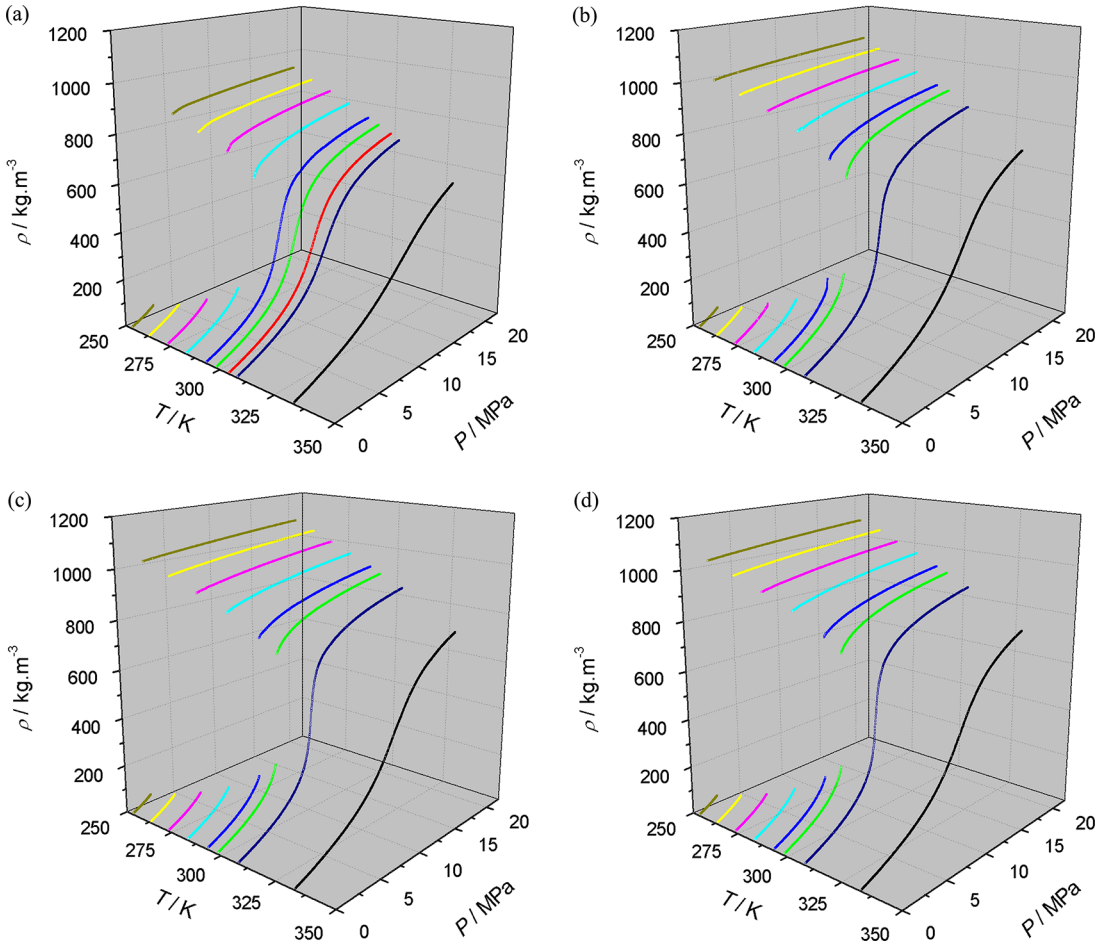

Figure 1. Experimental densities, ρ, for CO_2 + CH_4 mixtures with (a) x_{CO_2} = 0.8525; (b) x_{CO_2} = 0.9719; (c) x_{CO_2} = 0.9902, and (d) x_{CO_2} = 0.9961 at several temperatures and pressures.

Knowledge of the thermodynamic properties of the CO_2 + impurities mixtures, especially pressure−volume−temperature−composition (*PVTxy*) and vapor−liquid equilibrium (VLE), is therefore essential. This information will allow determination of composition specifications and purification requirements (if necessary) of the fluid in the different steps of this technology, and will enable design of efficient, safe, and economical processes.[9] These data are also necessary to develop reliable theoretical models for engineering applications, covering the large range of operative conditions (from atmospheric pressure to supercritical states) of multicomponent mixtures involved in CCS processes. Many equations of state (EoS), such as PR, RKS, SAFT, and GERG are available for thermodynamic calculations of CO_2 mixtures, but none of them show any clear advantage in CCS applications for the calculations of all *PVTxy* properties, thus a reference EoS for CCS should be a future goal.[9,13]

This is the first work in a systematic study on binary mixtures of CO_2 and the typical impurities found in industrial emissions. In this study we present reliable experimental data of pressure−density−temperature, $P\rho T$, and VLE, properties for mixtures of CO_2 and CH_4 at the compositions, *P*, and *T* ranges of interest for the transport and the storage in the CCS technologies. CO_2 and CH_4 are two of the six GHGs that have been targeted by the international community as causing global warming, being the environmental impact of methane emissions 21 times greater than that of carbon dioxide.[1] Our experimental data were compared with those predicted by GERG EoS which is, among the above-mentioned, the most recommended by the NIST for CO_2 + CH_4 mixtures and the most used for petroleum fluids and natural gas.[14]

From the $P\rho T$ experimental values of CO_2 + CH_4 mixtures, we evaluated the effect of impurities on several parameters related to transport, injection, and storage such as the minimal pressure for transport, the solubility parameter, the normalized storage capacity of the reservoir, the normalized rising velocity of the CO_2 plume, and the normalized permeation flux.

2. EXPERIMENTAL SECTION

Materials. Carbon dioxide (wt % > 99.998) and methane (wt % > 99.995) were obtained from Air Liquide.

In Spain, compositions of the emissions from different industries are characterized and recorded by the Registro Estatal de Emisiones y Fuentes Contaminantes (PRTR España).[15] The highest content of methane (wt % CH_4 ≈ 6.0%) is found in emissions from waste management (7% of the total of CO_2 emitted in Spain in 2010). In addition to this, wt % CH_4 varies from ≈1.0% for farming and livestock emissions to ≈0.36% for other industries such as ceramics production.[15] Having taken these figures into account, we chose six compositions ranging from 0.14% to 5.93% in wt % of CH_4 allowing us to study representative industrial emissions in Spain. In this composition range the percentages of methane from emissions of the main sources of anthropogenic CO_2 in

the EU and the U.S.[16−19] are included. The total emissions in Spain, EU, and U.S. contain wt % of CH_4 of 0.15%, 0.65%, and 0.55%, respectively. The mixtures were prepared by successive weighting of the components in a variable volume cell with a precision of 0.0002 g.

Apparatus and Procedures. The experimental setup used in this work for the determination of $P\rho T$ data of CO_2 + CH_4 mixtures is the same as that described in a previous study.[20] It was designed for fast, reliable, and accurate generation of $P\rho T$ data. Their quasi-continuous data acquisition along subcritical, critical, and supercritical regions (6000 points/isotherm evenly reduced to about 1000 points/isotherm for easier handling) allows the accurate determination of the limits of VLE and the calculation of derived properties from the experimental data.

The precision and accuracy in density results for mixtures were determined in a previous work;[20] the mean relative deviation, MRD (ρ) = 0.7% and mean standard deviation, $\overline{S}_\rho^r$ = 0.13% were obtained.

3. RESULTS AND DISCUSSION

In this work we present 49 experimental $P\rho T$ isotherms (containing a total of 49 000 points available in the Supporting Information) for six CO_2 + CH_4 mixtures (CO_2 mole fraction, x_{CO_2} = 0.8525, 0.9719, 0.9809, 0.9902, 0.9932, and 0.9961) from atmospheric pressure to 20 MPa, and at 253.15, 263.15, 273.15, 283.15, 293.15, 298.15, 308.15, and 333.15 K. In the case of the mixture with x_{CO_2} = 0.8525 the isotherm at 304.21 K (T_c of CO_2) is presented too. Properties were measured in P and T ranges which are within the estimated pressures and temperatures in CO_2 pipelines (7.5−20 MPa and 273−303 K)[9] and in geologic storage sites on the basis of a geothermic gradient[21] of 25 K/km and an average gradient of hydrostatic pressure of 10 MPa/km.

From these $P\rho T$ experimental data we obtained the dew and bubble pressures, P_{dew} and P_{bubble}, and the densities of the phases in equilibrium (ρ_{sat}) for each mixture at the corresponding subcritical temperatures, as well as the derivative properties α_P (isobaric thermal expansivity), κ_T (isothermal compressibility), and π (internal pressure). Besides, we evaluated the minimal pressures for transport, regarding the density and pipeline's capacity requirements, and the effect of impurities on the solubility parameter, δ. This parameter will govern the interactions between the injected CO_2 and the substances previously present in the reservoir, such as methane itself among others. Last, we calculated, using our experimental data, values for other parameters related to storage such as the normalized storage capacity of the reservoir and the normalized rising velocity of the plume by means of the approach that Wang et al. used for other impurities.[22] Acting in this fashion, the experimental data will give realistic information about what

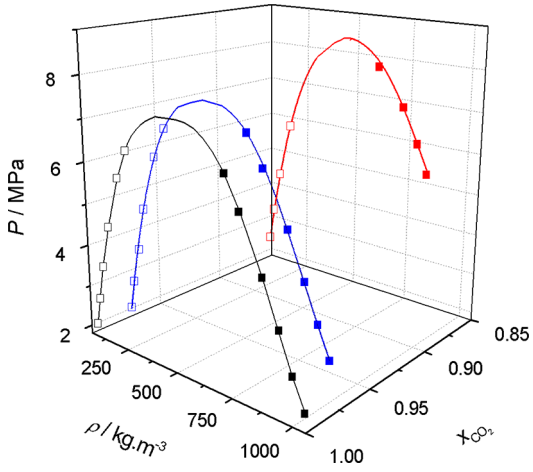

Figure 2. Experimental dew (blank symbols) and bubble (solid symbols) pressures, P_{dew} and P_{bubble}, and saturation densities, ρ_{sat}, of the phases in equilibrium for CO_2 + CH_4 mixtures with x_{CO_2} = 0.8525 (red), x_{CO_2} = 0.9719 (blue), and x_{CO_2} = 0.9961 (black).

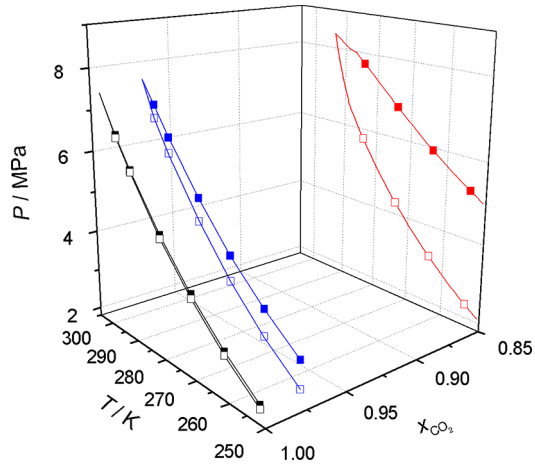

Figure 3. Phase envelopes for CO_2 + CH_4 mixtures with x_{CO_2} = 0.8525 (red), x_{CO_2} = 0.9719 (blue), and x_{CO_2} = 0.9961 (black). Open symbols, dew pressures, P_{dew}; solid symbols, bubble pressures, P_{bubble}.

Table 1. Values of Minimal Compressing Pressure, P, Required to Obtain a Density of 800 kg/m^3 for Transport of Pure CO_2[20] or a CO_2 + CH_4 Mixture with x_{CO_2} = 0.9961 or x_{CO_2} = 0.8525

	P (MPa)		
T (K)	pure CO_2[14,20]	x_{CO_2} = 0.9961	x_{CO_2} = 0.8525
253.15	1.970	2.094	5.233
263.15	2.649	2.758	6.031
273.15	3.485	3.626	12.859
283.15	4.502	4.700	18.951
293.15	6.626	7.014	>20
298.15	9.017	9.367	
304.21	11.987	12.359	
308.15	13.904	14.239	
333.15	26.398	>20	

Table 2. Bubble Pressure Values, P_{bubble}, for Pure CO_2[14] and for CO_2 + CH_4 Mixtures with x_{CO_2} = 0.9961 and x_{CO_2} = 0.8525

	P_{bubble} (MPa)		
T (K)	pure CO_2[14]	x_{CO_2} = 0.9961	x_{CO_2} = 0.8525
253.15	1.9696	2.073	5.232
263.15	2.6487	2.753	6.031
273.15	3.4851	3.622	7.000
283.15	4.5022	4.608	7.741
293.15	5.7291	5.827	
298.15	6.4342	6.532	

dx.doi.org/10.1021/es3037737 | Environ. Sci. Technol. 2012, 46, 13016−13023

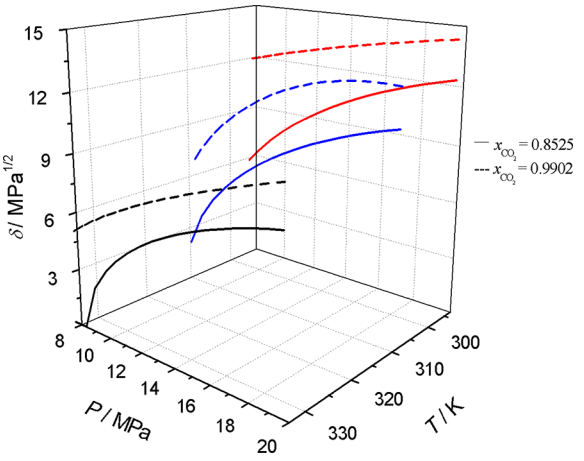

Figure 4. Solubility parameters, δ, for CO_2 + CH_4 mixtures with x_{CO_2} = 0.8525 (continuous line); x_{CO_2} = 0.9902 (dashed line) at 293.15 K (red), 308.15 K (blue), and 333.15 K (black).

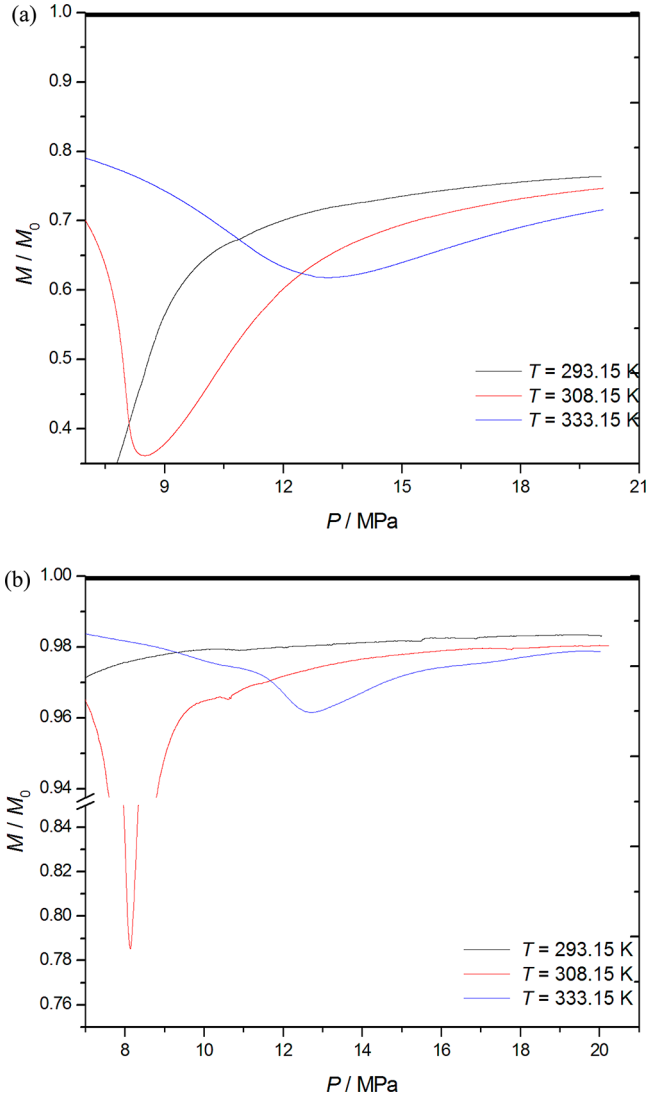

Figure 5. Normalized CO_2 storage capacity, M/M_0, for CO_2 + CH_4 mixtures with (a) x_{CO_2} = 0.8525 and (b) x_{CO_2} = 0.9902 at 293.15, 308.15, and 333.15 K.

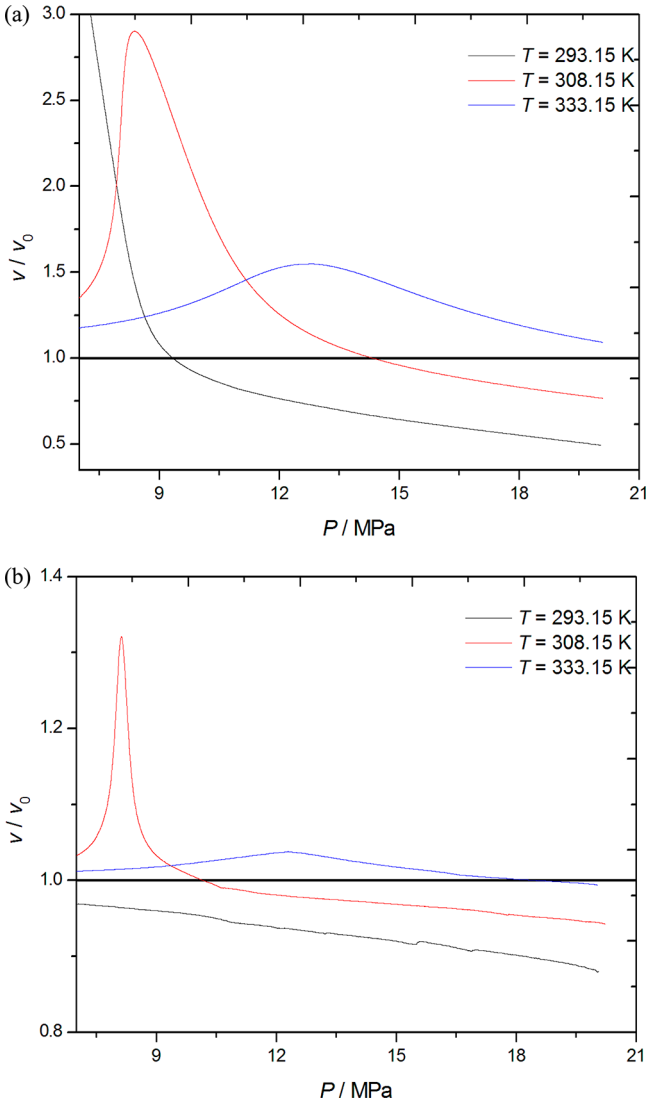

Figure 6. Normalized rising velocity of the plume, v/v_0, for CO_2 + CH_4 mixtures with (a) x_{CO_2} = 0.8525 and (b) x_{CO_2} = 0.9902 at 293.15, 308.15, and 333.15 K.

is happening inside the reservoirs after injection of CO_2. The normalized permeation flux,[22] which provides a measure of the relative injectivity of the impure CO_2 stream, has been also calculated from our data and the viscosity data from GERG EoS.[14]

Figure 1a, b, c, and d show the experimental densities for four of the six CO_2 + CH_4 mixtures which include the whole range of composition studied. The representations corresponding to the rest of the mixtures are included in Figures S1a and S1b and the complete $P\rho T$ experimental data are listed in Table S1, both in the Supporting Information. In these graphics, the density of the mixtures at subcritical temperatures shows a discontinuity in the liquid−vapor equilibrium zone which is limited by the dew point in the low pressure regions and by the bubble point in the high pressure regions. However, the representation at supercritical temperatures is a continuous line.

In Figures 2 and 3 the VLE properties are represented for the mixtures at x_{CO_2} = 0.8525, 0.9719, and 0.9961 (Figure 2, dew and bubble pressures and densities of the phases in equilibrium, hence the limits of the discontinuities in Figure 1 mentioned

dx.doi.org/10.1021/es3037737 | Environ. Sci. Technol. 2012, 46, 13016−13023

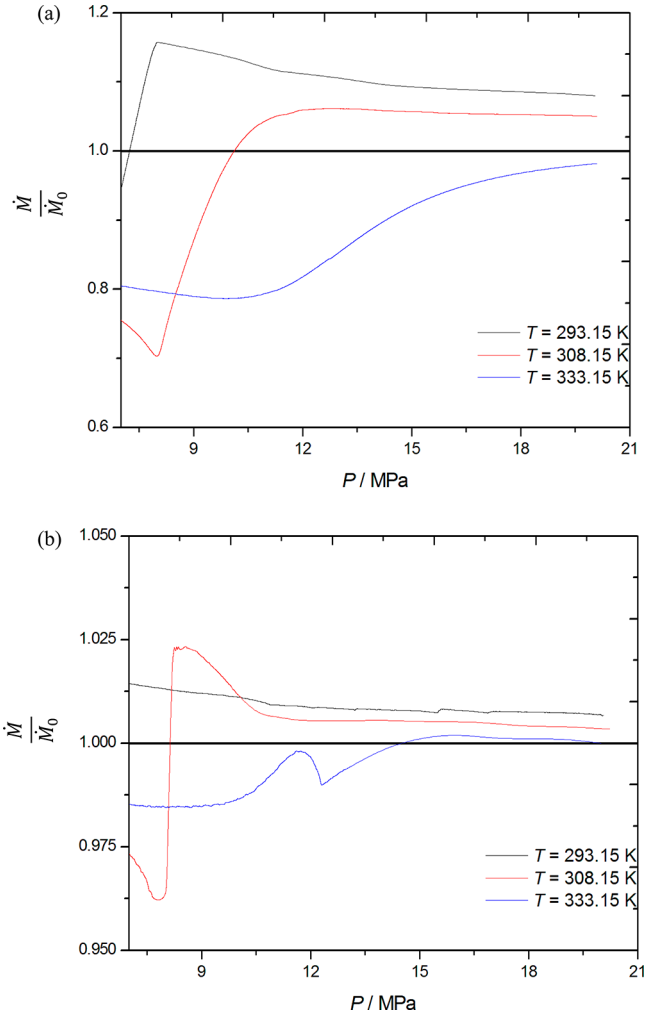

Figure 7. Normalized permeation flux, $\dot{M}/\dot{M}_0$, for CO_2 + CH_4 mixtures with (a) x_{CO_2} = 0.8525 and (b) x_{CO_2} = 0.9902 at 293.15, 308.15, and 333.15 K.

before; Figure 3, the corresponding $P-T-x_{CO_2}$ projections). For the rest of the mixtures similar representations can be found in Figures S2 and S3, and the corresponding values in Table S2.

There are numerous publications on CO_2 + CH_4 system in the literature, but not for the compositions and conditions of interest for CCS technology. We have found three publications which give values of density[23] and VLE properties[24,25] at conditions similar to ours (but not the same). Magee and Ely[23] give values for density of CO_2 + CH_4 with x_{CO_2} = 0.98 that are in good agreement with our data. Also, our value for bubble pressure at 293.15 K for this mixture agrees with that from these authors. Furthermore, we have found reasonable agreement between our pressures for VLE and those reported by Xu et al.[24] and Donnelly and Katz.[25]

Our experimental data for density and VLE have been compared with those predicted by GERG EoS.[14] The obtained deviations are MRD(ρ) = 0.28%, MRD(P_{dew}, P_{bubble}) = 0.15%, and MRD(ρ_{sat}) = 0.45%, which are within the margins of error given by the authors.

Influence of Impurities in Transport. CO_2 is transported through pipelines over long distances as a dense-phase fluid at densities from 800 to 1000 kg/m^3. To achieve this density requirement at the different operating temperatures, the minimal transport pressure will depend on the composition of the CO_2 transported. Table 1 shows the values of minimal compressing pressure required to obtain a density of 800 kg/m^3 if the fluid transported is pure CO_2,[14,20] or if it is a CO_2 + CH_4 mixture with x_{CO_2} = 0.8525 or x_{CO_2} = 0.9961 (from our experimental $P\rho T$ data). As it can be seen, for the CO_2 rich mixture the required values of pressure are slightly higher but similar to those for pure CO_2 at 253.15 K. For a mixture characterized as the binary CO_2 + CH_4 with x_{CO_2} = 0.8525, the minimal value of pressure required in the pipeline is almost three times that for pure CO_2, and this proportion increases as temperature increases, so that the required pressure at 283.15 K is more than four times the value for pure CO_2.

The presence of impurities in the transported fluid modifies the limits of VLE as well, and hence the value for the bubble pressure for a given temperature, as shown in Figure 2. In the transport by pipeline, the operating pressure cannot be lower than the bubble pressure of the fluid to avoid the presence of vapor phase which would diminish the pipeline's capacity. In Table 2 bubble pressure data for pure CO_2[14] and CO_2 + CH_4 (x_{CO_2}= 0.8525 and x_{CO_2} = 0.9961) mixtures are listed for the subcritical temperatures studied. Although these bubble pressures are lower than those necessary to fulfill the density requirements, the conditions in which the fluid's pressure is lower than those values of pressure should be avoided in the different types of operations that take place in the transport network.

Influence of Impurities in Storage and Injection. There are different sites which are suitable candidates for geological storage: deep saline aquifers, depleted oil and gas fields, and nonexploitable coal seams.[26] The anthropogenic CO_2-trapping mechanism and the influence of impurities can be different according to the kind of reservoir. Inside the reservoirs, there will be interactions between the substances present before the injection and the injected anthropogenic CO_2 (CO_2 + impurities). Methane can be present in the reservoir before injection and as a component of anthropogenic CO_2. In the study on solvent−solute intermolecular forces, we propose the anthropogenic CO_2 stream to be labeled as the solvent, and those substances present beforehand in the reservoir as solutes. The solvent will probably be in a supercritical state because of the conditions of temperature and pressure inside the reservoir. Fluid in this state presents two characteristic properties: a great ability to dissolve nonvolatile substances (several orders of magnitude greater than in the gas state), and a wide variability of this solvent's capacity with the operating conditions (T, P). The concept of solubility parameter, introduced by Hildebrand and Scott in 1950,[27] has been extensively used for more than sixty years to interpret and predict the thermodynamic behavior of liquid solutions in a semiquantitative way,[28−31] and has also been extended to nonpolar and slightly polar supercritical fluids.[20,32] The solubility parameter, δ, was defined by Hildebrand and Scott as

$$\delta = \left(\frac{-E(T)}{V(T, P)}\right)^{1/2} \quad (1)$$

where $-E$ is the cohesive energy and V is the molar volume of the liquid, with $(-E/V)$ being the so-called "cohesive energy density". Hansen[28] assumes the cohesive energy to be an

additive quantity composed of a dispersive (d), a polar (p), and a hydrogen-bond (h) contribution

$$E = E_d + E_p + E_h \tag{2}$$

and, therefore,

$$\delta^2 = \delta_d^2 + \delta_p^2 + \delta_h^2 \tag{3}$$

Bagley et al.[30] subdivide the solubility parameter in two parts:

$$\delta^2 = \delta_V^2 + \delta_R^2 \tag{4}$$

where $\delta_V^2 = \delta_d^2 + \delta_p^2$ corresponds to the "physical" or "non-chemical" effects and is known as the "volume-dependent solubility (or cohesion) parameter", which is defined by

$$\delta_V^2 = \pi \tag{5}$$

where π is the internal pressure. The other component, δ_R, is a "residual" parameter, which results from "chemical" effects. Since hydrogen bonding is not present in our system, it seems appropriate to neglect the residual contribution and to use the internal pressure to estimate the solubility parameter[31]

$$\delta^2 = \delta_V^2 = \pi \tag{6}$$

which is a relationship between the solubility parameter and the internal pressure earlier used by Hildebrand and Scott.[27] Allada et al.[32] suggest that the solubility parameters are the determinant key of solubility of the solutes in supercritical solvents and that they apparently unify diverse behaviors of solvents regardless of kind, T, or P. In this work, we propose to apply this concept to stored anthropogenic CO_2. Hence, in storage of anthropogenic CO_2, the solubilization of substances present beforehand will depend on interactions between these solutes and the supercritical fluid, and as we have shown this behavior can be approximated if we know the values for internal pressure of the mixture which is injected for storage.

The internal pressure is defined as

$$\pi = \left(\frac{\partial U}{\partial V}\right)_T = T\left(\frac{\partial P}{\partial T}\right)_V - P \tag{7}$$

In this equation, we can write

$$\left(\frac{\partial P}{\partial T}\right)_V = -\left(\frac{1}{\rho}\right)\left(\frac{\partial \rho}{\partial T}\right)_P \frac{1}{\left(\frac{1}{\rho}\right)\left(\frac{\partial \rho}{\partial P}\right)_T} = \frac{\alpha_p}{\kappa_T} \tag{8}$$

where α_P is the isobaric thermal expansivity and κ_T is the isothermal compressibility. We calculated α_P, κ_T, and π values (see Supporting Information) from our $P\rho T$ experimental data. Solubility parameters are represented in Figure 4 for mixtures with $x_{CO_2} = 0.8525$ and $x_{CO_2} = 0.9902$ at 293.15, 308.15, and 333.15 K. As can be seen, the solubility parameters decrease as the methane mole fraction increases in the anthropogenic CO_2. For each mole fraction studied, the greatest value of the parameter is obtained for the compressed liquid mixtures, and decreases as temperature increases and pressure decreases.

Noncondensable impurities, such as methane, will increase the compression pressure needed for injection and reduce the capacity of the storage sites because the density of the mixture will decrease. Wang, et al.[22] proposed the following expression for the storage capacity, expressed in mass, as a function of the density of the CO_2 stream:

$$\frac{M}{M_0} = \frac{\rho}{\rho_0\left[1 + \sum_i \left(\frac{m_i}{m_0}\right)\right]} \tag{9}$$

where M and M_0 denote, respectively, the mass of CO_2 in the mixture and in the pure CO_2 stream which occupies the same volume or its ratio per unit volume. ρ and ρ_0 are the densities of the mixture and the pure CO_2 stream, and m_i/m_0 is the ratio of the mass of impurity i to the mass of CO_2 in the mixture. The ratio M/M_0 on the left-hand side of this relation represents a normalized storage capacity for CO_2, i.e. the capacity for structural trapping of CO_2. In the case of pure CO_2 (zero impurity effect) the ratio equals unity. The right-hand side is a function of temperature, pressure, and mixture composition and has been calculated from our $P\rho T$ experimental data. Accordingly, the normalized storage capacity has been determined, and Figure 5a and b show the results for CO_2 + CH_4 mixtures with $x_{CO_2} = 0.8525$ and $x_{CO_2} = 0.9902$, respectively, at three temperatures that can be found in storage at different depths: 293.15, 308.15, and 333.15 K. As can be observed, the presence of CH_4 negatively affects the mass of CO_2 which can be stored in a given reservoir. At a given temperature, for any reservoir, the lowest value of anthropogenic CO_2 stored (expressed by mass) corresponds to the richest methane mole fractions (Figure 5a). The deeper the location of the reservoir (higher values of T and P) the greater is the mass of CO_2 which can be potentially stored. If we consider a depth from 1000 to 2000 m, the pressure of the injected CO_2 will range from 10 to 20 MPa, and the average temperature will be 333.15 K (for an average gradient of hydrostatic pressure of 10 MPa/km and a geothermic gradient[21] of 25 K/km). Under these conditions, the storage capacity can be reduced to a figure as low as 60% for the mixture with $x_{CO_2} = 0.8525$ and 96% for the mixture with $x_{CO_2} = 0.9902$ (Figure 5a and b).

In general, the presence of noncondensable impurities (i.e., methane) in anthropogenic CO_2 causes a decrease in the CO_2 storage capacity, with a minimum at a given P for each T (Figure 5a and b). As a consequence, the effect of pressure has to be taken into account in the estimation of the capacity of underground formations. To increase the efficiency of the storage, both the pressure of injection and the depth inside the reservoir should be combined. At a given depth (T = constant), increasing the storage pressure well beyond the minimum pressure would improve the storage efficiency (Figure 5a and b). For closed reservoirs, this may be achieved by increasing the injection pressure within the allowable overpressure range; for open formations where overpressure may not be attainable, increasing the depth of injection and storage is the only option.

In deep saline aquifers, the presence of impurities affects parameters related to storage, such as the buoyancy and the rising velocity. The presence of light-impurity species, such as CH_4, generates a greater buoyancy of the CO_2 plume, due to its lower density. For a given mass of the plume in a unit volume in contact with the site water, the buoyant force, F, can be expressed as

$$F = (\rho_{H_2O} - \rho)g \tag{10}$$

where ρ_{H_2O} and ρ are the densities of the water and the plume, respectively, and g is the gravitational acceleration. The effect of impurities on this force with reference to pure CO_2 may be given as

$$\frac{F}{F_0} = \frac{\rho_{H_2O} - \rho}{\rho_{H_2O} - \rho_0} \quad (11)$$

where F and F_0 are the buoyant forces for the CO_2 mixture and pure CO_2, respectively. The greater the difference between the densities of anthropogenic CO_2 (ρ) and pure CO_2 (ρ_0), the greater the change in the buoyancy will be. If impurities are noncondensable, $\rho < \rho_0$, the buoyancy increases, and this in turn will significantly increase the rising velocity of the plume, v. The rising velocity for the CO_2 mixture, v, can be related to that of the pure CO_2 stream, v_0, by[22]

$$\frac{v}{v_0} = \frac{F/(\rho\eta)}{F_0/(\rho_0\eta_0)} \quad (12)$$

where η is the viscosity of the CO_2 impure stream and η_0 is that of pure CO_2. In Figure 6, the relations v/v_0 for CO_2 + CH_4 with x_{CO_2} = 0.8525 (Figure 6a) and x_{CO2} = 0.9902 (Figure 6b) at 293.15, 308.15, and 333.15 K, are represented against pressure. The values for the relations were calculated from our experimental $P\rho T$ data and values for viscosity from GERG EoS.[14] For the two mixtures, the v/v_0 relations present maxima at 308.15 and 333.15 K inside the pressure range represented in the figures. For the CH_4-richest mixture at 308.15 K, the rising velocity can reach nearly three times that of the pure CO_2 plume. At 333.15 K, which would be the average temperature at depths from 1000 to 2000 m, the maxima, for the two compositions, are found exactly at pressures inside the ranges corresponding to those depths (10−20 MPa). For x_{CO_2} = 0.8525, the rising velocity of the fluid, at this temperature, can be more than 1.5 times that of the pure CO_2 plume (Figure 6a), but for x_{CO_2} = 0.9902 this relation diminishes to almost 1 (Figure 6b). An elevated rising velocity makes the time for CO_2−water contact in the reservoir shorten, with less dissolving effect. The lateral spreading of the plume will be diminished as well, and as a consequence the area for trapping CO_2 in the rock's pores will decrease, with a reduction in the formation of a residual phase. When the plume makes contact with the cap rock layer and is retained under, it spreads laterally, but the contact with saline water happens only at the interface. Moreover, near the cap rock, at a lower depth, the pressure is lower than in the deeper region, and therefore the efficiency of both solubility and residual trapping will be lower. Therefore, the risk for leakage increases if pathways are available.

In relation to injection, to analyze the differences due to the type of the fluid injected, pure CO_2 or anthropogenic CO_2, an expression based on Darcy's law can be used to calculate the permeation flux

$$\dot{M} = \frac{\rho k}{\eta}\nabla P \quad (13)$$

Where $\dot{M}$ is the mass flow per unit area, ρ and η are the density and the viscosity, respectively, of the injected fluid, k is the rock permeability, ∇ is the gradient operator, and P is the pressure. Noncondensable impurities reduce the density of the CO_2 stream, and the mass flux will decrease for the same pressure drop and viscosity. Additionally, impurities will also affect the viscosity of the fluid, and the mass flow will increase if the viscosity of the impure CO_2 stream is lower than the viscosity of pure CO_2. Therefore, the decrease in density may be compensated by a corresponding decrease in viscosity. Both density and viscosity are functions of temperature and pressure, and the rock permeability and pressure gradient vary for each particular site. Nevertheless, we may use the following relation for an estimation of the impurity effects under the same permeability and pressure drop conditions[22]

$$\frac{\dot{M}}{\dot{M}_0} = \frac{\rho\left(\frac{\eta_0}{\eta}\right)}{\rho_0\left[1 + \sum_i \left(\frac{m_i}{m_0}\right)\right]} \quad (14)$$

where $\dot{M}$, η, and ρ are the mass flow per unit area, viscosity, and density of the anthropogenic CO_2, and $\dot{M}_0$, η_0, and ρ_0 those of the pure CO_2. The bracket in the denominator introduces a correction for impurities as in eq 9. Equation 14 represents a normalized permeation flux and allows estimating the relative injectivity of the impure CO_2 stream.

We calculated the values of $\dot{M}/\dot{M}_0$ for mixtures with x_{CO_2} = 0.8525 and x_{CO_2} = 0.9902 at 293.15, 308.15, and 333.15 K, using our experimental $P\rho T$ data and calculated values for viscosity.[14] In Figure 7a and b, the values obtained for the relation are represented against pressure. It can be observed that for pressures from 10 to 20 MPa, the permeation flux at 293.15 and 308.15 K for the two mixtures is higher than that for pure CO_2. At 333.15 K the trend changes, and the permeation flux of the mixture poorest in CO_2 is lower than that of pure CO_2, trending toward 1 as pressure increases; for the other mixture, the permeation flux is lower than 1 up to 14 MPa, and approximately equals 1 from this pressure.

■ ASSOCIATED CONTENT

Supporting Information

P-ρ-T experimental values for CO_2 + CH_4 mixtures; ρ-T-P representations; P-ρ_{sat}-x_{CO_2} and P-T-x_{CO_2} values and representations of VLE; κ_T-T-P, α_P-T-P, and π-P-T values and representations. This material is available free of charge via the Internet at http://pubs.acs.org.

■ AUTHOR INFORMATION

Corresponding Author

*E-mail: curra@unizar.es.

Notes

The authors declare no competing financial interest.

■ ACKNOWLEDGMENTS

We gratefully acknowledge financial support received from the Ministerio de Ciencia e Innovación (CTQ2008-02037), Ministerio de Economía y Competitividad (CTQ2011-24875), and Convenio La Caixa - Gobierno de Aragón.

■ REFERENCES

(1) *Climate Change 2007: Working Group I: The Physical Science Basis.* IPCC (International Panel Climate Change), February 2007; www.ipcc.ch/publications_and_data/ar4/wg1/en/ch2s2-10-2.html.

(2) Bandyopadhyay, A.; Luo, G.; Fei, W. Preface. Special Issue: CO_2 Capture & Storage. *Sep. Purif. Technol.* **2012**, *94*, 85−86, DOI: 10.1016/j.seppur.2012.02.012.

(3) Wan, T.-J.; Shen, S.-M.; Bandyopadhyay, A.; Shu, C.-M. Bibliometric analysis of carbon dioxide reduction research trends during 1999−2009. *Sep. Purif. Technol.* **2012**, *94*, 87−91, DOI: 10.1016/j.seppur.2012.07.022.

(4) Figueroa, J. D.; Fout, T.; Plasynski, S.; McIlvried, H.; Srivastava, R. D. Advances in CO_2 capture technology—The U.S. Department of

Energy's Carbon Sequestration Program. *Int. J. Greenhouse Gas Control* **2008**, *2* (1), 9−20, DOI: 10.1016/S1750-5836(07)00094-1.
(5) Florin, N.; Fennell, P. *Review of Advanced Carbon Capture Technologies*; Grantham Institute for Climate Change, Imperial College: London, 2010.
(6) Olajire, A. A. CO_2 capture and separation technologies for end-of-pipe applications − A review. *Energy* **2010**, *35* (6), 2610−2628, DOI: 10.1016/j.energy.2010.02.030.
(7) Bandyopadhyay, A. Amine versus ammonia absorption of CO_2 as a measure of reducing GHG emission: A critical analysis. *Clean Technol. Environ. Policy* **2011**, *13* (2), 269−294, DOI: 10.1007/s10098-010-0299-z.
(8) Bandyopadhyay, A.; Biswas, M. N. CO_2 capture in a spray column using a critical flow atomizer. *Sep. Purif. Technol.* **2012**, *94*, 104−114, DOI: 10.1016/j.seppur.2011.11.039.
(9) Li, H.; Jakobsen, J. P.; Wilhelmsen, Ø.; Yan, J. PVTxy properties of CO_2 mixtures relevant for CO_2 capture, transport and storage: Review of available experimental data and theoretical models. *Appl. Energy* **2011**, *88* (11), 3567−3579, DOI: 10.1016/j.apenergy.2011.03.052.
(10) Cosham, A.; Eiber, R. J. Fracture propagation in CO_2 pipelines. *J. Pipeline Eng.* **2008**, *12*, 281−292.
(11) Community Research and Development Information Service, 2012 Work Programmes, Cooperation, Energy; www.cordis.europa.eu/fp7/wp-2012_en.html.
(12) Li, H.; Yan, J.; Yan, J.; Anheden, M. Impurity impacts on the purification process in oxy-fuel combustion based CO_2 capture and storage system. *Appl. Energy* **2009**, *86* (2), 202−213, DOI: 10.1016/j.apenergy.2008.05.006.
(13) Li, H.; Yan, J. Impacts of equations of state (EOS) and impurities on the volume calculation of CO_2 mixtures in the applications of CO_2 capture and storage (CCS) processes. *Appl. Energy* **2009**, *86* (12), 2760−2770, DOI: 10.1016/j.apenergy.2009.04.013.
(14) Kunz, O.; Klimeck, R.; Wagner, W.; Jaeschke, M. *GERG Technical Monograph*; Fortschr.-Ber.: VDI, VDI-Verlag: Dusseldorf, Germany, 2006.
(15) Registro Estatal de Emisiones y Fuentes Contaminantes (PRTR España); www.prtr-es.es.
(16) *Annual European Union Greenhouse Gas Inventory 1990−2010 and Inventory Report 2012*; Technical report 3/2012; EEA (European Environment Agency), 2012; www.eea.europa.eu/publications/european-union-greenhouse-gas-inventory-2012 .
(17) European Climate Change Programme; www.ec.europa.eu/clima/policies/eccp/index_en.htm.
(18) *Inventory of U.S. Greenhouse Gas Emissions and Sinks: 1990 − 2010*; EPA 430-R-12-001; U.S. Environmental Protection Agency, 2012; www.epa.gov/climatechange/ghgemissions/usinventoryreport.html.
(19) Last G. V.; Schmick M T. *Identification and Selection of Major Carbon Dioxide Stream Compositions*; PNNL-20493; U.S. Department of Energy, 2011; www.pnnl.gov/main/publications/external/technical_reports/PNNL-20493.pdf.
(20) Velasco, I.; Rivas, C.; Martínez-López, J. F.; Blanco, S. T.; Otín, S.; Artal, M. Accurate values of some thermodynamic properties for carbon dioxide, ethane, propane, and some binary mixtures. *J. Phys. Chem. B.* **2011**, *115* (25), 8216−8230, DOI: 10.1021/jp202317n.
(21) Bachu, S. Screening and ranking of sedimentary basins for sequestration of CO_2 in geological media in response to climate change. *Environ. Geol.* **2003**, *44* (3), 277−289, DOI: 10.1007/s00254-003-0762-9.
(22) Wang, J.; Ryan, D.; Anthony, E. J.; Wildgust, N.; Aiken, T. Effects of impurities on CO_2 transport, injection and storage. *Energy Procedia* **2011**, *4*, 3071−3078, DOI: 10.1016/j.egypro.2011.02.219.
(23) Magee, J. W.; Ely, J. F. Isochoric (p, v, T) measurements on CO_2 and (0.98 CO_2 + 0.02 CH_4) from 225 to 400 K and pressures to 35 MPa. *Int. J. Thermophys.* **1988**, *9* (4), 547−557, DOI: 10.1007/BF00503153.
(24) Xu, N.; Dong, J.; Wang, Y.; Shi, J. High pressure vapor liquid equilibria at 293 K for systems containing nitrogen, methane and carbon dioxide. *Fluid Phase Equilib.* **1992**, *81*, 175−186, DOI: 10.1016/0378-3812(92)85150-7.
(25) Donnelly, H. G.; Katz, D. L. Phase equilibria in the carbon dioxide-methane system. *Ind. Eng. Chem.* **1954**, *46*, 511−517, DOI: 10.1021/ie50531a036.
(26) Shukla, R.; Ranjith, P.; Haque, A.; Choi, X. A review of studies on CO_2 sequestration and caprock integrity. *Fuel* **2010**, *89* (10), 2651−2664, DOI: 10.1016/j.fuel.2010.05.012.
(27) Hildebrand, J. H.; Scott, R. L. *The Solubility of Nonelectrolytes*; Reinhold: New York, 1950.
(28) Hansen, C. M. The universality of the solubility parameter. *Ind. Eng. Chem. Prod. Res. Dev.* **1969**, *8* (1), 2−11, DOI: 10.1021/i360029a002.
(29) Hansen, C. M. *Hansen Solubility Parameters − A User's Handbook*; CRC Press: Boca Raton, FL, 2000.
(30) Bagley, E. B.; Nelson, T. P.; Scigliano, J. M. Three-dimensional solubility parameters and their relationship to internal pressure measurements in polar and hydrogen bonding solvents. *J. Paint Technol.* **1971**, *43* (555), 35−42.
(31) Verdier, S.; Duong, D.; Andersen, S. I. Experimental determination of solubility parameters of oils as a function of pressure. *Energy Fuels* **2005**, *19* (4), 1225−1229, DOI: 10.1021/ef049827v.
(32) Allada, S. R. Solubility parameters of supercritical fluids. *Ind. Eng. Chem. Proc. Des. Dev.* **1984**, *23* (2), 344−348, DOI: 10.1021/i200025a028.

International Journal of Greenhouse Gas Control 18 (2013) 264–276

Contents lists available at ScienceDirect

International Journal of Greenhouse Gas Control

journal homepage: www.elsevier.com/locate/ijggc

Influence of methane and carbon monoxide in the volumetric behaviour of the anthropogenic CO_2: Experimental data and modelling in the critical region

Clara Rivas, Sofía T. Blanco, Javier Fernández, Manuela Artal, Inmaculada Velasco*

Departamento de Química Física, Facultad de Ciencias, Universidad de Zaragoza, 50009 Zaragoza, Spain

ARTICLE INFO

Article history:
Received 16 April 2013
Received in revised form 24 July 2013
Accepted 26 July 2013
Available online 24 August 2013

Keywords:
Carbon dioxide
Impurities
Volumetric properties
EoS
Structural properties
CCS technology

ABSTRACT

Density measurements of the systems $CO_2 + CH_4$ at $T = 304.21$ K and $CO_2 + CO$ at $T = 304.21$ and 308.15 K were carried out at pressures and compositions of interest in the process of transport and storage of CO_2 (CCS technology): $P = 0.1$ to 20 MPa, and $x_{CO_2} \geq 0.97$. From the experimental P–ρ–T–x_{CO_2} data, we have studied the dependence of the isothermal compressibility, the excess molar volume, and the partial molar volume of the solute with composition, pressure and temperature within the critical region. We have modelled the volumetric behaviour of these systems with Peng–Robinson, PC-SAFT and GERG Equations of State, thus validating these equations under the conditions considered. Furthermore, we have confirmed the weakly attractive behaviour of these systems by performing a study of the interactions between solvent molecules, CO_2, and those of the solute, CO or CH_4, using the Krichevskii Function concept and the Kirkwood–Buff Theory. Finally, we have quantified the influence of small amounts of CH_4 and CO in the transport of anthropogenic CO_2 through several normalized parameters, related to the design and operation of the fluid transport process.

1. Introduction

Nowadays new technologies are being developed in order to reduce CO_2 emissions originated from industrial processes. For instance, CO_2 capture by algae and subsequent transformation into biomass in a process similar to photosynthesis (Ramachandriya et al., 2013); obtaining combustible materials or other high added value substances from its photocatalytic and electrochemical reduction (Ghasemi et al., 2013); purification and treatment of drinking water (Vo et al., 2013) and food preservation, (Al-Nehlawi et al., 2013). However, the technology that will furthest reduce carbon dioxide in the atmosphere is the capture, transport and storage of CO_2 (CCS technology). According to the International Energy Agency (IEA/CSLF, 2010), the contribution of this technology to atmospheric CO_2 reduction by 2050 is expected to be of the order of 20% and the reduction achieved by greater energy efficiency of 36% *(horizon 2050)*. In CCS, anthropogenic CO_2 (CO_2 from human activity) is processed in order to increase its CO_2 content (to 85–99.5% CO_2), then transported to a storage site and injected and stored in the chosen reservoir.

The phase diagram of a pure compound shows that at temperatures and pressures above its critical point (for pure CO_2, $P_c = 7.383$ MPa, $T_c = 304.21$ K (Gil et al., 2008)), the gas and liquid phases are indistinguishable and there is only one phase present, known as a supercritical phase, which exhibits viscosity and density values intermediate between the values of liquids and gases. If we consider that the volume occupied by CO_2 under supercritical conditions is about 350 times smaller than that occupied in gas phase, and that the viscosity under these conditions is relatively small, the most economical means of transporting CO_2 through pipelines is going to be either as a supercritical fluid or as a dense fluid. The supercritical region lies above the critical temperature and pressure and the "dense phase region" is located above the critical pressure, but below the critical temperature.

However, the transported fluid is not pure CO_2, as it contains other compounds derived from both the emission sources and the capture and conditioning processes. The presence of these "impurities" in CO_2 changes its thermodynamic properties: the position of the critical point is affected and the line of liquid–vapour equilibrium is transformed into a phase envelope, enclosing a two-phase region; thus fluid composition determines the minimum pressure necessary to ensure transport in supercritical or dense phase. There are different reasons why transport, and, in general, any operation should be avoided under two-phase flow in this technology (Knoope et al., 2013): (i) cavitation produced by bubble

* Corresponding author. Tel.: +34 976761197.
E-mail address: curra@unizar.es (I. Velasco).

1750-5836/$ – see front matter © 2013 Elsevier Ltd. All rights reserved.
http://dx.doi.org/10.1016/j.ijggc.2013.07.019

implosion in the two-phase region generates shock waves which may cause cracks in the pipeline; (ii) turbulence caused by the bubbles hinder the work of compressors and pumps; and (iii) two-phase flow reduces the quantity of fluid transported. In any case, multiphase flow conditions seem to be unavoidable at startup/failure modes. An equation of state, EoS, for solid CO_2 has been recently published (Trusler, 2011, 2012) that can be solved simultaneously with an equation for the fluid phases to obtain solid–vapour and solid–liquid equilibria, which can be of practical importance when calculating the discharge rate in the event of pipeline failure.

One of the characteristic properties of supercritical fluids in the region near the critical point is the wide variation caused in the density and compressibility values when small changes in pressure, temperature and composition occur. These properties, in turn, influence various parameters that affect the process of transport, having an impact on the overall economic cost of the facilities (ElementEnergy, 2010; Knoope et al., 2013): pipeline diameter, pressure drop, erosional velocity, capacity of the booster stations, etc. As for the injection and storage processes, the density variation due to the presence of impurities affects parameters such as injection flow, solubility parameter, storage capacity and rising velocity of the plume (Blanco et al., 2012).

The variety of emission sources, capture and conditioning processes as well as the storage reservoirs, can cause the composition of the stored fluid to be quite varied. In particular, CH_4 is a likely impurity in the CO_2 capturing process from natural gas sweetening, and is present in significant quantities in some reservoirs (reservoirs exhausted of coal and natural gas); CO is a likely impurity in processes from heavy oil production and upgrading, and both are expected impurities from power plants using pre-combustion capture. Additionally, there is a significant legislative gap regarding the range of compositions allowed in anthropogenic CO_2. As a consequence, the experimental study and thermodynamic modelling of these systems have become important: we must understand how the composition of these systems affect their behaviour and make technology profitable while ensuring maximum safety.

Knoope et al., 2013 recognize a significant knowledge gap in the calculation of the economic costs of the process since none of the models used take into account the impact of impurities on the various design parameters. Moreover, the shortage of experimental data, especially of volumetric properties under conditions relevant to CCS technology, means that there is not a preferred thermodynamic model to predict the behaviour of the fluid to be transported and stored (Li et al., 2011a,b; Sánchez-Vicente et al., 2013). The most common models are based on the use of Equations of State of different nature: cubic (Peng–Robinson, Patel–Teja, etc.), those derived from statistical mechanics (SAFT versions, CPA, etc.) or multiparameter approaches (GERG). However, all of them should be validated with experimental data of mixtures, under conditions at which transportation and storage of anthropogenic CO_2 take place: compositions rich in carbon dioxide, $x_{CO_2} > 0.85$, and pressure and temperature values corresponding to the critical region.

It is also important to know the nature of the interactions between CO_2 molecules and those of compounds which may appear in the capture and storage processes, since they may alter the selectivity in the capturing process or induce additional phenomena during storage. This study can be performed from ab initio calculations (Liu and Wilcox, 2013), molecular dynamics (Lachet et al., 2012) and statistical mechanics (Blanco et al., 2009).

In our current work we have studied the volumetric behaviour of mixtures of carbon dioxide with small amounts of methane or carbon monoxide, at compositions, temperatures and pressures of interest in CCS technology (ElementEnergy, 2010; Li et al., 2011a; ENCAP Project, 2008; EEA, 2012; EPA, 2012): $x_{CO_2} \geq 0.97$, $T = 304.21$ and 308.15 K, and $P = 0.1$–20 MPa. The $CO_2 + CH_4$ and $CO_2 + CO$ systems have been modelled using three different Equations of State: PR (Peng and Robinson, 1976), EoS widely used in engineering for their acceptable results despite the simplicity in implementation; PC-SAFT (Gross and Sadowski, 2001, 2002), EoS nowadays used in various applications including the study of supercritical fluids; and GERG-2008 (Kunz and Wagner, 2012), EoS developed for mixtures containing natural gas components. The three EoS have been validated for these systems under the aforesaid conditions. We have performed a theoretical study of the interactions that occur between the molecules involved in these mixtures near the critical point of the solvent, showing the affinity of the solvent molecules, CO_2, for the solute, CH_4 or CO. The study has been conducted using the Krichevskii function concept (Levelt Sengers, 1994; Japas et al., 1998) and the Kirkwood–Buff Theory (Kirkwood and Buff, 1951). Finally, we have calculated the effect of CH_4 and CO as impurities on various operating transport parameters in CCS technology, by comparing the physicochemical properties of the mixtures with those of pure CO_2. This aspect has not been well studied in the literature. To this end, we have used equations which have been reviewed and widely accepted for modelling by the industrial and engineering community (ElementEnergy, 2010).

2. Materials and methods

2.1. Chemicals

Carbon dioxide (mole fraction > 99.998%), methane (mole fraction > 99.995%) and carbon monoxide (mole fraction > 99.997%) were obtained from Air Liquide and used without further purification.

2.2. Apparatus

Density measurements were carried out using an experimental setup described in a previous work (Velasco et al., 2011). The apparatus was designed and built by ARMINES and the Laboratoire de Thermodynamique des Equilibres entre Phases de l'École Nationale Supérieure des Mines de Paris (France) for fast, reliable and accurate generation of $P\rho T$ data for pure compounds and mixtures over the whole state surface of a fluid encompassing the liquid and vapour compressed phases, and the saturation curve in the (253 to 423) K ± 0.006 K temperature range, up 70 MPa pressure with a precision of 0.025% FS.

The main component of the system is a vibrating tube densimeter Anton Paar DMA HPM which includes the measuring cell and an interface module. Increases or decreases in pressure inside the cell are obtained through mass transfers with respect to the measurement circuit. Connecting the unit to a mPDS 2000V3 evaluation unit allows quasi-continuous data acquisition. A schematic diagram is shown in Fig. S1 (Supporting Information).

2.3. Experimental procedure

A variable-volume cell is used for loading mixtures into the measurement circuit. Successive introduction of compounds allows the preparation of mixtures of accurately determined composition due to successive weighing of the cell on a mass comparator from Sartorius, model CCE 2004, with maximum masses of 2500 g and typical repeatability better than 0.0001 g. The components are introduced in order of increasing volatility and the mixture formed is homogenized through efficient stirring and kept at pressures higher than its bubble point pressure.

The fluid is transmitted from the loading cell to the measurement circuit through a manual pump, which makes it possible to achieve pressures up to 70 MPa inside the measurement circuit (in

this work, the maximum operating pressure was 20 MPa). When the fluid to be studied exhibits phase transition within the operating range of temperature and pressure, the density measurement is performed in two stages: (i) ascending from atmospheric pressure to the pressure corresponding to phase transition; and (ii) descending from the maximum operating pressure down to the pressure of the phase transition. However, when the fluid exhibits no phase transition, as is the case in this work, the measurement is only carried out with descending pressure.

Since we must ensure a quasi-static equilibrium, the pressure changes have been kept sufficiently low; they are usually below 0.005 MPa s^{-1}. Thus, each isotherm in the range of 0.1–20 MPa consists of about 4000 density–pressure points, which are evenly reduced to about 1000 points for easier handling in subsequent calculations. This large number of points makes quasi-continuous isotherms available along subcritical, critical and supercritical regions, and allows the accurate determination of density derivative properties.

2.4. Calibration and uncertainty

The general principle of the vibrating tube densimeter is based on the application of the relation between the vibrating period of a one-dimensional resonator and its vibrating mass. This system has a transversal stiffness, $K = K(T, P)$, and is vibrating with a period, τ, in an undamped harmonic way under the effect of a mechanical excitation. Considering the vibration period, τ, as a pseudo state variable, the $P\tau T$ variables can describe the $P\rho T$ state surface as long as a calibration may provide a direct relation between τ and ρ (Appendix A, Eqs. (A1) and (A2)). In this work, forced path mechanical calibration model, FPMC (Bouchot and Richon, 2001), has been used. This model includes realistic mechanical considerations and forces representing the stress and strain behaviour of the tube material.

In order to evaluate the precision in density results, $\rho = \rho(\rho_{ref}, \tau, P, T)$, uncertainty propagation law has been used (Appendix A, Eq. (A3)). The reference fluid to calibrate was pure CO_2 and the estimated uncertainty in P and T were $u(P) = \pm 0.008$ MPa and $u(P) = \pm 0.006$ K (Velasco et al., 2011). From those and $u(\rho_{ref}) = 0.03\%$ (Span and Wagner, 1996) and $u(\tau) = \pm 2 \times 10^{-5}$ ms (Bouchot and Richon, 2001), the expanded ($k = 2$) uncertainty in the density has been calculated for our mixtures: $u(\rho) = 0.4$–0.7 kg/m^3. On the other hand, the repeatability of the density measurements for mixtures, expressed as relative mean standard deviation (Appendix A, Eqs. (A4)–(A6)), is $\bar{S}^r_\rho = 0.13\%$ (Velasco et al., 2011).

3. Results

3.1. Experimental density

P–ρ–T–x_{CO_2} measurements for $\{CO_2 + CH_4\}$ ($x_{CO_2} = 0.9719$, 0.9809, 0.9902, 0.9932, 0.9961) at $T = 304.21$ K (critical temperature of pure CO_2, Gil et al., 2008) and $\{CO_2 + CO\}$ ($x_{CO_2} = 0.9700$, 0.9810, 0.9902, 0.9930, 0.9960) at $T = 304.21$ and 308.15 K were carried out in the pressure range from 0.1 to 20 MPa.

Experimental results are shown in Fig. 1 for the $CO_2 + CH_4$ system and Fig. 2 ($T = 304.21$ K) and 3 ($T = 308.15$ K) for $CO_2 + CO$ mixtures. Full numerical data are included in Tables S1–S3 in the Supporting Information. As shown in Figs. 1–3, at the studied temperatures the densities of all mixtures change continuously with pressure, and an inflection point appears in the isotherms; that is, the systems are at a supercritical temperature for any composition, a fact which is consistent with literature data on critical locus of these systems (Donnelly and Katz, 1954; Bian et al., 1993; Ke et al., 2001): the critical temperatures of all mixtures under study

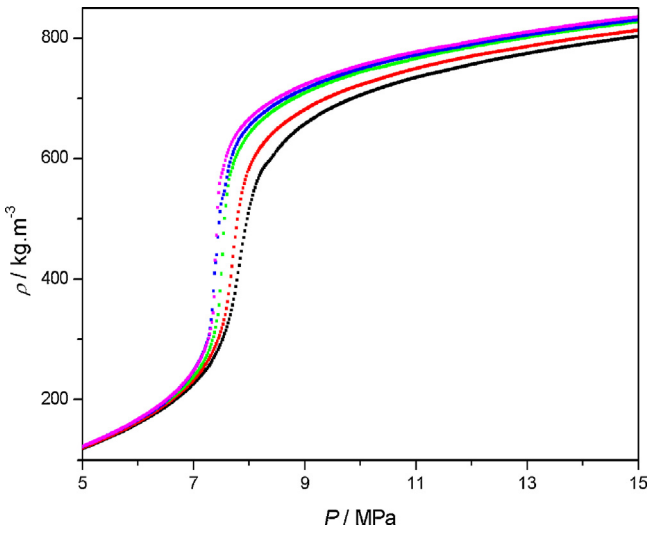

Fig. 1. Experimental densities, ρ, for $CO_2 + CH_4$ mixtures at $T = T_c$ (CO_2) = 304.21 K and several pressures.

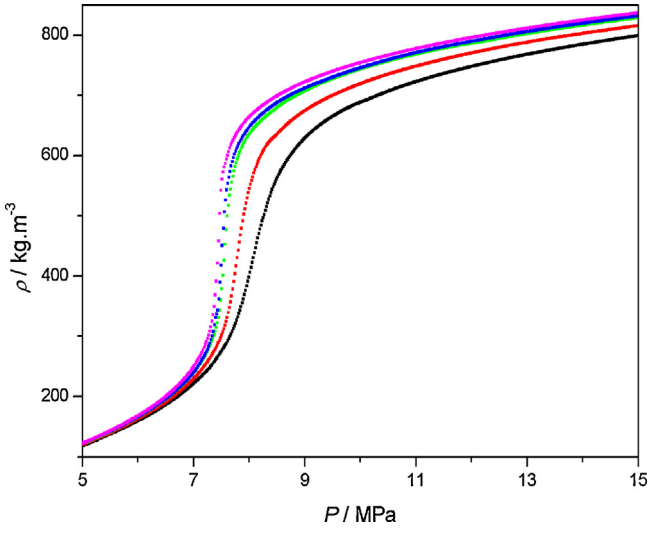

Fig. 2. Experimental densities, ρ, for $CO_2 + CO$ mixtures at $T = T_c$ (CO_2) = 304.21 K and several pressures.

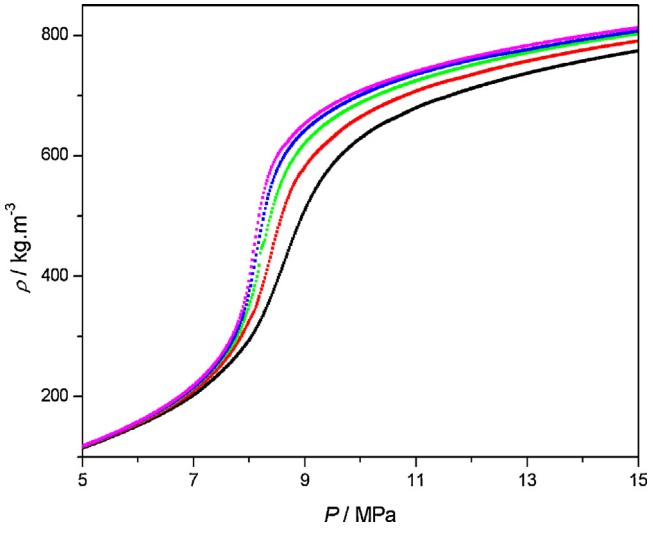

Fig. 3. Experimental densities, ρ, for $CO_2 + CO$ mixtures at $T = 308.15$ K and several pressures.

range from 302.6 K to 303.9 K. At the same temperature (304.21 K) the influence of the presence of CO on the density of the mixtures is higher than that of CH_4. For a given system (CO_2 + CO or CO_2 + CH_4), the influence of the presence of solute on the density of the mixtures is higher at 304.21 K (T_c of pure CO_2) than at 308.15 K (for CO_2 + CH_4 at 308.15, see Blanco et al., 2012).

Table 1 lists literature references for the volumetric properties of the two systems as well as the T–P–x_{CO_2} ranges of each study. As can be seen, the system CO_2 + CH_4 has been widely studied, however there are only eight studies in which the values of temperature, pressure and composition are of interest in CCS technology, and solely the data published by Zhang et al. (2002) and Blanco et al. (2012) analyzed the region of infinite dilution, IDS, the region that has been studied in our current work. Our experimental data are consistent with those but not directly comparable since temperature do not match. We have carried out a comparison between the experimental density data from Blanco et al. (2012), used further in this study, for the mixture of composition $x_{CO_2} = 0.9961$ and those published by Zhang et al. (2002) for the mixture $x_{CO_2} = 0.997$, both at T = 308.15 K, obtaining a mean relative deviation (Appendix A, Eq. (A7)): MRD_ρ = 2.2%

For the CO_2 + CO system the extent of literature data is rather small. Mallu et al. (1987) and Cipollina et al. (2007) have studied its volumetric behaviour, and our experimental data are consistent with those but not directly comparable, since the compositions do not match.

3.2. Isothermal compressibility

From the P–ρ–T–x_{CO_2} experimental values of the mixtures studied, we have evaluated the effect of pressure on density at the critical temperature of pure solvent, T = 304.21 K, by means of the isothermal compressibility, κ_T, defined as:

$$\kappa_T = \left(\frac{1}{\rho}\right)\left(\frac{\partial \rho}{\partial P}\right)_T \quad (1)$$

Figs. 4 and 5 show the κ_T–x_{CO_2}–P representations for CO_2 + CH_4 and CO_2 + CO mixtures, respectively. It can be seen that the dependence of the isothermal compressibility on pressure and composition is similar for both systems: (i) κ_T varies with pressure, going through a maximum; (ii) the maximum value of κ_T increases as the composition of CO_2 goes up, since the critical temperature of the increasingly CO_2 rich mixture approaches the critical temperature of CO_2; and (iii) the pressure at which the maximum in κ_T occurs decreases as the composition of CO_2 rises, since the critical pressures, P_c, of both systems decrease when x_{CO_2} increases (Donnelly and Katz, 1954; Bian et al., 1993; Ke et al., 2001). Moreover, when comparing the mixture compressibility for the two systems with the same concentration, we observe that if $x_{CO_2} < 0.99$, the maximum value for the isothermal compressibility of the CO_2 + CH_4 system is higher than that for CO_2 + CO and when $x_{CO_2} > 0.99$, this trend is reversed.

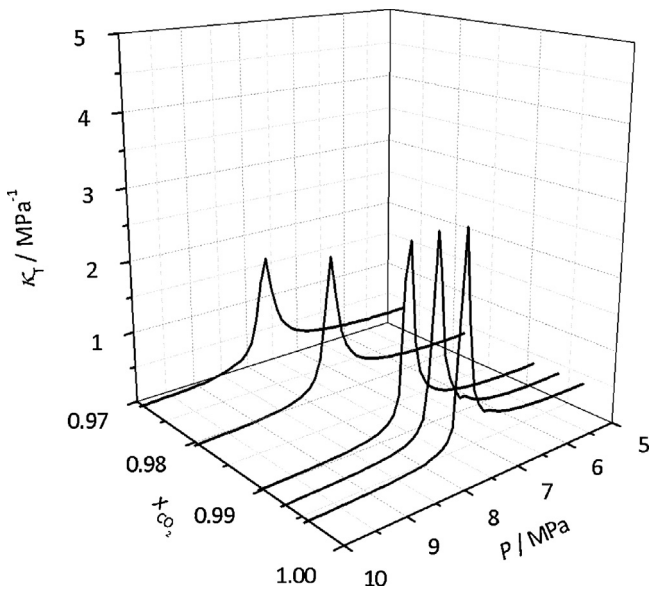

Fig. 4. The κ_T–x_{CO_2}–P representations for CO_2 + CH_4 mixtures at $T = T_c$ (CO_2) = 304.21 K.

3.3. Excess molar volume and solute partial molar volume

From experimental data obtained in this work and literature experimental values for the CO_2 + CH_4 system at 308.15 K (Blanco

Table 1
Summary of T–P–x_{CO_2} ranges of mixtures studied in this work.

System	No. points	Range T (K)	Range P (MPa)	Range x_{CO_2}	Reference
CO_2 + CH_4	476	311–478	1.4–68.9	0.15–0.80	Reamer et al. (1944)
	28	293–453	4.1–19.3	0.20–0.80	Beer (1969)
	186	253–288	2.4–14.5	0.45–0.96	Arai et al. (1971)
	63	283–322	4.7–20.7	0.91	Simon et al. (1977)
	118	220–320	0.1–48.3	0.48	Esper (1987)
	91	225–400	2.1–35.8	0.98	Magee and Ely (1988)
	155	300–320	0.2–9.8	0.10–0.90	Brugge et al. (1989)
	28	289	0.03–6.7	0.1	Lemming (1989)
	64	323–398	0.1–6.5	0.482	Mallu and Viswanath (1990)
	298	270–350	0.2–28.4	0.31	Jaeschke and Humphreys (1991)
	149	279–308	3.7–6.4	0.10–0.48	Jaeschke et al. (1997)
	44	673	19.9–99.9	0.10–0.90	Seitz and Blencoe (1996)
	194	323–573	9.9–99.9	0.10–0.90	Seitz et al. (1996)
	228	225–350	1.8–69.5	0.10–0.90	Hwang et al. (1997)
	17	273–290	2.0–9.5	0.06–0.15	Glos et al. (2001)
	22	308	5.4–12.1	0.997	Zhang et al. (2002)
	324	233–373	0.2–20.7	0.08–0.15	Wöll and El Hawary (2003)
	315	250–400	1–20	0.20–0.60	Móndejar et al. (2012)
	49,000	253–333	0.1–20	0.85–0.996	Blanco et al. (2012)
	5000	304	0.1–20	0.97–0.996	This work
CO_2 + CO	75	323–423	0.1–6.5	0.57	Mallu et al. (1987)
	56	308–343	26.0–47.0	0.86–0.93	Cipollina et al. (2007)
	10,000	304–308	0.1–20	0.97–0.996	This work

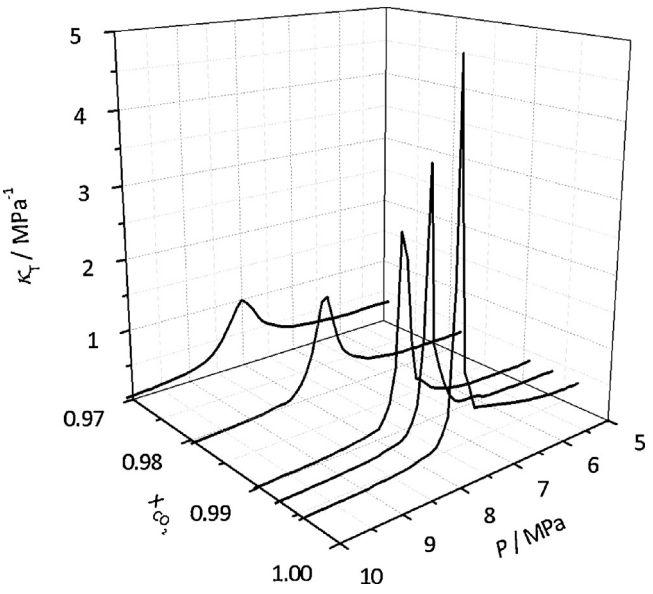

Fig. 5. The κ_T–x_{CO_2}–P representations for CO_2 + CO mixtures at $T = T_c$ (CO_2) = 304.21 K.

et al., 2012), we have calculated the excess molar volume of the mixture, V_m^E, using the following expression:

$$V_m^E = V_m - V_1 - V_2 = \frac{x_1M_1 + x_2M_2}{\rho_m} - \frac{x_1M_1}{\rho_1} - \frac{x_2M_2}{\rho_2} \quad (2)$$

where the subscripts 1, 2 and m refer to solvent (CO_2), solute (CH_4 or CO), and mixture, respectively; M_i is the molar mass of each component i in the mixture, and V_i, V_m, ρ_i and ρ_m are the molar volume and the density for the pure compounds and the mixture at temperature T and pressure P.

Due to the small values of the densities of these mixtures at low pressures, we have calculated the expanded (k = 2) uncertainties in the excess molar volumes in the 5–20 MPa range. The rules of propagation of errors (Appendix A, Eq. (A3)) have been used, obtaining the values $U(V_m^E)$ 0.1–1 cm^3.mol^{-1}.

Fig. 6 shows the trends in the excess molar volumes, V_m^E, with pressure and composition for two mixtures, $x_{CO_2} \cong 0.971$ and $x_{CO_2} \cong 0.993$, of both systems at the two operating temperatures.

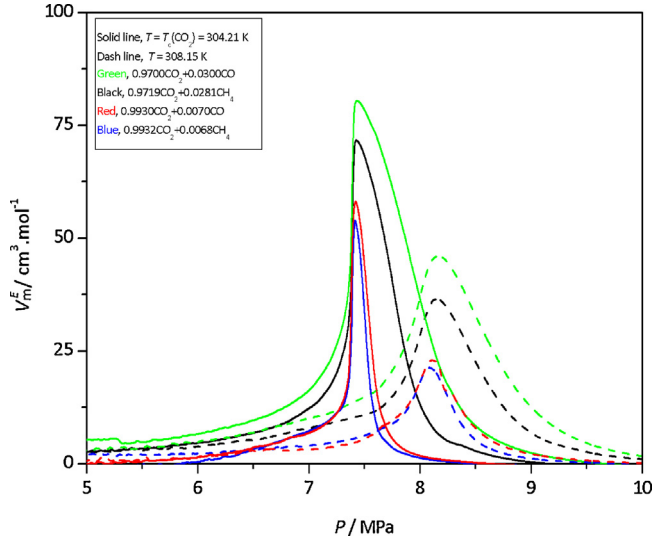

Fig. 6. The V_m^E–P representation for studied systems at $T = T_c$ (CO_2) = 304.21 K and T = 308.15 K, $x_{CO_2} \cong 0.971$ and $x_{CO_2} \cong 0.993$ mole fractions.

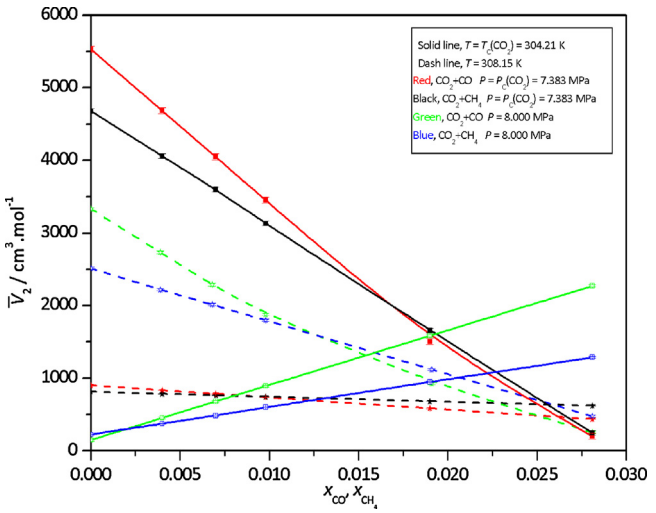

Fig. 7. Solute partial molar volume, $\bar{V}_2$, versus solute mole fraction, $x_{CH_4\text{-}CO}$, for studied systems at P = 7.383 and 8.000 MPa and at T = 304.21 and T = 308.15 K.

They are supercritical mixtures and we observe a peak in the excess molar volume: $P \cong 7.41$ MPa at T = 304.21 K and $P \cong 8.15$ MPa at T = 308.15 K. The value of the maximum for V_m^E decreases with increasing temperature and molar fraction of CO_2. Finally, the maxima in V_m^E for CO_2 + CO mixtures are higher than for mixtures CO_2 + CH_4, which means that the inclusion of a molecule of CO in pure CO_2 disturbs the system to a further extent than when introducing a molecule of CH_4. This may be due to either the dipolar moments ($\mu_{CO_2} = \mu_{CH_4} = 0$; $\mu_{CO} = 0.122$ D), the sizes of the components of each system (the size difference between the molecules of CO_2 and CH_4 is smaller than that between CO_2 and CO), or both.

From the density data, the partial molar volume of the solute, $\bar{V}_2$, has been calculated for the five studied compositions of each system at temperatures of 304.21 and 308.15 K and selected pressures of 7.383 MPa (critical pressure of pure CO_2) and 8.000 MPa (supercritical pressure). To this end we have used the following expression:

$$\bar{V}_2 = V_m + (1 - x_2)\left(\frac{\partial V_m}{\partial x_2}\right)_{P,T} \quad (3)$$

where the subscripts 2 and m refer to solute (CH_4 or CO) and mixture respectively, and Vm is the molar volume of the mixture at temperature T and pressure P. $(\partial V_m/\partial x_2)_{P,T}$ values have been calculated from polynomial fittings of V_m vs. x_2, V_m being the first term on the right hand side of Eq. (2).

The expanded (k = 2) uncertainty in $\bar{V}_2$ have been calculated using the rules of propagation of errors (Appendix A, Eq. (A3)). The values are $U(\bar{V}_2) = 3$–85 cm^3 mol^{-1}.

Fig. 7 shows trends in the partial molar volumes of the solute, $\bar{V}_2$, with solute concentration at the pressures and temperatures indicated above. A similar behaviour is observed for the two systems under study: at $P = P_c(CO_2) = 7.383$ MPa, $\bar{V}_2$ decreases with increasing solute concentration at both working temperatures, with a much smaller slope at 308.15 K. By contrast, at the supercritical pressure, P = 8.000 MPa, $\bar{V}_2$ increases with increasing solute concentration at T = 304.21 K, and decreases at T = 308.15 K.

We have compared (Fig. S2, Supporting Information) the values of $\bar{V}_2$ calculated in this work for the {0.9961CO_2 + 0.0039CH_4} mixture with those calculated by Zhang et al. (2002) for the {0.997CO_2 + 0.003CH_4} mixture at 308.15 K, observing good agreement, especially in the dense region. The mean relative deviation, calculated with Eq. (A7) (Appendix A), at the point corresponding to the maximum value of $\bar{V}_2$ is $MRD_{\bar{V}_2} < 6\%$.

Table 2
Parameters used for modelling the systems studied in this work with PR and PC-SAFT EoS.

Pure compound parameter	CO_2	CH_4	CO
T_c (K)	304.21[a]	190.56[b]	132.86[b]
P_c (MPa)	7.383[a]	4.599[b]	3.494[b]
ω	0.224[b]	0.011[b]	0.066[b]
m	2.0730[c]/2.1276[d]	1.0000[c]/1.0039[e]	1.3097[c]/1.3063[e]
σ (Å)	2.7852[c]/2.8251[d]	3.7039[c]/3.7126[e]	3.2507[c]/3.2565[e]
ε (K)	169.21[c]/163.76[d]	150.03[c]/149.11[e]	92.15[c]/91.48[e]
Δv_c (10^{-3} m^3/kg)	0.02[f]/0.17[d]	–	−0.1[f]/−0.1[e]

Used in PR and PC-SAFT EoS: T_c, critical temperature; P_c, critical pressure; ω, acentric factor.
Used in PC-SAFT EoS: m, segment number; σ, segment diameter; ε, segment energy parameter; Δv_c, volume shift.

Binary interaction parameter, k_{ij}	$CO_2 + CH_4$	CO_2 + CO
Peng–Robinson EoS	0.12[b]	−0.15[g]
PC-SAFT EoS	0.07[f]/0.05[e]	0.12[f]/0[e]

[a] Gil et al. (2008).
[b] Laursen (2012).
[c] PC-SAFT original model; Gross and Sadowski (2001).
[d] PC-SAFT rescaled model; Blanco et al. (2009).
[e] PC-SAFT rescaled model; this work.
[f] PC-SAFT original model; this work.
[g] Ke et al. (2001).

The strong dependence of V_m^E on pressure and composition (Fig. 6) demonstrates the non-ideality of the studied systems. However, the greater values of V_m^E and $(\partial \bar{V}_2/\partial x_2)$ exhibited by the CO_2 + CO system suggest that this system deviates from ideality further than $CO_2 + CH_4$

4. Modelling

Due to the variety of compositions that the transported and later stored fluid can present, as well as the pressure and temperature operational ranges within CCS technology, it is interesting to develop effective working tools which will allow to correctly predict the phase and volumetric behaviour of the fluid. To do this, our experimental P–ρ–T results have been compared, in terms of relative mean deviation, MRD_X (Appendix A, Eq. (A7)), with those calculated using three different types of Equations of State, validating them for these experimental conditions.

Peng–Robinson EOS (Peng and Robinson, 1976). The cubic equations are the simplest EoS which predict the existence of a critical point and quantitative representation of VLE. Their simple structure, which requires little input information, make them popular for engineering applications.

The parameters used for the pure components, as well as the binary interaction parameter, k_{ij}, included in the mixing rule of a van der Waals fluid, are shown in Table 2. A comparison between our experimental data and those calculated with the PR EoS are shown in Table 3. Despite its simplicity, the agreement with experimental data is good at pressures below the critical pressure, $MRD_\rho = 1.8\%$ for both systems, and acceptable at higher pressures: $MRD_\rho(CO_2 + CH_4) = 4.4\%$ and $MRD_\rho(CO_2 + CO) = 4.1\%$.

PC-SAFT EoS (Gross and Sadowski, 2001, 2002). In this model, based on Wertheim's first order thermodynamic perturbation theory, the reference fluid is the hard-chain fluid. Attractive intermolecular forces are further separated into different contributions, so that the Helmholtz energy, a, is written as the sum of the ideal-gas contribution, a^{id}, a hard-chain term, a^{hc}, a contribution for the dispersive attraction, a^{dis}, and several terms for associating, dipolar and quadrupolar interactions. In this work, we have not taken into account the polar and association contributions, therefore the terms contributing to the Helmholtz energy are as follows:

$$a = a^{id} + a^{hc} + a^{dis} \quad (4)$$

For the non-polar pure compounds, three parameters are needed: the segment number, m, the segment diameter, σ, and the segment energy parameter, ε. These parameters provide an accurate representation for both volumetric and VLE properties if they are obtained from vapour pressures and liquid densities; however, they always overestimate the critical properties. In order to describe the critical region, different authors (Cismondi et al., 2005; Blanco et al., 2009; Gil et al., 2010, 2012) perform a rescaling of pure–compound parameters using their T_c and P_c. In this work we have applied PC-SAFT EoS to our systems with both options, using pure compounds parameters (m,σ,ε) original and rescaled. Moreover, in both cases, we have adjusted the experimental density values of pure CO_2 and CO using volume shift, Δv_c.

The parameters used for the pure components, the mixing parameters and a comparison between our experimental data

Table 3
Comparison between the experimental P–ρ–T–x_{CO_2} data for the systems studied in this work and those calculated using PR, PC-SAFT and GERG EoS.

$CO_2 + CH_4$	MRD_ρ (%) T = 304.21 K			MRD_ρ[a] (%) T = 308.15 K		
	PR	PC-SAFT	GERG	PR	PC-SAFT	GERG
$x_{CO_2} = 0.9719$	3.4	1.4[b]/2.6[c]	0.5	3.4	1.4[b]/2.6[c]	0.4
$x_{CO_2} = 0.9809$	3.2	1.8[b]/2.7[c]	0.2	3.6	1.7[b]/2.9[c]	0.4
$x_{CO_2} = 0.9902$	3.4	1.7[b]/2.8[c]	0.4	3.6	2.0[b]/3.0[c]	0.3
$x_{CO_2} = 0.9932$	3.4	1.9[b]/2.8[c]	0.5	3.8	1.7[b]/3.0[c]	0.4
$x_{CO_2} = 0.9961$	3.4	1.8[b]/2.8[c]	0.3	3.8	1.7[b]/2.8[c]	0.4
MRD_ρ (%)	*3.4*	*1.7[b]/2.7[c]*	*0.4*	*3.7*	*1.7[b]/2.9[c]*	*0.4*
CO_2 + CO	MRD_ρ (%) T = 304.21 K			MRD_ρ (%) T = 308.15 K		
	PR	PC-SAFT	GERG	PR	PC-SAFT	GERG
$x_{CO_2} = 0.9700$	2.8	1.5[b]/2.6[c]	1.8	3.1	1.3[b]/2.4[c]	1.5
$x_{CO_2} = 0.9810$	3.1	1.4[b]/2.7[c]	1.4	3.4	1.2[b]/2.6[c]	1.6
$x_{CO_2} = 0.9902$	3.4	1.4[b]/2.8[c]	1.1	3.4	1.4[b]/2.7[c]	0.7
$x_{CO_2} = 0.9930$	3.2	1.6[b]/2.7[c]	0.7	3.7	1.4[b]/2.9[c]	0.8
$x_{CO_2} = 0.9960$	3.4	1.7[b]/2.7[c]	0.8	3.6	1.5[b]/2.8[c]	0.7
MRD_ρ (%)	*3.2*	*1.5[b]/2.7[c]*	*1.1*	*3.4*	*1.4[b]/2.7[c]*	*1.1*

[a] Experimental data from Blanco et al. (2012).
[b] PC-SAFT original model.
[c] PC-SAFT rescaled model.

and calculated values are found in Tables 2 and 3 respectively. When the original parameters for the pure compounds are used (Gross and Sadowski, 2001, 2002), the model predicts in the vicinity of the critical pressure, P_c, an erroneous subcritical state for many of our mixtures when in reality those are at supercritical conditions. Mean relative deviations in this region (P = 7–9 MPa) are $MRD_\rho(CO_2 + CH_4) = 12.8\%$ and $MRD_\rho(CO_2 + CO) = 8.1\%$. However, the agreement outside the critical region is much better: $MRD_\rho(CO_2 + CH_4) = 0.5\%$ and $MRD_\rho(CO_2 + CO) = 0.8\%$. On the other hand, if the parameters used are rescaled using the critical points of the pure compounds, the model predicts supercritical state for all mixtures and represents the critical region more accurately, with $MRD_\rho(CO_2 + CH_4) = 5.7\%$ and $MRD_\rho(CO_2 + CO) = 5.6\%$, although the deviation for the remaining pressures is higher: $MRD_\rho(CO_2 + CH_4) = 2.5\%$ and $MRD_\rho(CO_2 + CO) = 2.4\%$.

GERG EoS (Kunz and Wagner, 2012). International reference equation of state for natural gases based on a multi-fluid approximation. This approximation divides the Helmholtz energy formula into three terms: one term to account for ideal gas behaviour, a second term describing the contributions of pure substances and a third term for the departure function. This equation covers subcritical, critical and supercritical regions as well as liquid–vapour phase boundaries but its accuracy decreases when the GERG database contains few experimental data of the studied system. It should also be noted that the uncertainty increases in both density and VLE calculations of CO_2-rich mixtures (Li et al., 2011a).

As can be seen from Table 3, a comparison between our experimental data and those calculated with the GERG EoS is very good for both systems; the deviation for $CO_2 + CH_4$ is smaller, since the EoS developed for this system uses a larger number of experimental data, covering a wider range of pressures. However, for $CO_2 + CO$, the EoS GERG database only contains VLE data in the pressure range from 0.1 to 6 MPa. The deviations obtained are: $MRD_\rho(CO_2 + CH_4) = 0.4\%$ and $MRD_\rho(CO_2 + CO) = 1.0\%$.

GERG EOS is the equation that best represents our experimental results, although its extension to mixtures with compounds not included in their database is complex. By contrast, PC-SAFT EoS offers slightly higher deviations than GERG, but its use can be extended easily to multicomponent mixtures. Finally, PR EoS may be adequate, depending on the working pressure and the accuracy required.

Fig. 8a and b depicts the relative deviations between the experimental densities and the values calculated using PR, PC-SAFT and GERG EoS for selected mixtures studied in this work (different solute, composition and temperature). Deviations are similar at both temperatures for pressure values removed from the critical, while in the near-critical zone the nearer the temperature (to the critical value) the higher the deviations.

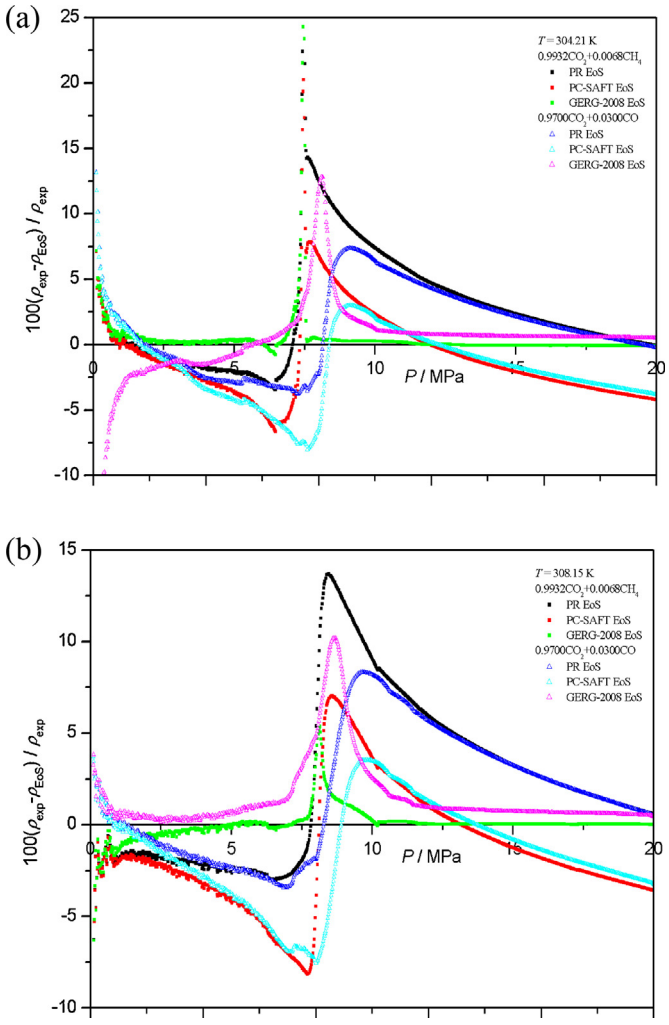

Fig. 8. Relative deviation between the experimental densities and the values calculated using different EoS, for several mixtures studied in this work. (a) T = 304.21 K; (b) T = 308.15 K.

5. Discussion

5.1. Study of the interaction CO_2 – impurity

The efficiency and selectivity of the capture processes are influenced by the type of interactions between the molecules present, that is, by their affinity. Moreover, once the fluid is stored, CO_2 molecules can interact with other molecules present in the reservoir, consequently modifying the behaviour of the plume (Blanco et al., 2012). In this section we determine the nature of the interactions between solvent molecules, CO_2, and those of the solute, CH_4 or CO, through a volumetric study in the critical region of infinitely dilute solutions, IDS, for systems {CO_2 (1) + CH_4 or CO (2)}. We use the Krichevskii function concept (Levelt Sengers, 1994; Japas et al., 1998) and the Kirkwood–Buff Theory (Kirkwood and Buff, 1951).

5.1.1. Krichevskii function

The Krichevskii function, J, represents the pressure change that occurs in a system when a molecule of solvent is replaced by one of the solute at constant T and V in IDS. When the conditions of T and V correspond to critical conditions for the pure solvent, the Krichevskii function, J, becomes the Krichevskii parameter, A_{Kr}:

$$J = \left(\frac{\partial P}{\partial x_2}\right)_{T,V}^{\infty} \tag{5}$$

$$A_{Kr} = \left(\frac{\partial P}{\partial x_2}\right)_{Tc,Vc}^{C,\infty} \tag{6}$$

According to Eqs. (5) and (6), given a number of volumetric data at infinite dilution, the values for the Krichevskii function (including the parameter A_{Kr}) can be calculated from the slopes of the isotherms–isochores P–x_2 when $x_2 \to 0$.

Fig. 9a and b shows some experimental results on the P–x_{CH_4} and P–x_{CO} planes at T = 304.21 K for mixtures studied along various isochores, including the critical. The slopes of the P–x_2 graphs increase in both systems with increasing density, being greater when CO is the solute. The slopes along the critical isothermal–isochoric, the Krichevskii parameter, for our systems are shown in Table 4. In the literature we have found some values for the $A_{Kr}(CO_2 + CH_4)$ parameter; the mean relative deviations between our results and the

Table 4
Comparison between the values obtained for the $CO_2 + CH_4$ and $CO_2 + CO$ systems for several structural parameters and properties: Krichevskii parameter, A_{Kr}; reduced Krichevskii parameter, A^*_{Kr}; maximum value of the partial molar volume of solute at infinite dilution at $T = 308.15$ K, $(\bar{V}_2^{\infty})_{max}$; minimum value of the excess solvent number at $T = 308.15$ K, $(N_{exc}^{\infty})_{min}$; cluster size at $T = 308.15$ K, $(N_1^{exc})_{max}$, and direct correlation function integrals, C_{ij} at $\rho = \rho_c$ (CO_2) and $T = 308.15$ K.

Parameter/property	T (K)	System	
		$CO_2 + CH_4$	$CO_2 + CO$
A_{Kr} (MPa)	304.21	20.383 ± 0.004	26.418 ± 0.005
A^*_{Kr}	304.21	0.76	0.98
$(\bar{V}_2^{\infty})_{max}$ (cm³/mol)	308.15	3300	3950
$(N_{exc}^{\infty})_{min}$	308.15	−33	−38
$(N_1^{exc})_{max}$	308.15	11	3
$10^{-3}(C_{12})_{\rho_c}$ (cm³/mol)	308.15	0.020	0.006
$10^{-3}(C_{11} - C_{12})_{\rho_c}$ (cm³/mol)	308.15	0.072	0.085

literature are: $MRD_{A_{Kr}} = 1.6\%$ (Furuja and Teja, 2000) and $MRD_{A_{Kr}} = 8.0\%$ (Abdulagatov et al., 2007).

The values of the P–x_2 slopes on the rest of isochores allow us to complete the study of the behaviour of IDS when expanding it to other states different to the critical point. Fig. 10 shows the evolution of the Krichevskii function, J, with the density of the pure solvent, ρ_{CO_2}, at $T = 304.21$ and 308.15 K for the two systems under study. As can be seen, J is positive over the entire range of densities and its values are slightly higher and less sensitive to temperature for $CO_2 + CO$ than for the $CO_2 + CH_4$ system.

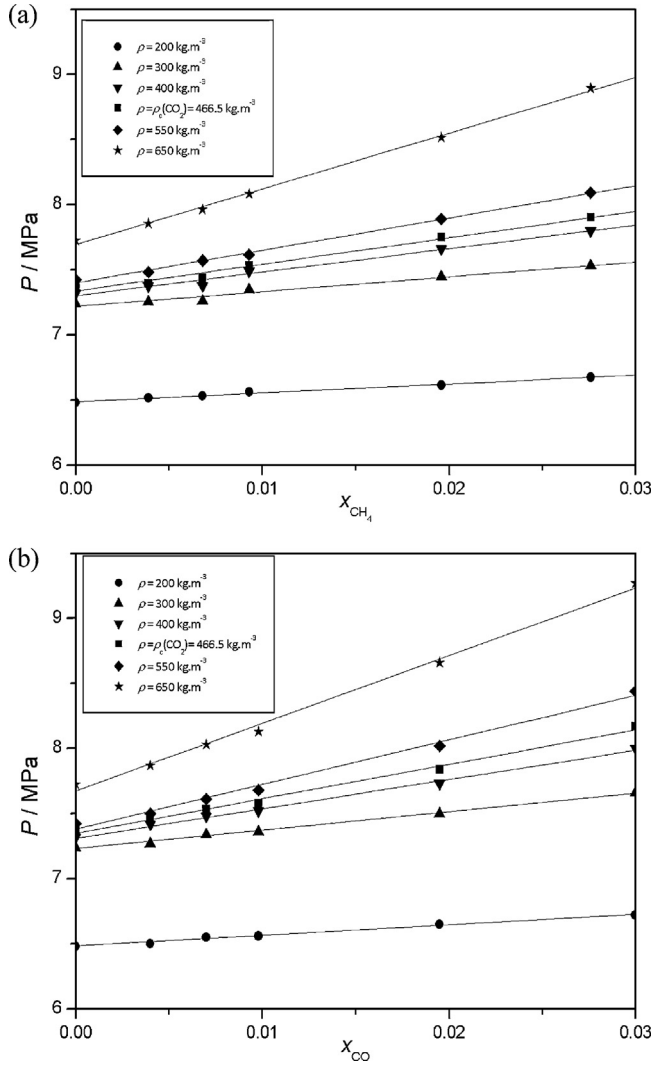

Fig. 9. (a) P–x_{CH_4} data for $\{CO_2\ (1) + CH_4\ (2)\}$ dilute mixtures and (b) P–x_{CO} data for $\{CO_2\ (1) + CO\ (2)\}$ dilute mixtures, for several isochores at $T = 304.21$ K.

The partial molar volume of solute at infinite dilution, $\bar{V}_2^{\infty}$, can be expressed in terms of the Krichevskii function, J (Blanco et al., 2009):

$$\rho_1^0 \bar{V}_2^{\infty} = [1 + \kappa_T^0 J] \quad (7)$$

where the superscripts 0 and ∞ denote pure component and infinite dilution, respectively, and ρ_1^0 and κ_T^0 are the density and the isothermal compressibility of the solvent.

In the vicinity of the critical point of the solvent, $J \to A_{Kr}$ and the compressibility of the pure solvent, κ_T^0, is a divergent function ($\kappa_T^0 \to +\infty$); therefore, under these conditions, the partial molar volume of the solute at infinite dilution will also be divergent $\bar{V}_2^{\infty} \to +\infty$, and the sign of the Krichevskii parameter will define the sign of such divergence. For the two mixtures studied in this work, the parameter $A_{Kr} > 0$, thus at the critical point of the solvent, $\bar{V}_2^{\infty} \to +\infty$. A representation of $\bar{V}_2^{\infty}$ vs ρ_{CO_2} can be seen in Fig. S3 (Supporting Information). Table 4 shows the maximum values of $\bar{V}_2^{\infty}$ exhibited by our systems at a temperature of 308.15 K; these peaks appear in the vicinity of the critical pressure (≅8 MPa) and the value is higher for the $CO_2 + CO$ mixture, which suggests that the substitution of a molecule of CO_2 by one of CO results in a bigger change in the volume of the system than if the replacing molecule were CH_4.

The only value found in the literature for the partial molar volume at infinite dilution of the systems studied has been published by Abdulagatov et al. (2007) for the $CO_2 + CH_4$ system. These authors find a negative sign for the divergence of $\bar{V}_2^{\infty}$, which is not consistent with the positive sign of their own value of A_{Kr}.

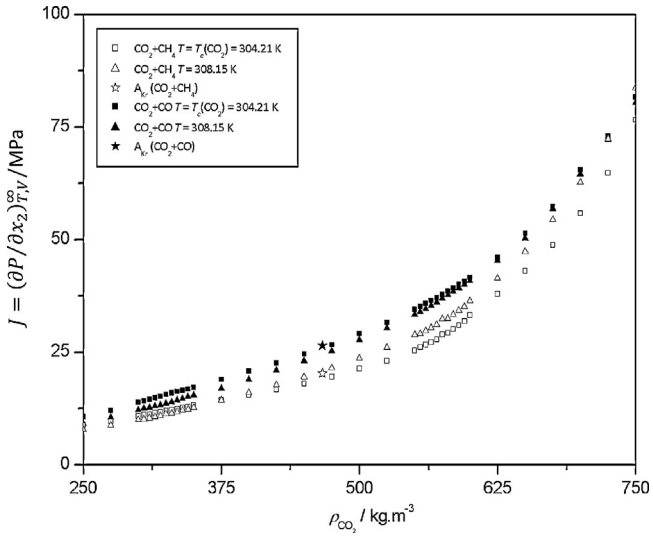

Fig. 10. Krichevskii function, J, versus density of the pure solvent, ρ_{CO_2}, for the $\{CO_2\ (1) + CH_4\ (2)\}$ and $\{CO_2\ (1) + CO\ (2)\}$ systems at $T = 304.21$ K and $T = 308.15$ K.

5.1.2. Structural properties

The study of a fluid structure can be conducted through the so-called Inversion of the Kirkwood–Buff Theory (Kirkwood and Buff, 1951), developed by Ben-Naim in 1977. In it, measurements of thermodynamic properties are used to calculate Kirkwood–Buff integrals, $G_{ij} = \int_0^\infty [g_{ij}(r) - 1]4\pi r^2\, dr$, where $g_{ij}(r)$ is the pair correlation function or radial distribution function for species i and j, and represents the probability of finding the particle i at a distance r of the particle j. Strictly speaking, the G_{ij} integrals are not molecular properties, however, they provide information about the species' local packing.

For a binary mixture at infinite dilution conditions, $x_2 \to 0$, the Kirkwood–Buff equations are simplified (Lee and Cochran, 1994; Chialvo and Cummings, 1995) to:

$$\rho_1^0 \bar{V}_2^\infty = 1 + \rho_1^0 (G_{11}^0 - G_{12}^\infty) \tag{8}$$

$$\rho_1^0 RT\kappa_T^0 = 1 + \rho_1^0 G_{11}^0 \tag{9}$$

Considering Eqs. (7) and (8):

$$J = \frac{\rho_1^0 (G_{11}^0 - G_{12}^\infty)}{\kappa_T^0} \tag{10}$$

Alternatively, the Kirkwood–Buff equations and the expression for the Krichevskii function can be written in terms of the direct correlation function integral (DCFI), $C_{ij} = \int c_{ij}\, dr$ where c_{ij} represents the direct correlation due solely to the interaction forces exerted between two particles in a system of N-2 particles.

$$\rho_1^0 \bar{V}_2^\infty = \rho_1^0 RT\kappa_T^0 (1 - C_{12}^\infty) \tag{11}$$

$$(\kappa_T^0)^{-1} = \rho_1^0 RT(1 - C_{11}^0) \tag{12}$$

$$J = \rho_1^0 RT(C_{11}^0 - C_{12}^\infty) \tag{13}$$

As can be seen in Eqs. (10) and (13), J represents the difference between solvent–solvent (1–1) and solvent–solute (1–2) interactions, making it possible to evaluate the ideality of the mixture: a value close to zero indicates that these interactions are very similar. The equations above show that, in IDS, the rearrangement of the solvent around the solute, in relation to the structure of the pure solvent, is not determined by the strength of the interaction between the molecules of solvent and solute, but defined by the intermolecular asymmetry. The values of the direct correlation function integrals, C_{ij}, for $CO_2 + CH_4$ are higher than for $CO_2 + CO$ (Table 4 shows one of them, $(C_{12})_{\rho_c}$). However, the greater asymmetry of the second system causes a more extensive change in the structure of the solvent, as evidenced by higher values of $(C_{11}–C_{12})$; a graphical representation is shown in Fig. S4 (Supporting Information).

N_{exc}^∞ is defined as the excess number of solvent molecules around a solute molecule in the IDS, in relation to the number of solvent molecules around another solvent molecule. This parameter is related to the radial distribution functions for the interactions solvent–solute (1–2) and solvent–solvent (1–1) and consequently with the Krichevskii function:

$$N_{exc}^\infty = (N_{12} - N_{11})4\pi\rho_1^0 \int_0^{R_{shell}} [g_{12}(r) - g_{11}(r)]r^2\, dr$$

$$= -\kappa_T^0 \left(\frac{\partial P}{\partial x_2}\right)_{T,V}^\infty \tag{14}$$

where N_{12} represents the number of solvent molecules around a solute molecule and N_{11} indicates that each solvent molecule is surrounded by a box of N_{11} solvent molecules. If we consider the sign obtained for the Krichevskii function in our current work, we realize that the replacement of one molecule of solvent by another of solute, at constant volume and temperature, causes a decrease in the local density of CO_2 molecules around a molecule of solute in the IDS compared to that of pure CO_2, and the effect is greater for CO than for CH_4. A plot of N_{exc}^∞ vs ρ_{CO_2} is shown in Fig S5 (Supporting Information), and Table 4 lists the minimum values found for the excess coordination number, N_{exc}^∞, of our systems at 308.15 K.

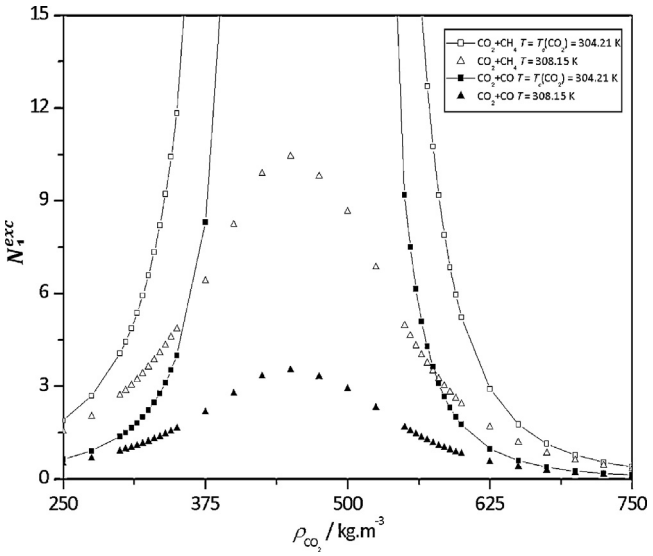

Fig. 11. Affinity of solvent molecules for a solute molecule (cluster size), N_1^{exc}, versus density of the pure solvent, ρ_{CO_2}, for the {CO_2 (1) + CH_4 (2)} and {CO_2 (1) + CO (2)} systems at T = 304.21 K and T = 308.15 K.

Moreover, the affinity of solvent molecules for a molecule of solute, or cluster size, N_1^{exc}, may be calculated from the properties of the pure solvent and from the so-called dimensionless Krichevskii parameter $A_{Kr}^* = A_{Kr}/\rho_1^0 RT$,

$$N_1^{exc} = 4\pi\rho_1^0 \int_0^{R_{shell}} [g_{12}(r) - 1]r^2\, dr = \rho_1^0 RT\kappa_T^0 (1 - A_{Kr}^*) \tag{15}$$

Fig. 11 shows the evolution of N_1^{exc} with the density of pure solvent for our systems: it becomes a divergent function at the solvent critical point, $N_1^{exc} \to +\infty$, and at 308.15 K, the maximum for the $CO_2 + CO$ system is smaller in magnitude than that for $CO_2 + CH_4$ (Table 4).

Finally, according to Wheeler's decorated lattice model (Wheeler, 1972), the behaviour of a near-critical system can be classified in terms of the solvent–solute interaction energy, ε_{12}, when adding a solute molecule to the solvent under isobaric and isothermal conditions: (i) attractive behaviour ($\varepsilon_{12} \ll 0$) which results in a volume contraction and an enrichment of solvent around the solute ($\bar{V}_2^\infty \to -\infty, N_1^{exc} \to +\infty$); (ii) weakly attractive behaviour ($\varepsilon_{12} < 0$), causing a volume expansion together with an enrichment in solvent ($\bar{V}_2^\infty \to +\infty, N_1^{exc} \to -\infty$); and (iii) repulsive behaviour ($\varepsilon_{12} > 0$) that leads to a volumetric expansion and a decrease in solvent around the solute ($\bar{V}_2^\infty \to +\infty, N_1^{exc} \to -\infty$). Debenedetti and Mohamed in 1989 and Lee and Cochran in 1994 established that for IDS in the vicinity of the critical point, mixtures can be classified within the previous regimes depending on the sign of the Krichevskii parameter, A_{Kr}, the value of the dimensionless parameter, A_{Kr}^*, and the divergence signs for different properties: $\bar{V}_2^\infty$, N_{exc}^∞, and N_1^{exc}.

For the mixtures included in this study:

$$A_{Kr} > 0; \quad \bar{V}_2^\infty \to +\infty; \quad N_1^{exc} \to -\infty; \quad 1 > A_{Kr}^* > 0; \quad N_1^{exc} \to +\infty$$

Therefore we can conclude that both systems, near the solvent critical point, behave as weakly attractive mixtures. There are studies in the literature on the nature of the $CO_2 + CH_4$ system based on Molecular Dynamics Simulation (Baglin et al., 2000; Skarmoutsos and Samios, 2006; Parris, 2010). Skarmoutsos and

Samios determined that this system shows repulsive behaviour with a value of the excess coordination number slightly negative, $N_{exc}^{\infty} = -0.261$. However, their calculations were performed under conditions of temperature and pressure away from the critical point: $T = 323.15$ K and $P = 9.94$ MPa.

5.2. Effect of impurities in the process design

Given that the technology for natural gas (NG) transport is well developed and that there are vast pipeline networks dedicated to this use, it would seem a possibility to use existing gas pipelines for CO_2 transport. However, the large differences between the behaviour of CH_4 (main component in NG) and that of CO_2 (main compound in CCS), in practice limit this use to transport in gas phase (ElementEnergy, 2010; Serpa et al., 2011). Therefore, it may become necessary to design a new pipeline network to transport CO_2 in dense or supercritical phase. Furthermore, the presence of impurities in the anthropogenic CO_2 stream, even in small proportions, can significantly modify the properties of the fluid to be transported, primarily the phase equilibrium, density and viscosity, which strongly affects pipeline hydraulics and many other aspects of pipeline design and operation (Seevam et al., 2008). In order to evaluate these effects the usual parameters related to transport have been used: mass flow, m, erosional velocity, v_E, pipeline inner diameter, D, Reynolds number, Re, Darcy–Weisbach friction factor, f, pressure drop per unit length $\Delta P/L$, and capacity of the booster stations, W (Table 5). To calculate them, models based on Bernoulli's law for incompressible flow, applied to full and turbulent flow in circular shaped pipelines, have been used. These models, relatively simple but pragmatic, have been reviewed and accepted by the industrial and engineering community (Vandeginste and Piessens, 2008; ElementEnergy 2010). To establish a comparison between the behaviour of the pure CO_2 stream and the stream containing impurities, normalized parameters have been defined, X/X_0, where X are the above mentioned parameters for the mixtures and X_0 for pure CO_2. Table S4 (Supporting Information) shows the equations for normalized parameters, as well as certain conditions that have been kept constant for both streams in the calculations. In this manner, the deviations from unity of the normalized parameters are due to the different compositions and, therefore, different properties of pure and anthropogenic CO_2 streams.

Conditions of composition ($x_{CO_2} \cong 0.97$), pressure ($P = 8.6$–20 MPa) and temperature ($T = 304.21$ and 308.15 K) used for the calculation are within customary in CCS technology (ElementEnergy, 2010, Li et al., 2011a; ENCAP Project, 2008; EEA, 2012; EPA, 2012). The experimental values of the densities used in the calculation have been taken from this work, from Blanco et al. (2012) and from Velasco et al. (2011). The viscosities have been obtained from REFPROP 9.0 (Lemmon et al., 2010) by using the extended corresponding states (ECS) model developed by Klein et al. (1997).

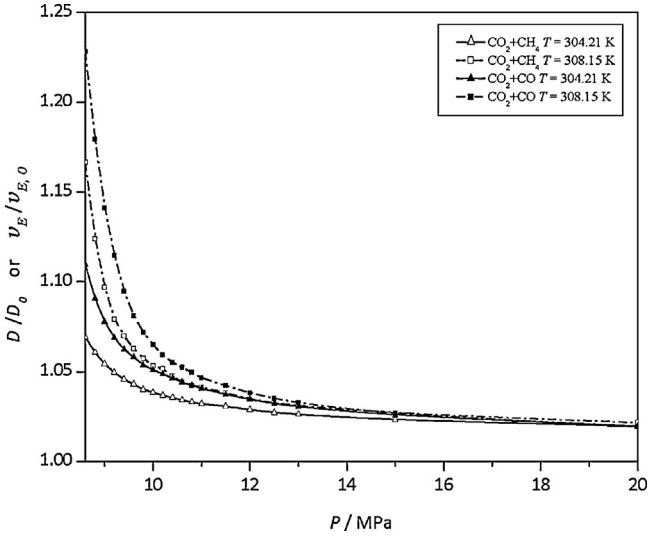

Fig. 12. Comparison of normalized pipeline inner diameter, D/D_0, (for a given mass flow and transport velocity) or erosional velocity, v_E/v_{E_0}, for mixtures $CO_2 + CH_4$ or +CO with $x_{CO_2} \cong 0.97$.

To obtain the friction factors, f, and the pressure drops per metre, $\Delta P/L$, standard values for pipeline inner diameter, $D = 0.508$ m, and mass flow, $m = 317$ kg/s (Serpa et al., 2011), and roughness height of commercial steel, $e = 4.6 \times 10^{-5}$ m (Vandeginste and Piessens, 2008), have been used.

The results are shown in Table S5 (Supporting Information) and in Figs. 12 and 13, and S6–S9 (Supporting Information). As can be seen, the differences with respect to the behaviour of pure CO_2 are greater for $CO_2 + CO$ than for $CO_2 + CH_4$ mixtures, in accordance with the conclusions drawn in Section 5.1 (the CO molecule provokes greater structural disruption than CH_4 in their respective mixtures with CO_2). For both systems, the differences increase with increasing T and decreasing P. They became significant at pressures ranged from 8.6 to 10 MPa, but they are smaller than 10% above 15 MPa.

Table 5
Equation overview for the calculation of several parameters in pipeline design and operation (ElementEnergy, 2010).

Parameter	Formula	Symbols
Mass flow	$m = \rho \times v \times A$	m = mass flow (kg/s); ρ = fluid density (kg/m^3); v = fluid velocity (m/s); A = pipeline inner section (m^2).
Pipeline inner diameter sizing	$D = \left(\frac{4 \times m}{v \times \pi \times \rho}\right)^{1/2}$	D = inner diameter (m); m = mass flow (kg/s); v = fluid velocity (m/s); ρ = fluid density (kg/m^3).
Erosional velocity	$v_E = \frac{C}{\sqrt{\rho}}$	v_E = erosional velocity (m/s); C = empirical constant; ρ = fluid density (kg/m^3).
Reynolds number	$Re = \frac{\rho \times v \times D}{\mu}$	Re = Reynolds number; ρ = fluid density (kg/m^3); v = fluid velocity (m/s); D = inner diameter (m); μ = fluid viscosity (Pa s).
Capacity of the booster stations	$W = \frac{m}{\rho} \times \frac{(P_{out} - P_{in})}{\eta_{booster}}$	W = capacity of the booster station (MW); m = mass flow (kg/s); ρ = fluid density (kg/m^3); P_{out} = booster outlet pressure (MPa); P_{in} = booster inlet pressure (MPa); $\eta_{booster}$ = booster efficiency.
Darcy–Weisbach friction factor	$f = \frac{1.325}{[\ln[(e/3.7 \times D) - (5.74/Re^{0.9})]]^2}$	f = Darcy–Weisbach friction factor; e = roughness height (m); D = inner diameter (m); Re = Reynolds number.
Pressure drop per metre	$\frac{\Delta p}{L} = \frac{8 \times f \times m^2}{\rho \times \pi^2 \times D^5}$	$(\Delta P/L)$ = pressure drop per metre (Pa/m); m = mass flow (kg/s); ρ = fluid density (kg/m^3); f = Darcy–Weisbach friction factor; D = inner diameter (m).

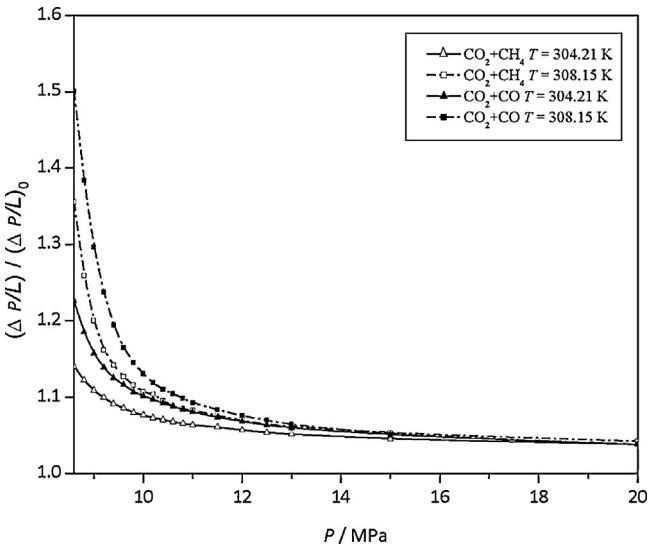

Fig. 13. Comparison of normalized pressure drop per metre, $(\Delta P/L)/(\Delta P/L)_0$, for a mass flow of 317 kg/s (10 Mt/year), a pipeline inner diameter of 0.508 m (20 inch) and a roughness height of 4.6×10^{-5} m (0.00015 ft) for mixtures $CO_2 + CH_4$ or + CO with $x_{CO_2} \cong 0.97$.

For a transport velocity and a pipeline inner diameter, the mass flow, m, is lower for mixtures than for pure CO_2 ($m/m_0 = 0.96$–0.66, Fig. S8, Supporting Information), due to the lower density of the mixtures. Normalized Darcy–Weisbach friction factors, f/f_0, are also lower than 1 (0.995–0.999, Fig. S9, for the utilized pipeline inner diameter, mass flow and roughness height). The rest of the normalized parameters are greater than 1, which means that the corresponding values for the mixtures parameters are higher than those for pure CO_2. The higher deviations appear in the CO_2 + CO mixture at 308.15 K and 8.6 MPa, with $Re/Re_0 = 1.75$ and $(\Delta P/L)/(\Delta P/L)_0 = 1.50$. Pressure drop per metre is higher for mixtures than for pure CO_2 in all the cases studied, a fact which might require an increase in the number of boosters along the network, especially if transport is carried out at low pressures.

6. Conclusions

Density measurements of the {CO_2 (1) + CH_4 (2)} and {CO_2 (1) + CO (2)} systems were carried out under conditions of composition, pressure and temperature of interest in CCS technology: $x_{CO_2} \geq 0.97$, $P = 0.1$–20 MPa, and $T = T_c(CO_2) = 304.21$ K for both systems and at $T = 308.15$ K for the CO_2 + CO system. All P–ρ–T–x_{CO_2} data have been obtained using a vibrating-tube densimeter. The expanded ($k = 2$) uncertainty and the repeatability (mean relative standard deviation) of the density measurements for our mixtures have been calculated: $U(\rho) = 0.4$–0.7 kg/m^3 and $\bar{S}^r_\rho = 0.13\%$. Other properties related to experimental data such as isothermal compressibility, κ_T, excess molar volume, V^E_m, and solute partial molar volume, $\bar{V}_2$, in the critical region ($T = 304.21$ and 308.15 K and $P = 5$–10 MPa) have been calculated as a function of pressure and composition.

The volumetric behaviour has been compared to literature data and it has been modelled with three Equations of State. The deviations obtained have been: Peng–Robinson, $MRD_\rho \leq 3.5\%$; rescaled PC-SAFT, $MRD_\rho \leq 2.8\%$; and GERG, $MRD_\rho \leq 1.0\%$. Thus the three EoS have been validated, for these binary systems, under CCS technology conditions.

Using the Krichevskii Function concept and the Kirkwood–Buff Theory, we have carried out a theoretical study of the interactions between CO_2 and CO, or CO_2 and CH_4 molecules. To this end we have calculated: (i) the Krichevskii function, J, and the Krichevskii parameter, A_{Kr}, which reflect the change experimented by the pressure when replacing a molecule of solvent by another of solute in infinitely dilute solutions, IDS, at constant T and V; (ii) the partial molar volume of the solute at infinite dilution, $\bar{V}_2^\infty$; (iii) the direct correlation function integrals, C_{ij}; (iv) the excess coordination number, N_{exc}^∞; and (v) the affinity of the solvent per solute molecule, or cluster size, N_1^{exc}. From the sign of the Krichevskii parameter, A_{Kr}, its dimensionless counterpart, A^*_{Kr}, and the divergence signs for different structural properties in the systems studied ($A_{Kr} > 0$; $\bar{V}_2^\infty \to +\infty$; $N_1^{exc} \to -\infty$; $1 > A^*_{Kr} > 0$; $N_1^{exc} \to +\infty$), we can conclude that these mixtures exhibit weakly attractive behaviour.

We have proven that the presence of impurities in CO_2, even in small proportions, modifies the properties of the mixtures. This results, in turn, in a modification of the parameters related to the design and operation in the process of fluid transport, depending on the nature of the mixture, the pressure and the temperature, and must be taken into account in the planning of CCS facilities. In this paper we have quantified the effect of small amounts of CH_4 and CO in CO_2 transport through various normalized parameters (related to their corresponding values when the fluid to be transported is pure CO_2). The parameters studied were: pipeline inner diameter, D, erosional velocity, v_E, transport velocity, v, Reynolds number, Re, booster capacity, W, mass flow, m, Darcy–Weisbach friction factor, f, and pressure drop per metre, $\Delta P/L$. Differences with respect to pure CO_2 increase with increasing temperature and decreasing pressure, becoming important (up to 75% in some cases) for 8.6 MPa < P < 10 MPa (working operating pressures in transport), and converge to smaller values (less than 10%) for P > 15 MPa.

We have observed, in all the properties studied in this work (volumetric, structural and operational for CCS technology), that the presence of CO as an impurity in anthropogenic CO_2 produces a greater disruption in relation to pure CO_2 than that of CH_4.

Acknowledgements

The authors gratefully acknowledge financial support received from the Ministerio de Educación y Ciencia of Spain (CTQ2005-02213), Ministerio de Ciencia e Innovación (CTQ2008-02037 and CTQ2011-24875), Convenio La Caixa – Gobierno de Aragón, and Universidad de Zaragoza (UZ2012-CIE-13).

Appendix A.

A.1. Relation between period, τ, and density, ρ

$$\rho(P,T) = \left(\frac{M_0}{V_i(P,T)}\right)\left[\left(\frac{K(P,T)}{K_0(T)}\right)\left(\frac{\tau^2(P,T)}{\tau_0^2(T)}\right) - 1\right] \tag{A1}$$

$$\rho(P,T) = \rho_{ref}(P,T)\frac{(K(P,T)/K_0(T))(\tau^2(p,T) - \tau_0^2(T))}{(K(P,T)/K_0(T))(\tau^2_{ref}(p,T) - \tau_0^2(T))} \tag{A2}$$

where $\rho(P, T)$ is the density of the inner fluid to be determined at pressure P and temperature T; $\rho_{ref}(P, T)$ is the density of the reference fluid at pressure P and temperature T; M_0 is the mass of the vibrating tube under vacuum; $V_i(P, T)$ is the internal volume of the vibrating tube at pressure P and temperature T; $K(P, T)$ is the transversal stiffness of the vibrating tube at pressure P and temperature T; $K_0(T)$ is the transversal stiffness under vacuum of the vibrating tube at temperature T; $\tau(P, T)$ is the period of the vibrating tube with inner fluid to be determined at pressure P and temperature T; $\tau_{ref}(P, T)$ is the period of the vibrating tube with reference fluid at pressure P and temperature T; $\tau_0(T)$ is the period under vacuum of the vibrating tube at temperature T.

A.2. Uncertainty, U(y)

The expanded ($k = 2$) uncertainty in the density, ρ, excess molar volumes, V_m^E, and solute molar partial volumes, $\bar{V}_2$, have been calculated by the rules of error propagation law (JCGM 100, 2008):

$$U(y) = ku_c(y) = k\left[\sum_{i=1}^{N}\left(\frac{\partial f}{\partial x_i}\right)^2 u^2(x_i)\right]^{1/2} \quad \text{(A3)}$$

where k is the coverage factor; u_c (y) is the combined standard uncertainty of the estimated y; x_i represent the input variables; $(\partial f/\partial x_i)$ is the sensivity coefficient of the input variable x_i; $u^2(x_i)$ is the variance of x_i.

A.3. Relative mean standard deviation, $\bar{S}_x^r$, and mean relative deviation, MRD_x

The relative mean standard deviation is calculated:

$$\bar{S}_x^r = \frac{100}{N}\sum_{j=1}^{N}({}_jS_x^r) \quad \text{(A4)}$$

where ${}_jS_x^r$ is the relative standard deviation by point:

$${}_jS_x^r = \frac{{}_jS_x}{(1/n)\sum_{i=1}^{n} x_i^{\exp}} \quad \text{(A5)}$$

and ${}_jS_x$ is the standard deviation by point:

$${}_jS_x = \sqrt{\frac{n\sum_{i=1}^{n}(x_i^{\exp})^2 - \left(\sum_{i=1}^{n} x_i^{\exp}\right)^2}{n(n-1)}} \quad \text{(A6)}$$

The relative mean deviation is calculated:

$$\mathrm{MRD}_x = \frac{100}{N}\sum_{i=1}^{N}\left|\frac{x_i^{\exp} - x_i^*}{x_i^{\exp}}\right| \quad \text{(A7)}$$

where $x_i^{\exp}$ are experimental data; x_i^* are bibliographic or calculated values; N is the number of points; n is the number of analysis for given T and P.

Appendix B. Supplementary data

Supplementary material related to this article can be found, in the online version, at doi:10.1016/j.ijggc.2013.07.019.

References

Abdulagatov, A.I., Stepanov, G.V., Abdulagatov, I.M., 2007. The critical properties of binary mixtures containing carbon dioxide: Krichevskii parameter and related thermodynamic properties. High Temperature 45, 408–424.

Al-Nehlawi, A., Saldo, J., Vega, L.F., Guri, S., 2013. Effect of high carbon dioxide atmosphere packaging and soluble gas stabilization pre-treatment on the shelf-life and quality of chicken drumsticks. Meat Science 94, 1–8.

Arai, Y., Kaminishi, G., Saito, S., 1971. The experimental determination of the P–V–T–x relations for the carbon dioxide–nitrogen and the carbon dioxide–methane systems. Journal Chemical and Engineering Japan 4, 113–122.

Baglin, F.G., Murray, S.K., Daugherty, J.E., Palmer, T.E., Stanbery, W., 2000. Interaction induced Raman light scattering as a probe of the local density structure of binary supercritical solutions. Molecular Physics 98, 409–418.

Beer, H., 1969. Compressibility factors for the argon–carbon dioxide system. Canadian Journal of Chemical Engineering 47, 92–94.

Ben-Naim, A., 1977. Inversion of the Kirkwood–Buff theory of solutions: application to the water–ethanol system. Journal of Chemical Physics 67, 4884–4890.

Bian, B., Wang, Y., Shi, J., Zhao, E., Lu, B.C.-Y., 1993. Simultaneous determination of vapor–liquid equilibrium and molar volumes for coexisting phases up to the critical temperature with a static method. Fluid Phase Equilibria 90, 177–187.

Blanco, S.T., Gil, L., Garcı′a-Giménez, P., Artal, M., Otı′n, S., Velasco, I., 2009. Critical properties and high-pressure volumetric behaviour of the carbon dioxide + propane system at $T = 308.15$ K. Krichevskii function and related thermodynamic properties. Journal of Physical Chemistry B 113, 7243–7256.

Blanco, S.T., Rivas, C., Fernández, J., Artal, M., Velasco, I., 2012. Influence of methane in CO_2 transport and storage for CCS technology. Environmental Science and Technology 46, 13016–13023.

Bouchot, C., Richon, D., 2001. An enhanced method to calibrate vibrating tube densimeters. Fluid Phase Equilibria 191, 189–208.

Brugge, H.B., Hwang, C.A., Rogers, W.J., Holste, J.C., Hall, K.R., Lemming, W., Esper, G.J., Marsh, K.N., Gammon, B.E., 1989. Experimental cross virial coefficients for binary mixtures of carbon dioxide with nitrogen, methane and ethane at 300 and 320 K. Physica A 156, 382–416.

Chialvo, A.A., Cummings, P.T., 1995. Comment on "Near critical phase behaviour of dilute mixtures". Molecular Physics 84, 41–48.

Cipollina, A., Anselmo, R., Scialdone, O., Filardo, G., Galia, A., 2007. Experimental P–T–ρ measurements of supercritical mixtures of carbon dioxide, carbon monoxide, and hydrogen and semiquantitative estimation of their solvent power using the solubility parameter concept. Journal of Chemical and Engineering Data 52, 2291–2297.

Cismondi, M., Brignole, E.A., Mollerup, J., 2005. Rescaling of three-parameter equations of state: PC-SAFT and SPHCT. Fluid Phase Equilibria 234, 108–121.

Debenedetti, P.G., Mohamed, R.S., 1989. Attractive, weakly attractive, and repulsive near-critical systems. Journal of Chemical Physics 90, 4528–4536.

Donnelly, H.G., Katz, D.L., 1954. Phase equilibria in the carbon dioxide–methane system. Industrial and Engineering Chemistry 46, 511–517.

EEA (European Environment Agency), 2012. Annual European Union Greenhouse Gas Inventory 1990–2010 and Inventory Report 2012. Technical Report No. 3/2012. http://www.eea.europa.eu/publications/european-union-greenhouse-gas-inventory-2012

ElementEnergy, 2010. CO_2 pipeline infrastructure: an analysis of global challenges and opportunities. In: Final Report for IEA Greenhouse Gas Programme, 1-134. EON UK, 2011, Kingsnorth Carbon Capture & Storage Project. Post-FEED Project Cost.

ENCAP-WP1.1 Deliverable D1.1.1 & D1.1.2, 2008. Reference Cases and Guidelines for Technology Concepts, Vattenfall A/S Report No.: 55431, Issue No. 4.

EPA (Environmental Protection Agency), 2012. Inventory of U.S. Greenhouse Gas Emissions and Sinks: 1990-2010. EPA 430-R-12-001. U.S. http://www.epa.gov/climatechange/ghgemissions/usinventoryreport.html

Esper, G.J., 1987. Fortschritt-Berichte VDI, Reihe 3, Nr. 148. VDI-Verlag, Düsseldorf.

Furuja, T., Teja, A.S., 2000. Krichevskii Parameters and the Solubility of Heavy n-Alkanes in Supercritical Carbon Dioxide. Industrial and Engineering Chemistry Research 39, 4828–4830.

Ghasemi, M., Daud, W.R.W., Hassan, S.H.A., Oh, S.-E., Ismail, M., Rahimnejad, M., Jahim, J.Md, 2013. Nano-structured carbon as electrode material in microbial fuel cells: a comprehensive review. Journal of Alloys and Compounds 580, 245–255.

Gil, L., Otín, S., Muñoz Embid, J., Gallardo, A., Blanco, S.T., Artal, M., Velasco, I., 2008. Experimental setup to measure critical properties of pure and binary mixtures and their densities at different pressures and temperatures: determination of the precision and uncertainty in the results. Journal of the Supercritical Fluids 44, 123–138.

Gil, L., Martı′nez-Lo′pez, J.F., Artal, M., Blanco, S.T., Muñoz Embid, J., Fernández, J., Otı′n, S., Velasco, I., 2010. Volumetric behaviour of the {CO_2 (1) + C_2H_6 (2)} system in the subcritical ($T = 293.15$ K), critical, and supercritical ($T = 308.15$ K) regions. Journal of Physical Chemistry B 114, 5447–5469.

Gil, L., Blanco, S.T., Rivas, C., Laga, E., Fernández, J., Artal, M., Velasco, I., 2012. Experimental determination of the critical loci for {n-C_6H_{14} or CO_2 + alkan-1-ol} mixtures. Evaluation of their critical and subcritical behaviour using PC-SAFT EoS. Journal of the Supercritical Fluids 71, 26–44.

Glos, S., Kleinrahm, R., Wagner, W., 2001. Density measurements on the binary gas mixture ($CH_4 + CO_2$) at temperatures 273.15 and 290 K and pressures up to 9.5 MPa. In: Claus, P., Kleinrahm, R., Wagner, W. (Eds.), Density Measurements on Ethane and Propane in the Temperature Range from 340 to 520 K at Pressures up to 30 MPa, Report to GERG WG 1.34. Lehrstuhl fur Thermodynamik, Ruhr-Universitat Bochum, Bochum, Germany.

Gross, J., Sadowski, G., 2001. Perturbed-chain SAFT: an equation of state based on a perturbation theory for chain molecules. Industrial and Engineering Chemistry Research 40, 1244–1260.

Gross, J., Sadowski, G., 2002. Application of the perturbed-chain SAFT equation of state to associating systems. Industrial and Engineering Chemistry Research 41, 5510–5515.

Hwang, C.A., Iglesias-Silva, G.A., Holste, J.C., Hall, K.R., Gammon, B.E., Marsh, K.N., 1997. Densities of Carbon Dioxide + Methane Mixtures from 225 K to 350 K at Pressures up to 35 MPa. Journal of Chemical and Engineering Data 42, 897–899.

IEA/CSLF Report to the Musoka 2010 g-8, 2010. Carbon Capture and Storage. Progress and Next Steps.

Jaeschke, M., Humphreys, A.E., 1991. The GERG databank of high accuracy compressibility factor measurements. GERG TM4 1990. Fortschritt-Berichte VDI, Reihe 6, Nr. 251. VDI-Verlag, Düsseldorf.

Jaeschke, M., Hinze, H.M., Humphreys, A.E., 1997. Supplement to the GERG databank of high accuracy compressibility factor measurements GERG TM7 1996. Fortschritt-Berichte VDI, Reihe 6, Nr. 355. VDI Verlag, Düsseldorf.

Japas, M.L., Alvarez, J.L., Gutkowski, K., Fernandez-Prini, R., 1998. Determination of the Krichevskii function in near-critical dilute solutions of I_2(s) and CHI_3(s). Journal of Chemical Thermodynamics 30, 1603–1615.

JCGM 100, 2008. Evaluation of Measurement Data – Guide to Expression of Uncertainty in Measurement. Joint Committee for Guides in Metrology, Serves Cedex, France.

Ke, J., Han, B., George, M.W., Yan, H., Poliakoff, M., 2001. How does the critical point change during a chemical reaction in supercritical fluids? A study of the hydroformylation of propene in supercritical CO_2. Journal of the American Chemical Society 123, 3661–3670.

Kirkwood, J.G., Buff, F.P., 1951. The statistical mechanical theory of solutions. I. Journal of Chemical Physics 19, 774–777.

Klein, S.A., McLinden, M.O., Laesecke, A., 1997. An improved extended corresponding states method for estimation of viscosity of pure refrigerants and mixtures. International Journal of the Refrigeration 20, 208–217.

Knoope, M.M.J., Ramírez, A., Faaij, A.P.C., 2013. A state-of-the-art review of techno-economic models predicting the costs of CO_2 pipeline transport. International Journal of Greenhouse Gas Control 16, 241–270.

Kunz, O., Wagner, W., 2012. The GERG-2008 wide-range equation of state for natural gases and other mixtures: an expansion of GERG-2004. Journal of Chemical and Engineering Data 57, 3032–3091.

Lachet, V., Creton, B., deBruin, T., Bourasseau, E., Desbiens, N., Wilhelmsen, O., Hammer, M., 2012. Equilibrium and transport properties of $CO_2 + N_2O$ and $CO_2 + NO$ mixtures: molecular simulation and equation of state modelling study. Fluid Phase Equilibria 322–323, 66–78.

Laursen, T., 2012. VLXE ApS. Scion-DTU, Diplomvej, Denmark.

Lee, L.L., Cochran, H.D., 1994. Integral equations for microestructures of supercritical fluids. In: Kiran, E., Levelt Sengers, J.M.H. (Eds.), Supercritical Fluids: Fundamentals for Application. NATO, ASI Ser. 273. Kluwer Academic Publishers, The Netherlands, pp. 365–383.

Lemming, W., 1989. Fortschritt-Berichte VDI, Reihe 19, Nr. 32. VDI-Verlag, Düsseldorf.

Lemmon, E.W., Huber, M.L., McLinden, M.O., 2010. NIST Standard Reference Database 23: Reference Fluid Thermodynamic and Transport Properties-REFPROP, Version 9.0. National Institute of Standards and Technology, Standard Reference Data Program, Gaithersburg.

Levelt Sengers, J.M.H., 1994. Critical behavior of fluids: concepts and applications. In: Kiran, E., Levelt Sengers, J.M.H. (Eds.), Supercritical Fluids: Fundamentals for Application. NATO, ASI Ser. 273. Kluwer Academic Publishers, The Netherlands, pp. 3–38.

Li, H., Jakobsen, J.P., Wilhelmsen, O., Yan, J., 2011a. PVTxy properties of CO_2 mixtures relevant for CO_2 capture, transport and storage: review of available experimental data and theoretical models. Applied Energy 88, 3567–3579.

Li, H., Wilhelmsen, O., Lv, Y., Wang, W., Yan, J., 2011b. Viscosities, thermal conductivities and diffusion coefficients of CO_2 mixtures: review of experimental data and theoretical models. International Journal of Greenhouse Gas Control 5, 1119–1139.

Liu, Y., Wilcox, J., 2013. Molecular Simulation Studies of CO_2 Adsorption by Carbon Model Compounds for Carbon Capture and Sequestration Applications. Environmental Science and Technology, http://dx.doi.org/10.1021/es3012029.

Magee, J.W., Ely, J.F., 1988. Isochoric (p,v,T) measurements on CO_2 and (0.98 CO_2 + 0.02 CH_4) from 225 to 400 K and pressures to 35 MPa. International Journal of Thermophysics 9, 547–557.

Mallu, B.V., Natarajan, G., Viswanath, D.S., 1987. Compression factors and second virial coefficients of CO_2, CO, and $\{x\,CO + (1-x)\,CO_2\}$. Journal of Chemical Thermodynamics 19, 549–554.

Mallu, B.V., Viswanath, D.S., 1990. Compression factors and second virial coefficients of hydrogen, methane and carbon dioxide mixtures $\{x\,CO_2 + (1-x)\,H_2\}$, and $\{x\,CO_2 + (1-x)CH_4\}$. Journal of Chemical Thermodynamics 22, 997–1006.

Móndejar, M.E., Fernández-Vicente, T.E., Haloua, F., Chamorro, C.R., 2012. Experimental determination of (P, ρ, T) data for three mixtures of carbon dioxide with methane for the thermodynamic characterization of nonconventional energy gases. Journal of Chemical and Engineering Data 57, 2581–2588.

Parris, P., 2010. Molecular Simulation Studies in the Supercritical Region. University College London, London, WC1E 7JE (Thesis).

Peng, D.Y., Robinson, D.B., 1976. A new two-constant equation of state. Industrial and Engineering Chemistry Fundamentals 15, 59–64.

Ramachandriya, K.D., Kundiyana, D.K., Wilkins, M.R., Terrill, J.B., Atiyeh, H.K., Huhnke, R.L., 2013. Carbon dioxide conversion to fuels and chemicals using a hybrid green process. Applied Energy 112, 289–299.

Reamer, H.H., Olds, R.H., Sage, B.H., Lacey, W.N., 1944. Phase equilibria in hydrocarbon systems. Industrial and Engineering Chemistry 36, 88–90.

Sánchez-Vicente, Y., Drage, T.C., Poliakoff, M., Ke, J., George, M.W., 2013. Densities of the carbon dioxide + hydrogen, a system of relevance to carbon capture and storage. International Journal of Greenhouse Gas Control 13, 78–86.

Seevam, P.N., Race, J.M., Downie, J.M., Hopkins, P., 2008. Transporting the next generation of CO_2 for carbon, capture and storage: the impact of impurities on supercritical CO_2 pipelines. In: Proceedings of IPC2008 7th International Pipeline Conference (Canada), pp. 39–51.

Seitz, J.C., Blencoe, J.G., 1996. Volumetric properties for $\{(1-x)CO_2 + xCH_4\}$, $\{(1-x)CO_2 + xN_2\}$, and $\{(1-x)CH_4 + xN_2\}$ at the pressures (19.94, 29.94, 39.94, 59.93, 79.93, and 99.93) MPa and the temperature 673.15 K. Journal of Chemical Thermodynamics 28, 1207–1213.

Seitz, J.C., Blencoe, J.G., Bodnar, R.J., 1996. Volumetric properties of for $\{(1-x)CO_2 + xCH_4\}$, $\{(1-x)CO_2 + xN_2\}$, and $\{(1-x)CH_4 + xN_2\}$ at the temperatures (323.15, 373.15, 473.15, 573.15) K and pressures (9.84, 19.84, 29.84, 39.84, 59.83, 79.83, 99.83) MPa. Journal of Chemical Thermodynamics 28, 521–538.

Serpa, J., Morbee, J., Tzimas, E., 2011. Technical and economic characteristics of a CO_2 transmission pipeline infraestructure. In: JRC62502, pp. 1–43.

Simon, R., Fesmire, C.J., Dicharry, R.M., Vorhis, F.H., 1977. Compressibility factors for carbon dioxide–methane mixtures. Journal of Petroleum Technology 29, 81–85.

Skarmoutsos, I., Samios, J., 2006. Local intermolecular structure and dynamics in binary supercritical solutions. A molecular dynamics simulation study of methane in carbon dioxide. Journal of Molecular Liquids 125, 181–186.

Span, R., Wagner, W., 1996. A new equation of state for carbon dioxide covering the fluid region from the triple-point temperature to 1100 K at pressures up to 800 MPa. Journal of Physical and Chemical Reference Data 25, 1509–1596.

Trusler, J.P.M., 2011. Equation of state for solid phase I of carbon dioxide valid for temperatures up to 800 K and pressures up to 12 GPa. Journal of Physical and Chemical Reference Data 40, 043105.

Trusler, J.P.M., 2012. Erratum: Equation of state for solid phase I of carbon dioxide valid for temperatures up to 800 K and Pressures up to 12 GPa [J. Phys. Chem. Ref. Data 40, 043105 (2011)]. Journal of Physical and Chemical Reference Data 41, 039901.

Vandeginste, V., Piessens, K., 2008. Pipeline design for a least-cost router application for CO_2 transport in the CO_2 sequestration cycle. International Journal of Greenhouse Gas Control 2, 571–581.

Velasco, I., Rivas, C., Martínez-Lopez, J.F., Blanco, S.T., Otín, S., Artal, M., 2011. Accurate values of some thermodynamic properties for carbon dioxide, ethane, propane, and some binary mixtures. Journal of Physical Chemistry B 115, 8216–8230.

Vo, H.T., Imai, T., Teeka, J., Sekine, M., Kanno, A., Le, T.V., Higuchi, T., Phummala, K., Yamamoto, K., 2013. Comparison of disinfection effect of pressurized gases of CO_2, N_2O, and N_2 on *Escherichia coli*. Water Research 47, 4286–4293.

Wheeler, J.C., 1972. Behaviour of a solute near the critical point of an almost pure solvent. Berichte der Bunsengesellschaft für Physikalische Chemie 76, 308–318.

Wöll, O., El Hawary, T., 2003. Private Communication. Lehrstuhl für Thermodynamik, Ruhr-Universität Bochum.

Zhang, J., Zhang, X., Han, B., He, H., Liu, Z., Yang, G., 2002. Study on intermolecular interactions in supercritical fluids by partial molar volume and isothermal compressibility. Journal of Supercritical Fluids 22, 15–19.

Environmental Science & Technology

Article

pubs.acs.org/est

Discussion of the Influence of CO and CH_4 in CO_2 Transport, Injection, and Storage for CCS Technology

Sofía T. Blanco,[†] Clara Rivas,[†] Ramón Bravo,[‡] Javier Fernández,[†] Manuela Artal,[†] and Inmaculada Velasco*[,†]

[†]Departamento de Química Física, Facultad de Ciencias, Universidad de Zaragoza, 50009 Zaragoza, Spain

[‡]Departamento de Física Aplicada, Facultad de Física, Universidad de Santiago de Compostela, 15782 Santiago de Compostela, Spain

Supporting Information

ABSTRACT: This paper discusses the influence of the noncondensable impurities CO and CH_4 on Carbon Capture and Storage (CCS) technology. We calculated and drew conclusions about the impact of both impurities in the CO_2 on selected transport, injection, and storage parameters (pipeline pressure drop, storage capacity, etc.), whose analysis is necessary for the safe construction and operation of CO_2 pipelines and for the secure long-term geological storage of anthropogenic CO_2. To calculate these parameters, it is necessary to acquire data on the volumetric properties and the vapor−liquid equilibrium of the fluid being subjected to CCS. In addition to literature data, we used new experimental data, which are presented here and were obtained for five mixtures of CO_2+CO with compositions characteristic of the typical emissions of the E.U. and the U.S.A. Temperatures and pressures are based on relevant CO_2 pipeline and geological storage site values. From our experimental results, Peng−Robinson, PC-SAFT, and GERG Equations of State for were validated CO_2+CO under the conditions of CCS. We conclude that the concentration of both impurities strongly affects the studied parameters, with CO being the most influential and problematic. The overall result of these negative effects is an increase in the difficulties, risks, and overall costs of CCS.

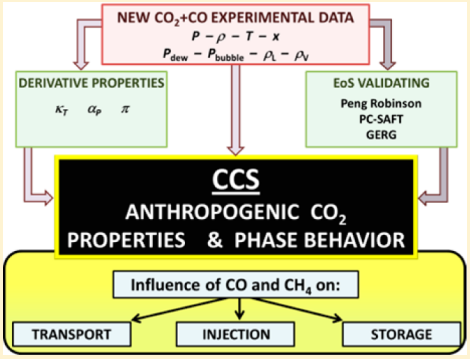

1. INTRODUCTION

Carbon Capture and Storage (CCS) technology is one of the most effective climate change mitigation strategies in the medium term. In 2013, the Global CCS Institute identified 65 large-scale CCS projects in various stages of development, of which only 19 will be operational by 2016.[1] The capture and storage capacity of these 19 projects is approximately 38.5 megatons per year, while the storage forecasts are more than 7 gigatons per year in 2050.[2]

The goal of CCS is to avoid the release to the atmosphere of anthropogenic CO_2 generated by industrial and energy-related sources. CO_2 is captured in individual producer facilities and subsequently conditioned, transported, and injected into an underground geological storage field.[3−5] CO_2 capture can be accomplished by different techniques: postcombustion, precombustion, and oxy-combustion. Conditioning can be carried out by dehydration, separation of noncondensable gases and/or liquefaction, and compression/pumping. Transport is usually performed by pipeline, and the anthropogenic CO_2 is finally injected and stored in depleted oil and gas fields, deep saline formations or deep unmineable coal seams.

The source of the CO_2 as well as the capture and conditioning processes used will determine the composition of the transported and stored CO_2. High purification is technically possible but not economically viable.[4] In addition, recent literature focuses on the potential benefits and limitations of the combined capture (cocapture) and storage of multiple gases (CO_2 and at least one other gas).[6−9] The presence of impurities in the fluid and the wide ranges of temperature, T, and pressure, P, involved in CCS cause the physicochemical properties of the current anthropogenic CO_2 to vary significantly according to its origin and to change significantly throughout the process.[10−12]

CO_2QUEST[13] and Impacts[14] are two research projects of the seventh Framework Programme of the European Commission, among others, that are currently devoted to evaluating the impact of CO_2 quality on its transport and storage behavior. However, there is a shortage of experimental data on the mixtures of interest specific to this technology.[15,16]

This work is part of a study we are carrying out[17−20] on CO_2 systems containing noncondensable or condensable impurities, with the ultimate goal of validating equations of state, EoS, and obtaining interaction parameters, if necessary, from synthetic multicomponent mixtures with compositions representative of actual anthropogenic CO_2. The first objective of this work was to quantify fundamental properties, such as volumetric and phase behavior, of mixtures of CO_2 with a noncondensable impurity, CO, using our experimental installations. CO is a highly toxic impurity whose presence is especially important in

Received: May 9, 2014
Revised: July 22, 2014
Accepted: August 20, 2014
Published: August 20, 2014

precombustion capture processes.[11] We present new and accurate pressure−density−temperature−composition, $P\rho Tx_{CO_2}$, and vapor−liquid equilibrium, VLE, experimental data for five mixtures of CO_2+CO whose compositions, temperatures and pressures are within the range of interest applicable to CCS conditions.[12,15,21−28]

There are experimental studies in the literature on the volumetric properties[20,29,30] and the vapor−liquid equilibrium[31] of CO_2+CO, but none cover the range of interest for CCS technology to the extent of this work. Due to the scarce experimental data on this and other impurities, most of the studies performed simulations to predict both the thermodynamic behavior and the values of the parameters associated with transport, injection and storage.[11,12,32−34]

Using experimental data from this work for the CO_2+CO system, and from literature for pure CO_2,[18] CO_2+CH_4,[19,20] and CO_2+CO,[20] we have quantified and compared the effect of the presence of CO and CH_4 (another noncondensable impurity), evaluating several selected transport, injection and storage parameters.[12,25,32] The analysis of these parameters is necessary for the safe and reliable design, construction, and operation of CO_2 pipelines and injection equipment, as well as the secure long-term geological storage of CO_2.

In addition, we validate with our experimental data three equations of state: Peng−Robinson (PR) EoS, widely used in industry;[35] GERG EoS, developed for natural gas;[36] and PC-SAFT EoS, one of the most used in this technology for the calculation of thermodynamic properties.[37,38] Given that there remains no one single equation whose characteristics are ideally suited for this technology, it is essential to have experimental data to draw realistic conclusions and to aid in the rational selection of the optimal equation.[11,15,39,40]

Because some impurities of anthropogenic CO_2 are toxic, and CO_2 itself is directly toxic in air when inhaled at concentrations above approximately 5%, the safe operation of CO_2 pipelines is of paramount importance.[41] Due to the relatively high Joule−Thomson expansion coefficient of CO_2 and its triple point coordinates, the rapid expansion of an accidental release may lead to solids formation following a pipeline rupture or puncture. In this regard, several publications devoted to the prediction of phase equilibria involving solids, either validating existing EoS or proposing new ones, are found in the literature.[42−46]

In summary, this work provides new experimental volumetric and VLE data of the system CO_2+CO at compositions, pressures, and temperatures of interest for CCS technology. Using these data, we validate several equations of state under CCS conditions.[35−38] From this work and literature experimental data,[18−20] we calculate and draw conclusions about the impact of both CO and CH_4 impurities in the CO_2 on selected engineering parameters related to the transport, injection, and geological storage of the CO_2.[12,25,32]

2. EXPERIMENTAL SECTION

2.1. Materials. Carbon dioxide (wt % > 99.998) and carbon monoxide (wt % > 99.997) were obtained from Air Liquide and used without further purification.

The CO_2+CO mixtures with a CO_2 mole fraction, x_{CO_2}, from 0.9700 to 0.9960 were prepared by successive introduction of the components (in order of increasing volatility) into a variable-volume cell, which was weighed on a mass comparator with a precision of 0.0002 g.

2.2. Apparatus and Procedures. The experimental setup used in this work for the determination of $P\rho T$ data of CO_2+CO mixtures is the same as that described in a previous study.[18] Its main component is a vibrating tube densimeter Anton Paar HPM, which is connected to a MPDS 2000 V3 evaluation unit. The use of two thermostatic baths at two different temperatures ($\Delta T \cong 0.3°$), one for the densimeter and the other for the rest of the installation, assures that the first drop of liquid (at dew pressure, P_{dew}) or the first vapor bubble (at bubble pressure, P_{bubble}) is formed inside the vibrating tube. Moreover, the quasi continuous acquisition of $P\rho T$ data (6000 points/isotherm evenly reduced to approximately 1000 points/isotherm for easier handling) allows the determination of the limits of VLE and the calculation of derivative properties, both with adequate accuracy. The temperature and pressure ranges are 253 to 423 K ± 0.006 K and from atmospheric pressure to 70 MPa with a precision of 0.025% FS, respectively.

The uncertainty propagation law was used[47] to evaluate the precision in the density of our mixtures; the expanded (k = 2) uncertainty obtained is $U(\rho)$ = 0.35−0.80 kg.m^{-3}. The repeatability of the density measurements for mixtures, expressed as the relative mean standard deviation, is $\overline{S}_\rho^r$ = 0.13%.[18]

3. RESULTS AND DISCUSSION

$P\rho Tx_{CO_2}$ measurements for CO_2+CO mixtures (x_{CO_2} = 0.9700, 0.9810, 0.9902, 0.9930, and 0.9960) at T = 253.15, 263.15, 273.15, 283.15, 293.15, 323.15, 333.15, and 343.15 K were carried out in the pressure range from 0.1 to 20 MPa. The CO mole fractions of this work include the compositions of the typical emissions in the E.U. and the U.S.A., whose values range approximately from 0.007 to 0.030 and from 0.011 to 0.016, respectively.[26,28] The experiments were performed at T and P relevant to those in CO_2 pipelines and in geologic storage sites (geothermic gradient = 25 K/km; hydrostatic pressure gradient = 10 MPa/km).[15,21,22]

In the Supporting Information, SI, Table S1 contains a total of 40 000 $P\rho Tx_{CO_2}$ points. Figure 1 shows the experimental densities for the CO_2+CO mixture with x_{CO_2} = 0.9700; analogous representations for the rest of the mixtures are included in SI Figure S1. In these figures, the density of the mixtures at supercritical temperatures is a continuous line

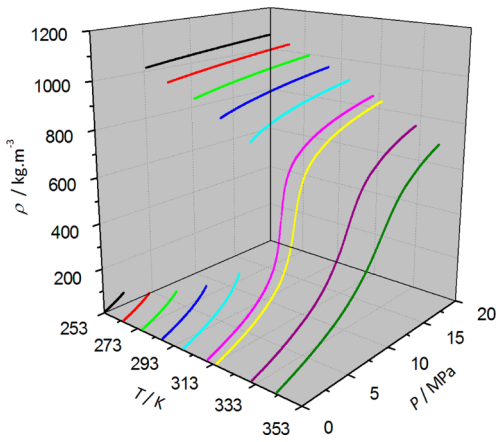

Figure 1. Experimental densities, ρ, for CO_2+CO mixtures with x_{CO_2} = 0.9700 at several temperatures and pressures.

whose slope diminishes as T increases; the maximum slope is at the critical conditions of the mixture. This is consistent with the fact that the isothermal compressibility of the mixtures is maximum at the critical point and diminishes as T increases away from the critical value. The mixtures studied in this work have critical temperatures between 302.6 and 303.9 K.[20] The subcritical isotherms show a discontinuity in the VLE region, which is limited by P_{dew} and P_{bubble} (Figure 2); these values and those for the densities of the liquid and vapor phases in equilibrium, ρ_L and ρ_V, respectively, (Figure S2) are shown in Table S2 in the SI.

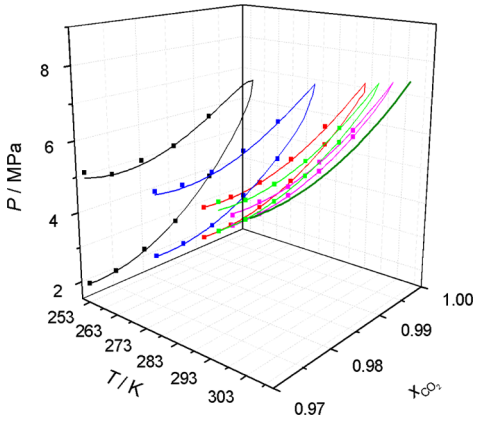

Figure 2. Vapor pressure of CO_2[48] (olive green) and experimental phase envelopes for CO_2+CO mixtures with x_{CO_2} = 0.9700 (black), x_{CO_2} = 0.9810 (blue), x_{CO_2} = 0.9902 (red), x_{CO_2} = 0.9930 (green), and x_{CO_2} = 0.9960 (pink).

We have found studies in the literature on VLE[31] and the volumetric[20,29,30] behavior of CO_2+CO. The values taken from the VLE graphical representations of Kaminishi and Toriumi do not agree with our experimental values or with the values predicted by the EoS used in this work. Our volumetric experimental data are consistent with those from literature, but cannot be directly compared because either the compositions[29,30] or the temperatures[20] do not match.

The composition of the anthropogenic CO_2 and the temperature and pressure during its transport and storage will vary based on multiple factors: different regulations regarding quality requirements of the fluid, different emission sources and capture and conditioning processes, emission plants operating under variable external demands, operational depressurizations, and off-shore versus on-shore transport. Given the variability of the conditions involved in CCS technology, it becomes necessary to use a predictive tool, such as an EoS, to calculate the values of essential properties, such as density and phase equilibria, for the optimal design and operation of the facilities involved in CCS. However, none of the current EoS presents marked advantages over the others.[11,15,39,40] In this regard, we have compared, in terms of relative mean deviation, MRD_x, our experimental data for density and VLE with those calculated using three different types of equations of state: PR EoS,[35] GERG EoS,[36] and PC-SAFT EoS.[37,38]

The parameters used for the pure components in PR and PC-SAFT EoS, as well as the binary interaction parameter, k_{ij}, included in the mixing rule of a van der Waals fluid are shown in SI Table S3. The MRD_x values are tabulated in the SI (Tables S4 and S5). The MRD_ρ values obtained for CO_2+CO mixtures with x_{CO_2} = 0.9810 and x_{CO_2} = 0.9930 at 253.15 K (subcritical T) and 343.15 K (supercritical T) are represented in SI Figure S3. From the results obtained, it can be concluded that (i) the PR EoS provides a reasonable prediction of the volumetric behavior and a good representation of VLE despite its simplicity (MRD_ρ = 2.87%, $MRD_{P_{bubble}}$ = 1.89%, $MRD_{P_{dew}}$ = 0.47%); (ii) the GERG EoS is the equation that best represents our experimental density and VLE data (MRD_ρ = 0.73%, $MRD_{P_{bubble}}$ = 1.30%, $MRD_{P_{dew}}$ = 0.38%), although it requires substantial computation time[39] and its extension to mixtures containing compounds not included in its database is complex; and (iii) the PC-SAFT EoS adequately predicts $P\rho T$ and VLE (MRD_ρ = 1.19%, $MRD_{P_{bubble}}$ = 1.58%, $MRD_{P_{dew}}$ = 1.45%) and can easily be extended to multicomponent mixtures.

3.1. Influence of Impurities on Transport. The presence of impurities in the anthropogenic CO_2 greatly affects both the phase and the volumetric behaviors of the fluid, thereby modifying the parameters utilized in the design and operation of transport by pipeline. Some of these parameters will be discussed in this section: the minimum operational pressure, P_{min}; the pressure profile along the pipeline, $P(d)$, where d is the distance; the maximum repressurization distance (maximum separation distance between boosters), L; the booster stations power, W; and the inner diameter of the pipeline, D. These, and other required parameters (Reynolds number, friction factor and pressure drop per meter), were calculated using the recommended equations[25,32] shown in SI Table S6. When fixed values were assumed for certain parameters in the calculations of others, it is indicated in the text and in the figure captions. The results for CO_2+CO were compared with those calculated for CO_2+CH_4 mixtures and for pure CO_2 under the same conditions. We used the phase equilibria and volumetric experimental data obtained from this work and from the literature.[18−20] Viscosity values were calculated using REFPROP 9.0.[48]

3.1.1. Minimum Operational Pressure, P_{min}. Although the transport by pipeline of anthropogenic CO_2 in gaseous phase has been considered in several studies[49,50] and may be cost-effective for low mass flow rates and short distances,[50] it is most commonly transported in a supercritical or dense phase. In any case, it is important to avoid phase changes and two-phase flow during pipeline operation.

Transporting in a dense phase is achieved by setting P_{min} to always be higher than P_{bubble} of the transported fluid. The impurities accompanying the anthropogenic CO_2 significantly influence the characteristics and location of the two-phase region. Thus, for pure CO_2 transported at 283.15 K, the vapor phase appears at the saturation pressure P_{sat} = 4.50 MPa (SI Table S2). However, if the fluid contains 3% by mole CH_4, then the vapor will appear at P_{bubble} = 5.85 MPa, and it will coexist with the liquid until P_{dew} = 4.69 MPa, below which there will be a single-phase gas.[19] If the impurity is 3% by mole CO, the two-phase flow would take place from 6.57 to 4.72 MPa (P_{bubble} and P_{dew}, respectively) (SI Table S2, Figure 2, and SI Figure S2).

Another issue to be considered when anthropogenic CO_2 is transported in the dense phase is the possible proximity of the operational conditions to the critical point of the fluid. Under these conditions, density values change significantly with small changes in P, T, or x_{CO_2} (e.g., compressibility will be very high, $(\kappa_T)_{T_c,P_c} \rightarrow \infty$), which influences the transport parameters.

For the anthropogenic CO_2 transport pressure in a supercritical or dense phase, the literature provides ranges of 7.5−11 MPa for P_{min} and 9−30 MPa for the maximum pressure, P_{max}; minimum values ensure dense or supercritical conditions for the fluid, and maximum values depend more on economic factors than technical ones.[51] Temperatures range from a lower limit, usually above −2 °C (271 K), set by winter surrounding temperatures, and an upper limit, 30−44 °C (303−317 K), determined by the compressor station discharge temperature and the external pipeline coating material. Both onshore and offshore references have been considered.[7,11,15,16,22,25,51−60]

Some previous studies propose, instead of pressure ranges, a reference value of 800 kg/m^3 as the minimum density of the fluid during the transport.[25,32] SI Table S7 presents the minimum operational pressure needed to ensure this density value, P_{min}^{800}, if the transported fluid is pure CO_2 or for CO_2+CO mixtures with compositions x_{CO_2} = 0.9902 and x_{CO_2} = 0.9700. Again, the impurities are very important; considering the fluid to be pure CO_2 can introduce an error of up to 62% in P_{min}^{800} if the anthropogenic CO_2 is actually a mixture with 3% by mole CO. The same amount of CH_4 would lead to an error of up to 27%.[19]

We calculated the remaining mentioned parameters for the transport of pure CO_2, CO_2+CO, and CO_2+CH_4 systems, both with $x_{CO_2} \cong 0.99$ and $x_{CO_2} \cong 0.97$, between P_{max} = 20.0 MPa and P_{min} = 9.0 MPa (the average maximum and minimum literature values) and temperatures from 273.15 to 308.15 K. In addition, we calculated the L and W required to maintain the density of the fluid above 800 kg/m^3 during transport. In this case, the transport is considered to be between P_{max} = 20.0 MPa and the corresponding P_{min}^{800} at each composition and transport temperature. The pressure profile, L and W, were all calculated for a mass flow, m, of 317 kg/s (10 Mt/year) in a D = 0.508 m (20 in.) pipeline with a roughness height, e, of 4.6 × 10^{-5} m (0.000 15 ft.).[32,56]

3.1.2. Pressure Profile along the Pipeline, P(d). SI Figure S4 shows the influence of impurities on the pressure drop along a pipeline for these systems at various transport temperatures, T_{tr}, and a pipeline inlet pressure (P_{max}) of 20.0 MPa. The pressure drop increases with increasing temperature and (noncondensable) impurity concentration, due to the decrease in the density and the viscosity of the mixture (see SI Tables S1 and S6), and the presence of CO or CH_4 has a very similar influence on it. For example: in scenario of SI Figure S4, and for a distance, d, of 250 km, for pure CO_2 pressure drops from 20 MPa down to 12.7 MPa at 273.15 K, and to 11.2 MPa at 308.15 K; if the fluid is a mixture with $x_{CO_2} \cong 0.97$, then the pressure drops down to 12.5 MPa at 273.15 K and to 10.6 MPa at 308.15 K.

Pressure drop, itself related to the diameter of the pipeline, the inlet pressure and the properties of the transported fluid, determines the placement and number of pumping (booster) stations, if needed. However, most techno-economic models do not take into account pumping stations, or they include them with a simplified approach, resulting in a large uncertainty in their costs and placement.[50,61] To choose the most cost-effective option, the trade-offs between diameter, inlet pressure, and pumping stations must be considered.

3.1.3. Maximum Repressurization Distance, L, and Booster Stations Power, W. Figure 3 shows the maximum repressurization distance, L, versus the transport temperature, T_{tr}, for the fluid transported by pipeline. Two sets of lines are represented: set A shows L required to maintain the density of the fluid above 800 kg/m^3, and set B shows L required to maintain the pressure above 9.0 MPa. In both sets, L decreases as both T_{tr} and CO or CH_4 concentrations increase due to the increase in the pressure drop which in turn is due to the decrease in the density and the viscosity (SI Figure S4). In set A, L varies approximately 470 km between the represented ranges of composition, pressure and temperature. Moreover, at low T_{tr}, both the type of impurity (CO or CH_4) and its concentration affect L strongly, whereas at high T_{tr}, only the concentration has an influence (CO_2+CO and CO_2+CH_4 systems exhibit a similar behavior). In set B, the variation of T_{tr} and CO or CH_4 concentration has a less pronounced effect on L (approximately 85 km).

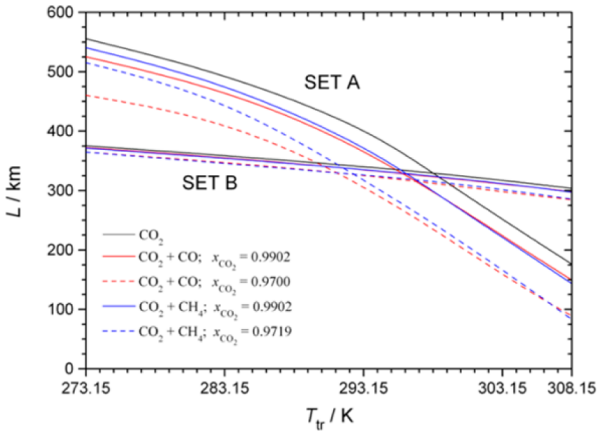

Figure 3. Maximum repressurization (pumping) distances, L, versus transport temperature, T_{tr}, for pure CO_2, CO_2+CO, and CO_2+CH_4 mixtures. Set A: L required to maintain the density of the fluid above 800 kg/m^3. Set B: L required to maintain the pressure above 9.0 MPa. Mass flow was taken to be m = 317 kg/s, inner diameter of the pipeline D = 0.508 m, and roughness height e = 4.6 × 10^{-5} m. The pipeline inlet pressure was set at 20.0 MPa.

SI Figure S5 shows an estimation of the booster power required to repressurize the fluid up to a booster outlet pressure P_{out} = P_{max} = 20.0 MPa, W_{20}, versus the transport temperature, T_{tr}. It was assumed that the fluid enters the booster at the inlet temperature, T_{in} = T_{tr}, and leaves it at the outlet temperature T_{out} = 38 °C (311 K).[11,25,51,54,60] The average in−out values for each fluid density were used. Set A presents W_{20} required when the booster inlet pressure, P_{in}, is P_{min}^{800} at T_{in}; set B presents W_{20} when P_{in} = P_{min} is 9.0 MPa. In set A, the variation of W_{20} with both T_{tr} and composition is similar to that found for L in the same set in Figure 3, and W_{20} varies within the represented range of composition, T and P by approximately 6.9 MW. In set B, the variation is the opposite: the higher the temperature or the impurity concentration, the higher W_{20} becomes, with $\Delta W_{20} \cong 1.8$ MW.

Thus, at 283.15 K, a typical T_{tr}, one must repressurize at a maximum distance of ≅ 420−497 km (depending on the composition of the fluid) to keep the density above 800 kg/m^3, and the required booster power ranges from approximately 7.0 to 7.9 MW. However, to keep the pressure above 9.0 MPa, the repressurization distance varies from ≅ 346 to 359 km, and the booster power varies between ≅ 5.3 and 5.5 MW (Figure 3 and SI Figures S5, S6, and S7). The best operational options for a given network can be calculated. For instance, for a 400 km pipeline, no booster stations would be necessary to maintain

the density above 800 kg/m^3; however, one booster would be required to maintain the pressure above 9.0 MPa.

3.1.4. Pipeline Inner Diameter, D. SI Figure S8 shows the inner diameter of a pipeline, D, versus its capacity (mass flow, m) for the studied systems at several values for T and P under the transport conditions. The represented range of capacity was chosen to be approximately 317 kg/s (10.0 Mt/year). Diameters were iteratively calculated for each mass flow assuming an average pressure drop per meter of 33 Pa/m and a roughness height of the pipeline of 4.6×10^{-5} m.[32] The transported mass flow for a given diameter decreases as P decreases and as T increases or as impurity concentration rises. For identical mole fractions at low temperature and high pressure, the behaviors of the mixtures containing either CO or CH_4 are very similar. However, greater differences appear at high temperature, high concentration of impurities, and at low pressure. Within the represented capacities, the largest difference between the pipeline diameter calculated for pure CO_2 and those for the studied mixtures is 27 mm (corresponding to the CO_2+CO system with x_{CO_2} = 0.9700 at T = 308.15 K and P = 9.0 MPa, SI Figure S8e). The increase of 27 mm in the inner diameter means an increase of approximately 11 tons (approximately 5% of the total weight) of steel per km of pipeline (standard carbon steel pipeline, API 5L X70, inner diameter 536 mm, wall thickness 16.5 mm,[62] and mass flow 317 kg/s).

3.2. Influence of Impurities on Storage and Injection. In CO_2 storage, impurities have different effects depending on the type of reservoir and the interaction between the injected anthropogenic CO_2 and the substances present beforehand. The effects of CO on several parameters related to the storage and injection steps and the comparison with those of CH_4 are discussed below.

3.2.1. Solubility Parameter, δ. Given the values of temperature and pressure inside the reservoirs, the fluid is in a supercritical state and therefore has one of the characteristic properties of this state, which is a large solvent capacity. The solubility parameter (eq 1)[63] has been extensively used to predict in a semiquantitative manner the behavior of liquid mixtures[64−67] and slightly polar supercritical fluids.[18,68] We utilized δ to study the interactions between the injected fluid (considered as the solvent) and other substances in the reservoir.

$$\delta = \left(\frac{-E(T)}{V(T, P)}\right)^{1/2} \quad (1)$$

where $(-E/V)$ is the so-called "cohesive energy density". In this work, we used the internal pressure, π, to estimate the solubility parameter, thus applying the approach made by Hansen[64] and neglecting the small dipole moment of CO (0.12 D):[69]

$$\delta = \pi^{1/2} \quad (2)$$

$$\pi = \left(\frac{\partial U}{\partial V}\right)_T = T\left(\frac{\partial P}{\partial T}\right)_V - P = T\frac{\alpha_P}{\kappa_T} - P \quad (3)$$

where α_P is the isobaric thermal expansivity, and κ_T is the isothermal compressibility. We obtained values for α_P, κ_T, and δ from the $P\rho T x_{CO_2}$ measurements (SI Table S8), with the following MRD$_x$ values calculated in relation to values from the best EoS, the GERG EoS, to reproduce our experimental values:[36] MRD$_{\alpha_P}$ = 2.54%, MRD$_{\kappa_T}$ = 1.47% and MRD$_\delta$ = 1.59% (subcritical temperatures, 253.15 K ≤ T ≤ 293.15 K) and MRD$_{\alpha_P}$ = 5.04%, MRD$_{\kappa_T}$ = 4.27% and MRD$_\delta$ = 3.04% (supercritical isotherms, 304.21 K ≤ T ≤ 333.15 K).

Solubility parameters are represented in SI Figure S9 for pure CO_2 and CO_2+CO mixtures with x_{CO_2}= 0.9902 and x_{CO_2} = 0.9700 at 293.15, 308.15, and 333.15 K. As seen, the presence of CO in the anthropogenic CO_2 causes δ to diminish compared to pure CO_2, reducing the solvent power of the fluid and consequently hindering fluid trapping. The same effect was already observed for the CO_2+CH_4 system.[19] For the studied conditions, the solubility parameter decreases as temperature increases and pressure decreases. Our values for the solubility parameter are consistent with those from the literature for CO_2+CO at 333.15 K,[30] but they are not directly comparable due to their different compositions.

Allada et al.[68] suggest that the solubility parameter is the key determinant of solubility in supercritical solvents, and they were able to unify diverse behaviors of solvents regardless of T, P, and their nature. Moreover, different authors[18,30] note that density has the strongest influence on the solvent capacity of dense fluids. Figure 4 shows δ versus ρ for pure CO_2 and six

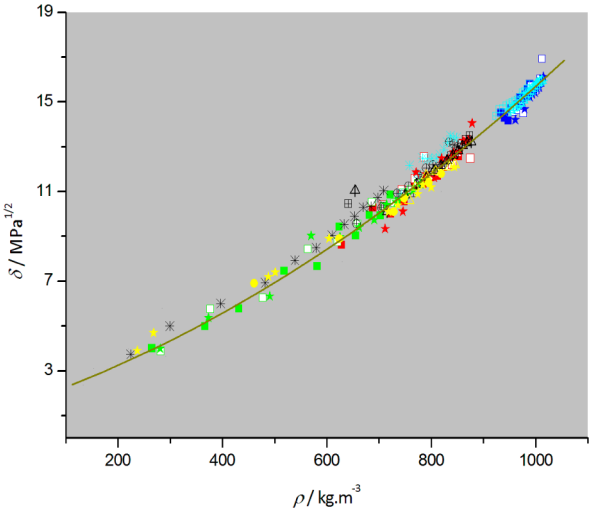

Figure 4. Solubility parameter, δ, against density, ρ, for pure CO_2[18] (line); CO_2+CO mixtures with x_{CO_2} = 0.9700 (■), x_{CO_2} = 0.9902 (□) and x_{CO_2} = 0.9930 (★) at 273.15 K (blue), 304.21 K (red) and 323.15 K (green); CO_2+CH_4 mixtures[19] with x_{CO_2} = 0.8525 (*), x_{CO_2} = 0.9719 (⊕) and x_{CO_2} =0.9932 (⊞) at 273.15 K (cyan) and 304.21 K (black); and CO_2+CO (▲), CO_2+H_2 (●) and CO_2+CO+H_2 (★) mixtures[30] (yellow).

CO_2+CO, CO_2+CH_4, CO_2+H_2, and CO_2+CO+H_2 mixtures from this work and other literature.[18−20,30] The graphic shows a good δ−ρ correlation within the represented density range. This means that systems with different T and/or P, but with the same density, will have the same solubility parameter and, therefore, that the solubilization capacity of the injected CO_2 could be known from its density at storage conditions.

In the following, we compare the influence of two noncondensable impurities, CO or CH_4, on the storage capacity, M, the rising velocity of the plume inside deep saline aquifers, v, and the permeation flux during injection, $\dot{M}$. For this purpose, we use normalized parameters, X/X_0, where X is the value corresponding to the CO_2+CO or CO_2+CH_4 systems and X_0 corresponds to pure CO_2. The studied T and P ranges are

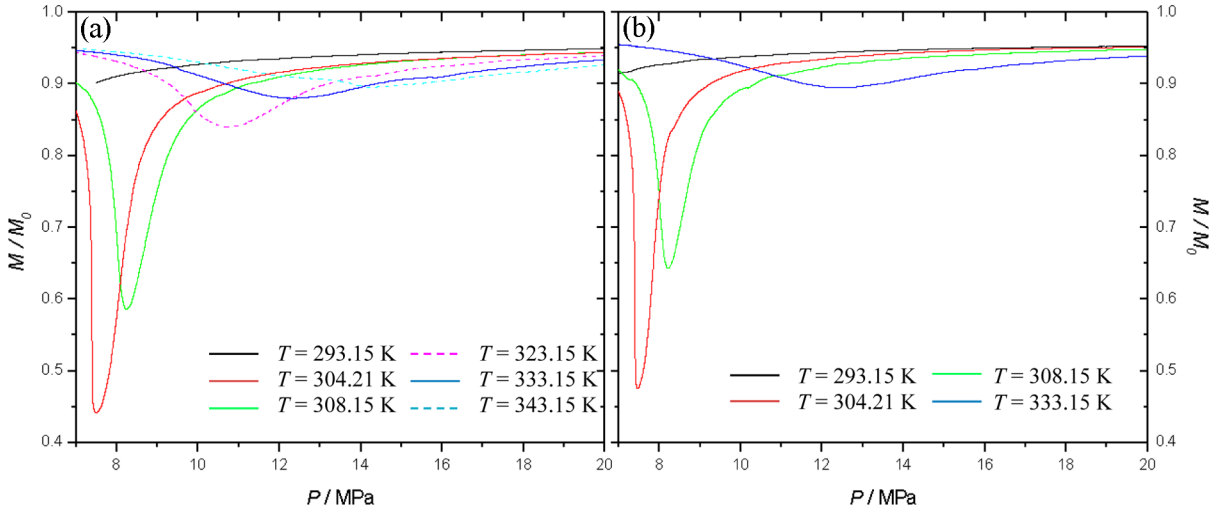

Figure 5. Normalized storage capacity, M/M_0, versus pressure at several temperatures for (a) CO_2+CO (x_{CO_2} = 0.9700) and (b) CO_2+CH_4[19] (x_{CO_2} = 0.9719) mixtures.

293.15 K − 343.15 K and 7 MPa−20 MPa, respectively, and are within the temperature and pressure ranges of the operating reservoirs in different scenarios.[12,24] The equations used are as follows:[12,19]

$$\frac{M}{M_0} = \frac{\rho}{\rho_0\left[1 + \sum_i \left(\frac{m_i}{m_0}\right)\right]} \quad (4)$$

$$\frac{v}{v_0} = \frac{F/(\rho\eta)}{F_0/(\rho_0\eta_0)} = \frac{(\rho_{br} - \rho)(\rho_0\eta_0)}{(\rho_{br} - \rho_0)(\rho\eta)} \quad (5)$$

$$\frac{\dot{M}}{\dot{M}_0} = \frac{\rho\left(\frac{\eta_0}{\eta}\right)}{\rho_0\left[1 + \sum_i \left(\frac{m_i}{m_0}\right)\right]} \quad (6)$$

where m_i/m_0 is the ratio of the mass of impurity i to the mass of CO_2 in the mixture; (ρ,η,F) and (ρ_0,η_0,F_0) are the density, the viscosity, and the buoyancy force of the mixture and the pure CO_2 stream, respectively; and ρ_{br} is the density of the brine.

Density values were taken from experimental $P\rho Tx_{CO_2}$ data for pure CO_2,[18] CO_2+CO (this work and literature values[20]), and CO_2+CH_4.[19,20] The values of 1025 kg/m^3 and 1250 kg/m^3, representative of dilute and highly concentrated brines,[70] were used for ρ_{br}. Viscosity data were calculated as previously described.[48]

3.2.2. Normalized Storage Capacity, M/M_0. This parameter is dependent on composition, T and P. Streams with high concentrations of noncondensable impurities reduce the storage capacity by a large amount if T and P are near of the critical values of the mixture. For example, an impurity of 15% by mole CH_4 reduces M/M_0 to approximately 0.35 at 308.15 K and 8.5 MPa,[19] revealing that a relatively shallow site may not be appropriate for storing high impurity streams. Figure 5 shows M/M_0 versus P at several T for the two systems with x_{CO_2} 0.97, the highest impurity concentration in this work. The maximum decrease appears near the critical point of anthropogenic CO_2 ($M/M_0 \cong 0.44$ for CO_2+CO at 304.21 K and 7.5 MPa). An increase in temperature shifts this maximum decrease to a higher pressure, and its magnitude decreases ($M/M_0 \cong 0.89$ at 343.15 K and 14.1 MPa). Likewise, as the depth of the geological formation increases, the influence of the type of impurity on storage capacity decreases. It can be seen that CO affects the mass of anthropogenic CO_2 that can be stored in a reservoir more negatively than CH_4 so that, for the same mass of fluid, it would be necessary to confine the CO_2+CO system at higher pressure than CO_2+CH_4. Storage efficiency can be improved if the injection pressure is well above the minimum values shown in these representations. In the case of closed reservoirs, this value for pressure has to be within the allowable overpressure range. For open formations, an option could be to increase the depth of storage, given that overpressure may not be attainable.

3.2.3. Normalized Rising Velocity, v/v_0. If the reservoir is a saline aquifer, then the stored fluid pushes up with a buoyancy force, F, which is given by the difference between its density and that of brine (eq 5). The speed of the plume, ν, is directly proportional to the buoyancy force and inversely proportional to its viscosity. The presence of noncondensable impurities increases the rising velocity, although the values of the normalized parameter depend on temperature and pressure. The v/v_0 relations, represented in SI, Figure S10 versus P at several T for the two systems with ρ_{br}= 1025 kg/m^3, present maxima at $T \geq 304.21$ K, which are higher for the CO_2+CO mixtures than for CO_2+CH_4 (9.2 and 7.7 at 304.21 K, respectively). The maxima for each temperature are found at pressures inside the depth range corresponding to a saline aquifer.[24] The presence of CO or CH_4 leads to an increase in the rising velocity of the plume, which is significant near the critical point of the fluid, resulting in the decrease of the CO_2−brine contact and therefore the solvent effect. The lateral spreading of the plume also decreases, and as a consequence, the amount of trapped fluid in the rock's pores diminishes. These effects reduce the CO_2 storage security and become even more important near the cap rock, at a lower depth (low pressure range of the representation where the highest peaks are found), and the risk of leakage could increase. An increase in the density of the brine reduces F/F_0 and v/v_0 (SI Figures S10 and S11).

3.2.4. Normalized Permeation Flux, $\dot{M}/\dot{M}_0$. The relative injectivity of the impure CO_2 stream depends on the effect of impurities, T and P, on both the density and the viscosity. $\dot{M}$ reduces as a result of the lower density of these mixtures in

relation to CO_2; however, due to the compensation by increased viscosity, the reduction is smaller than that of the storage capacity discussed before. In the studied systems $\rho < \rho_0$ and $\eta < \eta_0$ and given the relative values of ρ/ρ_0 and η_0/η in eq 6, the normalized permeation flux can be higher or lower than unity. Figure S12 shows that the largest differences from 1 appear in the vicinity of the critical point. At high pressures throughout the studied T range, the effect of temperature diminishes, and $\dot{M}/\dot{M}_0$ tends to values approaching unity. It can be seen that the influence of CO is greater than that of CH_4 on this parameter. Another effect of noncondensable impurities, such as CO or CH_4, on the injection step is the need to increase the headhole pressure as a consequence of the lower hydrostatic pressure of the injection well.[71]

From the obtained results for the three normalized storage and injection parameters, we verified the following trends with composition, T and P: (i) a high impurity composition modifies these parameters by a large amount; (ii) for the same composition, the highest deviations from pure CO_2 appear near the critical point of the mixture; (iii) as pressure increases, the influence of temperature becomes less important; (iv) as the pressure and temperature increase, the influence of the presence of impurities is attenuated; (v) the parameter most affected by impurities is the rising velocity over the entire studied ranges of T and P; and (vi) CO has a greater effect than CH_4 on all the studied normalized parameters and becomes the most problematic of the two impurities.

In summary, the presence of the studied impurities, CO and CH_4, leads to (i) a decrease in the interactions that enable CO_2 to become trapped inside the storage area; (ii) the need for greater storage capacity reservoirs and/or a larger number of sites to confine the same mass of fluid; (iii) an increased risk of leakage in saline aquifers; (iv) the need to increase the injection pressure; and (v) a need to increase the number of monitoring units to ensure a safe process. All these effects result in an increase in the overall cost of the process. Similar observations have been found in literature for other noncondensable impurities.[12]

■ ASSOCIATED CONTENT

Supporting Information

Additional tables and figures regarding experimental data, derivative properties, EoS modeling and transport and storage parameters are presented. This material is available free of charge via the Internet at http://pubs.acs.org.

■ AUTHOR INFORMATION

Corresponding Author

*E-mail: curra@unizar.es.

Notes

The authors declare no competing financial interest.

■ ACKNOWLEDGMENTS

The authors gratefully acknowledge financial support received from the Ministerio de Ciencia e Innovación (CTQ2008-02037), Ministerio de Economía y Competitividad (CTQ2011-24875), Convenio La Caixa—Gobierno de Aragón and Universidad de Zaragoza (UZ2012-CIE-13).

■ REFERENCES

(1) *The Global Status of CCS: 2013*; Global CCS Institute: Melbourne, Australia, 2013; http://www.globalccsinstitute.com/publications/global-status-ccs-2013.

(2) *The Global Status of CCS: 2012*; Global CCS Institute: Canberra, Australia, 2012; http://www.globalccsinstitute.com/publications/global-status-ccs-2012.

(3) *Geological Storage of Carbon Dioxide: Staying Safely Underground*; International Energy Agency, Greenhouse Gas R&D Programme, January 2008; http://www.co2crc.com.au/dls/external/geostoragesafe-IEA.pdf.

(4) Olajire, A. A. CO_2 capture and separation technologies for end-of-pipe applications—A review. *Energy* **2010**, *35* (6), 2610−2628, DOI: 10.1016/j.energy.2010.02.030.

(5) Boot-Handford, M. E.; Abanades, J. C.; Anthony, E. J.; Blunt, M. J.; Brandani, S.; Mac Dowell, N.; Fernandez, J. R.; Ferrari, M.-C.; Gross, R.; Hallett, J. P.; Haszeldine, R. S.; Heptonstall, P.; Lyngfelt, A.; Makuch, Z.; Mangano, E.; Porter, R. T. J.; Pourkashanian, M.; Rochelle, G. T.; Shah, N.; Yao, J. G.; Fennell, P. S. Carbon capture and storage update. *Energy Environ. Sci.* **2014**, *7*, 130−189, DOI: 10.1039/c3ee42350f.

(6) Xu, T.; Apps, J. A.; Pruess, K.; Yamamoto, H. Numerical modeling of injection and mineral trapping of CO_2 with H_2S and SO_2 in a sandstone formation. *Chem. Geol.* **2007**, *242*, 319−346, DOI: 10.1016/j.chemgeo.2007.03.022.

(7) *Capture and Storage of CO_2 with other Air Pollutants*; International Energy Agency, Clean Coal Centre, January 2010; http://www.uscsc.org/Files/Admin/Educational_Papers/IEA_Co-Sequestration_Paper.pdf.

(8) Misiak, K.; Sanchez Sanchez, C.; van Os, P.; Goetheer, E. Next generation post-combustion capture: Combined CO_2 and SO_2 removal. *Energy Procedia* **2013**, *37*, 1150−1159, DOI: 10.1016/j.egypro.2013.05.212.

(9) Corvisier, J.; Bonvalot, A.-F.; Lagneau, V.; Chiquet, S. R.; Sterpenich, J.; Pironon, J. Impact of co-injected gases on CO_2 storage sites: Geochemical modeling of experimental results. *Energy Procedia* **2013**, *37*, 3699−3710, DOI: 10.1016/j.egypro.2013.06.264.

(10) Li. H.; Yan, J. Impacts of impurities in CO_2-fluids on CO_2 transport process. *Proceedings of GT200, ASME Turbo Expo 2006*, Barcelona, Spain, May 8−11, 2006; GT2006−90954.

(11) Seevam, P. N.; Race, J. M.; Downie, J. M.; Hopkins, P. Transporting the next generation of CO_2 for carbon, capture and storage: The impact of impurities on supercritical CO_2 pipelines. *Proceedings of IPC2008, 7th International Pipeline Conference*, Calgary, Alberta, Canada, September 29-October 3, 2008; IPC2008−64063.

(12) *Effects of impurities on geological storage of CO_2*; IEAGHG, Report: 2011/04, June 2011. http://cdn.globalccsinstitute.com/sites/default/files/publications/16876/effects-impurities-geological-storage-co2.pdf.

(13) *CO_2QUEST* Website; http://www.co2quest.eu/.

(14) *IMPACTS* Website; http://www.sintef.no/Projectweb/IMPACTS/.

(15) Li, H.; Jakobsen, J. P.; Wilhelmsen, Ø.; Yan, J. PVTxy properties of CO_2 mixtures relevant for CO_2 capture, transport and storage: Review of available experimental data and theoretical models. *Appl. Energy* **2011**, *88* (11), 3567−3579, DOI: 10.1016/j.apenergy.2011.03.052.

(16) Løvseth, S. W.; Skaugen, G.; Stang, H. G. J.; Jakobsen, J. P.; Wilhelmsen, Ø.; Span, R.; Wegge, R. CO_2Mix Project: Experimental determination of thermo-physical properties of CO_2-rich mixtures. *Energy Procedia* **2013**, *37*, 2888−2896, DOI: 10.1016/j.egypro.2013.06.174.

(17) Gil, L.; Otín, S. F.; Muñoz Embid, J.; Gallardo, M. A.; Blanco, S.; Artal, M.; Velasco, I. Experimental setup to measure critical properties of pure and binary mixtures and their densities at different pressures and temperatures. Determination of the precision and uncertainty in the results. *J. Sup. Fluids* **2008**, *44*, 123−138, DOI: 10.1016/j.supflu.2007.11.003.

(18) Velasco, I.; Rivas, C.; Martínez-López, J. F.; Blanco, S. T.; Otín, S.; Artal, M. Accurate values of some thermodynamic properties for carbon dioxide, ethane, propane, and some binary mixtures. *J. Phys. Chem. B* **2011**, *115* (25), 8216−8230, DOI: 10.1021/jp202317n.
(19) Blanco, S. T.; Rivas, C.; Fernández, J.; Artal, M.; Velasco, I. Influence of methane in CO_2 transport and storage for CCS technology. *Environ. Sci. Technol.* **2012**, *46*, 13016−13023, DOI: 10.1021/es3037737.
(20) Rivas, C.; Blanco, S. T.; Fernández, J.; Artal, M.; Velasco, I. Influence of methane and carbon monoxide in the volumetric behaviour of the anthropogenic CO_2: Experimental data and modelling in the critical region. *Int. J. Greenh. Gas Con.* **2013**, *18*, 264−276, DOI: 10.1016/j.ijggc.2013.07.019.
(21) Bachu, S. Screening and ranking of sedimentary basins for sequestration of CO_2 in geological media in response to climate change. *Environ. Geol.* **2003**, *44* (3), 277−289, DOI: 10.1007/s00254-003-0762-9.
(22) *Reference cases and guidelines for technology concepts*; ENCAP-WP1.1, Deliverable D1.1.1 & D1.1.2; Vattenfall A/S Report No.: 55431, Issue No. 4, February 2008; http://refman.et-model.com/publications/433.
(23) *State-of-the-Art Overview of CO_2 Pipeline Transport with relevance to offshore pipelines*; POLYTEC, Report number POL-O-2007−138-A, 8 January 2008; https://www.researchgate.net/publication/228688545_State-of-the-Art_overview_of_CO2_pipeline_transport_with_relevance_to_offshore_pipelines.
(24) Michael, K.; Golab, A.; Shulakova, V.; Ennis-King, J.; Allison, G.; Sharma, S.; Aiken, T. Geological storage of CO_2 in saline aquifers—A review of the experience from existing storage operations. *Int. J. Greenhouse Gas Control* **2010**, *4*, 659−667, DOI: 10.1016/j.ijggc.2009.12.011.
(25) *CO_2 pipeline infrastructure: An analysis of global challenges and opportunities*; ElementEnergy for International Energy Agency, Greenhouse Gas Programme Final Report, April 2010; http://www.ccsassociation.org.uk/docs/2010/IEA%20Pipeline%20final%20report%20270410.pdf.
(26) *Annual European Union greenhouse gas inventory 1990−2011 and inventory report 2013*. Technical report No 8/2013. EEA (European Environment Agency), 2012; http://www.eea.europa.eu/publications/european-union-greenhouse-gas-inventory-2013.
(27) *CO_2 Pipeline Infrastructure*; IEAGHG, Report: 2013/18, December 2013; http://cdn.globalccsinstitute.com/sites/default/files/publications/16876/effects-impurities-geological-storage-co2.pdf.
(28) *Inventory of U.S. greenhouse gas emissions and sinks: 1990 − 2011*. EPA 430-R-13−001. U.S. Environmental Protection Agency, 2013; http://www.epa.gov/climatechange/ghgemissions/usinventoryreport/archive.html.
(29) Mallu, B. V.; Viswanath, D. S. Compression factors and second virial coefficients of hydrogen, methane and carbon dioxide mixtures $\{xCO_2 + (1 - x)H_2\}$,and $\{xCO_2 + (1 - x)CH_4\}$. *J. Chem. Thermodyn.* **1990**, *22*, 997−1006, DOI: 10.1016/0021-9614(90)90189-W.
(30) Cipollina, A.; Anselmo, R.; Scialdone, O.; Filardo, G.; Galia, A. Experimental $P-T-\rho$ measurements of supercritical mixtures of carbon dioxide, carbon monoxide, and hydrogen and semiquantitative estimation of their solvent power using the solubility parameter concept. *J. Chem. Eng. Data* **2007**, *52*, 2291−2297, DOI: 10.1021/je700307r.
(31) Kaminishi, G.; Toriumi, T. Vapor−liquid equilibria in the systems: CO_2—CO, CO_2—CO—H_2 and CO_2—CH_4. *Rev. Phys. Chem. Jpn.* **1968**, *38* (1), 79−84.
(32) Vandeginste, V.; Piessens, K. Pipeline design for a least-cost router application for CO_2 transport in the CO_2 sequestration cycle. *Int. J. Greenhouse Gas Control* **2008**, *2*, 571−58, DOI: 10.1016/j.ijggc.2008.02.001.
(33) Munkenjord, S. T.; Bernstone, C.; Clausen, S.; de Koejir, G.; Mølnvik, J. Combining thermodynamic and fluid modelling for CO_2 flow assurance. *Energy Procedia* **2013**, *37*, 2904−2913, DOI: 10.1016/j.egypro.2013.06.176.
(34) Ziabakhsh-Ganji, Z.; Kooi, H. Sensitivity of Joule−Thomson cooling to impure CO_2 injection in depleted gas reservoirs. *Appl. Energy* **2014**, *113*, 434−451, DOI: 10.1016/j.apenergy.2013.07.059.
(35) Peng, D. Y.; Robinson, D. B. A new two-constant equation of state. *Ind. Eng. Chem. Fundam.* **1976**, *15*, 59−64, DOI: 10.1021/i160057a011.
(36) Kunz, O.; Klimeck, R.; Wagner, W.; Jaeschke, M. *GERG Technical Monograph*; Fortschr.-Ber.: VDI, VDI-Verlag: Dusseldorf, Germany, 2006.
(37) Gross, J.; Sadowski, G. Perturbed-chain SAFT: An equation of state based on a perturbation theory for chain molecules. *Ind. Eng. Chem. Res.* **2001**, *40*, 1244−1260, DOI: 10.1021/ie0003887.
(38) Gross, J.; Sadowski, G. Application of the perturbed-chain SAFT equation of state to associating systems. *Ind. Eng. Chem. Res.* **2002**, *41*, 5510−5515, DOI: 10.1021/ie010954d.
(39) Wilhelmsen, Ø.; Skaugen, G.; Jørstad, O.; Li, H. Evaluation of SPUNG# and other equations of state for use in carbon capture and storage modelling. *Energy Procedia* **2012**, *23*, 236−245, DOI: 10.1016/j.egypro.2012.06.024.
(40) Diamantonis, N. I.; Boulougouris, G. C.; Tsangaris, D. M.; El Kadi, M.; Saadawi, H.; Economou, I. G. Thermodynamic and transport property models for carbon capture and sequestration (CCS) processes with emphasis on CO_2 transport. *Chem. Eng. Res. Des.* **2013**, *91*, 1793−1806, DOI: 10.1016/j.cherd.2013.06.017.
(41) Wareing, C. J.; Woolley, R. M.; Fairweather, M.; Falle, S. A. G. E.; Cleaver, R. P. Large-Scale Validation of a Numerical Model of Accidental Releases from Buried CO_2 Pipelines. *Proceedings of the 23rd European Symposium on Computer Aided Process Engineering—ESCAPE 23*; Lappeenranta, Finland, June 9−12, 2013.
(42) Yokozeki, A. Analytical equation of state for solid−liquid−vapor phases. *Int. J. Thermophys.* **2003**, *24* (3), 589−620, DOI: 10.1023/A:102401572909.
(43) Trusler, J. P. M. Equation of state for solid phase I of carbon dioxide valid for temperatures up to 800 K and pressures up to 12 GPa. *J. Phys. Chem. Ref. Data* **2011**, *40*, 043105 DOI: 10.1063/1.3664915.
(44) Trusler, J. P. M. Erratum: Equation of state for solid phase I of carbon dioxide valid for temperatures up to 800 K and pressures up to 12 GPa [*J. Phys. Chem. Ref. Data 40*, 043105 (**2011**)]. *J. Phys. Chem. Ref. Data* **2012**, *41*, 039901 DOI: 10.1063/1.4745598.
(45) Diamantonis, N.; Boulougouris, G.; Tsangaris, D. M.; Economou, I. Modelling solid-fluid equilibria using the Yokozeki EoS. *CO_2QUEST Newsletter* **2013**, *Autumn*, 11−13.
(46) Jager, A.; Span, R. Equation of state for solid carbon dioxide based on the Gibbs free energy. *J. Chem. Eng. Data* **2012**, *57* (2), 590−597, DOI: 10.1021/je2011677.
(47) *JCGM 100:2008. Evaluation of measurement data—Guide to expression of uncertainty in measurement*; Joint Committee for Guides in Metrology, Serves Cedex, France, 2008;http://www.bipm.org/utils/common/documents/jcgm/JCGM_100_2008_E.pdf.
(48) Lemmon, E. W.; Huber, M. L.; McLinden, M. O. NIST Standard Reference Database 23: Reference Fluid Thermodynamic and Transport Properties-REFPROP, Version 9.0; National Institute of Standards and Technology, Standard Reference Data Program: Gaithersburg, 2010.
(49) West, J. M. Design and operation of a supercritical CO_2 pipeline-compression system, SACROC unit, Scurry County, Society of Petroleum Engineers Permian Basin Oil and Gas Recovery Conference. TX, paper SPE 4804, 1974.
(50) Knoope, M. M. J.; Guijt, W.; Ramírez, A.; Faaij, A. P. C. Improved cost models for optimizing pipeline configuration for point-to-point pipelines and simple networks. *Int. J. Greenhouse Gas Control* **2014**, *22*, 25−46, DOI: 10.1016/j.ijggc.2013.12.016.
(51) Farris, C. B. Usual design factors for supercritical CO_2 pipelines. *Energy Progress* **1983**, *3* (3), 150−158.
(52) McCollough, D. E. The central basin pipeline: A CO_2 system in West Texas. *Energy Progress* **1986**, *6* (4), 230−234.
(53) Svensson, R.; Odenberger, M.; Johnsson, F.; Strömberg, L. Transportation infrastructure for CCS—Experiences and expected

development. *Greenhouse Gas Control Technologies 7. Proceedings of the 7th International Conference on Greenhouse Gas Control Technologies*; *Vol. II*, 2535−2539, Vancouver, Canada, September 5, 2004; DOI 10.1016/B978-008044704-9/50367-0.
(54) Mohitpour, M.; Golshan, H.; Murray, A. *Pipeline Design & Construction: A Practical Approach*, 3rd ed.; The American Society of Mechanical Engineers: New York, 2007.
(55) Kaufmann, K.-D. Carbon dioxide transport in pipelines—Under special consideration of safety-related aspects. Pipeline Technology Conference 2008, Munich, Germany, 2008.
(56) *Technical and Economic Characteristics of a CO_2 Transmission Pipeline Infraestructure*; European Commission, JRC62502, 2011; DOI 10.2790/30861; http://publications.jrc.ec.europa.eu/repository/bitstream/111111111/16038/1/reqno_jrc62502_aspublished.pdf.
(57) Botnen, H. A.; Omar, A. M.; Aavatsmark, G.; Alendal, G.; Johannessen, T. PVTx properties of two-phase CO_2 jet from ruptured pipeline. *Energy Procedia* **2013**, *37*, 3031−3038, DOI: 10.1016/j.egypro.2013.06.189.
(58) Patchigolla, K.; Oakey, J. E. Design overview of high pressure dense phase CO_2 pipeline transport in flow mode. *Energy Procedia* **2013**, *37*, 3121−3130, DOI: 10.1016/j.egypro.2013.06.198.
(59) Jung, J.-Y.; Huh, C.; Kang, S.-G.; Seo, Y.; Chang, D. CO_2 transport strategy and its cost estimation for the offshore CCS in Korea. *Appl. Energy* **2013**, *111*, 1054−1060, DOI: 10.1016/j.apenergy.2013.06.055.
(60) Witkowski, A.; Rusin, A.; Majkut, M.; Rulik, S.; Stolecka, K. Comprehensive analysis of pipeline transportation systems for CO_2 sequestration. Thermodynamics and safety problems. *Energy Convers. Manage.* **2013**, *76*, 665−673, DOI: 10.1016/j.enconman.2013.07.087.
(61) Knoope, M. M. J; Ramírez, A.; Faaij, A. P. C. A state-of-the-art review of techno-economic models predicting the costs of CO_2 pipeline transport. *Int. J. Greenhouse Gas Conrol* **2013**, *16*, 241−270, DOI: 10.1016/j.ijggc.2013.01.005.
(62) McCoy, S. T.; Rubin, E. S. An engineering-economic model of pipeline transport of CO_2 with application to carbon capture and storage. *Int. J. Greenhouse Gas Conrol* **2008**, *2*, 219−229, DOI: 10.1016/S1750-5836(07)00119-3.
(63) Hildebrand, J. H.; Scott, R. L. *The Solubility of Nonelectrolytes*; Reinhold: New York, 1950.
(64) Hansen, C. M. The universality of the solubility parameter. *Ind. Eng. Chem. Prod.* **1969**, *8* (1), 2−11, DOI: 10.1021/i360029a002.
(65) Hansen, C. M. *Hansen Solubility Parameters—A User's Handbook*; CRC Press: Boca Raton, FL, 2000.
(66) Bagley, E. B.; Nelson, T. P.; Scigliano, J. M. Three-dimensional solubility parameters and their relationship to internal pressure measurements in polar and hydrogen bonding solvents. *J. Paint Technol.* **1971**, *43* (555), 35−42.
(67) Verdier, S.; Duong, D.; Andersen, S. I. Experimental determination of solubility parameters of oils as a function of pressure. *Energy Fuels* **2005**, *19* (4), 1225−1229, DOI: 10.1021/ef049827v.
(68) Allada, S. R. Solubility parameters of supercritical fluids. *Ind. Eng. Chem. Proc.* **1984**, *23* (2), 344−348, DOI: 10.1021/i200025a028.
(69) Williams, L. L.; Rubin, J. B.; Edwards, H. W. Calculation of Hansen solubility parameter values for a range of pressure and temperature conditions, including the supercritical fluid region. *Ind. Eng. Chem. Res.* **2004**, *43*, 4967−4972, DOI: 10.1021/ie0497543.
(70) Some Fundamentals of Mineralogy and Geochemistry. Deep-basins brines I: Density, TDS, and chloride; http://www.gly.uga.edu/railsback/Fundamentals/815BrinesDiagrams07IP.pdf.
(71) Sass, B. M.; Farzan, H.; Prabhakar, R.; Gerst, J.; Sminchak, J.; Bhargava, M.; Nestleroth, B.; Figueroa, J. Considerations for treating impurities in oxy-combustion flue gas prior to sequestration. *Energy Procedia* **2009**, *1*, 535−542, DOI: 10.1016/j.egypro.2009.01.071.
(72) Laursen, T. *VLXE ApS*; Scion-DTU: Diplomvej, Denmark, 2012.

J. Chem. Thermodynamics 98 (2016) 272–281

Contents lists available at ScienceDirect

J. Chem. Thermodynamics

journal homepage: www.elsevier.com/locate/jct

Thermodynamic properties of a CO_2 – rich mixture (CO_2 + CH_3OH) in conditions of interest for carbon dioxide capture and storage technology and other applications

Clara Rivas [a], Beatriz Gimeno [a], Ramón Bravo [b], Manuela Artal [a], Javier Fernández [a], Sofía Teresa Blanco [a], María Inmaculada Velasco [a,*]

[a] Departamento de Química Física, Facultad de Ciencias, Universidad de Zaragoza, 50009 Zaragoza, Spain
[b] Departamento de Física Aplicada, Facultad de Física, Universidad de Santiago de Compostela, 15782 Santiago de Compostela, Spain

ARTICLE INFO

Article history:
Received 12 January 2016
Received in revised form 14 March 2016
Accepted 15 March 2016
Available online 16 March 2016

Keywords:
CO_2
Methanol
Density
Speed of sound
PC-SAFT EoS
GERG EoS

ABSTRACT

Methanol can be an impurity in transported and stored anthropogenic CO_2 in carbon dioxide capture and storage technology; likewise, methanol is one of the most useful CO_2 modifiers for supercritical processes. Therefore reliable values of thermodynamic properties of CO_2 – rich mixtures CO_2 + CH_3OH are needed. We measured the following properties of a (CO_2 + CH_3OH) mixture with $x_{CO_2} = 0.9700$ in dense phase at six temperatures from 263.15 K to 313.15 K:

- The speed of sound, c, up to 194.49 MPa, using a double-path pulse-echo method at 5 MHz, for which a repeatability study gave an overall standard uncertainty of c, $u(c) = 5.9 \times 10^{-4} c$.
- The density, ρ, at pressures $\leqslant$20.00 MPa using a vibrating-tube densimeter with a standard uncertainty, $u(\rho) = 0.4$ kg/m^{-3}.

Combining our c and ρ experimental values and the isobaric specific heat capacity, c_p, from the GERG equation of state (EoS), we calculated ρ, c_p, the volume-dependent solubility parameter, δ_V, and the Joule–Thomson coefficient, μ_{JT}, at pressures $\leqslant$195.0 MPa. We are the first to report the adaptation for compressed gases of a calculation method based on numerical integration previously used only for liquids. The experimental and calculated values were compared with those from the PC-SAFT and GERG EoSs, allowing us to validate both EoSs to represent the experimental properties of the system under most conditions studied and the calculation method up to 195.0 MPa.

1. Introduction

Carbon dioxide capture and storage (CCS) is considered one of the most important technologies to reduce the world's emissions of greenhouse gases. In the International Energy Agency's two-degree scenario (2DS), CCS is expected to help reduce global CO_2 emissions by storing approximately 7 gigatons per year by 2050 [1]. This amount is much greater than that used for enhanced oil and gas recovery purposes (approximately 50 megatons per year in the USA [2]). To optimize the process efficiency, the CO_2 will have to be transported from the capture plants to reservoirs predominantly in high-pressure pipelines [3].

CCS technology comprises three main steps: anthropogenic CO_2 capture, transport and storage. The design of each step is influenced by the thermodynamic procedure used to model the fluid behaviour [3]. Whether using an existing procedure or developing a new one, experimental data on the physicochemical properties of CO_2 mixtures with the impurities typically present in anthropogenic CO_2 are needed in wider composition, temperature and pressure ranges than those associated with CCS technology [4]. However, the paucity of experimental values precludes the development of a reference model for this technology, especially an equation of state (EoS), which is one of the most critical future challenges [5].

To develop an EoS, the essential data are the volumetric properties (pressure–density–temperature, p–ρ–T) and the vapor-liquid equilibrium, VLE, although reliable values for the speed of sound, c, and the isobaric specific heat capacity, c_p are necessary as well. Using acoustic results to formulate EoSs is particularly attractive given that the speed of sound can be measured with outstanding precision over wide temperature and pressure ranges.

* Corresponding author.
E-mail address: curra@unizar.es (M.I. Velasco).

http://dx.doi.org/10.1016/j.jct.2016.03.026
0021-9614/

Furthermore, all the thermodynamic properties of a fluid can be obtained from speed of sound measurements by integrating the partial differential equations that relate c to other thermodynamic properties [6]. Currently, accurately measuring the speed of sound propagation in high-pressure fluids is one of the standard methods to precisely determine such fluids' thermophysical properties [7].

In practice, reliable $p-\rho-T$ values, among others, are necessary to evaluate parameters related to transport, injection and storage [8]. Moreover, the speed of sound enables detection of the pressure drop along the pipeline and leaks, monitoring of changes in composition and the performance of seismic studies [9–11].

To estimate the temperature variations at various stages of the process, precise data from additional thermodynamic properties such as c_p and the Joule–Thomson coefficient, μ_{JT}, are required [9,12]. The solubility parameter, δ, provides information about the interactions between the injected fluid and other substances present in the storage reservoir.

All these properties are affected to a great extent by the nature and quantity of the impurities present in the anthropogenic CO_2, which, in turn, depend on the CO_2 source and the capture and conditioning processes [5]. Although the main impurities are N_2, H_2, O_2, Ar, SO_2, NO_x, CO and water [4,13], methanol can be present in transported and injected anthropogenic CO_2 because of its use as a hydrate inhibitor and as a residue from pipeline drying. Thus, quantification of the effect of this impurity on the thermodynamic properties that influence CCS processes is necessary.

Furthermore, supercritical CO_2, $ScCO_2$, is the most widely used supercritical solvent in a broad range of applications, and methanol is one of the most common modifiers added to enhance the solvating power of $ScCO_2$ to target polar species [14]. The solvent strength of a supercritical fluid solvent is related to its density, and it may be quantitatively represented by the solubility parameter [15]. In addition, c_p and μ_{JT} of the (CO_2 + CH_3OH) system acting as the mobile phase affect to resolution properties in supercritical fluid chromatography [16].

Density and VLE have been widely studied in the literature [17–37] for the (CO_2 + CH_3OH) system, however we note that little information is available on its volumetric behaviour at $T \leqslant 313$ K and at mole fractions of CO_2, x_{CO_2}, greater than 0.75 [19–21,32,34]. Values of δ have been obtained at $T \geqslant 313$ K [14,38–40]; however, no numerical values for c, c_p or μ_{JT} are available in the literature.

The aim of this work was to conduct an extensive thermodynamic study of a CO_2 – rich mixture with CH_3OH ($x_{CO_2} = 0.9700$) under T and p conditions compatible with CCS and other applications. We therefore:

(i) Adapted and used an experimental apparatus to measure accurately the speed of sound in mixtures containing sufficiently dense compressed gases. We also determined the uncertainty of the experimental speed of sound measurements for the (CO_2 + CH_3OH) system.
(ii) Experimentally measured the following properties for the (CO_2 + CH_3OH) mixture with $x_{CO_2} = 0.9700$:
  – The speed of sound, $p-c-T$, between 263.16 K and 313.15 K and at pressures up to 194.49 MPa.
  – The density, $p-\rho-T$, from 263.15 K to 313.15 K and up to 20.00 MPa.
(iii) Adapted and validated a calculation method to obtain ρ and c_p values and derived properties such as the volume-dependent solubility parameter, δ_V, and μ_{JT} for systems containing compressed gases at pressures up to 195.0 MPa. All properties were obtained for (CO_2 + CH_3OH) with $x_{CO_2} = 0.9700$ within the working temperature range. Several authors [41–45] have used the same fundamental approach for liquid compounds; however, this work represents its first application to compressed gases.
(iv) Compared either the experimental results or the calculated values of the aforementioned thermodynamic properties with two different formulation EoS: PC-SAFT [46,47] and GERG [48,49].

In summary, in this article we implement an experimental setup to measure c in mixtures containing compressed gases. We present the experimental results for the speed of sound (at pressures up to 194.49 MPa), and density (up to 20.00 MPa) for the (CO_2 + CH_3OH) mixture ($x_{CO_2} = 0.9700$); together, these results allow us to evaluate the predictive power of the PC-SAFT and GERG EoSs for these properties. From our c values and both our ρ and the GERG EoS c_p at a reference pressure, we calculate ρ, c_p, δ_V, and μ_{JT} for pressures up to 195.0 MPa. This method of calculating thermodynamic properties up to high pressures, which is applied here to compressed gases for the first time, is validated by comparing the results with the values obtained from the PC-SAFT and GERG EoSs.

2. Materials and methods

2.1. Chemicals

Methanol from Sigma–Aldrich (biotech. grade, mole fraction 0.9993) and carbon dioxide from Air Liquide (mole fraction >0.99998) were used without further purification. The details, including purities and sources of the materials used in this work are listed in Table 1.

2.2. Speed of sound data acquisition: experimental setup and procedure

To determine the speed of sound, we used a 5 MHz ultrasonic pulse device previously described for its application to pure fluids [50]. It was originally designed to work with liquids, and we demonstrated that it is also adequate for sufficiently dense compressed gases [50]. The device operates between 253 K and 473 K and from atmospheric pressure to 200 MPa, with standard uncertainties $u(T) = 0.015$ K and $u(p) = 0.02$ MPa, respectively.

The (CO_2 + CH_3OH) mixtures were prepared in a variable-volume cell provided by Top Industrie S.A.S. with a maximum volume of 0.51 L and a maximum working pressure of 30 MPa. The cell was first evacuated, and methanol was the first component added to the evacuated cell. Next, CO_2 was injected using an ISCO model-260D syringe pump for a chromatography instrument; this pump operates at pressures up to 50 MPa. After the mixture was prepared, it was transferred to a syringe pump by pushing the embolus of the cell with an inert gas. It was then transferred from the syringe pump to the experimental setup in several steps. This method allowed us to accumulate enough fluid mass to reach pressures as high as 195.0 MPa using the manual pump in the installation. The mixture was homogenized by stirring inside the

Table 1
The sources and mole fraction purity of the materials used in this paper.

Chemical name	Source	Mole fraction purity	Purification method
Methanol	Sigma Aldrich	0.9993[a]	None
Carbon dioxide	Air Liquide	>0.99998[a]	None

[a] The mole fraction was given by the supplier.

variable-volume cell, the syringe pump and the manual pump; it was homogenized using a recirculation pump inside the setup.

The masses of the different components were determined by successive weighing in a mass comparator from Sartorius, model CCE 2004, with a repeatability better than 0.0002 g. The mole fraction of the component that was first introduced, x_1, was determined by the relation

$$x_1 = \left[\frac{(m_2 - m_1)}{M_1}\right] \Big/ \left[\frac{(m_3 - m_2)}{M_2} + \frac{(m_2 - m_1)}{M_1}\right] \tag{1}$$

where m_1 is the empty cell mass, m_2 and m_3 are the masses after the first and second components were added, respectively, and M_1 and M_2 are the molar masses of the first and second components, respectively. The standard uncertainty in the mole fraction was calculated to be $u(x) = 2 \times 10^{-6}$ using the following:

$$u^2(x) = [(\partial x/\partial m_1)u(m)]^2 + [(\partial x/\partial m_2)u(m)]^2 + [(\partial x/\partial m_3)u(m)]^2 \tag{2}$$

where $u(m) = 2 \times 10^{-4}$ g is the uncertainty of the balance.

2.3. Volumetric data acquisition: experimental setup and procedure

The apparatus and the experimental procedure used to measure densities were previously described [8]. In this setup, T ranges from (263 to 473) K ± 0.006 K and p ranges between atmospheric pressure and 70 MPa with 0.025% FS precision. The main component is an Anton Paar DMA HPM vibrating-tube densimeter connected to an MPDS V3 evaluation unit.

3. Calculation method of thermodynamic properties up to high pressures

Various methods have been proposed in the literature to obtain other thermodynamic properties from the speed of sound [51], thus exploiting the high precision of its experimental determination. These methods use experimental values of c obtained at high pressures and several temperatures and ρ and c_p both at a reference pressure $p^{\neq}$ and as a function of temperature. From these data, calculated values of ρ, the isobaric thermal expansivity, α_p, the isothermal compressibility, κ_T, and c_p are obtained as functions of pressure and temperature. In liquid systems $p^{\neq}$ is equal to atmospheric pressure [7,41–45,52,53]. The method we used is based on these studies, except that $p^{\neq}$ must be above atmospheric pressure to ensure that the fluid is in a dense phase along all working pressure and temperature ranges; thus, $p^{\neq}$ depends on the studied system. Moreover, at the chosen $p^{\neq}$ value, the experimental density $\rho^{\neq}$ obtained at $p^{\neq}$ must correlate well with T. In this method, the input thermodynamic properties are correlated using the following equations:

$$(p - p^{\neq})/\text{MPa} = \sum_{i=1}^{3}\sum_{j=0}^{2} a_{ij}\{(c - c^{\neq})/(\text{m s}^{-1})\}^i (T/K)^{-j} \tag{3}$$

$$c^{\neq}/(\text{m s}^{-1}) = \sum_{j=0}^{2} b_j (T/K)^j \tag{4}$$

$$c_p^{\neq}/(\text{J kg}^{-1}\ \text{K}^{-1}) = \sum_{j=0}^{3} c_j (T/K)^j \tag{5}$$

$$\rho^{\neq}/(\text{kg m}^{-3}) = \sum_{j=0}^{3} d_j (T/K)^j \tag{6}$$

The calculated thermodynamic properties of the system are obtained for a given composition up to high pressures by numerical integration of the following system of partial differential equations:

$$\left.\begin{aligned} c^{-2} &= (\partial\rho/\partial p)_T - (T/\rho^2 c_p)(\partial\rho/\partial T)_p^2 \\ (\partial c_p/\partial p)_T &= -(T/\rho^3)\left[2(\partial\rho/\partial T)_p^2 - \rho(\partial^2\rho/\partial T^2)_p\right] \end{aligned}\right\} \tag{7}$$

The solution to the system (7) is obtained using the initial conditions $\rho^{\neq}(T)$ and $c_p^{\neq}(T)$ and a simple predictor–corrector algorithm [43] with step lengths $\Delta p = 0.1$ MPa and $\Delta T = 5$ K. The values of $\rho^{\neq}(T)$ were determined experimentally, whereas $c_p^{\neq}(T)$ values were calculated with the GERG EoS [48,49] using REFPROP 9.0 [54]. The values of δ_V [55–57] and μ_{JT} were calculated up to high pressures using the preceding and the following equations:

$$\delta_V^2 = \left(\frac{\partial U}{\partial V}\right)_T = T\left(\frac{\partial p}{\partial T}\right)_V - p = T\frac{\alpha_p}{\kappa_T} - p \tag{8}$$

$$\mu_{JT} = \left(\frac{\partial T}{\partial p}\right)_H = -\frac{1}{c_p}\left[T\frac{(\partial p/\partial T)_V}{(\partial p/\partial V)_T} + V\right] = \frac{(T\alpha_p - 1)}{\rho c_p} \tag{9}$$

4. Equations of state

In this work, we compared both our experimental values (c, ρ), and the calculated values explained previously (ρ, c_p, δ_V, μ_{JT}) with data obtained from the PC-SAFT and the GERG EoS using VLXE [58] and REFPROP 9.0 [54] software, respectively.

4.1. PC-SAFT EoS

The PC-SAFT EoS [46,47] describes the Helmholtz dimensionless energy, $\tilde{a}$, as the sum of several contributions: ideal gas (*id*), hard chain (*hc*), dispersive attraction (*dis*), association (*assoc*) and multipolar interactions (*QQ*: quadrupole–quadrupole, *DD*: dipole–dipole, *QD*: quadrupole–dipole).

$$\tilde{a} = \tilde{a}^{id} + \tilde{a}^{hc} + \tilde{a}^{dis} + \tilde{a}^{assoc} + (\tilde{a}^{QQ} + \tilde{a}^{DD} + \tilde{a}^{QD}) \tag{10}$$

In this model, three geometrical parameters are needed to describe the non-associated and non-polar pure components: the segment number, m; the segment diameter, σ; and the segment energy parameter, ε. Generally, these parameters are calculated from VLE and density data; however, in such cases the critical region is not correctly represented. An alternative is to recalculate the parameters from the pure compounds' critical temperatures and pressures [17].

The mixing parameters σ_{ij} and ε_{ij} are obtained from the Berthelot–Lorentz rules, which include an adjustable binary interaction parameter, k_{ij}:

$$\sigma_{ij} = \frac{1}{2}(\sigma_i + \sigma_j) \tag{11}$$

$$\varepsilon_{ij} = \sqrt{\varepsilon_i \varepsilon_j}(1 - k_{ij}) \tag{12}$$

where the subscripts i and j refer to each of the compounds present in the mixture.

When pure compounds exhibit association, two additional parameters are required: the association volume, $\kappa^{A_iB_i}$, and the association energy, $\varepsilon^{A_iB_i}$. These parameters can be obtained from experimental hydrogen-bonding enthalpies and entropies of the pure compounds or from molecular simulations. Moreover, an association scheme must be defined.

For mixtures of such compounds, the cross-association parameters, $\kappa^{A_iB_j}$ and $\varepsilon^{A_iB_j}$, can be calculated using the following combination rules:

$$\kappa^{A_iB_j} = \sqrt{\kappa^{A_iB_i} \cdot \kappa^{A_jB_j}} \tag{13}$$

$$\varepsilon^{A_iB_j} = \frac{1}{2}\left(\varepsilon^{A_iB_i} + \varepsilon^{A_jB_j}\right) \tag{14}$$

The interactions present in the mixtures between a self-associated compound and another non-self-associated compound, which has either proton donor sites or proton acceptor sites (*e.g.*, CO_2), were named *induced association* by Kleiner and Sadowski [59]. In this case, they suggested a simple approach: the association energy parameter, $\varepsilon^{A_iB_i}$, of the non-self-associating compound is zero, and the association volume parameter, $\kappa^{A_iB_i}$, of this component is assumed to be equal to the value of the associating component in the mixture:

$$\kappa^{A_iB_j} = \kappa^{assoc.comp}; \quad \varepsilon^{A_iB_j} = \frac{\varepsilon^{assoc.comp}}{2} \tag{15}$$

A detailed explanation of this model applied to the (CO_2 + CH_3OH) system is given in a previous work [17], where we studied the VLE and the critical region of this system. For this study, the geometrical parameters of the pure compounds were recalculated from their critical points, and a temperature-dependent binary interaction parameter, $k_{ij}(T)$, was introduced. For methanol, we used a 2B association scheme (*i.e.*, two association sites: a one-electron donor and a one-electron acceptor). Because of the presence of specific interactions between the carbon atom of CO_2 and the oxygen atom of alcohol and CO_2–alcohol hydrogen bonding, we treated this system as *induced association*. We then used $\varepsilon^{A_iB_i} = 0$ and $\kappa^{A_iB_i} = \kappa^{methanol}$ and a 2C association scheme (*i.e.*, two negative sites that are active only when mixed with a molecule with at least one positive or neutral site) for CO_2. Multipole interactions were not considered. This procedure is also that used in the present study.

Neither the PC-SAFT EoS nor cubic EoSs adequately predict density at moderate and high pressures. To enhance the precision in the density calculation, some authors have recalculated the geometrical parameters by introducing the density in the objective function and even varying it with pressure [60,61]. Similar to our earlier work [8], we chose to add the volume translation, Δv_c, for each pure component. We used a constant Δv_c value for all T to avoid unphysical results [62]. Because Δv_c depends on the value of the molar volume of the component, v, we here used a Δv_c value for CO_2 that differs from that used in previous works [8] because we extended the pressure range to 195.0 MPa.

In summary, in applying the PC-SAFT EoS to the (CO_2 + CH_3OH) system, we used the same procedure as in our previous work [17] except that we added Δv_c to accurately predict the density. Thus, we used a minimum number of parameters (Table S1) to model the investigated thermodynamic properties (vapor-liquid equilibrium, critical locus, speed of sound and density).

4.2. The GERG EoS

The GERG EoS [48,49] is based on a multi-fluid approximation where the dimensionless Helmholtz energy, $\tilde{a}$, is expressed as the sum of two contributions: an ideal-gas mixture (id) and a residual component (res):

$$\tilde{a} = \tilde{a}^{id} + \tilde{a}^{res} = \sum_{i=1}^{N} x_i[\tilde{a}^{id} + \ln x_i] + \sum_{i=1}^{N} x_i \tilde{a}^{res} + \Delta\tilde{a}^{res} \tag{16}$$

where the subscript i indicates the pure compound and $\Delta\tilde{a}^{res}$ is the departure function. Initially, this EoS was developed as a reference EoS for natural gas mixtures, and it generally provides better results than other EoSs for systems whose components are implemented in the equation.

Although methanol is not one of the 21 compounds included in the Kunz and Wagner article [49], it has been implemented in the REFPROP 9.0 software; thus, we were able to use the equation to calculate the thermodynamic properties of the system under investigation in the present work. The calculations are based in the reference EoS for CO_2 [63] and methanol [64] together with the GERG EoS mixture model. The predicted values are slightly more accurate than those from GERG EoS as published because the pure-component EoSs are more elaborate.

5. Results

5.1. Experimental results obtained using the newly implemented apparatus to measure the speed of sound in mixtures

The system (CO_2 + CH_3OH) was studied to develop the experimental procedure for mixtures containing sufficiently dense compressed gases and to determine the uncertainty of the speed of sound measurements in those gases. The chosen compositions were $x_{CO_2} = (0.7534,\ 0.8502,\ 0.9250$ and $0.9803)$ at nominal temperatures of 263.15 K, 298.15 K and 323.15 K and pressures from 6.00 MPa to 190.04 MPa. The p—c—T values used in this section are listed in Table S2.

The overall standard uncertainty of the experimental c measurements, $u(c)$, was calculated from the following equation [65]:

$$u^2(c) = \left[(\partial c/\partial T)_{p,x} u(T)\right]^2 + \left[(\partial c/\partial p)_{T,x} u(p)\right]^2 + \left[(\partial c/\partial x)_{T,p} u(x)\right]^2 + (u^*(c))^2 \tag{17}$$

where $u(T)$, $u(p)$, and $u(x)$ are given in Section 2.2, and $(\partial c/\partial T)_{p,x}$ and $(\partial c/\partial p)_{T,x}$ were obtained from Eqs. (3) and (4). Correlated c—x data for the four mixtures allowed us to evaluate $(\partial c/\partial x)_{T,p}$.

To determine the standard repeatability uncertainty, $u^*(c)$, two mixtures with $x_{CO_2} = 0.9250$ were prepared. For each one, two isotherms were determined at each of the three temperatures (Table S2). The deviations between the c values of each isotherm for both mixtures are represented in Fig. 1. The value determined for $u^*(c)$ was $5.3 \times 10^{-4} \cdot c$, and the overall standard uncertainty of c was $u(c) = 5.9 \times 10^{-4} \cdot c$. The last value lies within the range of standard uncertainties ($3 \times 10^{-4} \cdot c$ to $10 \times 10^{-4} \cdot c$) obtained by other authors using similar apparatus for liquid mixtures and binary mixtures of compressed gases [43,65,66].

5.2. Experimental results for the mixture ($CO_2 + CH_3OH$) ($x_{CO_2} = 0.9700$)

5.2.1. Speed of sound

Experimental values p—c—T were measured along six isotherms at nominal temperatures = (263.15, 273.15, 283.15, 293.15, 304.21 and 313.15) K and at pressures from 3.28 MPa to 194.49 MPa (Fig. 2, Table S3). The standard uncertainty was $u(c) = 5.9 \times 10^{-4} \cdot c$, as previously indicated. The speed of sound increases as pressure increases and as temperature decreases. No values were found in the literature for this system.

5.2.2. Density

The density was measured at the same nominal temperatures as the speed of sound and the pressure ranged from 4.00 MPa to 20.00 MPa. The experimentally determined density values of the six isotherms correspond to dense phase of the mixture. The isotherms at temperatures from 263.15 K to 304.21 K are subcritical and that at 313.15 K is supercritical. The standard uncertainty in the experimental determination of the density was $u(\rho) = 0.4\ kg\ m^{-3}$, which was obtained following the procedure described in the Supplementary material (S.M.) (pp S11). Similar to the speed of sound, values of ρ in the liquid phase of this mixture also increase with increasing pressure and with decreasing temperature (Fig. 3, Table S4).

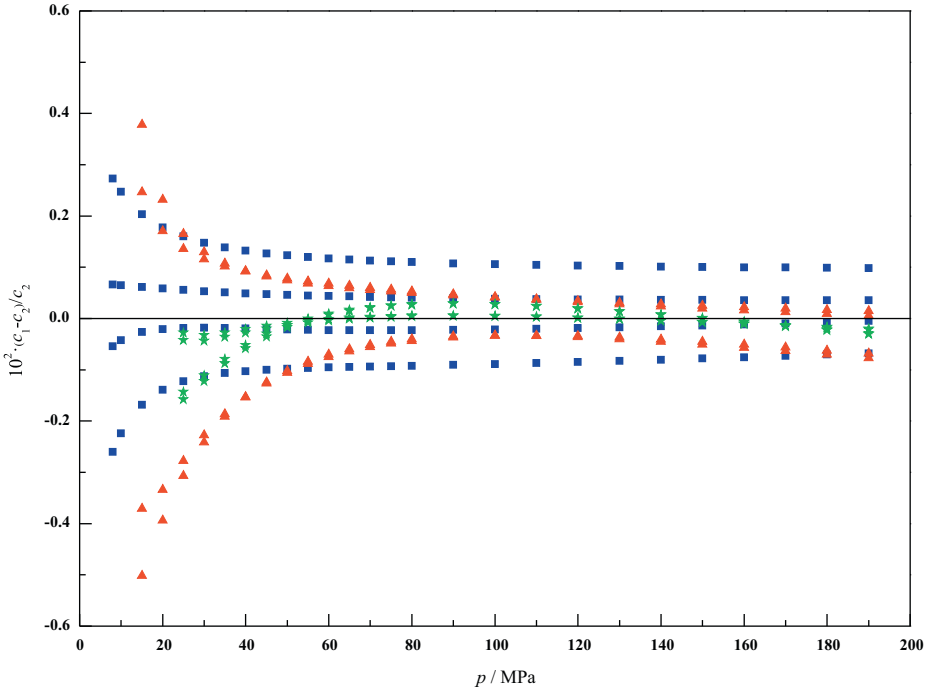

Fig. 1. Deviations between the c values in two mixtures (1, 2) $CO_2 + CH_3OH$ with $x_{CO_2} = 0.9250$, at three temperatures, T, and versus pressure, p. Each mixture was measured twice at each temperature. ■, T = 263.15 K; ▲, T = 298.15 K; and ★, T = 323.15 K.

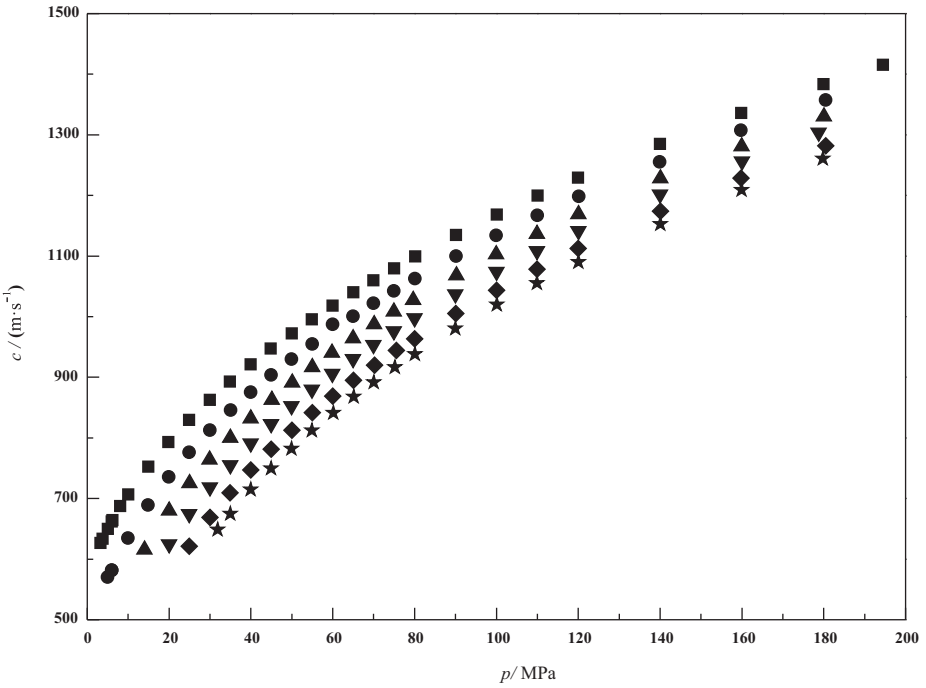

Fig. 2. Experimental speeds of sound, c, versus pressure, p, for $CO_2 + CH_3OH$ with $x_{CO_2} = 0.9700$ at several temperatures: ■, T = 263.15 K; ●, T = 273.15 K; ▲, T = 283.15 K; ▼, T = 293.15 K; ◆, T = 304.21 K; ★, T = 313.15 K.

Despite the abundance of density data in the literature, we could quantitatively compare our values only with those of Berger and Deye ($x_{CO_2} = 0.9777$ at 313.15 K) [20] and Cao et al. ($x_{CO_2} = 0.9657$–0.9760 at 313.15 K) [32], where the deviations $MRD_\rho = 1.30\%$ and 5.52%, respectively. Our results are consistent with the remainder of the literature data at $T \leqslant 313$ K and at $x_{CO_2} > 0.75$ [19–21,32,34].

5.3. Results from the thermodynamic property calculation method for the mixture ($CO_2 + CH_3OH$) ($x_{CO_2} = 0.9700$) at high pressures

From our experimental p–c–T and $\rho^{\neq}$–T and our calculated $c_p^{\neq}$–T values (GERG EoS), we obtained ρ, c_p, δ_V and μ_{JT} for temperatures from 263.15 K to 313.15 K and for pressures up to 195.0 MPa using the aforementioned calculation method

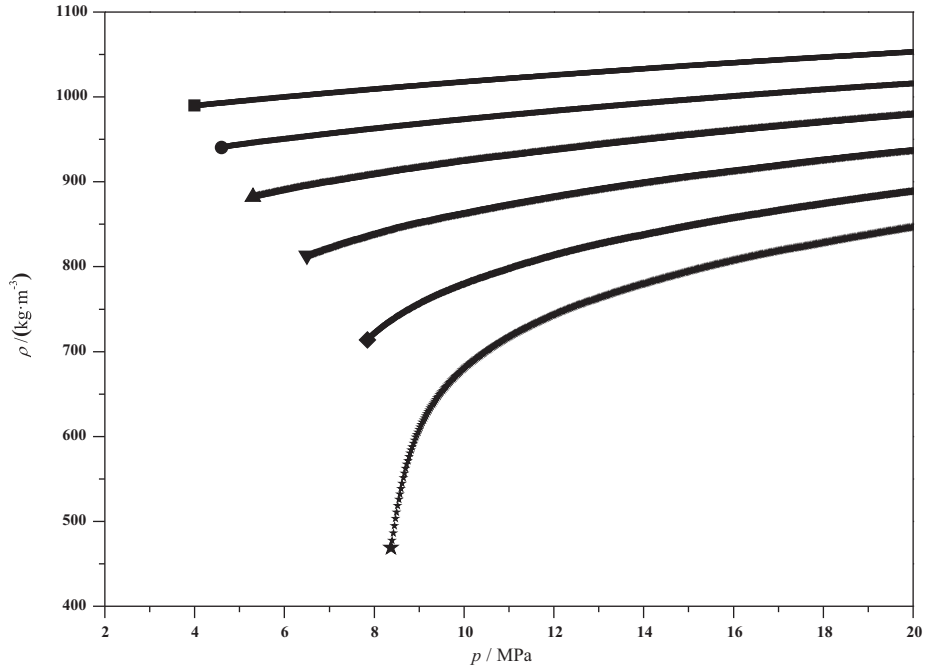

Fig. 3. Experimental densities, ρ, versus pressure, p, for $CO_2 + CH_3OH$ with $x_{CO_2} = 0.9700$ at several temperatures: ■, $T = 263.15$ K; ●, $T = 273.15$ K; ▲, $T = 283.15$ K; ▼, $T = 293.15$ K; ◆, $T = 304.21$ K; ★, $T = 313.15$ K.

(Table S5 and Fig. 4a–d). Eqs. (3)–(6) of this method were applied with $p^{\neq} = 14.0$ MPa and with the values of the parameters a_{ij}, b_j, c_j and d_j given in Table 2.

5.3.1. Density

Because we have experimental values for ρ for pressures up to 20.00 MPa and calculated values starting from 14.0 MPa, we compared the values in the overlapping range from 14.0 MPa to 20.0 MPa. The experimental and calculated values agreed well with an $MRD_\rho = 0.075\%$. We compared our calculated density values with the experimental values of Berger and Deye [20]; the deviation is $MRD_\rho = 0.35\%$. Our results are consistent with the experimental results of Maiwald et al. [34].

5.3.2. Isobaric specific heat capacity

The calculated values of this property vary between 2734.6 J K^{-1} kg^{-1} (14.0 MPa, 313.15 K) and 1551.6 J K^{-1} kg^{-1} (195.0 MPa, 313.15 K). The variation of c_p with pressure diminishes gradually as temperature decreases, showing a crossing region at approximately 1865 J K^{-1} kg^{-1} and 35 MPa. No c_p values for the mixture studied were found in the literature.

5.3.3. Volume-dependent solubility parameter

The calculated values for the δ_V increase as pressure increases and temperature decreases. We found values of the solubility parameter, δ, in the literature for $T \geqslant 313.15$ K [14,38–40], which cannot be compared with our δ_V values because of the different effects included and the temperature or composition.

5.3.4. Joule–Thomson coefficient

The evolution of μ_{JT} values with pressure and temperature is similar to that of c_p. The greatest variation with pressure is shown for the supercritical isotherm (0.82597 K MPa^{-1} at 14.0 MPa and −0.33179 K MPa^{-1} at 195.0 MPa) and the lowest variation corresponds to 263.15 K, which causes a crossing of all isotherms in the vicinity of −0.25 K MPa^{-1} and 100 MPa. The Joule–Thomson coefficient changes its sign for the five upper isotherms in the pressure range studied. No μ_{JT} values were found in the literature.

6. Discussion

The repeatability and overall standard uncertainty results obtained in this work, together with the agreement with the data from the literature, allow us to use our experimental c and ρ values to evaluate whether the PC-SAFT and GERG EoSs properly predict the studied thermodynamic behaviour for ($CO_2 + CH_3OH$). If the two EoSs are successful, we will use both to validate the method for calculating ρ, δ_v, c_P and μ_{JT} up to 195.0 MPa.

6.1. Experimental results for ($CO_2 + CH_3OH$) ($x_{CO_2} = 0.9700$)

6.1.1. Speed of sound ($p \leqslant 194.49$ MPa; 263.16 K $\leqslant T \leqslant 313.15$ K)

We observed that the PC-SAFT EoS tends to underestimate the speed of sound when we compared the experimental and EoS results (Fig. S1); we also observed that the divergence increases with decreasing temperature. The calculated value of the average PC-SAFT EoS deviation for all isotherms is $\overline{MRD}_c = 2.77\%$ (Table S6). The GERG EoS values of c are always greater than the experimental values, with the largest deviations at low pressures (Fig. S1). The average value of the GERG EoS deviations for all isotherms is slightly lower than that from the PC-SAFT EoS, $\overline{MRD}_c = 2.65\%$ (Table S6).

To calculate the overall standard uncertainty in the speed of sound, $u(c)$, experimental values of c for four mixtures of ($CO_2 + CH_3OH$) ($0.7534 \leqslant x_{CO_2} \leqslant 0.9803$) were determined. All of them were modelled to investigate possible trends with respect to composition. The PC-SAFT EoS deviations are similar for all mixtures. However, the GERG EoS provides better results than the PC-SAFT EoS for the two CO_2 – richest mixtures and significantly higher deviations with increasing values of x_{CH_3OH}. Thus, the GERG EoS

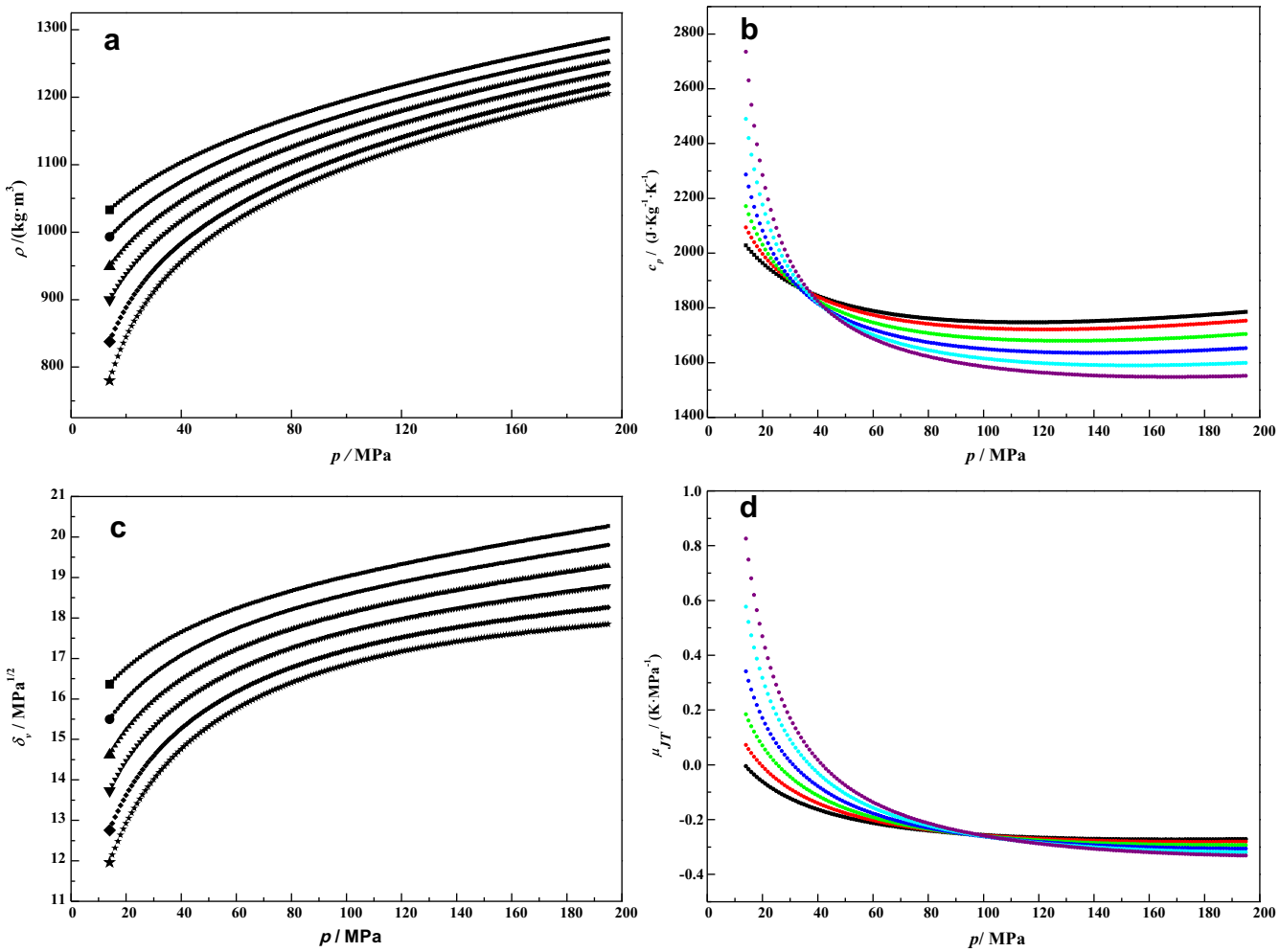

Fig. 4. (a) Calculated densities, ρ; (b) calculated isobaric specific heat capacities, c_p; (c) calculated volume-dependent solubility parameters, δ_V; (d) calculated Joule–Thomson coefficients, μ_{JT}, versus pressure, p, for the mixture $CO_2 + CH_3OH$ with $x_{CO_2} = 0.9700$ at several temperatures; (a and c) ■, $T = 263.15$ K; ●, $T = 273.15$ K; ▲, $T = 283.15$ K; ▼, $T = 293.15$ K; ◆, $T = 304.21$ K; ★, $T = 313.15$ K; (b and d) ●, $T = 263.15$ K; ●, $T = 273.15$ K; ●, $T = 283.15$ K; ●, $T = 293.15$ K; ●, $T = 304.21$ K; ●, $T = 313.15$ K.

$\overline{MRD}_c$ is 1.88% for $x_{CO_2} = 0.9803$ and 14.1% for $x_{CO_2} = 0.7534$ (Table S7).

6.1.2. Density ($p \leqslant 20.00$ MPa; 263.15 K $\leqslant T \leqslant$ 313.15 K)

Deviations in density values increase with increasing temperature and decreasing pressure for both EoSs (Fig. S2). The PC-SAFT EoS predicts that the density values will be lower than the experimental values for subcritical isotherms. For this EoS, the largest deviations are observed at $T = 313.15$ K, near the critical point of the mixture ($T_c \cong 310$ K [17]) (Fig. S2). The mean value of all PC-SAFT EoS deviations is $\overline{MRD}_\rho = 3.96\%$ (Table S6). The GERG EoS overestimates ρ with a significantly lower $\overline{MRD}_\rho = 0.58\%$, although its deviation is more than double that of the PC-SAFT EoS at the supercritical temperature, $(MRD_\rho)_{max} = 23\%$. Density values from the literature [18–37] show similar or higher deviations with PC-SAFT EoS predictions than our experimental values and greater differences with GERG EoSs than our values (Table S8).

On the basis of the deviations between the experimental values and those calculated by each EoS for the two properties, we conclude that both equations are valid to represent the behaviour of this system under most of the studied conditions. However, we observed exceptions, such as the evaluation of the density near the critical point of the mixture, where the deviations were significant for both EoSs, and the GERG EoS's prediction for the speed of sound within mixtures with $x_{CO_2} < 0.97$.

The experimental results are a useful contribution to the body of scientific knowledge because no c values have been reported and because volumetric information at $T \leqslant 313$ K and $x_{CO_2} > 0.75$ is scarce. Accurate values for these properties are needed to evaluate several parameters related to transport, injection and storage in CCS technology and also for other applications. In addition, these values will allow the research community to develop and improve EoSs in the future.

6.2. Calculated results for (CO_2 + CH_3OH) ($x_{CO_2} = 0.9700$) up to 195.0 MPa

Given the satisfactory results obtained in the previous section, we will use both EoSs to discuss our results calculated from the experimental values at pressures up to 195.0 MPa. The calculated ρ, c_P, δ_V and μ_{JT} values are compared to those obtained from the PC-SAFT and GERG EoSs (Figs. S3–S6) at temperatures from 263.15 K to 313.15 K and at pressures from 14.0 MPa to 195.0 MPa. The deviations thus obtained are expressed as $MRD_x(\%)$ or *AAD* in Table S9.

6.2.1. Density

Fig. S3 shows the deviations between the calculated ρ values and those from both EoSs. Our obtained values are greater than the values obtained using the PC-SAFT EoS at pressures below

Table 2
Parameters in Eq. (3)–(6) for the correlation for the speed of sound, isobaric heat capacity, and density of $CO_2 + CH_3OH$ with $x_{CO_2} = 0.9700$ and *MRD* (%) values.

Parameters	Eq. (3)
a_{10}	$1.803588 \cdot 10^{0}$
a_{11}	$-1.057660 \cdot 10^{3}$
a_{12}	$1.613456 \cdot 10^{5}$
a_{20}	$-2.893926 \cdot 10^{-3}$
a_{21}	$1.590804 \cdot 10^{0}$
a_{22}	$-2.057073 \cdot 10^{2}$
a_{30}	$2.153084 \cdot 10^{-6}$
a_{31}	$-1.154812 \cdot 10^{-3}$
a_{32}	$1.601533 \cdot 10^{-1}$
MRD (%)	0.08
Parameters	**Eq. (4)**
b_0	$4.551011383 \cdot 10^{3}$
b_1	$-2.1725446 \cdot 10^{1}$
b_2	$2.7618 \cdot 10^{-3}$
MRD (%)	0.27
Parameters	**Eq. (5)**
c_0	$-8.2772910000 \cdot 10^{4}$
c_1	$9.35309155 \cdot 10^{2}$
c_2	$-3.460573 \cdot 10^{0}$
c_3	$4.297499 \cdot 10^{-3}$
MRD (%)	0.11
Parameters	**Eq. (6)**
d_0	$5.897805216 \cdot 10^{3}$
d_1	$-5.0584614 \cdot 10^{1}$
d_2	$0.188454 \cdot 10^{0}$
d_3	$-2.526272E \cdot 10^{-4}$
MRD (%)	0.02

$MRD\ (\%) = \frac{10^2}{N}\sum_{i=1}^{N}\left|\frac{x_i - x_{fit}}{x_i}\right|$
x_i: experimental datum; x_{fit}: value obtained for that property at the same state point from the corresponding correlating equation; N: number of points.

(40–60) MPa, whereas they are lower at higher pressures; the average deviations obtained for each isotherm are nearly equal, and $\overline{MRD}_{\rho} = 1.90\%$. In relation to the GERG EoS, we obtain deviations no higher than 1%, with an average value $\overline{MRD}_{\rho} = 0.46\%$, where our calculated values are usually higher than the predicted values.

6.2.2. Isobaric specific heat capacity

A comparison of the calculated values with those from the two EoSs (Fig. S4) shows that calculated values are higher than the values predicted by the PC-SAFT EoS. The deviations are significant and generally increase with increasing pressure, with an average value of $\overline{MRD}_{c_p} = 10.3\%$. Deviations of the values calculated using the GERG EoS are much lower than those calculated using the PC-SAFT EoS, with an average value of $\overline{MRD}_{c_p} = 2.47\%$. The calculated crossing region for this property ($c_p \cong 1865\ J\ K^{-1}\ kg^{-1}$ and $p \cong 35$ MPa) agrees better with predictions from the GERG EoS ($c_p \cong 1780\ J\ K^{-1}\ kg^{-1}$ and $p \cong 55$ MPa) than with predictions from the PC-SAFT EoS ($c_p \cong 1460\ J\ K^{-1}\ kg^{-1}$ and $p \cong 155$ MPa).

6.2.3. Volume-dependent solubility parameter

In Fig. 5, δ_V values are represented as a function of ρ for pure CO_2 [50], for the $(CO_2 + CH_3OH)$ mixture studied in this work and for six $(CO_2 + CO)$, $(CO_2 + CH_4)$, $(CO_2 + H_2)$, $(CO_2 + CO + H_2)$, mixtures from the literature [8]. The graph shows a good $\delta_V - \rho$ correlation at densities less than $\cong 1050\ kg\ m^{-3}$, as shown in a previous study [8]. This result indicates that within this density range, different systems at various T or p conditions, but with the same density, will have the same δ_V. For $\rho > 1050\ kg\ m^{-3}$, deviations between the δ_V values for the $(CO_2 + CH_3OH)$ mixture and those for pure CO_2 depend on T; however, these deviations are not greater than those observed for other systems in other regions of the graph.

Our δ_V values are lower than the values obtained from the PC-SAFT EoS within the full range of pressures, with larger deviations at both higher pressures and higher temperatures, with an $\overline{MRD}_{\delta_V} = 3.28\%$. The GERG deviations are smaller than those obtained from the PC-SAFT EoS, and their average value is $\overline{MRD}_{\delta_V} = 1.60\%$. Comparisons with both EoSs are shown in Fig. S5.

6.2.4. Joule–Thomson coefficient

Because the numerical values of this property were so small, deviations were expressed as *AADs*. The PC-SAFT EoS deviations are much larger than those from the GERG EoS, as shown in Fig. S6, which is reflected in the average values of $\overline{AAD}_{\mu_{JT}} = 0.056\ K\ MPa^{-1}$ from the PC-SAFT EoS and $\overline{AAD}_{\mu_{JT}} = 0.013\ K\ MPa^{-1}$ from the GERG EoS. The crossing region obtained from the calculation method ($\mu_{JT} \cong -0.25\ K\ MPa^{-1}$ and $p \cong 100$ MPa) differs more from that predicted by the PC-SAFT EoS ($\mu_{JT} \cong -0.43\ K\ MPa^{-1}$ and $p \cong 220$ MPa) than that from the GERG EoS ($\mu_{JT} \cong -0.32\ K\ MPa^{-1}$ and $p \cong 180$ MPa).

We consider the results obtained adequate in the comparison between the calculated values of the four properties ρ, c_P, δ_V and μ_{JT} and the data provided by both EoSs, except for c_P and μ_{JT} in relation to the PC-SAFT EoS.

7. Conclusions

An ultrasonic pulse apparatus and the experimental procedure were adapted to measure the speed of sound in mixtures containing compressed gases, and c was measured for four $(CO_2 + CH_3OH)$ mixtures ($x_{CO_2} = 0.7534$, 0.8502, 0.9250 and 0.9803) at nominal temperatures $T = (263.15,\ 298.15,$ and $323.15)$ K and at pressures up to 190.04 MPa. The overall standard uncertainty of the experimental speed of sound was evaluated for the $(CO_2 + CH_3OH)$ system, where the contributions of temperature, pressure, composition and repeatability were taken into account. The value obtained, $u_c = 5.9 \times 10^{-4} \cdot c$, is within values reported in the literature.

The speed of sound was experimentally determined for the $(CO_2 + CH_3OH)$ mixture with $x_{CO_2} = 0.9700$ at nominal $T = (263.15,\ 273.15,\ 283.15,\ 293.15,\ 304.21$ and $313.15)$ K and at pressures from 3.28 MPa to 194.49 MPa. The density of the mixture in the dense phase was measured at the same nominal temperatures, including five subcritical and one supercritical, and at pressures up to 20.00 MPa.

This system was modelled with two different formulation EoSs: PC-SAFT and GERG. From the obtained deviations, we conclude that both equations are valid to represent the studied experimental thermodynamic properties of the system except for in the critical region and, in the case of the GERG EoS, the speed of sound in the mixtures poorest in CO_2.

Values of ρ, c_p, δ_V and μ_{JT} were calculated for the T range from 263.15 K to 313.15 K and from 14.0 MPa to 195.0 MPa for the $(CO_2 + CH_3OH)$ mixture with $x_{CO_2} = 0.9700$. For this calculation, we used a method based on numerical integration and previously used for liquid systems by adapting it for compressed gases. The values thus obtained were compared with those obtained from the PC-SAFT and GERG EoSs. The results of this comparison, together with the agreement between our experimental and calculated densities in the overlapping pressure range, validate the calculation method.

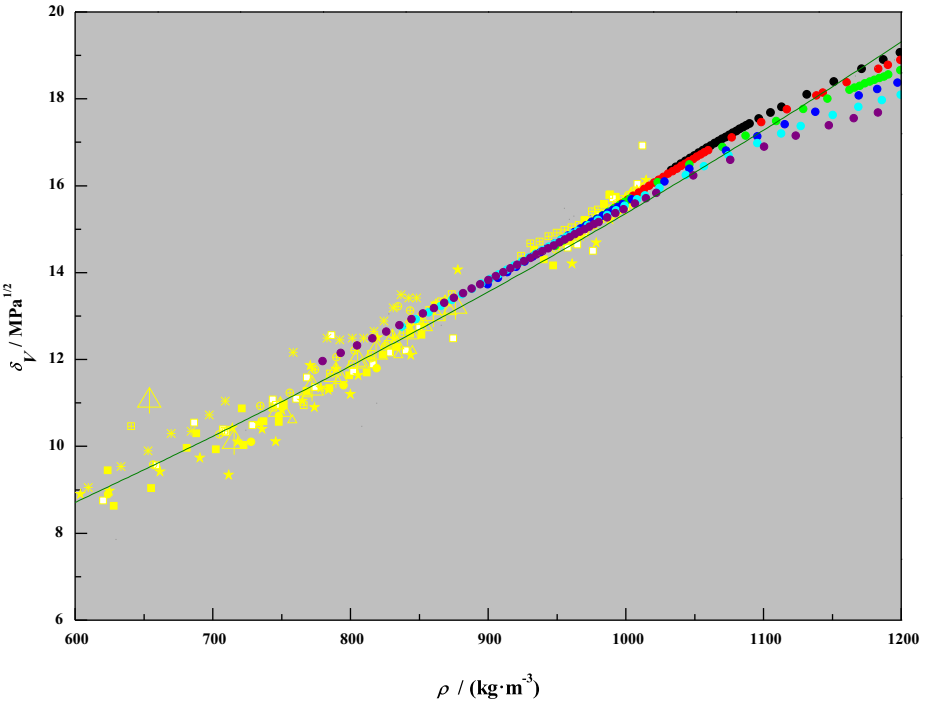

Fig. 5. Volume-dependent solubility parameter, δ_V, versus density, ρ, for pure CO_2 [50] (line); $CO_2 + CH_3OH$ with $x_{CO_2} = 0.9700$ at several temperatures: ●, T = 263.15 K; ●, T = 273.15 K; ●, T = 283.15 K; ●, T = 293.15 K; ●, T = 304.21 K; ●, T = 313.15 K; $CO_2 + CO$, $CO_2 + CH_4$, $CO_2 + H_2$ and $CO_2 + CO + H_2$ mixtures (yellow) [8]. (For interpretation of the references to colour in this figure legend, the reader is referred to the web version of this article.)

Therefore, we have achieved the aim of this work, which was to comprehensively study the thermodynamics of a CO_2 – rich mixture of (CO_2 + CH_3OH) at T and p conditions of interest for CCS technology and other applications. The results reported in this paper are a useful contribution to mitigate the lack of information in the literature on the thermodynamic behaviour of such mixtures. Acoustic, volumetric, c_p and μ_{JT} data are important for the calculation of several parameters related to transport, injection and storage in CCS and for supercritical processes. In addition, these data will allow the future improvement, development and validation of new theoretical models for this technology. Neither of the two studied EoSs satisfactorily represents all the properties studied in this work, although the GERG EoS correctly predicts the system behaviour at high pressures.

Acknowledgements

This research received funding from the Ministry of Economy and Competitiveness of Spain ENE2013-44336-R and from the Government of Aragon and the European Social Fund.

Appendix A. Supplementary data

Supplementary data associated with this article can be found, in the online version, at http://dx.doi.org/10.1016/j.jct.2016.03.026.

References

[1] IEA, Energy Technology Perspectives 2012. Pathways to a Clean Energy System, 2012.
[2] US DOE, Interagency Task Force on Carbon Capture and Storage Washington, DC, USA, 2010.
[3] P. Aursand, M. Hammer, S.T. Munkejord, Ø. Wilhelmsen, Pipeline transport of CO_2 mixtures: models for transient simulation, Int. J. Greenhouse Gas Control 15 (2013) 174–185, http://dx.doi.org/10.1016/j.ijggc.2013.02.012.
[4] S.W. Løvseth, G. Skaugen, H.G. Jacob Stang, J.P. Jakobsen, Ø. Wilhelmsen, R. Span, R. Wegge, CO_2 mix project: experimental determination of thermo physical properties of CO_2 – rich mixtures, Energy Proc. 37 (2013) 2888–2896, http://dx.doi.org/10.1016/j.egypro.2013.06.174.
[5] H. Li, J.P. Jakobsen, O. Wilhelmsen, J. Yan, PVTxy properties of CO_2 mixtures relevant for CO_2 capture, transport and storage: review of available experimental data and theoretical models, Appl. Energy 88 (2011) 3567–3579, http://dx.doi.org/10.1016/j.apenergy.2011.03.052.
[6] A.F. Estrada-Alexanders, J.P.M. Trusler, M.P. Zarari, Determination of thermodynamic properties from the speed of sound, Int. J. Thermophys. 16 (1995) 663–673, http://dx.doi.org/10.1007/BF01438851.
[7] M. Chorazewski, E.B. Postnikov, Thermal properties of compressed liquids: experimental determination via an indirect acoustic technique and modeling using the volume fluctuations approach, Int. J. Therm. Sci. 90 (2015) 62–69, http://dx.doi.org/10.1016/j.ijthermalsci.2014.11.028.
[8] S.T. Blanco, C. Rivas, R. Bravo, J. Fernández, M. Artal, I. Velasco, Discussion of the influence of CO and CH_4 in CO_2 transport, injection, and storage for CCS technology, Environ. Sci. Technol. 48 (2014) 10984–10992, http://dx.doi.org/10.1021/es502306k.
[9] H. Lund, T. Flåtten, S.T. Munkejord, Depressurization of carbon dioxide in pipelines – models and methods, Energy Proc. 4 (2011) 2984–2991, http://dx.doi.org/10.1016/j.egypro.2011.02.208.
[10] N.I. Diamantonis, G.C. Boulougouris, D.M. Tsangaris, M.J. El Kadi, H. Saadawi, S. Negahban, I.G. Economou, Thermodynamic and transport property models for carbon capture and sequestration (CCS) processes with emphasis on CO_2 transport, Chem. Eng. Res. Des. 91 (2013) 1793–1806, http://dx.doi.org/10.1016/j.cherd.2013.06.017.
[11] R.M. Woolley, M. Fairweather, C.J. Wareing, C. Proust, J. Hebrard, D. Jamois, V. D. Narasimhamurthy, I.E. Storvik, T. Skjold, S.A.E.G. Falle, S. Brown, H. Mahgerefteh, S. Martynov, S.E. Gant, D.M. Tsangaris, I.G. Economou, G.C. Boulougouris, N.I. Diamantonis, An integrated, multi-scale modelling approach for the simulation of multiphase dispersion from accidental CO_2 pipeline releases in realistic terrain, Int. J. Greenhouse Gas Control 27 (2014) 221–238, http://dx.doi.org/10.1016/j.ijggc.2014.06.001.
[12] Z. Ziabakhsh-Ganji, H. Kooi, Sensitivity of Joule–Thomson cooling to impure CO_2 injection in depleted gas reservoirs, Appl. Energy 113 (2014) 434–451, http://dx.doi.org/10.1016/j.apenergy.2013.07.059.
[13] R.T.J. Porter, M. Fairweather, M. Pourkashanian, R.M. Woolley, The range and level of impurities in CO_2 streams from different carbon capture sources, Int. J. Greenhouse Gas Control 36 (2015) 161–174, http://dx.doi.org/10.1016/j.ijggc.2015.02.016.
[14] Z. Huang, J.H. Li, H.S. Li, L.J. Teng, S. Kawi, M.W. Lai, Effects of polar modifiers on supercritical extraction efficiency for organic template removal from mesoporous MCM-41 materials, J. Supercrit. Fluids 82 (2013) 96–105, http://dx.doi.org/10.1016/j.supflu.2013.06.012.
[15] Z. Huang, J.-H. Li, H.-S. Li, H. Miao, S. Kawi, A.H. Goh, Sep. Purif. Technol. 118 (2013) 120–126, http://dx.doi.org/10.1016/j.seppur.2013.06.047.
[16] F. Gritti, G. Guiochon, Effect of methanol concentration on the speed-resolution properties in adiabatic supercritical fluid chromatography, J.

Chromatogr. A 1314 (2013) 255–265, http://dx.doi.org/10.1016/j.chroma.2013.07.082.
[17] L. Gil, S.T. Blanco, C. Rivas, E. Laga, J. Fernández, M. Artal, I. Velasco, Experimental determination of the critical loci for {n-C_6H_{14} or CO_2 +alkan-1-ol} mixtures. Evaluation of their critical and subcritical behaviour using PC-SAFT EoS, J. Supercrit. Fluids 71 (2012) 26–44, http://dx.doi.org/10.1016/j.supflu.2012.07.008.
[18] A.W. Francis, Ternary systems of liquid carbon dioxide, Chem. Ber. 87 (1954) 1099–1114.
[19] E. Brunner, W. Hültenschmidt, G. Schlichthärle, Fluid mixtures at high pressures IV. Isothermal phase equilibria in binary mixtures consisting of (methanol + hydrogen or nitrogen or methane or carbon monoxide or carbon dioxide), J. Chem. Thermodyn. 19 (1987) 273–291, http://dx.doi.org/10.1016/0021-9614(87)90135-2.
[20] T.A. Berger, J.F. Deye, Composition and density effects using methanol/carbon dioxide in packed column supercritical fluid chromatography, Anal. Chem. 62 (1990) 1181–1185, http://dx.doi.org/10.1021/ac00210a017.
[21] Y. Yong, J. Zhangli, L. Kunyuan, L. Huanzhang, Determination and correlation of saturated liquid density for binary systems of carbon dioxide with acetone, ethyl ether and methanol, J. Chem. Eng. Chin. Univ. 1 (1992).
[22] J.J. Langenfeld, S.B. Hawthorne, D.J. Miller, J. Tehrani, Method for determining the density of pure and modified supercritical fluids, Anal. Chem. 64 (1992) 2263–2266.
[23] L.A. Galicia-Luna, D. Richon, H. Renon, New loading technique for a vibrating tube densimeter and measurements of liquid densities up to 39.5 MPa for binary and ternary mixtures of the carbon dioxide–methanol–propane system, J. Chem. Eng. Data 39 (1994) 424–431.
[24] D. Kodama, N. Kubota, Y. Yamaki, H. Tanaka, M. Kato, High pressure behaviour-liquid equilibria and density behaviours for carbon dioxide + methanol system at 313.15 K, Netsu Bussei 10 (1996) 16–20.
[25] C.J. Chang, C.-Y. Day, C.-M. Ko, K.-L. Chiu, Densities and P-x-y diagrams for carbon dioxide dissolution in methanol, ethanol, and acetone mixtures, Fluid Phase Equilib. 131 (1997) 243–258.
[26] C.J. Chang, K.-L. Chiu, C.-Y. Day, A new apparatus for the determination of P-x-y diagrams and Henry's constants in high pressure alcohols with critical carbon dioxide, J. Supercrit. Fluids 12 (1998) 223–237.
[27] D. Kodama, N. Kubota, Y. Yamaki, H. Tanaka, M. Kato, Partial molar volumes of methanol and ethanol at infinite dilution in supercritical carbon dioxide, Netsu Bussei 12 (1998) 186–190.
[28] D.L. Goldfarb, D.P. Fernández, H. Corti, Dielectric and volumetric properties of supercritical carbon dioxide (1) + methanol (2) mixtures at 323.15 K, Fluid Phase Equilib. 158 (1999) 1011–1019.
[29] R.L. Smith, B.L. Sung, S. Suzuki, C. Saito, H. Inomata, K. Arai, Densities of carbon dioxide + methanol mixtures at temperatures from 313.2 to 323.2 K and at pressures from 10 to 20 MPa, J. Chem. Eng. 47 (2002) 608–612.
[30] K. Bezanehtak, G.B. Combes, F. Dehghani, N.R. Foster, D.L. Tomasko, Behaviour-liquid equilibrium for binary systems of carbon dioxide + methanol, hydrogen + methanol, and hydrogen + carbon dioxide at high pressures, J. Chem. Eng. Data 47 (2002) 161–168.
[31] J.C. Zhang, X.Y. Wu, W.L. Cao, Phase equilibrium properties of supercritical carbon dioxide in binary system, Chem. J. Chin. Univ. 23 (2002) 10–13.
[32] W. Cao, X. Li, J. Zhang, Partial molar volumes of solutes and molecular interaction in binary mixed CO_2-cosolvent supercritical fluids, Huagong Xuebao 55 (7) (2004) 1614–1620.
[33] R. Sih, F. Dehghani, N.R. Foster, Viscosity measurements on gas expanded liquid systems – methanol and carbon dioxide, J. Supercrit. Fluids 41 (2007) 148–157.
[34] M. Maiwald, H. Li, T. Schnabel, K. Braun, H. Hasse, On-line ^{1}H NMR spectroscopic investigation of hydrogen bonding in supercritical and near critical CO_2–methanol up to 35 and 403 K, J. Supercrit. Fluids 43 (2007) 267–275, http://dx.doi.org/10.1016/j.supflu.2007.05.009.
[35] T. Aida, T. Aizawa, M. Kanakubo, H. Nanjo, Relation between volume expansion and hydrogen bond networks for CO_2–alcohol mixtures at 40 °C, J. Phys. Chem. B 114 (2010) 13628–13636.
[36] M. Kariznovi, H. Nourozieh, J. Abedi, Experimental measurements and predictions of density, viscosity, and carbon dioxide solubility in methanol, ethanol, and 1-propanol, J. Chem. Thermodyn. 57 (2013) 408–415.
[37] A.H. Jalili, M. Shokouhi, F. Samani, M. Hosseini-Jenab, Measuring the solubility of CO_2 and H_2S in sulfolane and the density and viscosity of saturated liquid binary mixtures of (sulfolane + CO_2) and (sulfolane + H_2S), J. Chem. Thermodyn. 85 (2015) 13–25.
[38] M.G. Sajilata, M.V. Bule, P. Chavan, R.S. Singhal, M.Y. Kamat, Development of efficient supercritical carbon dioxide extraction methodology for zeaxanthin from dried biomass of *Paracoccus zeaxanthinifaciens*, Sep. Purif. Technol. 71 (2010) 173–177, http://dx.doi.org/10.1016/j.seppur.2009.11.017.
[39] M.V. Bule, R.S. Singhal, Development of a protocol for supercritical carbon dioxide extraction of ubiquinone-10 from dried biomass of *Pseudomonas diminuta*, Bioprocess Biosyst. Eng. 35 (2012) 809–816, http://dx.doi.org/10.1007/s00449-011-0661-5.
[40] Z. Huang, J.H. Li, H.S. Li, H. Miao, S. Kawi, A.H. Goh, Effect of the polar modifiers on supercritical extraction efficiency for template removal from hexagonal mesoporous silica materials: solubility parameter and polarity considerations, Sep. Purif. Technol. 118 (2013) 120–126, http://dx.doi.org/10.1016/j.seppur.2013.06.047.
[41] M.M. Piñeiro, F. Plantier, D. Bessières, J.L. Legido, J.L. Daridon, High-pressure speed of sound measurements in methyl nonafluorobutyl ether and ethyl nonafluorobutyl ether, Fluid Phase Equilib. 222–223 (2004) 297–302, http://dx.doi.org/10.1016/j.fluid.2004.06.013.
[42] D. González-Salgado, J. Troncoso, F. Plantier, J.L. Daridon, D. Bessières, Study of the volumetric properties of weakly associated alcohols by means of high-pressure speed of sound measurements, J. Chem. Thermodyn. 38 (2006) 893–899, http://dx.doi.org/10.1016/j.jct.2005.10.002.
[43] M.J. Dávila, J.P.M. Trusler, Thermodynamic properties of mixtures of *N*-methyl-2-pyrrolidinone and methanol at temperatures between 298.15 K and 343.15 K and pressures up to 60 MPa, J. Chem. Thermodyn. 41 (2009) 35–45, http://dx.doi.org/10.1016/j.jct.2008.08.003.
[44] M. Dzida, L. Waleczek, Speed of sound, density, and heat capacity for (2-methyl-2-butanol + heptane) at pressures up to 100 MPa and temperatures from (293 to 318) K. Experimental results and theoretical investigations, J. Chem. Thermodyn. 42 (2010) 312–322, http://dx.doi.org/10.1016/j.jct.2009.09.001.
[45] F. Peleties, J.J. Segovia, J.P.M. Trusler, D. Vega-Maza, Thermodynamic properties and equation of state of liquid di-isodecyl phthalate at temperature between (273 and 423) K and at pressures up to 140, J. Chem. Thermodyn. 42 (2010) 631–639, http://dx.doi.org/10.1016/j.jct.2009.12.002.
[46] J. Gross, G. Sadowski, Perturbed-chain SAFT: an equation of state based on a perturbation theory for chain molecules, Ind. Eng. Chem. Res. 40 (2001) 1244–1260, http://dx.doi.org/10.1021/ie0003887.
[47] J. Gross, G. Sadowski, Application of the perturbed-chain SAFT equation of state to associating systems, Ind. Eng. Chem. Res. 41 (2002) 5510–5515, http://dx.doi.org/10.1021/ie010954d.
[48] O. Kunz, R. Klimeck, W. Wagner, M. Jaeschke, The GERG-2004 Wide-Range Equation of State for Natural Gases and Other Mixtures; GERG TM15; Fortschr.-Ber. VDI, Reihe 6, Nr. 557, VDI Verlag, Düsseldorf, 2007.
[49] O. Kunz, W. Wagner, The GERG-2008 wide-range equation of state for natural gases and other mixtures: an expansion of GERG-2004, J. Chem. Eng. Data 57 (2012) 3032–3091, http://dx.doi.org/10.1021/je300655b.
[50] I. Velasco, C. Rivas, J.F. Martínez-López, S.T. Blanco, S. Otín, M. Artal, Accurate values of some thermodynamic properties for carbon dioxide, ethane, propane, and some binary mixtures, J. Phys. Chem. B 115 (2011) 8216–8230, http://dx.doi.org/10.1021/jp202317n.
[51] A.F. Estrada-Alexanders, D. Justo, New method for deriving accurate thermodynamic properties from speed-of-sound, J. Chem. Thermodyn. 36 (1995) 419–429, http://dx.doi.org/10.1016/j.jct.2004.02.002.
[52] L.A. Davis, R.B. Gordon, Compression of mercury at high pressure, J. Chem. Phys. 46 (1967) 2650–2660, http://dx.doi.org/10.1063/1.1841095.
[53] T.F. Sun, C.A. Ten Seldam, P.J. Kortbeek, N.J. Trappeniers, S.N. Biswas, Acoustic and thermodynamic properties of ethanol from 273.15 to 333.15 K and up to 280 MPa, Phys. Chem. Liq. 18 (1988) 107–116, http://dx.doi.org/10.1080/00319108808078584.
[54] E.W. Lemmon, M.L. Huber, M.O. McLinden, NIST Standard Reference Database 23: Reference Fluid Thermodynamic and Transport Properties-REFPROP, Version 9.0, National Institute of Standards and Technology, Standard Reference Data Program, Gaithersburg, 2010.
[55] J.H. Hildebrand, R.L. Scott, The Solubility of Nonelectrolytes, Reinhold, New York, 1950.
[56] C.M. Hansen, The universality of the solubility parameter, Ind. Eng. Chem. Prod. Res. Dev. 8 (1) (1969) 2–11, http://dx.doi.org/10.1021/i360029a002.
[57] E.B. Bagley, T.P. Nelson, J.M. Scigliano, Three-dimensional solubility parameters and their relationship to internal pressure measurements in polar and hydrogen bonding solvents, J. Paint Technol. 43 (555) (1971) 35–42.
[58] T. Laursen, VLXE ApS, Scion-DTU, Diplomvej, Denmark, 2012.
[59] M. Kleiner, G. Sadowski, Modeling of polar systems using PCP-SAFT: an approach to account for induced-association interactions, J. Phys. Chem. C 111 (2007) 15544–15553, http://dx.doi.org/10.1021/jp072640v.
[60] N.I. Diamantonis, I.G. Economou, Evaluation of statistical associating fluid theory (SAFT) and perturbed chain-saft equations of state for the calculation of thermodynamic derivative properties of fluids related to carbon capture and sequestration, Energy Fuels 25 (2011) 3334–3343, http://dx.doi.org/10.1021/ef200387p.
[61] D. Tapriyal, R. Enick, M. McHugh, I.K. Gamwo, B. Morreale, High Temperature, High Pressure Equation of State Density Correlations and Viscosity Correlations; NETL-TRS-1-2012, National Energy Technology Laboratory, 2012.
[62] O. Pfohl, Evaluation of an improved volume translation for the prediction of hydrocarbon volumetric properties, Fluid Phase Equilib. 163 (1999) 157–159.
[63] R. Span, W. Wagner, A new equation of state for carbon dioxide covering the fluid region from the triple-point temperature to 1100 K at pressures up to 800 MPa, J. Phys. Chem. Ref. Data 25 (6) (1996) 1509–1596, http://dx.doi.org/10.1063/1.555991.
[64] K.M. de Reuck, R.J.B. Craven, Methanol, International Thermodynamic Tables of the Fluid State – 12, IUPAC, Blackwell Scientific Publications, London, 1993.
[65] C.W. Lin, J.P.M. Trusler, Speed of sound in (carbon dioxide + propane) and derived sound speed of pure carbon dioxide at temperatures between (248 and 373) K and at pressures up to 200 MPa, J. Chem. Eng. Data 59 (2014) 4099–4109, http://dx.doi.org/10.1021/je5007407.
[66] S.J. Ball, J.P.M. Trusler, Speed of sound of n-hexane and n-hexadecane at temperatures between 298 and 373 K and pressures up to 100 MPa, Int. J. Thermophys. 22 (2001) 427–443, http://dx.doi.org/10.1023/A:1010770730612.